NATIONAL AND KAPODISTRIAN UNIVERSITY OF ATHENS

SCHOOL OF HEALTH SCIENCES

DEPARTMENT OF PHARMACY

DOCTORAL DISSERTATION

Studies of the Membrane Influenza A/M2 Protein with Aminoadamantane Drugs Using Experimental and Computational Biophysics

ATHINA KONSTANTINIDI

Chemist

ATHENS

DECEMBER 2021

DOCTORAL DISSERTATION

Studies of the Membrane Influenza A/M2 Protein with Aminoadamantane Drugs Using Experimental and Computational Biophysics

ATHINA KONSTANTINIDI

SUPERVISOR

Antonios Kolocouris**,** Professor, National and Kapodistrian University of Athens (NKUA)

THREE-MEMBER COMMITTEE

Antonios Kolocouris, Professor, NKUA

Emmanuel Mikros, Professor, NKUA

Andrew Tsotinis, Professor, NKUA

SEVEN-MEMBER EXAMINATION COMMITTEE

Antonios Kolocouris, Professor, NKUA

Emmanuel Mikros, Professor, NKUA

Andrew Tsotinis, Professor, NKUA

Costas Demetzos, Professor, NKUA

Santiago Vazquez, Professor, University of Barcelona

Thomas Mavromoustakos, Professor, NKUA

Ioannis Papanastasiou, Assistant Professor, NKUA

PhD THESIS PRESENTATION 20/12/2021

ABSTRACT

Chapter 1 refers to the description of the basic features for influenza A virus replication, with emphasis on the function of influenza A M2.

In **Chapter 2**, is described the structure of influenza A matrix 2 (M2) wild type (WT) proton protein channel, which is an archetypal ion channel. It is the target of the antiviral drugs amantadine and rimantadine. A number of methods were used to understand structural and functional features of this channel included neutron diffraction, electrophysiology, solution NMR spectroscopy, solid state NMR (ssNMR) spectroscopy, X-ray crystallography etc during an adventure of three decades with a lot of controversies.

The experimental structure of influenza A M2(22-46) transmembrane domain (M2TM), the pore of the M2 protein channel, was solved in 2000 and X-ray structures of its complexes with amantadine, rimantadine etc were published by 2018. Till now basic characteristics of the influenza A M2 conductance domain (CD) protein M2CD or M2AH including M2TM and the amphipathic helices (46-62) have been also solved using ssNMR.

The basic features of the experimental biophysical methods used in this PhD thesis, i.e. Differential Scanning Calorimetry (DSC), X-ray scattering at small and wide angles (SAXS/WAXS) and ssNMR are discussed in **Chapter 3**.

Aminoadamantane drugs, e.g. amantadine and rimantadine, are lipophilic amines that bind to membrane embedded influenza A WT M2 protein. In **Chapter 4**, are investigated the comparative perturbation effects exerted by the influenza M2 WT protein inhibitors amantadine and it's spiro[pyrrolidine-2,2'-adamantane] variant AK13 to membrane bilayers using biophysical methods and molecular dynamics (MD) simulations. This is a work performed in close collaboration with Professor's Thomas Mavromoustakos and Professor's Costas Demetzos groups as well as Dr Barbara Sartori and Professor Heinz Amenitsch.

The experimental biophysical methods used included, DSC, X-ray scattering and ssNMR. All three experimental methods pointed out that the two analogs perturbed drastically the DMPC bilayers with AK13 to be more effective at high concentrations. At high ligand concentrations AK13 was tolerated in lipid bilayers while *Amt* was crystallized. This is an important consideration in possible

formulations of these drugs as it designates a limitation of aminoadamantane drug incorporation.

MD simulations provided details about the strong interactions of the drugs in the interface region between glycerol backbone and lipophilic segments. The two drugs form hydrogen bonding with both water and *sn*-2 carbonyls or phosphate oxygens. Such localization of the drugs explains their strong perturbing effect evidenced by all biophysical methodologies applied.

In **Chapter 5**, is described our work to investigate the interactions of M2TM WT with bilayers. This is a work performed in close collaboration with Professor Thomas Mavromoustakos, Professor Costas Demetzos, groups as well as Dr Barbara Sartori and Professor Heinz Amenitsch. The M2TM peptide was synthesized by Professor Thedoros Tselios group. We focused on (a) the characterization of changes in bilayer organization from changes in micromolar concentrations of M2TM WT without or with aminoadamantane (*Aamt*) ligands, and from changes in *Aamt* ligand structure included with M2TM, (b) exploring how common biophysical methods can be applied to identify the membrane perturbations effected by the protein without or with the ligand.

A variety of biophysical methods, including DSC, SAXS/WAXS, MD simulations, and one-dimension (1D) ssNMR, were used to study two micromolar concentrations of M2TM without or with a small excess of amantadine or its spiro-pyrrolidine analogue, AK13, in DMPC bilayers.

DSC and SAXS showed that at a low micromolar M2TM concentration, two lipid domains are observed, which likely correspond to M2TM boundary lipids and bulk lipids. At a higher M2TM concentration, only one domain is identified, indicating that all of the lipids behave as boundary lipids.

^{1}H and ^{31}P ssNMR showed that M2TM in either apo or drug-bound form spans the membrane, interacting strongly with lipid acyl chain-tails and the phosphate groups of the polar head surface. The ^{13}C ssNMR experiments allowed the inspection of excess drug molecules and the assessment of their impact on the lipid head group region.

According to SAXS, WAXS, and DSC, in the absence of M2TM both aminoadamantane drugs exert a similar perturbing effect on the bilayer at low

concentrations, i.e., mole fractions (relative to lipid) of x=0.05-0.08. At the same concentrations of the drug when M2TM is present, the amantadine and, to a lesser extent, AK13 cause a significant disordering of chain-stacking. This different effect between the two drugs is likely due, according to the MD simulations, to the preference of the excess of the more lipophilic AK13 to locate closer to M2TM. In contrast, amantadine perturbs the lipids through the stronger ionic interactions of its ammonium group with phosphate groups (compared with the buried ammonium group in AK13) and influences the formation of two lipid domains. The preference of AK13 to concentrate inside the lipid may contribute to its six-fold higher binding affinity (compared to amantadine) if drug binding occurs from the lipid by way of a path between the transmembrane helices.

The results showed that DSC and SAXS are useful methods to detect changes in membrane organization caused by small changes in M2TM or aminoadamantane drug concentration and structure and that WAXS and MD simulations can suggest details of ligand topology.

Water-mediated interactions play key roles in drug binding. In protein sites with sparse polar functionality, a ligand-based only approach is often viewed as insufficient to achieve high affinity and specificity. In **Chapter 6**, are showed that small molecules, i.e. amantadine and rimantadine, can enable potent inhibition by targeting key waters using as example the M2 WT proton channel of influenza A which is the target of the antiviral drugs amantadine and rimantadine. This is a work performed in close collaboration with Professor William DeGrado and Associate Professor Jun Wang groups. Structural studies of drug binding to the channel using X-ray crystallography have been limited due to the challenging nature of the target, with the first crystal structure solved in 2008 limited to 3.5 Å resolution. We described crystal structures of amantadine bound to M2 in the $Inward_{closed}$ conformation (2.00 Å), rimantadine bound to M2 in both the $Inward_{closed}$ (2.00 Å) and $Inward_{open}$ (2.25 Å) conformations, and a spiro-adamantyl amine inhibitor bound to M2 in the $Inward_{closed}$ conformation (2.63 Å). These X-ray crystal structures of the M2 proton channel with bound inhibitors reveal that ammonium groups bind to water-lined sites, formed by two layers of waters close to Ala30 and Gly34, respectively, observed in the X-ray structures, that are hypothesized to stabilize transient hydronium ions formed in the proton-

conduction mechanism. Furthermore, the ammonium and adamantyl groups of the adamantyl-amine class of drugs are free to rotate in the channel, minimizing the entropic cost of binding. The MD simulation reproduced perfectly the X-ray structures of cautiously tuned. These drug-bound complexes provide the first high-resolution structures of drugs that interact with and disrupt networks of hydrogen-bonded waters that are widely utilized throughout nature to facilitate proton diffusion within proteins.

The V27A mutation confers amantadine resistance to the influenza A M2 WT proton channel and is becoming more prevalent in circulating populations of influenza A virus. In **Chapter 7**, is described our collaborative work with DeGrado and Wang groups to solve M2TM V27A structure in complex with a spiro-adamantyl amine inhibitor bound to M2(22-46) V27A and also to M2(21-61) V27A in the $Inward_{closed}$ conformation using X-ray crystallography and MD simulations. The spiro-adamantyl amine binding site is nearly identical for the two crystal structures. Compared to the M2 WT with valine at position 27, we observed that the channel pore is wider at its N-terminus as a result of the V27A mutation and that this removes V27 side chain hydrophobic interactions that are important for binding of amantadine and rimantadine. The spiro-adamantyl amine inhibitor blocks proton conductance in both the WT and V27A mutant channels by shifting its binding site in the pore depending on which residue is present at position 27. Additionally, in the structure of the M2(21-61) V27A construct, the C-terminus of the channel is tightly packed relative to the M2(22-46) construct. We observed that residues Asp44, Arg45, and Phe48 face the center of the channel pore and would be well-positioned to interact with protons exiting the M2 channel after passing through the His37 gate. However, the orientation of AHs after residue 48 did not reproduce the almost vertical orientation as regards the M2TM, that found by Professor Tim Cross experimentally with ssNMR experiments. The MD simulations of the M2(22-46) V27A - spiro-adamantyl amine complex predicted with accuracy the position of the ligands and waters inside the pore in the X-ray crystal structure of the M2 V27A complex.

The influenza A M2 wild type proton channel is the target of the anti-influenza drug rimantadine. Rimantadine has two enantiomers, though most investigations into drug binding and inhibition have used a racemic mixture. ssNMR experiments

by Professor Tim Cross have shown significant spectral differences that were interpreted to indicate tighter binding for (*R*)- vs. (*S*)- rimantadine. However, it was unclear if this is due to the specific condition of the ssNMR experiments (i.e. close to 0 ^{o}C), correlates with a functional difference in drug binding and inhibition and we undertook to investigate this in collaboration with Professor DeGrado, Associate Professor Jun Wang and Professor Jon Essex. Thus, in **Chapter 8**, using X-ray crystallography, we have determined that both (*R*)- and (*S*)-rimantadine bind to the M2 pore with slight differences in the hydration of each enantiomer. However, this did not result in a difference in potency or binding kinetics, as we measured similar values for k_{on}, k_{off}, and K_d in electrophysiological assays and EC_{50} values in cellular assays. We concluded that the slight differences in hydration we observed in the X-ray structures for the (*R*)- and (*S*)-rimantadine enantiomers were not relevant to drug binding or channel inhibition. To further explore the effect of the hydration of the M2 pore on binding affinity, the water structure was evaluated by waters titration calculations Grand Canonical Monte Carlo simulations as a function of the chemical potential of the water. Initially, the two layers of ordered water molecules between the bound drug and the channel's gating His37 residues mask the drug's chirality. As the chemical potential becomes more unfavorable and the waters from the two layers were removed from the M2 pore, the drug translocated down to the lower water layer, towards the His37 at the C-terminus of M2TM, and the interaction becomes more sensitive to chirality. These studies suggested the feasibility of displacing the upper water layer (toward the N-end close to Ala30) and specifically recognizing the lower water layers by novel chiral drugs.

SUBJECT AREA: Computational and experimental biophysics

KEYWORDS: influenza A M2, X-ray, ssNMR, SAXS/WAXS, DSC, MD simulations, amantadine, rimantadine, DMPC, GCMD simulations, kinetic studies, k_{on}, k_{off}, channel hydration, waters titration calculations

ACKNOWLEDGEMENTS

First of all I would like to thank my supervisor Professor Antonios Kolocouris, for the opportunity he gaved me to work on this project under his constant guidance also for his scientific support and encouragement during the research and the writing of this thesis.

Next, I would like to acknowledge Professor Thomas Mavromoustakos for his great help in performing the ssNMR and SAXS/WAXS experiments, presentation of the plots and peaks assignment. Then, Professor Costas Demetzos and his group members Dr Nikolaos Naziris and Dr Maria Chountoulesi for running the DSC experiments.

I thank Professor Thedore Tselios for the synthesis of the M2TM WT peptide. Professor Heinz Amenitsch and Dr Barbara Sartori, Trieste Italy for their help with SAXS/WAXS data acquisition and Dr Mali for running the ssNMR experiments in Slovenia.

I also thank Professor Jonathan Essex and Dr Marley Samways for GCMD simulations. Dr George Lamprinidis for simulations algorithms and computer maintanace.

Professor Emmanuel Mikros and Professor Andrew Tsotinis which are members of my three-member thesis committee, for their useful remarks and suggestions.

Professor Santiago Vazquez and Assistant Professor Ioannis Papanastasiou for their collaboration and insightful comments.

I would like to thank Chiesi Hellas for the financial support that provided me throughout my PhD thesis, CERIC program for providing the funding to travel abroad and running the SAXS/WAXS experiments in Trieste, Italy and ssNMR in Ljubljana, Slovenia and ARIS for providing supercomputer time for the simulations.

My lab partners Dr Panagiotis Lagarias, Marianna Stampolaki, Dimitirs Stamatis, Dimitris Kolokouris, Eva Tzortzini, Margarita Stampelou, Dr Christina Tzitzoglaki and Dr Eleni Vrontaki for the scientific atmosphere in the laboratory.

TABLE OF CONTENTS

LIST OF FIGURES

LIST OF TABLES

CHAPTER 1

Influenza A/M2 Protein Structure and Function

1.1 Influenza A virus

Influenza A virus is a species of the genus *Alpha influenza virus* of the virus family *Orthomyxoviridae with* enveloped virion and contains a segmented single-stranded negative-sense RNA genome (-)RNA. The virus particles or virions are usually spherical with diameter of 100 nm or are filamentous with a length of reaching 300 nm [1-3] and are surrounded by an envelope. The viral envelope is a lipid bilayer which accommodates two types of surface or spike glycoproteins, the hemagglutinin (HA) and the neuraminidase (NA), which are the two main surface antigenic determinants of the virus, anchored in lipid raft domains, as well as the transmembrane protein matrix-2 (M2), not tightly associated with lipid rafts. [3-5] The matrix-1 (M1) protein is underneath the membrane and the virion core (see Figure 1.1).

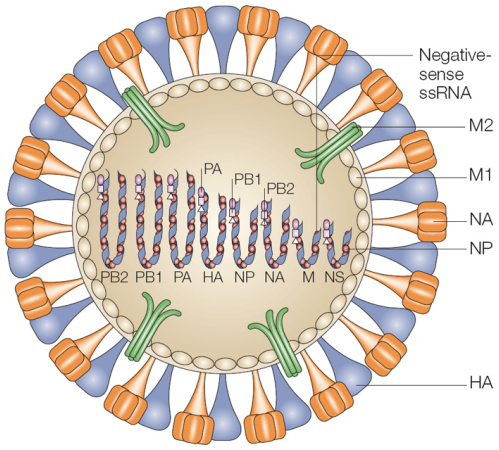

Figure 1.1: Structure of an influenza A virus particle. [6]

The HA protein is responsible for the attachment of the virus to neuraminic acid of the host cellular receptors and the penetration of the virus into the cells. The NA protein functions through an enzymatic cleavage of neuraminic acid from cell surface receptors and is crucial for releasing newly formed virions from infected cells. [5, 7] M2 protein forms a homotetramer, functioning as a proton-selective ion channel, playing a critical role in the early phase of infection leading to the virus uncoating through HA conformational change and release of the viral

ribonucleoproteins (vRNPs) from M1 protein at low pH as well as virus budding. [7-9] The virion core consists of negative stranded viral RNAs (vRNAs) incorporated in helical vRNPs, nucleoprotein (NP), as well as lower quantities of nuclear export protein (NEP) and the heterotrimeric RNA-dependent RNA polymerase complex (3P complex) formed by three polymerase subunits (PB1, PB2, PA). [2, 3, 5, 7] vRNPs is comprised by eight viral RNA (vRNA) segments (PB2, PB1, PA, HA, NP, NA, M and NS genes) encoding the viral proteins. [5, 10]

1.2 Infection and replication cycle of influenza A virus

Regardless of the cell type, the first step of the infection pathway is the attachment of the viral HA glycoprotein to terminal sialic acid (SIA) in glycoproteins and glycolipids on the surface of the target cell (see Figure 1.2). [4]

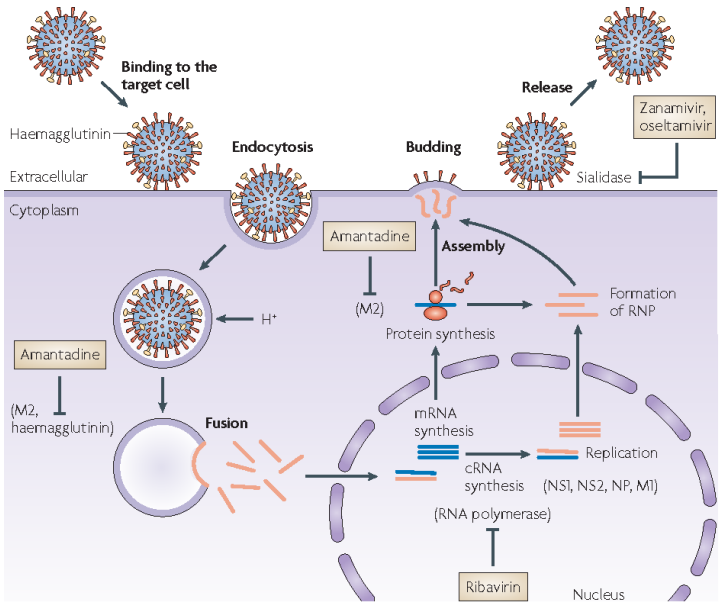

Figure 1.2: The infection process of influenza A virus cycle. A/M2 protein channel acidifies the virion with concomitant uncoating of the viral RNA. [11]

Subsequently to the virus attachment, virus enters cell by receptor-mediated endocytosis, then moves from endocytic vesicles to early endosomes and finally to late endosomes. Inside late endosomes the viral HA is activated through a pH-dependent conformational change, uncovering the fusion peptide, which is

responsible for fusion by attaching to the endosomal membrane and releasing viral genes. [12, 13] The M2 ion channel acidifies the interior of the virus particle, resulting in the dissociation of M1 from the viral ribonucleoproteins (vRNPs). [12] Uncoated vRNPs are released through the fusion pore into the cytosol and then imported into the host cell nucleus, serving as templates for genome transcription and replication processes from host cell replicases. [13, 14] After replication of the viral genome, synthesis of viral mRNAs and translation of more than ten different viral proteins, an assembly of the new virions at the host cell surface occurs. [4] The HA and NA glycoproteins as well as M2 protein are positioned to lipid rafts resulting in plasma membrane deformation and M2 mediated membrane scission initiating virus budding. Viral glycoprotein NA cleaves SIA, preventing virus aggregation at the cell surface and mediate release of newly synthesised virions from infected cells. [15]

1.3 Biochemical and functional role of A/M2 protein

The M2 protein ion channel of influenza A (A/M2) has received much attention in recent years due to virus increased drug resistance caused by mutant strains and genetic reassortment. Influenza A/M2 protein plays key roles during the early and late stages of the virus life cycle. The A/M2 protein forms a membrane-spanning homotetrameric and it is acid-activated proton selective channel. [16-21] When the virus enters the infected cell by endocytosis, the influenza M2 channel is activated in response to the lowered pH of the endosome, resulting in proton transport into the virus interior, which triggers the dissociation of the viral RNA from M1 protein and the fusion of the viral and endosomal membranes. After these events the viral RNA is released to the cytoplasm and replicated by the host cell. [17, 22, 23] In later stage of virus replication, the M2 protein maintains the high pH of the trans-Golgi network and thus prevents the premature conformational change of HA at low pH which triggers the HA-induced fusion. [24] As mentioned before, M2 protein also effectes plasma membrane deformation and membrane scission, which is needed for virus budding.

The A/M2 protein is a 97-residue single-pass membrane homotetrameric protein. It contains a short unstructured N-terminal extracellular domain (residues 1-21) which is highly conserved and suggest to assists M incorporation into the virion [25], a single transmembrane (TM) domain (residues 22-46), and a long C-terminal intracellular tail (residues 47-97) which interact with the M1 protein. [26, 27]

The channel activity is associated with a single TM helix that as a tetramer forms a pore, which is interrupted by the H37xxxW41 sequence in the C-terminal half of the TM helix (see Figure 1.3), a characteristic motif for influenza proton channels. It is the unique chemistry of these four H37xxxW41 moeties of M2 tetramer that accounts for acid activation, proton selectivity and gating of the channel. [28]

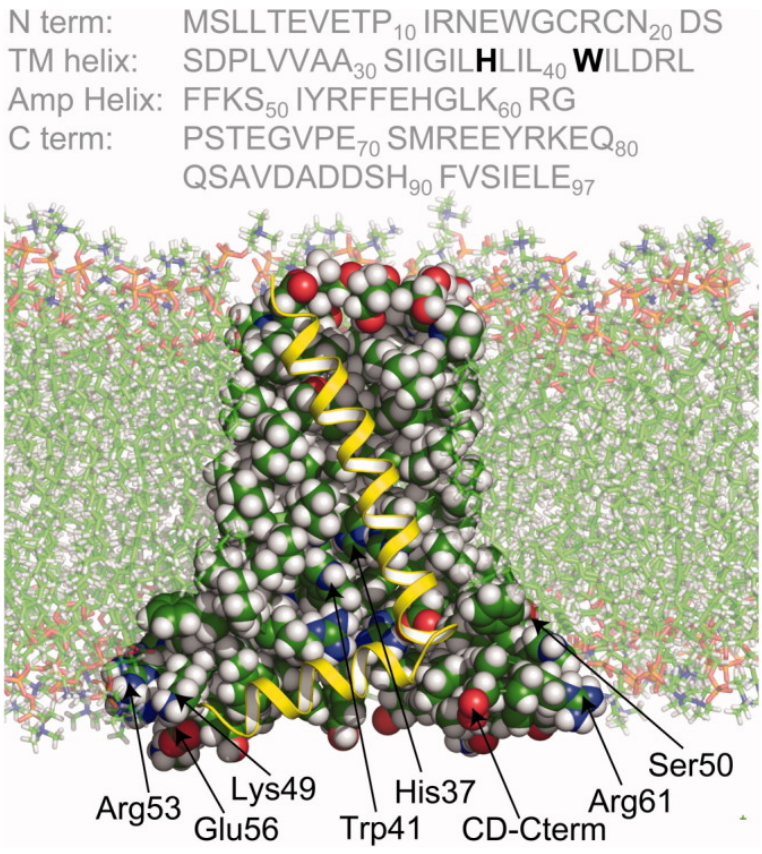

Figure 1.3: The amino acid sequence and functional domains of the C50S M2 protein from influenza A virus. The 22 amino acids of N-terminal domain have an unknown function but could induce tetramer stabilization via inter-chain disulfide bond formation of Cys17 and Cys19. The amino acids 23–46 form a TM helix, with the signature H37xxxW41 motif located in the C-terminal domain, amino acids 47–62 form an amphipathic helix (AH). The TM and AHs tetramer,

produce the channel properties of the full-length protein. [29] The structure (PDB ID 2L0J) of this conductance domain, characterized and refined in liquid crystalline lipid bilayers, [30] is shown in spacing-filling mode for the sidechains of three chains and as a yellow ribbon for the fourth chain. Some of the key residues are labeled. The C-terminal 35 amino acids bind the M1 protein. [31]

The transmembrane domain of A/M2 protein (A/M2TM) comprises the pore of the proton channel. The A/M2TM is the minimal construct needed for tetramerization, selective proton transport and amantadine binding since the rate of conductance of the A/M2TM domain and the inhibition by *Amt* correspond to those of the full-length protein. [29, 32-35] Aminoadamantane (*Aamt*) class of antiviral drugs such as, amantadine or 1-aminoadamantane (*Amt*) and rimantadine or *α*-methyl-1-adamantane-methalamine (*Rim*) (see Figure 1.4), inhibit M2 wild type (WT) proton by blocking proton conductance mediated through A/M2TM. [36]

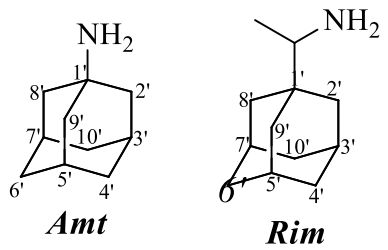

***Figure 1.4*:** Structures of amantadine (*Amt*) and rimantadine (*Rim*).

In M2TM domain, histidine 37 (His37) is the proton-conducting residue of the channel [37] and Trp41 is the channel-gating residue. [38] The open state of the channel is a result of the low pH in the viral endosome, when the imidazole rings of the four His37 residues are protonated causing opening of channel by electrostatic repulsion and destabilization of helix-helix packing. The His37 tetrad is located near the center of the channel acting as a pH sensor and control the activation of the channel at pH lower than 6.0, leading ultimately to the unpacking of the influenza viral genome and to pathogenesis. [39] His37 is a filter conducting selectively only protons rather than other cations and serves as a shuttle that is sequentially protonated and deprotonated as an excess proton transits the activated channel. Inside the pore, ordered waters form continuous hydrogen-

bonding networks that span the pore from the Val27 tetrad to His37 and transport protons. [40, 41] Under basic conditions the imidazole ring of the His37 residues at $N_{\delta 1}$ are deprotonated and the Trp41 side chains, C-ward from His37, effectively block proton flow by forming hydrogen bonding interactions with imidazoles of His37 (see Figure 1.4). [42] Thus, Trp41 tetrad form a pH-dependent gate that prevent proton flow through the pore. [35, 38] The cooperativity between the protonation state of the His37 tetrad and conformations of the protein backbone and Trp41 side chains is critical for the pH dependent activation mechanism of the channel which allows proton transport only from the N-end to the C-end direction. [30, 43, 44]

While the function of the N-terminal 22 amino acids is not well characterized, the C-terminal 35 amino acids are associated with binding the M1 protein. The structure for neither of these terminal segments are known for M2 from Influenza A (AM2), but the C-terminal segment of the Influenza B M2 protein (BM2), which has no sequence homology with the counterpart of AM2, has been characterized as well as a complex with the M1 protein. [45] Between the TM helix and the M1-binding segment of M2 is an amphipathic helix (AH, residues 47–62) that is located in the membrane inner interface and is important for viral budding. [46] It is thought that this amphipathic helix induces membrane curvature required for viral budding that arises from raft-like domains rich in cholesterol and sphingomyelin. [27, 47] The amphipathic helix appears to have a cholesterol recognition amino acid consensus motif indicative [48] of a cholesterol binding site, and Cys50 in the amphipathic helix is known to be palmitylated (see Figure 1.3), a post-translational modification that is sometimes found to accompany cholesterol binding. [49] The combination of the TM and amphipathic helices, known as the conductance domain, in synthetic lipid bilayers appears to contain all of the residues and interactions with the environment necessary for achieving the detailed conductance properties of the native protein in oocytes. [29] According to functional studies the C-terminal domain is crucial for a stable tetramer formation, [33, 50] native-like conductance [51] and sensitivity to rimantadine. [52] Thus, M2AH comprises the functional core of M2.

CHAPTER 2

Influenza A/M2 Protein Structure

2.1 Experimental M2 protein structures by different biophysical methods

More than a dozen high-resolution structures of the influenza A M2 protein using X-ray crystallography, solution and solid-state NMR spectroscopy as well as structural data from infrared spectroscopy, have been obtained and elevate the mechanistic understanding of the M2 protein to atomic level and glean a considerable understanding of the influence of membrane mimetic environments on membrane protein structure. [53, 54] Additionally, because of the different sample requirements of these techniques, the structures were solved in different membrane mimetic media, making M2 protein channel a valuable case for understanding how conformation of a membrane protein is affected by the membrane-like environment. [16, 54]

An assortment of these structures is shown in Figure 2.1 and Table 2.1 presents detailed information about the samples and the methods of characterization as well as some key structural features. Even though these structures are not of the full-length protein, there has been considerable structural and functional validation of the constructs and of the use of synthetic lipid bilayers as models of the native membrane environment. As a result, there are numerous important ramifications for the structures of helical membrane proteins determined in a wide range of detergent-based membrane mimetics that are being deposited in the Protein Data Bank (PDB).

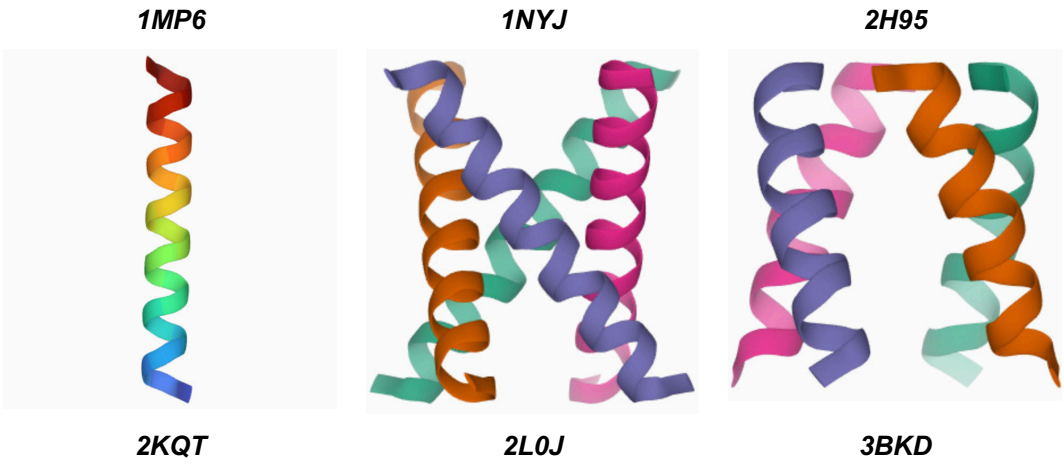

3C9J

3LBW

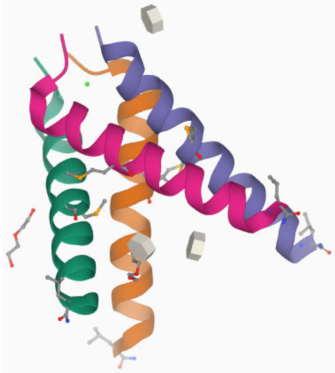

2RLF

2KWX

2LJC

4QKC

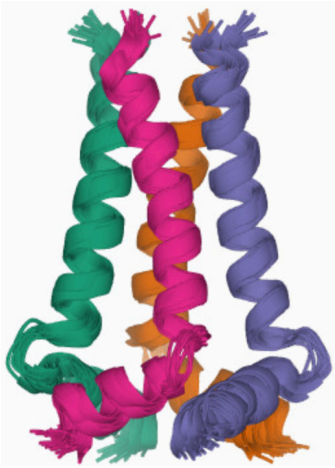

4QK7

4QKL

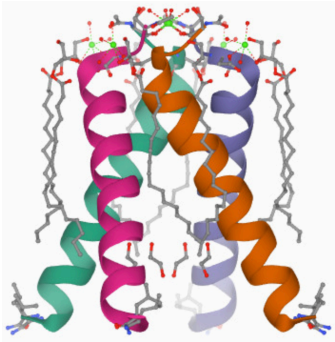

4QKM

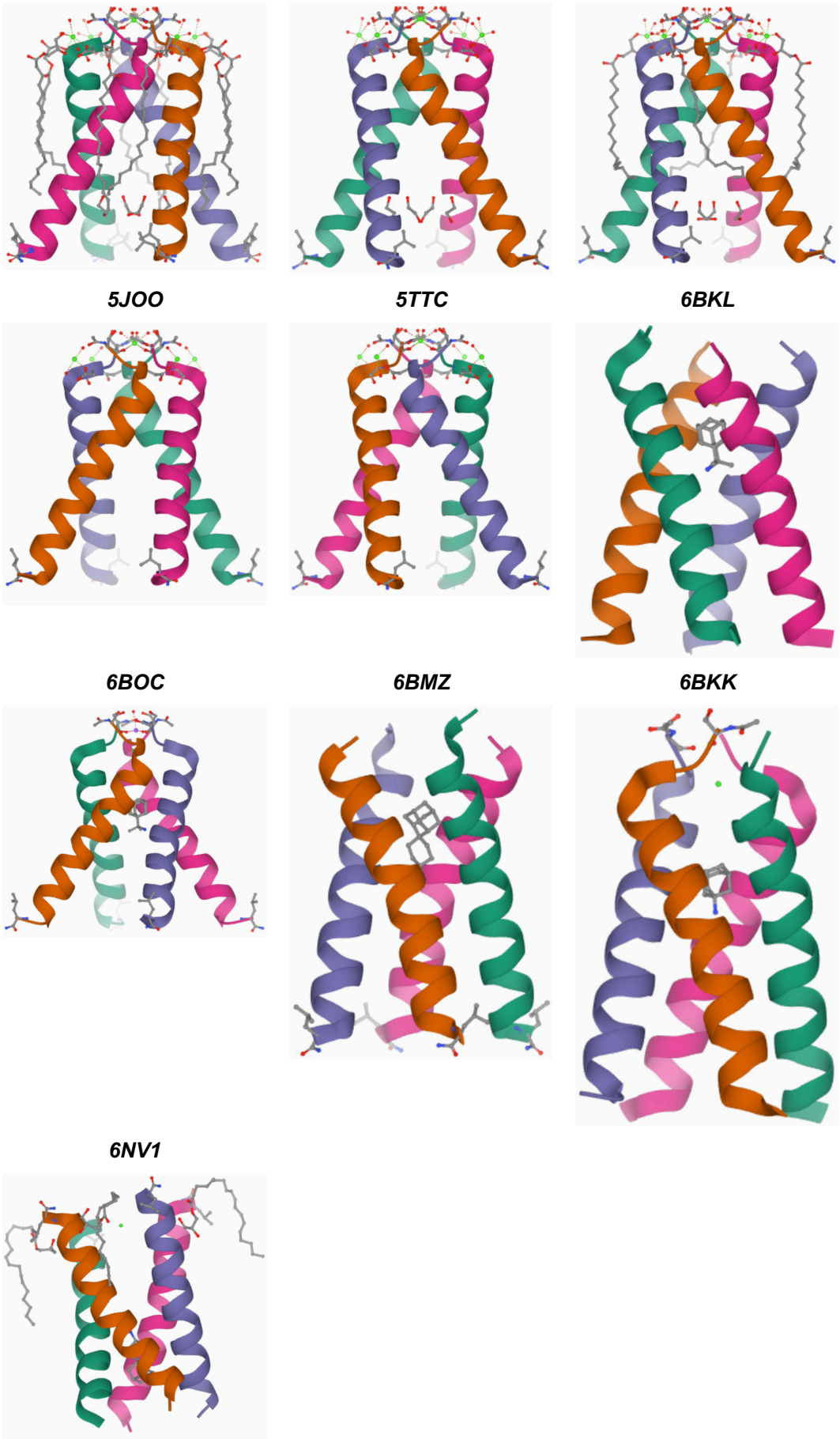

Figure 2.1: Various M2 protein structures

Table 2.1: Information for various M2 protein structures

PDB ID	Construct	Environment	pH	X-ray or NMR	Drug	Helix tilt (º)[a]
1MP6 [55] (2002)	Ser22-Leu46	DMPC bilayer	7.0	ssNMR		38
1NYJ [56] (2003)	Ser22-Leu46	DMPC bilayer	7.0	ssNMR		38
2H95 [57] (2006)	Ser22-Leu46	DMPC bilayer	8.8	ssNMR	Amt in pore	30 N; 21 C
2KQT [58] (2009)	Ser22-Leu46	DMPC bilayer	7.5	ssNMR	Amt in pore	32 N; 18 C
2L0J [30] (2010)	Ser22-Gly62 (C50S)	DOPC/DOPE bilayer	7.5	ssNMR		32 N; 22 C
3BKD [34] (2007)	Ser22-Leu46 (I33SeM)	OG/PEG bilayer-like	7.3	X-ray (2.05Å)		33
3C9J [34] (2008)	Ser22-Leu46 (G34A)	OG/PEG bilayer-like	5.3	X-ray (3.50Å)	Amt in pore	36
3LBW [43] (2010)	Pro25-Leu46 (G34A)	OG/PEG bilayer-like	6.5	X-ray (1.65Å)		32 N; 17 C
2RLF [50] (2007)	Arg18-Lys60 (C50S)	DHPC micelles	7.5	solution NMR	Rim in external site	16
2KWX [59] (2010)	Arg18-Lys60 (V27A, C50S)	DHPC micelles	7.5	solution NMR		15
2LJC [60] (2011)	Arg18-Gly52 (C19S)	DHPC micelles	7.5	solution NMR	Rim in pore	
4QKC [40] (2014)	Ser22-Leu46	LCP crystallization	5.5	X-ray (1.10Å)		
4QK7 [40] (2014)	Ser22-Leu46	LCP crystallization	8.0	X-ray (1.10Å)		
4QKL [40] (2014)	Ser22-Leu46	LCP crystallization	8.0	X-ray (1.71Å)		

4QKM [40] (2014)	Ser22-Leu46	LCP crystallization	5.5	X-ray (1.44Å)		
5JOO [41] (2016)	Ser22-Leu46	LCP crystallization	5.5	X-ray (1.41Å)		
5TTC [41] (2016)	Ser22-Leu46	LCP crystallization	8.0	X-ray (1.40Å)		
6BKL [61] (2017)	Ser22-Leu46	LCP crystallization	4.5	X-ray (2.00Å)	Rim in pore	
6BOC [61] (2017)	Ser22-Leu46	LCP crystallization	3.5	X-ray (2.00Å)	Rim in pore	
6BMZ [61] (2017)	Ser22-Leu46	LCP crystallization	7.0	X-ray (2.63Å)	spiroadamantyl amine in pore	
6BKK [61] (2017)	Ser22-Leu46	LCP crystallization	5.6	X-ray (2.00Å)	Amt in pore	
6NV1 [62] (2019)	Ser22-Leu46 (V27A)	LCP crystallization	7.5	X-ray (2.50Å)	spiroadamantyl amine in pore	

[a] Tilt angles were calculated using residues 23 to 46 for the TM helix or using residues 23 to 32 and 35 to 46 separately for the N-terminal and C-terminal halves when a kink near Gly34 is apparent. Fewer residues were used when terminal residues were either missing or not helical; these exceptions were: 2H95, starting at residue 24 and ending at residue 43; and 2KQT and 3C9J, both starting at residue 24; 2H95 and 3LBW each had two residues added at the N-terminus, by modeling after 2KQT and 2L0J, respectively. SeM, selenomethionine; OG, octylglucoside; PEG, polyethylene glycol; *Amt*, amantadine; *Rim*, rimantadine.

2.2 Early models of M2: 1980-2000

Even before the first experimental structure for the M2TM domain was determined, molecular modeling was used, [63] in conjunction with experimental restraints such as from cysteine scanning or site-directed infrared dichroism [64-68], and solid-state NMR (ssNMR) spectroscopy [55, 57, 68-71] to build structural models. [63, 65, 66, 72]

Before the availability of high-resolution structures, the binding site of *Amt* and *Rim* has been predicted from the location of drug resistance mutations by Hay, who was the first to suggest M2 as the target of *Amt*, Lamb and Pinto [12, 73] Most of the residues in certain positions, i.e. Val27, Ala30, Ser31 and Gly34, were

predicted to face the channel interior leading to the correct hypothesis that the drugs bind inside of the channel.

Using mutagenesis analysis these early models also suggested that adamantyl ring of *Amt* or *Rim* is located within the M2TM pore (see Figure 2.2) a hydrophobic pocket formed predominantly by the side chains of Val27 and Ala30 blocking the transport of proton flow mediated through M2 pore. [12]

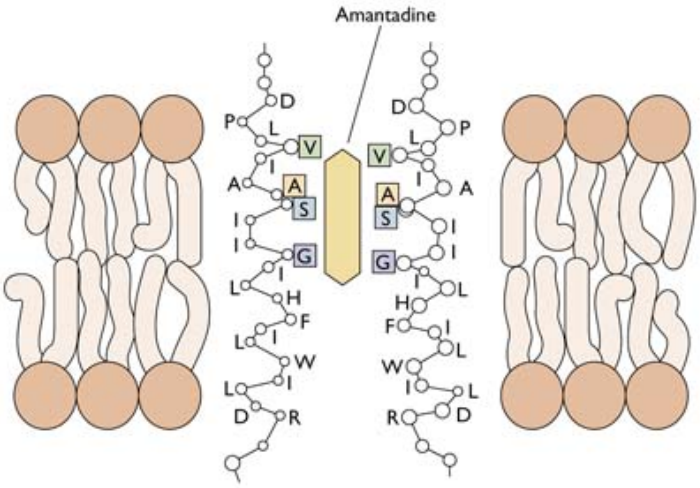

***Figure 2.2*:** Schematic illustration of *Amt* complexed inside the lumen of A/M2TM and interacting with the pore-lining residues Val27, Ala30, Ser31 and Gly34. The *Amt*-M2TM complex is inside lipid bilayers. [63]

Initially, the small size of M2 membrane protein made it difficult to crystalize and obtain high-resolution structures. However, a long struggle solution NMR technology demonstrated the capability of tackling oligomeric channel-like membrane protein systems. [74] Similarly, solid state NMR (ssNMR) advances resulted in spectrum resolution similar to solution NMR but in native membrane environment for these proteins.

The first study using ssNMR which examined the M2TM in hydrated dimyristroylphosphotidylcholine (DMPC) lipid bilayers was published in 1997 by Cross and used isotopically labelled peptide samples and mechanically aligned between thin glass plates to obtain orientational constraints. Molecular frame was also constrained with respect to the magnetic field, by utilizing ^{15}N chemical shifts from single site labelled samples. These constraints were applied to the peptide

resulting in a uniform α-helix, and a tilt of the helix with respect to the bilayer normal to be 33 ± 3°. Since the orientation about the helix axis was determined within an error of ± 30°, it indicated that the packing of this tetrameric protein is in a left-handed four-helix bundle. It was suggested that only hydrophilic residues can align to the channel axis when the tilt angle is so large. [69]

2.3 First structures of M2 in protein data bank: 2000-2010

The first M2 protein structures in the PDB were deposited in 2002 by Cross of the TM helix monomer and tetramer at pH 7.0 showing a left-handed helical bundle with Val27, Ser31, Gly34, His37, and Trp41 lining the pore i.e. PDB ID 1MP6 and 1NYJ respectively (see Figure 2.1), [56, 75] and are based on high resolution OS ssNMR spectroscopy of the polypeptide backbone in synthetic lipid bilayers. The helix tilt of 38º was greater than previously envisioned based on cross-linking studies [64] and MD simulations. [72] However, the helix tilt and rotation angles of the four-fold symmetric helices were consistent with site-directed infrared dichroism results from a few labeled sites. [65] Over the years considerable MAS spectral results were published supporting the TM helical structure, *Amt* binding site, and confirming which residues are facing the pore. [76, 77]

In 2007 the structure of the same construct in the presence of the antiviral drug amantadine at pH 8.8 (PDB ID 2H95) [57] was published by Cross and orientational constrains were obtained using the nuclear spin relaxation data and polarization inversion spin exchange at the magic angle (PISEMA) experiments [78] on uniformly and selectively labeled aligned samples. Through comparative CP-MAS spectra between the apo-protein and the complex the influence of *Amt* binding was monitored. [57] In the presence of *Amt* inside M2TM pore the structural or sample heterogeneity is reduced, i.e. the structural stability is enhanced. [57] Thus, the spectra showed that both the polypeptide backbone and His37 side chain are more constrained and stabilized in the presence of *Amt*. The dynamics and structural plasticity are essential for the functional complexity of the M2 ion channel opening, gating and proton conduction. According to the PISEMA experiments results the primary structural influence of drug binding was to induce a kink in the TM helix just C-ward of what was presumed to be the binding site of *Amt*, at Gly34. The kink in the monomer between two helical

fragments have 21° and 31° tilt angles with respect to membrane normal, i.e the kink had only a small effect on the tilt of the N-terminal portion of the helix, but reduced the tilt of the C-terminal portion to 21°. In the MD simulations of the M2 TM domain starting from both the 2002 ssNMR structure in the absence of a drug molecule i.e PDB 1NYJ (see Figure 1.6A) [56] and the 2007 ssNMR structure in the presence of amantadine (PDB 2H95), [57] the packing of the helix bundle tightened, resulting in a distinct reduction in the pore size, in line with the more recent ssNMR and X-ray crystal structures (see Figure 2.1D,F). Moreover, the Val27 sidechains were found to extend into the pore to form a constriction, leading to the proposition of a secondary gate. [79] This secondary-gate configuration of Val27 from a structure measured in the most realistic representation of the lipid environment has been confirmed in all recent structures.

Moreover, the protonation of His37 of M2TM inside lipid bilayers was titrated by Cross in 2007 in the absence and presence of *Amt* as a function of pH, using ^{15}N cross-polarization magic-angle spinning (CP-MAS) NMR spectroscopy. The effect of *Amt* binding on the His37 side-chain motion was studied by comparing the CP for the His37 $^{15}N_{\delta 1}$ signal with and without *Amt*. It was found that the binding of *Amt* drastically lowers the His37 pKa values by three orders of magnitude compared with the initial pKa of His37 in A/M2TM apo-protein and that the His-HisH$^+$ dimer does not form in the presence of *Amt* [23, 80]. Furthermore, this perturbation of the His37 pKa is consistent with the suggestion that the ammonium group of *Amt* points toward the C-terminus of the channel (see Figure 2.7). Thus, *Amt*'s influence on the chemical properties of His37 tetrad can contribute to inhibit proton conductance, more than just *Amt* molecule sterically blocking A/M2TM pore. The lack of His-HisH$^+$ dimer when *Amt* is present suggests that low-barrier His-HisH$^+$ hydrogens bonds are needed to transport protons through water network inside the pore.

In 2008 the first X-ray crystal structures of the M2TM was solved by DeGrado in β-octylglucoside detergent, showing a tetrameric left-handed bundle (consistent with the ssNMR structures) both in the absence i.e., PDB ID 3BKD (see Figure 2.1C) and presence of amantadine i.e., PDB ID 3C9J, at pH 7.3 and 5.3, respectively. [34] The former had a 2.05 Å resolution and a I33M mutation while

the latter structure had a 3.5 Å resolution and the stabilizing mutation G34A. [34, 43] Both structures solved at pH 7.3 or 5.3 were almost identical and it was unclear if the crystal structure corresponded to the closed or the open state based on pH.They appeared to be significantly perturbed by the membrane mimetic environment, as evidenced by the severe splaying of the TM helices and, in the case of PDB ID 3BKD, the presence of octylglucoside and polyethylene glycol in the pore and the interhelical interface. Thus, while the helices are tightly assembled at the N-terminal domain, they adequately splay outward at an average tilt of c.a. 35^{o} at the C-terminal domain resulting in a wide open channel at the C-terminus end - where Trp41 indoles from 1,3-TM helices are on average 9.5 Å apart - with no obvious structural features that support proton opening. They adopted the inward$_{open}$ conformation. The wide opening of the channel seems to be inconsistent since that structure was determined at pH 7.3, which in principle favors the closed channel conformation.

The same G34A mutant at pH 6.5 without drug and using a smaller construct (25-46) was characterized in 2010 i.e PDB ID 3LBW (see Figure 2.2 D) presenting a better packed tetrameric structure, with no detergent in the pore or interhelical interface. [34, 43] The backbone structure of PDB ID 3LBW is very similar to the TM helical bundle of 2L0J characterized in lipid bilayers (Ca RMSD of 0.6 Å for P25-W41), but the H37xxxW41 sidechain conformations are different (see Figure 2.4). Due to the relatively low resolution of 3.5 Å in the X-ray structure PDB ID 3C9J the presence of the *Amt* inside the pore was considered ambiguous. An electron density on the axis of the pore adjacent to Ser31 was interpreted as bound *Amt* molecule. The relatively low resolution 3.5 Å of the crystal structure is insufficient for unambiguous identification of small molecules such as *Amt*, having a maximum diameter of the roughly spherical adamantyl cage ~ 3.4 Å. Therefore, the structure was questioned by Chou who suggested for Amt an external position and an allosteric mechanism of channel inhibition as described next.

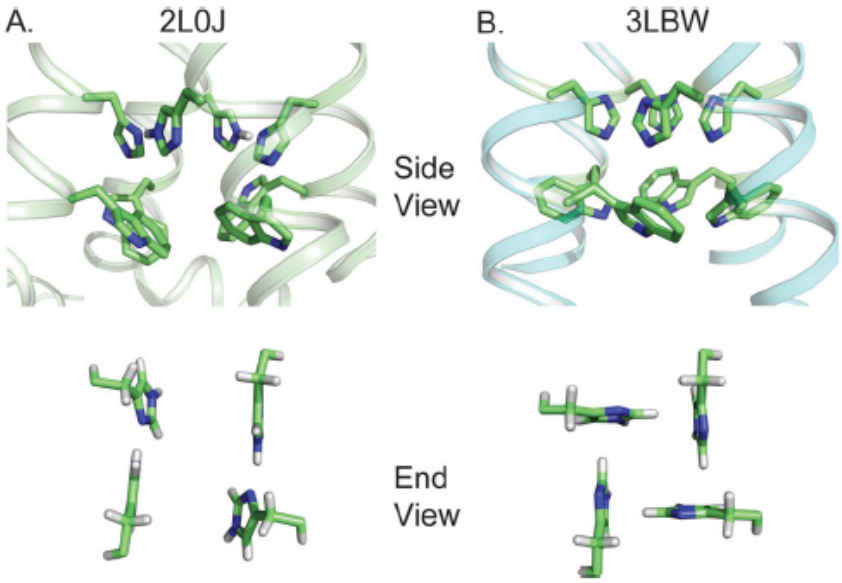

Figure 2.3**:** Conformations of the H37xxxW41 quartet in the ssNMR structure 2L0J [30] and X-ray structure 3LBW, shown in both side and top views. (*a*) The dimer of dimers conformation in 2L0J was [43] refined by QM/MM calculations based on significantly downfield-shifted imidazolium ^{15}Nδ1 and ^{15}Nε2 resonances, obtained in lipid bilayers, that indicated strong imidazole-imidazolium hydrogen bonds at pH 7.5. [23] (*b*) The fourfold symmetric conformation in 3LBW was from the TM domain in an octylglucoside and polyethylene glycol preparation at pH 6.5. Both structures show the Trp41 residues forming a basket as a gate for proton conductance.

Also, in 2008 the first solution NMR structure of M2 was determined in dihexanoylphosphatidylcholine (DHPC) micelles, providing the first structure of the conductance domain i.e. PDB ID 2RLF (see Figure 2.1E). In this structure, based on NMR NOE, Trp41 is essentially locked in the closed channeland the indole amine of one subunit is within hydrogen bonding distance of the Asp44 carboxyl carbon of the adjacent subunit. The two residues can form an intermolecular hydrogen bond that stabilizes the channel gate in the closed conformation (see Figure 2.3). The sidechain of Arg45 is also in the vicinity for forming inter subunit salt bridge with Asp4, confirming the increased pH-modulated activity of channels like M2 in which asparagine has replaced Asp44 [50, 81] This structure had the surprising result that the antiviral drug rimantadine did not bind in the pore but to an external site on each chain of the tetramer, facing what would be the viral membrane inner interfacial region (see Figure 2.3B). The authors suggest that drug binding has the effect of stabilizing the

closed state of the channel for NMR structure determination, with *Rim* binding at a lipid-facing pocket near the C-terminal side of the channel domain. The ammonium group of *Rim* is in contact with the polar sidechain of Asp44 and possibly with Arg45, according to observation of independent inter-molecular NOEs between *Rim* and a lipid-facing pocket at position 44. The polycyclic hydrocarbon cage of the drug forms hydrophobic interactions with Ile42 from one TM helix and Leu40 and Leu43 from the adjacent helix. For long time there was a debate, about the relevance of this biding site to channel inhibition. [82] However, the solution NMR structure was measured using a 200-fold excess of *Rim* in which ligand molecules due to the large excess can reach and form ionic hydrogen bonding interactions with Asp44 but this cannot define this position as a specific binding site. Additionally, the amphipathic helix is not positioned in the membrane interface (see Figure 1E,F), but formed a separate water-soluble four-helix bundle that was completely H/D exchangeable. The latter observation was in contrast to H/D exchange results from the full-length protein in lipid bilayers.

Amphipathic helices that interact with the lipid interfacial region take advantage of the steep dielectric and water concentration gradients between the hydrophobic core and lipid headgroup region. [83] This is also where the largest feature of the lateral pressure profile is located and where curvature and scission is effected by AHs of M2. In detergent micelles these gradients and the lateral pressure profile are much weaker. The curvature of the monolayer surface weakens the propensity of amphipathic helices to interact with the detergent interfacial region. In 2010 a drug resistant mutant (V27A) of the conductance domain was characterized in the same DHPC micelles i.e., PDB ID 2KWX (see Figure 2.1G). On the other hand, the solution NMR structure of the V27A mutant i.e. PDB ID 2KWX (see Figure 2.1G) had the amphipathic helices interacting with the detergent interfacial region, with the same helix rotation, but somewhat different helix tilt, lateral position, and depth compared with the structure obtained in the bilayer environment i.e. 2L0J; (see Figure 2.1F).

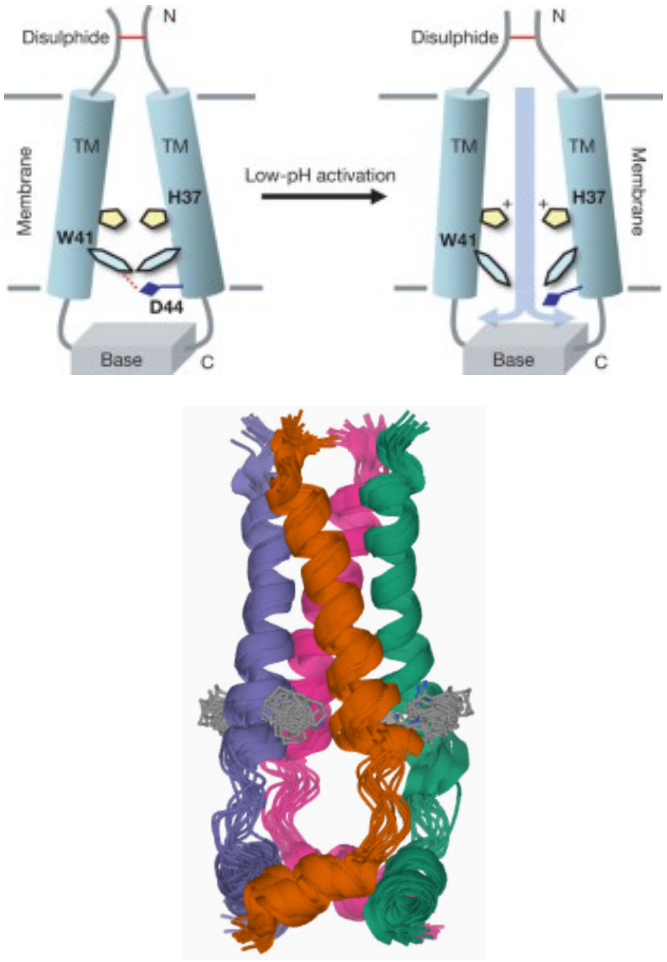

***Figure 2.4*:** (*a*) Schematic illustration of M2 ion channel activation. At high pH, the TM helices are packed tightly and the Trp41 gate is locked through intermolecular interactions with Asp44. At low pH, protonation of the His37 imidazoles destabilizes the TM helix packing, resulting in the hydration of the channel pore, and proton conductance. The C-terminal base of the tetramer and N-terminal disulfide bonds keep the channel from completely disassembling. For clarity, only two of the four monomers are shown. [50]. (*b*) Structure of M2 ion channel showing the left-handed packing of the TM helices, right-handed packing of the AH helices and the sidechains of residues His37 and Trp41. *Rim* (red) is located near the Asp44.

In 2010 the TM domain structure in the presence of perdeuterated *Amt* was later refined by Hong with MAS ssNMR-derived distance measurements at pH 7.5 between helices as well as between the helices i.e., PDB ID 2KQT (see Figure 2.1B). [58] In the PDB ID 2KQT structure of 2010, refined from PDB ID 2H95, the pore was identified as the primary drug binding site (see Figure 2.1B). [58]The external drug-binding site appeared to be in conflict with a variety of studies, including stoichiometry experiments, [84] but with the 2010 ssNMR structure for the conductance domain (PDB ID 2L0J) it was realized that, when the

amphipathic helix binds to the membrane interface, the potential drug binding site suggested by the solution NMR structure becomes occluded by two hydrophobic amino acids. [30] This time [82]the amphipathic helix was found to bind in the lipids interfacial region. In 2011 Chou came around with a rimantadine-bound structure of an AM2-BM2 chimera for the TM domain, showing the drug in the pore (PDB ID 2LJC). [60] The controversy regarding the drug binding site now seems firmly settled on the pore site.

In 2010 the structure of the M2 conductance domain M2AH was characterized by OS ssNMR at pH 8 and refined by restrained MD simulations in the same explicit lipid bilayer showing a dimer of dimer structure compared to the fourfold symmetric homotetramer i.e. PDB ID 2L0J (see Figure 2.1(F). [30] The TM helical bundle was more tightly packed than in the original 2002 structure (see Figure 2.1A,F).The amphipathic helices were positioned in the membrane interface with the hydrophobic residues facing into the lipid hydrophobic region and the numerous charged residues (dominated by lysine and arginine residues) interacting with the lipid headgroups (see Figure 1.3). Furthermore, the Ser50 residue (replacing the native Cys50) is positioned so that its hydroxyl is at a level in the bilayer consistent with the glycerol backbone of the lipids, an appropriate position for palmitylation.

It now seems clear that the TM helices in the $inward_{closed}$ conformation form a tetrameric structure similar to the 2002 structure i.e. PDB ID 1NYJ (see Figure 2.1A), but with somewhat tighter packing and somewhat larger tilt angles for the helices relative to the pore axis (32º for the N-terminal half; Table 2.1), as visualized in the recent ssNMR and X-ray structures i.e. 2L0J and 3LBW (see Figure 2.1F,D). In both of the solution NMR structures i.re. 2RLF and 2KWX (see Figure 2.1E,G), the TM helices in DHPC micelles have much smaller tilt angles (16º and 15º, respectively) relative to the pore axis. The result is that the secondary gate formed by the Val27 residues, first identified through MD simulations, [79] appears to be more tightly shut than when the helices are tilted at a 32º angle as in 2L0J and 3LBW. In the native membrane the protein and membrane environment are likely to be mutually involved in determining the hydrophobic dimension of the protein. Detergent micelles are much more adaptable to the hydrophobic dimension presented by the membrane protein than

a lipid bilayer. Consequently, while *Amt* and *Rim* bind to M2 in the pore when it is in the virion or in DMPC bilayers (see below discussion for PBD ID 2KQT, these drugs do not bind to WT M2 in the pore when it is in DHPC micelles (as in PDB ID 2RLF) because of the small helix tilt angles that close the secondary gate too tightly for the drug to enter. This emphasizes the need for membrane mimetics that are similar to the native membrane in restraining the membrane protein structure. [85] So although the orientational restraints from ssNMR do not define all of the sidechain conformations in the TM helices, the precision in determining the tilt of the helices is 2º, i.e. it is equivalent to the precision in a high-resolution X-ray structure, but with the sample for the ssNMR structure in a native-like bilayer environment. Of course, detergent-based crystals can also produce native-like structures, as in 3LBW (see Figure 2.1D).

As mentioned, the 2010 PDB ID 2KQT structure suggests that *Amt* is inside the pore between V27 secondary gate and His37 sensor. The adamantyl ring of *Amt* is located in the lumen of the four-helix bundle of M2TM within a hydrophobic pocket formed predominantly by the side chains of pore-lining residues Val27 and Ala30. [57, 64, 79, 86] Elucidation of the ammonium group direction shed light on the exact mechanism by which drug binding inhibits M2 proton channel which eventually can facilitate the design of new inhibitors. [87] The ammonium group at pH 8 was determined using ^{13}C-labeled M2TM reconstituted in lipid bilayers and in DMPC liposomes, with methyl-deuterated Rim (see Figure 2.5). ^{13}C-^{2}H rotational-echo double-resonance NMR experiments showed that the amino pointed to the C-terminus of the channel, i.e. toward His37, with the methyl group close to Gly34.

The proximity of the methyl group to the Gly34 backbone suggests for the higher affinity of *Rim* to M2 compared to *Amt* [88] as a result of better space filling of the drug in the channel and dehydration by the additional hydrophobic methylene and methyl groups. *Rim* binds inside the pore with the molecular axis of adamantyl roughly parallel to the bilayer normal at stoichiometric drug concentration.

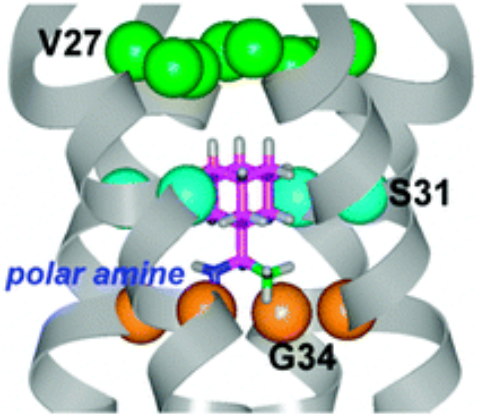

***Figure 2.5*:** Schematic of CD_3-*Rim* structure in the pore, with the polar amine pointing toward the C-terminus of the ion channel. Methyl group of CD_3-*Rim* is in vicinity of Gly34 residues. [87]

2.4 Experimental structures of M2: 2011-2021

2.4.1 M2 apo-protein structures

The conformational states of the conductance domain occur when the C-terminus is either largely closed or open to the viral interior, $inward_{closed}$ and $inward_{open}$ respectively. The $Inward_{closed}$ conformation has been characterized through solution NMR [50, 89], ssNMR [30, 90] and X-ray crystallography [43]. The $Inward_{open}$ state, is an intermediate that accumulates at high protonation i.e., +3 or more, of the His37 tetrad.

Hong continues previous experiments by Cross and showed using ssNMR that both closed ($inward_{closed}$ or C_{closed}) and open ($inward_{open}$ or C_{open}) conformations of M2TM equilibrate at any pH differing in the percentage of existence (see Figure 2.6). [91-94] Without the presence of the C-terminal region (residues 47-60), i.e. the AH domain, TM helixes are unable to assemble into stable tetramer in closed state at high pH = 7.3, hence the crystal structure PDB ID 3C9J obtained at pH 5.5 could represent an intermediate of channel opening state. NMR resonances of the AH domain showed that it is unaffected by the pH indicating that the C-domain base of the tetramer remains intact possibly to preserve the overall tetrameric state of M2 when the open state destabilizes the TM helixes. [95] Variety in helix-helix packing arrangements, can be changed partially in the intermediate states of channel opening.

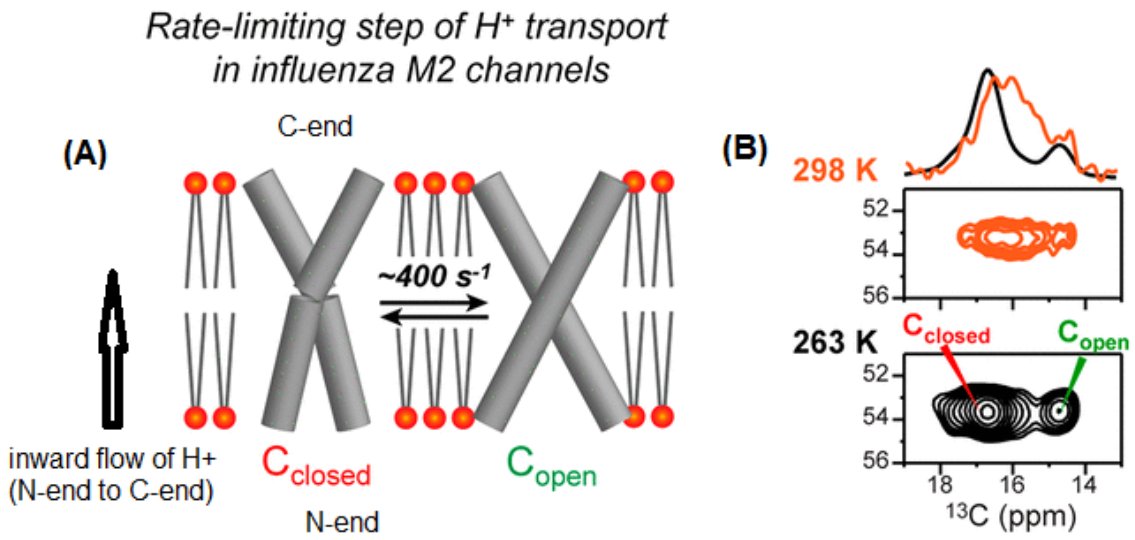

Figure 2.6: (*a*) Equilibration between inward$_{closed}$ (C_{closed}) and inward$_{open}$ (C_{open}) conformations. (*b*) Evidence from ssNMR. [92]

Additionally after initial experiments in 2009, Hong in 2011 performed ssNMR experiments examining the influence of lipid bilayer composition on the conformational equilibrium with respect to *Amt*'s binding to the pore, using DMPC and two virus mimetic membranes containing varying amounts of cholesterol, sphingomyelin and glycerophospholipids (eg POPC, POPS), M2TM and the fully functional cytoplasmic helices construct M2AH(21-61) [85, 96]. Interestingly, when M2AH(21-61) was reconstituted into virus-mimetic membrane containing 30% cholesterol, chemical shift perturbation wasn't observed for pore-lining residues, in contrast with M2TM which exhibited drug-induced chemical shift changes in the same membrane. Reduction of the cholesterol level and the use of unsaturated phospholipids shifted the conformational equilibrium of M2TM completely to the bound state but not in the case of M2AH(21-61).These experiments revealed that virus mimetic membranes shift the conformation equilibrium of the longer M2 construct to the unbound state, because of the small helix tilt angles that close the secondary gate too tightly for the drug to enter, while retaining the bound conformation of the shorter M2TM. The results showed the role of AHs in modulating the TM helixes conformation to facilitate or weaken drug binding to the channel pore, likely by interacting with cholesterol. Even though the detergent environment differs from the virus-mimetic membranes, the

cytoplasmic AHs may be affected by DHPC micelles in like a manner, causing an alteration in packing of TM helixes and drug binding abolishment as detailed previously in Section 2.2. [85] The findings imply that the amphipathic helix, together with cholesterol modulates the ability of the TM domain to bind *Amt*, establishing the M2 protein interaction with the lipid membrane and small-molecule inhibitors in a complex fashion. [85]

Experiments in DMPC bilayers also confirmed further the drug binding site and shed light further to the previous discrepancy about the type of inhibition mechanism, i.e. occlusion or allosteric inhibition, showing that the surface binding site was populated only by excess drugs from the membrane side, whereas the first equivalent of drug bound the N-terminal pore with much higher affinity. [58, 86, 97] Additionally, direct ^{13}C-^{2}H REDOR distance data of drug-complexed M2(21-61) in DMPC bilayers showed unambiguously that *Amt* binds Ser31 inside the pore, similar to M2TM in the same membrane, with the amphipathic helixes just shifting the drug-binding equilibrium more toward the unbound state compared to M2TM. In this study is established the pharmacologically relevant drug-binding site in the TM pore of the fully functional M2AH(21-61).

In 2012 the ^{13}C MAS resonances of the TM helix of the conductance domain were substantially assigned and multiple distance restraints observed, confirming the 2010 ssNMR structure PDB ID 2L0J. [98] In addition, the first MAS spectra of the full-length M2 protein have been obtained, [99] showing that the conformations of the TM helices are the same in the conductance domain and in the full-length protein. In addition, MAS spectra of the full-length protein directly observed in Escherichia coli membranes has been obtained where the protein was inserted into the membrane via the cellular machinery and was never exposed to detergents. [99] Once again the spectra were the same as that observed for the full-length protein that had been isolated from E. coli, purified in detergents and reconstituted into synthetic lipids. This provided excellent validation for the structure obtained in synthetic lipid bilayers.

It is widely accepted that the open ($inward_{open}$) i.e. active state of the channel requires a hydrated pore for conducting protons because the hydrophilic residue 31 and His37 are in a great distance inside the TM to relay protons in the absence of water molecules. Water-protein chemical exchange has been investigated in

M2 primarily through ^{1}H-^{15}N heteronuclear correlation (HETCOR) experiments. [90, 100, 101]

In most recent and remarkable studies, using lipid cubic phase (LCP) crystallization techniques, DeGrado solved [102] the structure of a waters wire by obtaining a high resolution (1.10 Å) cryogenic (100 K) and at room temperature crystallographic structures of M2TM at low (pH 5.5) (PDB ID 4QKC) and high pH (pH 8) (PDB ID 4QK7) in the $inward_{open}$ conformation (see Figure 2.7). Only c.a.16 water molecules [40] are placed at a given time inside the 16.8 Å of the lumen path, which spans between the channel entrance Val27 and His37. Pore-lining carbonyl groups are well situated to stabilize hydronium via second-shell interactions involving bridging water molecules. At pH 8, a clathrate-like structure is observed below Val27 and is anchored by hydrogen bonds to the main chain carbonyls facing the pore, but the water layer connecting to the hydrated His37 residues has become too diffuse to be seen clearly in the electron density. At pH 5.5, the water density in most of the pore is diffuse and a fully connected hydrogen bond network cannot be observed. Two additional structures were determined at 273 K at high pH (PDB ID 4QKL) and low pH (PDB ID 4QKM) to 1.71 Å and 1.44 Å resolution, respectively. The room temperature crystallographic structures indicate that water becomes increasingly fluid with increasing temperature and decreasing pH, despite the higher electrostatic field.

In order to visualize the solvent in the pore of the channel at room temperature while minimizing the effects of radiation damage, DeGrado collected data to a resolution of 1.4 Å using an X-ray free-electron laser (XFEL) at three different pH conditions: pH 5.5, pH 6.5, and pH 8.0 (see Figure 2.7). Data were collected [41] on the $Inward_{open}$ state, which is an intermediate that accumulates at high protonation of the His37 tetrad. At pH 5.5, a continuous hydrogen-bonded network of water molecules spans the vertical length of the channel, consistent with a Grotthuss mechanism model for proton transport to the His37 tetrad. This ordered solvent at pH 5.5 could act to stabilize the positive charges that build up on the gating His37 tetrad during the proton conduction cycle. The number of ordered pore waters decreases at pH 6.5 and 8.0, where the $inward_{open}$ state is less stable.

As shown in Figure 2.7, water wires inferred from crystallographic water positions from the 1.10-Å resolution cryo-crystal structures form a continuous network of water wires within the N-terminal half of the pore leading to the gating His37 residue, with some positional changes in the waters between the two pH conditions. Continuous water wires span 16.8 Å of the channel pore. In room temperature waters are less ordered, i.e. structures have fewer ordered waters and no longer form a continuous path leading to His37; in the low-pH structure, the waters do not form ordered networks at all and instead appear fluid-like.

The various crystallographic structures of the $Inward_{open}$ state are in good agreement with MD simulations by Voth that quantitatively explain experimental conductance curves. [103]

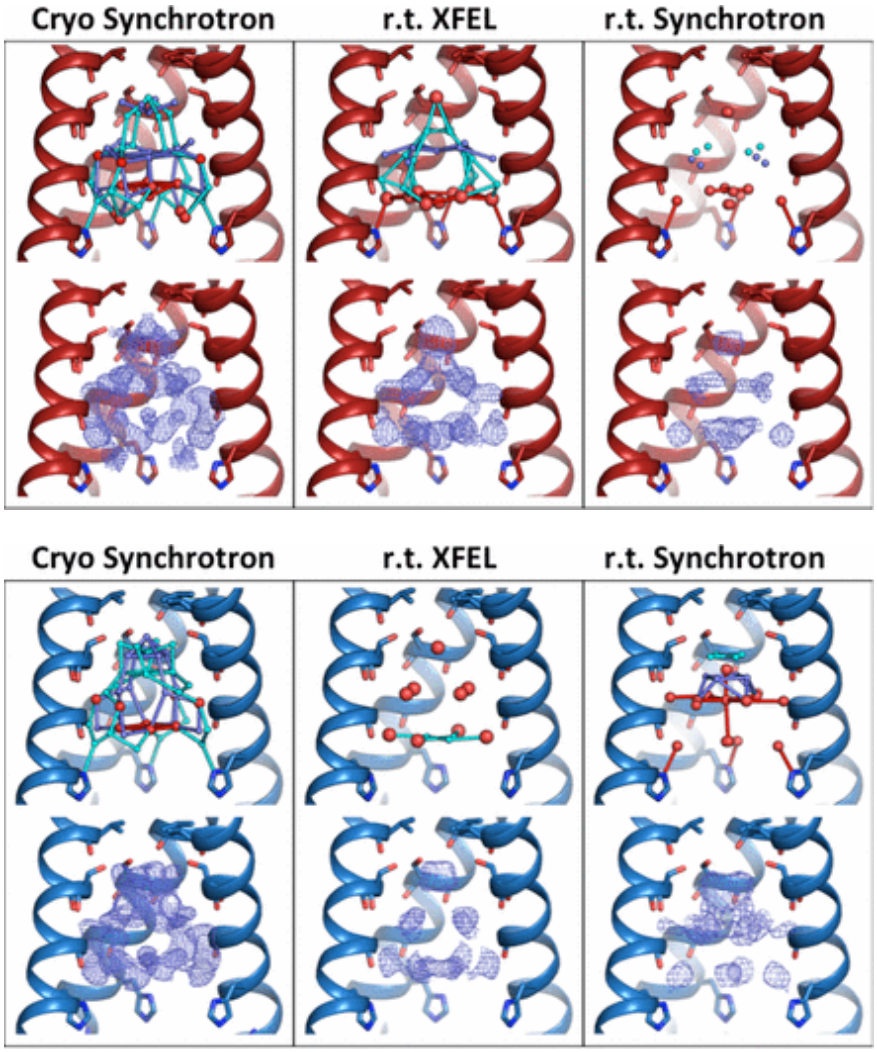

Figure 2.7**:** (*top*) Low-pH (pH 5.5) structures of M2TM under cryogenic synchrotron (PDB ID 4QKC, 1.10-Å, left), room temperature XFEL (PDB ID 5JOO, center), and room temperature (PDB ID 4QKM, 1.44-Å) synchrotron (PDB ID 4QKM, right) diffraction conditions. (*top*)The front helix of each tetramer has been removed; waters are modeled as spheres, with red spheres representing full-occupancy waters and light and dark blue spheres as half-occupancy waters in alternate-occupancy networks. Waters within hydrogen-bonding distance of each other are connected by sticks. The number of ordered waters decreases moving from left to right across the figure. (*bottom*) Electron density for the pore solvent network (blue mesh) is shown to a contour of 0.5 σ. The largest amount of ordered density is present in the cryogenic synchrotron data collection condition. The volume and shape of the solvent density for the room temperature structures collected using XFEL and synchrotron sources are similar. (*bottom*) High-pH (pH 8.0) structures of M2TM under cryogenic synchrotron (PDB ID 4QK7, 1.10-Å, left), room temperature XFEL (PDB ID 5TTC, center), and room temperature synchrotron (PDB ID 4QKL, 1.71-Å, right) diffraction conditions. (*top*) Waters are shown as spheres (red, full occupancy; light and dark blue, half-occupancy); potential hydrogen bonds are shown as sticks. (*bottom*). Electron density for the pore solvent network (blue mesh) is shown to a contour of 0.5 σ. The largest amount of ordered solvent electron density is observed under cryogenic diffraction conditions; the volume and shape of the solvent density for the two room temperature conditions are similar. [41]

2.4.2 M2 structures bound with aminoadamantane ligands

In 2016 the differential binding of *Rim* enantiomers to influenza M2 full protein (M2FL) was studied. M2FL was reconstituted in 1,2-dimyristoyl-sn-glycero-3-phosphocholine/1,2-dimyristoyl-sn-glycero-3phospho-(1'-rac-glycerol) (DMPC/DMPG) at a protein to lipid ratio of 1:30. Until this research, antiviral activity and protein-ligand interactions of *Rim* in complex with M2 proton channel of influenza A virus, have always been evaluated as a racemic mixture of the drug. The characterization of protein-ligand interactions at atomic level for each enantiomer separately is crucial for identifying potential stereospecific *Rim* binding interactions to the M2 proton channel, aiding the design of novel inhibitors. Cross using ^{13}C-^{2}H rotational echo double resonance ssNMR observed isotropic chemical shift changes at -10 ºC suggesting the differential binding of the *Rim* enantiomers to the proton channel. Cross group performed position restrained MD simulations satisfying distance restrains form ^{13}C-^{2}H spectra and suggest (*R*)-*Rim* to form a complex of higher stability with M2FL [104] but no unrestrained MD simulations that support the differential complex formation of the Rim enantiomers was not performed.

Eventually, the most direct evidence of a pore binding site came from crystallographic study of the M2TM in the presence of *Amt*. [34] Till 2010 decade high-resolution structural studies of M2 bound to inhibitors and particularly with high resolution to examine the critical role of water in drug binding were limited to 3.5 Å resolution.

Ordered water molecules arranged in wires inside the channel play a role in conduction of protons through M2 pore. Water-mediated interactions play key roles in drug binding. The mentioned structures show that small molecules can enable potent inhibition by targeting key waters. [34] In 2018 DeGrado and Kolocouris [61] demonstrate structures of *Amt* bound to M2TM in the $inward_{closed}$ conformation (2.00 Å), *Rim* bound to M2TM in both the $inward_{closed}$ (PDB ID 6BKL; 2.00 Å) and $inward_{open}$ (PDB ID 6BOC; 2.25 Å) conformations and a spiro-adamantyl amine inhibitor bound to M2TM in the $inward_{closed}$ conformation (PDB ID 6BMZ; 2.63 Å) (see Figure 2.8). The four X-ray crystal structures of M2TM ion channel with bound inhibitors reveal that ammonium group is directed toward His37 and binds to water-lined sites that are hypothesized to stabilize transient hydronium ions formed in the proton-conduction mechanism. In particular, as supported by MD simulations the ammonium group is stabilized through three hydrogen bonds with proximal waters comprising the Ala30 layer, followed by the Gly34 water layer and the His37 tetrad. Placement of the drug within the pore the hydrophobic adamantyl cage of the above adamantyl-amine molecules displace waters near Val27 and disturbs M2 water network which is essential for proton transport. [61] The hydroxyl of Ser31 forms an internal hydrogen bond to a peptidic carbonyl of Val27 increasing the effective hydrophobicity of the environment. [61] These drug-M2TM complexes provide the first high resolution structures of drugs that interact with and disrupt networks of hydrogen-bonded waters that are widely utilized throughout nature to facilitate proton diffusion within proteins. Moreover, the entropic cost of binding is minimized due to capability of the symmetric ammonium and adamantyl groups of the adamantyl-amine class of drugs freely rotate inside the channel. [61, 105, 106] Crystal structures define similar modes of drug binding in the $inward_{closed}$ and the $inward_{open}$ form. 300-ns MD simulations of the M2TM with the three adamantyl-amine drugs predict with accuracy the position of the ligands and waters inside

the pore in the X-ray crystal structure of the M2 complexes. Further details will be discussed in Chapter 7.

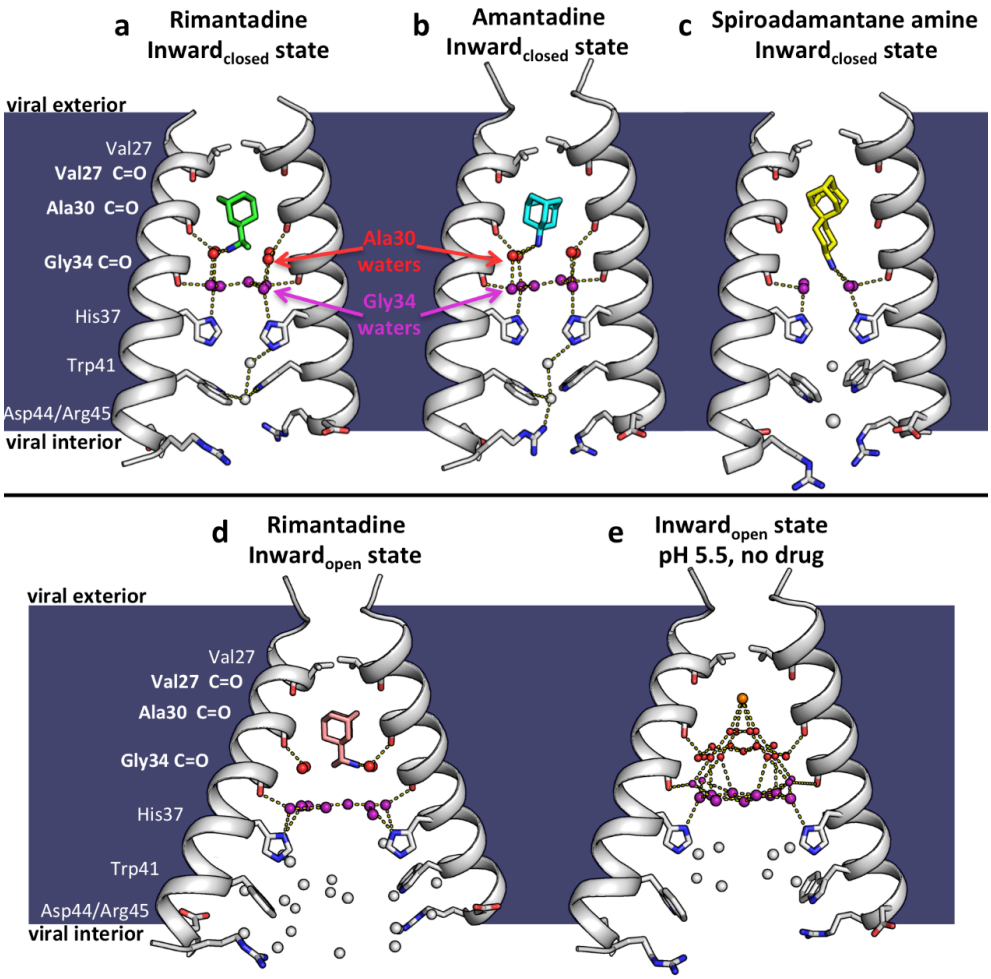

Figure 2.8: X-ray crystal structures of the M2 proton channel bound to drugs and inhibitors. The channel is a homotetramer, but here the front and back monomers have been removed to show the contents of the channel pore. Hydrogen bonds are shown as yellow dashes. The layer of waters forming H-bonds to Ala30 carbonyls ("Ala30 layer") is shown as red spheres; the layer of waters forming H-bonds to Gly34 carbonyls ("Gly34 layer") is shown as purple spheres. Top, left to right: a. M2 bound to rimantadine in the Inward$_{closed}$ state; PDB ID 6BKL, 2.00 Å resolution, monomer subunits F and H; b. M2 bound to amantadine in the Inward$_{closed}$ state; PDB ID 6BKK, 2.00 Å resolution, monomers B and D; c. M2 bound to spiro-adamantyl amine in the Inward$_{closed}$ state; PDB ID 6BMZ, 2.63 Å resolution, monomers B and D. Bottom, left to right: d. M2 bound to rimantadine in the Inward$_{open}$ state; PDB ID 6BOC, 2.25 Å resolution, monomers B and D; e. Previously solved structure of M2 in the Inward$_{open}$ state at pH 5.0 in the absence of bound drug,[31] PDB ID 5JOO, 1.41 Å resolution. [61]

The V27A mutation confers adamantane resistance to the influenza A M2 proton channel and is becoming more prevalent in circulating populations of influenza A virus. In 2020 DeGrado and Kolocouris used X-ray crystallography to solve structures of a spiro-adamantyl amine inhibitor bound to M2(22-46) V27A and also to M2(21-61) V27A in the $Inward_{closed}$ conformation (see Figure 2.9). [62] A spiro-adamantyl amine binding site is nearly identical for the two crystal structures. Compared to the M2 WT with valine at position 27 the channel pore is wider at the N-terminus as a result of the V27A mutation and this removes V27 side chain hydrophobic interactions that are important for binding of amantadine and rimantadine. The spiro-adamantyl amine inhibitor blocks proton conductance in both the WT and V27A mutant channels by shifting its binding site in the pore depending on which residue is present at position 27. Additionally, in the structure of the M2(21-61) V27A construct, the C-terminus of the channel is tightly packed relative to the M2(22-46) construct. Residues Asp44, Arg45, and Phe48 face the center of the channel pore and would be well-positioned to interact with protons exiting the M2 channel after passing through the His37 gate. A 300 ns molecular dynamics (MD) simulation of the M2(22-46) V27A - spiro-adamantyl amine complex predicts with accuracy the position of the ligands and waters inside the pore in the X-ray crystal structure of the M2 V27A complex. Further details will be discussed in Chapter 7.

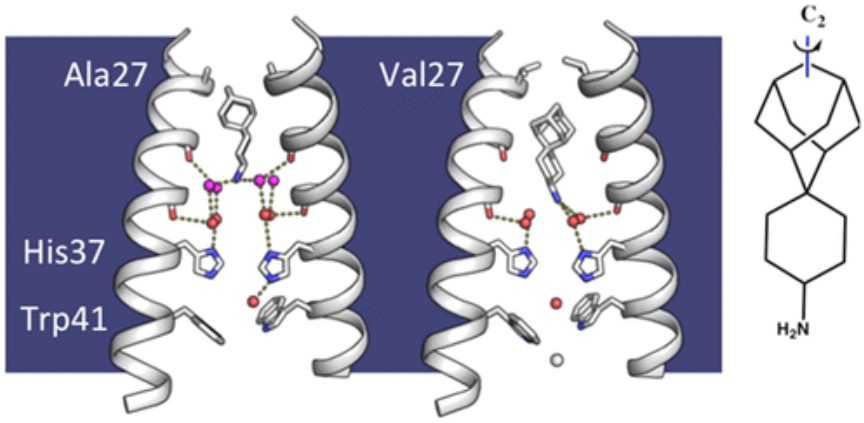

***Figure 2.9*:** Mechanism of adamantane drug resistance in the V27A mutant channel and mechanism of dual inhibition by spiro-adamantyl amine. Front and back monomer helices have been removed to clearly show the contents of the channel pore. Pink spheres correspond to waters that form hydrogen bonds with the Ala30 carbonyls, and red spheres correspond to waters forming hydrogen bonds with Gly34 carbonyls. Newly determined structure of M2(22−46)

V27A bound to a spiro-adamantyl amine inhibitor (PDB entry 6NV1, monomer chains B and D), M2(22−46) WT bound to amantadine (PDB entry 6BKK, chains B and D), and M2(22−46) WT bound to spiro-adamantyl amine (PDB entry 6BMZ, chains B and D) from left to right, respectively. When spiro-adamantyl amine binds to the V27A channel (PDB entry 6NV1), the ammonium group of the inhibitor localizes to the same position as the ammonium of amantadine in the WT structure (PDB entry 6BKK). The adamantyl group is positioned higher in the channel pore, occupying the extra space created by the Val27 to Ala mutation. In the previously determined structure of the spiro-adamantyl amine inhibitor bound to the WT channel (PDB entry 6BMZ), the adamantyl group of the inhibitor binds lower in the channel pore, and the four waters in the Ala30 layer are displaced. For the spiro-adamantyl amine-bound structures, a network of one or two layers of hydrogen-bonded waters is formed depending on whether Val or Ala is present at position 27. [62]

In 2021 the structure of each of the enantiomer of Rim with M2TM was also published and the binding free energy of water layers in the complexes was evaluated through Monte Carlo simulations. Further details will be discussed in Chapter 7.

2.5 Characterization of the H37xxxW41 Quartet – Mechanism of proton transport

The heart of the M2 proton conductance capability is in the H37xxxW41 sequence that is the signature motif for Influenza proton channels (see Figure 2.3). [28]

The stability of the $Inward_{open}$ and $Inward_{closed}$ states is defined by the degree of protonation of His37 near the C-terminal region of the pore and the small energetic difference between them assures switching between states during the transportation mechanism. A “recycling step” between different protonation states is a key step at the conductance mechanism implies that the protein undergoes conformational changes (assigned to Trp41 and Val27) during transport which have to be reset before the next proton can be transported (see Figure 2.10). [107]

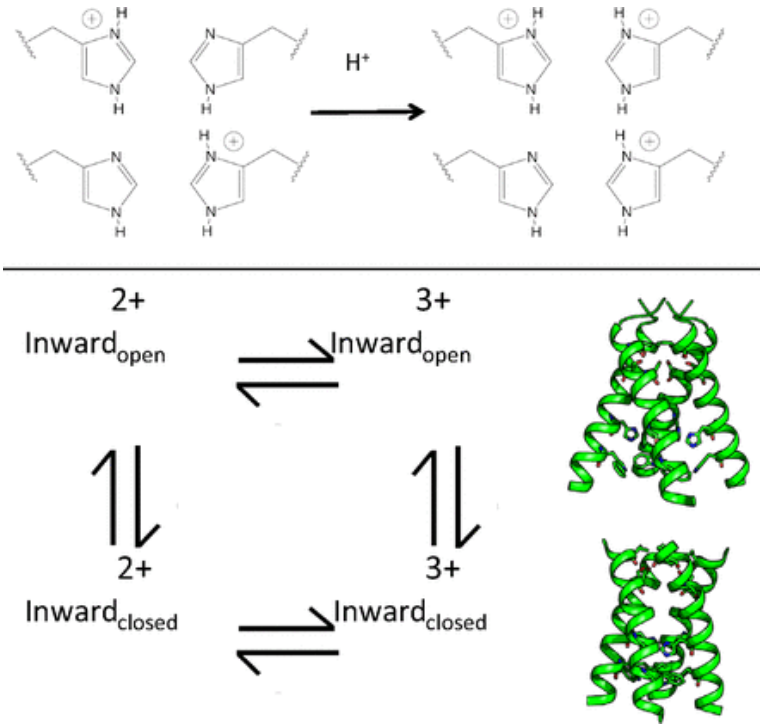

Figure 2.10: M2's proton conduction rate is 100–1000 s^{-1}, more than 2 orders of magnitude slower than the histidine-water proton-exchange rate. [41]

There were two debated proton transport mechanisms. The first suggests that the proton is transferred through the breaking and reforming of H-bonds between two pairs of His37 dimers [23, 30], the second that individual His37 residue shuttles protons through imidazole ring reorientations and exchanging protons with water without the process of forming intermonomer His37 H-bonds [90, 100] (see Figure 2.11).

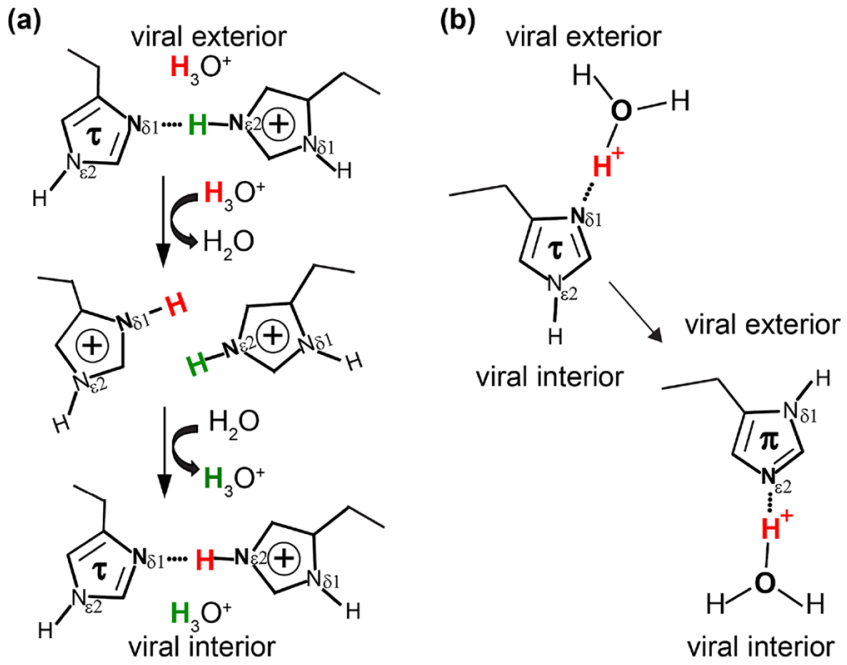

Figure 2.11: Two possible hydrogen bonding partnerships in the His37 tetrad of the M2 proton channel. (*a*) One of two pairs of His37 residues showing the low-barrier hydrogen bond model, in which the proton is transferred through the breaking and reforming of the intermonomer imidazole-imidazolium hydrogen bonds between His37 residues (*b*) the water-His37 hydrogen bonding model, in which the His37 shuttles protons through imidazole ring reorientations and exchanging protons with water. [108]

Thus, an early favored model posits that protonation of His37 residues leads to their repulsion, creating an open pore with a continuous water wire for proton conduction. [72, 109-111] The proton conductance calculated from such a model was $3x10^8$ protons per second. However, conductance measurements, especially more recent ones using liposome preparations, place the conductance at the level of $3x10^2$ protons per second. [18, 30, 112-115] The six orders of magnitude discrepancy casts doubt on this gating model.

The crystal structure with PDB ID 3LBW shows a four-fold symmetric $inward_{open}$ structure for the His37 sidechain even though the sample was prepared at pH 6.5. Consequently, this structure presumably with two or three charges on the histidine tetrad does not provide an explanation for the cooperativity in proton binding, the enhanced stability of the tetramer at pH 6.5 nor the exchange broadening of the His37 resonances. It was realized that much more work is needed to characterize not only the dynamics, but also the pH-dependent

conformational states of the H37xxxW41 quartet so that the functional mechanism of M2 can be refined.

The arrangement of histidine side chains in influenza A M2 tetramer determines their pKa values, which define pH controlled proton conduction critical to the virus lifecycle. The pKas of the histidines were first characterized by Cross [23] with the surprising finding that two of the His37 residues of this tetrad in the middle of the bilayer environment had higher affinity for protons than His residues on the surface of water soluble proteins. These two high proton-affinity pKa values for the M2 tetramer were both 8.2. In comparison, the His37 residue in the M2 monomeric TM helix in detergent micelles is about 1.5 pH units lower at 6.8. The latter value is similar to that of a water-exposed histidine. The identical value of the first two pKas of the M2 histidine tetrad further suggests cooperative proton binding. That is, the first protonation results in a structural change that facilitates the second protonation. It is known that M2 becomes activated at a pH of approximately 6.5. [37] The third pKa for the histidine tetrad determined in the bilayer environment was approximately 6.3, [23] consistent with this third proton being the charge responsible for activating the proton channel. A fourth pKa was suggested in this study to be below pH 5.

Therefore, from the set of His37 pKas one can conclude that the tetramer stability increases as the pH is lowered from 9.0 to 6.5 and then decreases as the pH is further lowered. This is exactly what was observed by DeGrado and Pinto, the pH dependence of the tetramer stability calculated from the set of observed His37 pKas was in quantitative agreement with their measurement. [29] As noted by these authors it might seem counterintuitive that placing two charges in close proximity (within ~ 6 A°) in a low dielectric environment should increase the stability of the tetramer. Based on the appearance of imidazolium $^{15}N_{\delta 1}$ and $^{15}N_{\varepsilon 2}$ resonances that are significantly downfield-shifted, similar to model imidazole-imidazolium spectra, Cross proposed [23] that the His37 residues formed a pair of imidazoleimidazolium hydrogen bonded dimers, which would significantly enhance tetramer stability. [30] In addition, the strong hydrogen bonds could disperse each charge over two rings, thereby reducing the charge-charge repulsion that could be anticipated. The exchange broadening of the resonances suggests His37 sidechain dynamics (see below).

This model was proposed originally by DeGrado and Pinto in 1997 [66], i.e. that His37 tetrad relays the proton from one side of the membrane to another. Quantum mechanics/molecular mechanics (QM/MM) calculations on the H37xxxW41 quartet, constrained by the backbone structure of 2L0J, were carried out to investigate the plausibility and provide atomic details of this model. [30] These calculations first confirmed that the doubly protonated His37 tetrad can form a stable dimer of dimers configuration (see Figure2.9). Interestingly, unlike imidazole-imidazolium crystals, where the two imidazole rings sharing a proton are perpendicular to each other, the two His37 sidechains forming a dimer within the confines of the backbone structure are nearly coplanar. The QM/MM calculations further showed that a dimer can receive a proton from a hydronium ion from the N-terminal side of the pore, and pass it onto a water molecule on the C-terminal side of the pore via a 45 change in the His37 v2 torsion angle and relaxation of the His37 Ca-Cb-Cc angle if the Trp41 primary gate is open.

Until 2010 the dimer (or pair) of dimers symmetry appeared to be associated with just the His37 sidechain. Griffin group showed in 2010 that this symmetry also extended to multiple backbone sites in studies of the conductance domain by MAS spectroscopy in POPC bilayers above the gel to liquid crystalline phase transition temperature. [116] They also observed a similar doubling of specific backbone resonances of the conductance domain in DPhPC bilayers. Cross confirmed these results in MAS spectra of DOPC bilayer preparations below the phase transition temperature. [98] A model for the subtle conformational difference originating at His37 has been suggested by Cross (see Figure 2.12).19 The Ca-Ca separation in an imidazole-imidazolium dimer appears to be slightly larger than the Ca-Ca separation between His37 residues in different dimers. That is, in a pair of dimers configuration, the four His37 Ca atoms form a rectangle with short distances between the dimers and longer distances within the dimers. Since the dimers appear to interconvert slowly based on the exchange broadening observed in the His37 titration, [23] this could explain the MAS spectra showing that the dimer of dimers symmetry extends throughout much of the TM domain.

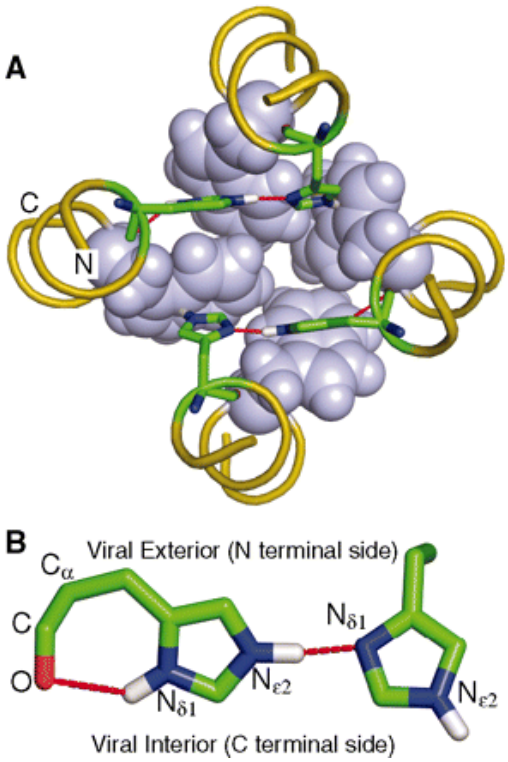

Figure 2.12: The structure of the HxxxW quartet in the histidine-locked state. (*a*) Top view of the tetrameric cluster of $H^{37}xxxW^{41}$ (His^{37} as sticks and Trp^{41} as spheres). Note the near-coplanar arrangement of each imidazole-imidazolium dimer that forms a strong hydrogen bond between $N_{\delta1}$ and $N_{\varepsilon2}$. In each dimer, the remaining $N_{\varepsilon2}$ interacts with the indole of a Trp^{41} residue through a cation-π interaction. The backbones have four-fold symmetry, as defined by the time-averaged NMR data. (*b*) Side view of one of the two imidazole-imidazolium dimers. Both the intraresidue $N_{\delta1}$-H-O hydrogen bond and the interresidue $N_{\varepsilon2}$-H-$N_{\delta1}$ strong hydrogen bond can be seen. The near-linearity of the interresidue hydrogen bond is obtained at the expense of a strained C_α-C_β-C_γ angle (enlarged by ~10°) of the residue on the left. [30]

M2 spectra dramatically vary depending on the M2 constructs and lipids used in sample preparation. For instance, a set of two resonances for His37 was observed in the conductance domain M2AH, i.e. M2(22-62) in DOPC/DOPE lipids [98] and M2(18-60) in POPC and DPhPC, [116-119] as well as the M2FL protein in Escherichia coli membranes, [99] suggesting that the His37 tetrad exhibits a dimer of dimer conformation. However, the M2(22-62) in viral-envelope-mimetic lipid membranes shows a single set of His37 resonances and did not bind amantadine. [90]

The ^{1}H-^{15}N HETCOR spectra from either the M2FL in DOPC/DOPE [101] or the truncated M2 protein M2TM in viral-envelope-mimetic lipid membranes [100]

show correlations between water and His37 imidazolium nitrogen. These results indicate that water molecules are involved in proton conductance, although their interpretations yielded different conductance mechanisms. A direct measurement of the water−protein chemical exchange may shed light onto how the water with hydronium ions interacts with the protons in the His37 tetrad. [95, 120] In an elegant ssNMR study Hong in 2018 the protein ^{13}C-detected water ^{1}H T2 relaxation measurements show that channel water relaxes an order of magnitude faster than bulk water and membrane-associated water, indicating that channel water undergoes nanosecond motion in a pH-independent fashion. These results connect motions on three timescales to explain M2's proton-conduction mechanism: picosecond-to-nanosecond motions of water molecules facilitate proton Grotthuss hopping, microsecond motions of the histidine sidechain allow water-histidine proton transfer, while millisecond motions of the entire four-helix bundle constitute the rate-limiting step, dictating the number of protons released into the virion. [92]

In 2020 Loren showed by applying MAS ssNMR in samples of M2(18-6) in 1,2-diphytanoyl-sn-glycero-3-phosphatidylcholine bilayers at pH 7.8 that the imidazole rings are hydrogen bonded even at a pH of 7.8 in the neutral charge state. An intermolecular 8.9 ± 0.3 Hz J_{NN} hydrogen bond is observed between H37 N_{ε} and N_{δ} recorded. This interaction could not be detected in the drug-bound sample (see Figure 2.13).

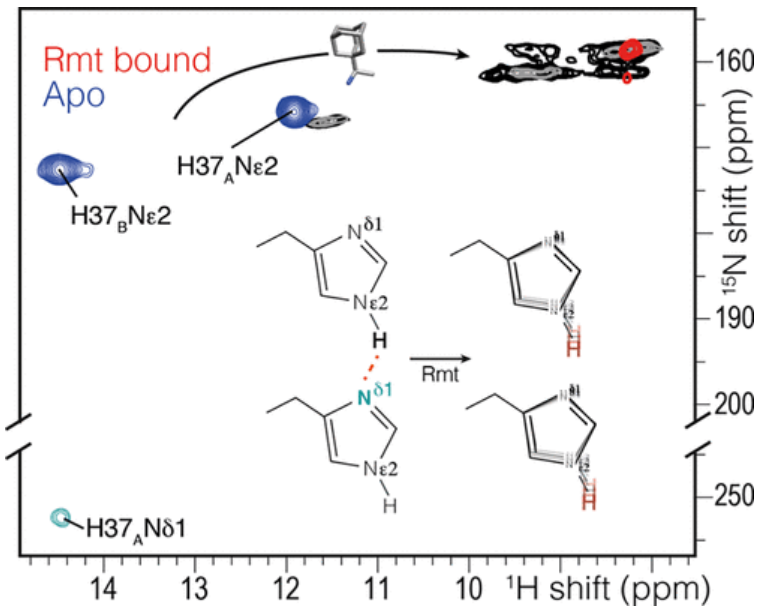

***Figure 2.13*:** Chemical shift changes in the histidine side chain upon addition of the drug *Rmt* of and (H)NH spectra with 25 ms (gray) or 200 ms (black) in spectra showing the ^{15}N exchange during the water suppression. A 3−5 ppm change is observed in the drug-bound spectrum (red), and no J_{NHN} *J*-coupling was observed. Instead, the imidazole NH peaks are broadened, and the peaks at 9 ppm are in exchange. The (H)NH spectra were acquired at 250 K. [121]

Cross applied spin-locking of the ^{1}H magnetization along the magic angle in samples of His37-labeled M2FL (pH 6.2) in DOPC/DOPE liposomes, to supress the ^{1}H spin diffusion such that water−protein chemical exchange process was monitored indirectly by dipolar-dephased ^{15}N signals through polarization transfer from ^{1}H. [108] Figure 2.11(A) shows a model for the water−protein exchange process for the His37 NH bonds at the heart of the His37 tetrad. The “initial” NH protons in the His37 tetrad are colored green and blue for the His C−D pair. The hydronium ion is attracted by the non-protonated Nδ1 site resulting in both His37 residues in a dimer becoming charged. The hydronium ion based proton is colored red. These two imidazolium residues conformationally rearrange, due to charge repulsion with the newly protonated Nδ1+H site oriented toward the pool of externally exposed waters, whereas the original Nε2+H and the newly formed Nε2+H are both exposed to waters of the viral interior. The return of the His Nδ1+H proton to the waters of the viral exterior results in a futile cycle, while the absorbance of either His Nε2+H protons by waters of the viral interior results in a successful transport of a proton across the membrane. If the proton in the original imidazole-imidazolium H-bond is reabsorbed by water (right-hand path), the imidazolium donates its H-Nδ1 proton to reform the same His37 C−D pair with an imidazolium-imidazole H-bond utilizing a π state. This proton rapidly rearranges crossing the H-bond barrier to form a τ-charge H-bonded pair, back to the starting state. This model confirms that hydronium ions are in exchange with protons in the His37 NH bonds at the heart of the M2 proton conduction mechanism, with an exchange rate on a sub-ms scale with an exchange constant of c.a. 1750 s^{-1} for pH 6.2 at −10 °C.

CHAPTER 3
Biophysical Methods

3.1 Solid-state NMR spectroscopy

Solid-state (ssNMR) spectroscopy is an atomic level method to determine the chemical structure, 3D structure and dynamics of solids and semi-solids. [122] It is necessary to understand and classify compounds that would not work well in solutions such as powders and complex proteins or study crystals too small for a different characterization method i.e., X-ray crystallography. [123]

SsNMR spectroscopy is a type of nuclear magnetic resonance spectroscopy, characterised by the presence of anisotropic interactions. Generally, in NMR spectroscopy the resonance frequencies of a nuclei spin depend on the strength of the applied magnetic field at the nucleus. The nuclear spin interactions and the effects of magnetic fields and radiofrequency pulses on nuclear spins in solid state NMR are the same as in liquid state NMR, but the sample is solid instead of solution or liquid. [122] The interactions that essentially influence the resulting spectra in solution state NMR are chemical shift and J-coupling i.e. spin-spin splitting. The ^{1}H-^{13}C dipole-dipole couplings and chemical shift anisotropy (CSA) interactions, are averaged in solution-state NMR due to the rapid tumbling of the molecules in solution. These interactions depend on the orientation of the molecules, relative to the magnetic field direction. However, in solids e.g. a media with no or little mobility, molecules do not tumble thus the direction matters. So anisotropic local fields or interactions in ssNMR have significant influence on the behaviour of nuclear spins, resulting in much broader peaks compared to solution-state NMR. [123]

The basic principle of NMR consists of measuring the nuclear shielding, which can also be seen as the electron density of a particular element. Nuclear shielding is affected by the chemical environment, as different neighbouring atoms will have different effects on nuclear shielding, for instance electronegative atoms will tend to decrease shielding and vice versa. The oscillatory response of nuclei with non-zero spins in a magnetic field to resonant excitation by radiofrequency irradiation. [122] When atoms containing non-zero nuclear spins are placed in an external magnetic field, the degeneracy of the nuclear spin states is lifted, leading

to energy difference ΔE (see Figure 3.1). Commonly used elements are ^{1}H, ^{13}C, ^{19}F, ^{31}P, ^{29}Si, because in the presence of a magnetic field the spin state splits. [123]

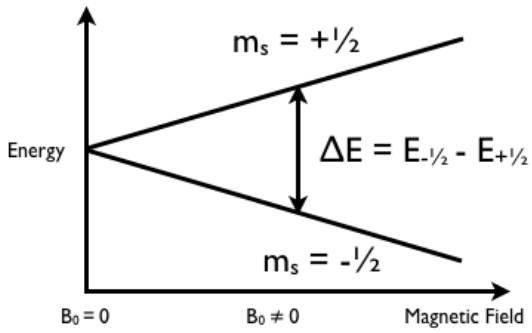

***Figure 3.1*:** Spin state splitting as a function of applied magnetic field. [123]

A spin state of ½ is split into two spin states and in general the number of spin states increases proportionally with the spin state. A spin of 1 will have three spin states, 3/2 will have four spin states and so on. However, in higher spin states the difficulty to accurately read NMR results is increased due to confounding peaks and decreased resolution, making the ½ spin states preferred. The radiofrequency (E) is described by the equation below, where μ is the magnetic moment, a property intrinsic to each individual element. This constant can be derived from the equation below, where γ is the gyromagnetic ratio, a fundamental property associated with each isotope, B_o is the strength of the static magnetic field, h is Planck's constant and I is the spin. [123]

$$E = \mu B_o H_o$$

$$\mu = \gamma h\big(I(I+1)\big)^{1/2}$$

Radiofrequency can be substituted for hv, leading to a new equation, which can be solved for the NMR resonance frequency (v). Using the resonance frequency, the expected chemical shift (δ) may be computed.

$$hv = \mu B_o H_o$$

$$\delta = \frac{\left(v_{obseerved} - v_{reference}\right)}{v_{spectometer}}$$

Expected chemical shift or delta (δ) is observed in ppm and gives the distance from a set reference. Delta is directly related to the chemical environment of the particular atom i.e., the NMR transition frequencies are sensitive to the electron distribution around the nucleus, which shields the nucleus from applied magnetic field. Low field or high delta indicates that an atom is in environment which induces less shielding than in a high field or low delta. Thus, NMR frequencies reveal the chemical structure of the sample. [124, 125]

As mentioned above, the most notable difference between solid and solution NMR spectroscopy occurs from the state of the samples. In solution molecules rotate rapidly while those in a solid are fixed in a lattice. Different peak readings will be produced depending on the orientation of the molecules in magnetic field, because chemical shielding depends upon the orientation of a molecule causing chemical shift anisotropy. Therefore, the effect of the chemical shielding also depends upon the orientation of the molecule with respect to the spectrometer. In solutions these counteracting forces are balanced out due to randomization of the molecular movements, but in solid samples the molecules are fixed. If the chemical shielding is not determined accurately neither will the chemical shifts (δ). [123]

Another issue with solid samples are dipolar interactions which can be very large in solid samples causing linewidths of tens to hundreds of kilohertz to be generated. Dipolar interactions are tensor quantities, which demonstrate values dependent on the orientation and placement of a molecule in reference to its surroundings. The molecules themselves are fixed and evenly spread apart, but this does not apply for the nuclei. Closer nuclei display greater dipolar interactions and vice versa, creating the noise seen in spectra of NMR not adapted for solid samples. Dipolar interactions are averaged out in solution samples because of randomized movement and spin state repulsions by molecular motion. However, in solid state these interactions are not averaged and become a third source of line broadening. [122]

The application of NMR spectroscopy to rigid or semi-rigid solid samples spans an inexhaustible variety of systems, like membrane proteins and amyloid fibrils in biochemistry. In solids, the orientation dependence of NMR frequencies causes powder patterns for each nuclear spin. In most cases, this anisotropic contribution

needs to be removed to obtain site-resolved spectra. Thus, magic angle spinning (MAS) was developed, to counteract chemical shift anisotropy and dipolar interactions. The description of dipolar splitting and chemical shift anisotropy interactions depends on the geometric factor ($3\cos^2\theta$-1).

$$Dipolar\ splitting = \mathrm{C}\left({}^{\mu_o}/_{8\pi}\right)\left({}^{\gamma_a\gamma_x}/_{r_{ax}^2}\right)(3\cos^2\theta_{iz} - 1)$$

$$\sigma_{zz} = \bar{\sigma} + {}^{1}/_{3}\sum \sigma_{ii}\,(3\cos^2\theta_{iz} - 1)$$

If this factor is decreased to 0, then line broadening due to chemical shift anisotropy and dipolar interactions will disappear. Therefore, solid samples are physically spun around an axis that is tilted by 54.74° from the static magnetic field [126, 127], effectively allowing solid samples to behave similarly to solutions/gases in NMR spectroscopy. Standard spinning rates range from 12kHz to an upper limit of 35kHz, where higher spin rates are necessary to remove higher intermolecular interactions. Because MAS averages out the information rich anisotropic chemical shift and dipolar interactions, many radiofrequency pulse sequences have been designed to selectively reintroduce the desired spin interactions while retaining spectral resolution. Such multi-pulse and multidimensional experiments are the basis of many modern solid-state NMR experiments. [124, 128]

In NMR spectroscopy multiple radiofrequency pulses can be applied with specific timings, phases and amplitudes to manipulate the nuclear magnetic moments in order to obtain the structural information of interest. The first, and simplest experiment that is conducted during the analysis of most samples is 1D MAS experiment involving either direct excitation of the nuclear spin or cross polarization from protons (CPMAS). [127, 129] CPMAS is the principal experiment for ^{1}H-rich organic compounds because it enhances the signal sensitivity of a rare and low γ nucleus X i.e., any nucleus other than ^{1}H, by transferring magnetization from the abundant and high γ protons. ^{1}H decoupling is applied during X-nucleus detection to enhance spectral resolution. 1D CPMAS spectra show one peak for each chemically distinct site. [122]

3.2 Differential scanning calorimetry

Differential scanning calorimetry (DSC) is a versatile technique and has been used to study hydrated phospholipid membranes. [130-133] Among thermoanalytical techniques, DSC is the most applicable in research and drug development process. It is used for determining the thermal effects of a variety of materials, including biologically relevant systems that are characterized by an enthalpy change by the temperature range. [133] In pure lipids, DSC can accurately determine the phase transition temperatures and the associated enthalpies, and therefore systematically can be strudied how chemical structure of lipids translates into thermodynamic properties. In addition to determining the physical properties of pure lipids, the miscibility and phase behaviour of lipid mixtures can also be determined. It is suitable technique to monitor the interactions that take place among the drug delivery systems of liposomes and the potential bioactive molecules that are incorporated inside them. Moreover, it is considered to be a useful tool to characterize the thermal behaviour of lipid bilayers in the absence and presence of drugs and to highlight parameters, such as the cooperativity between the lipids and the guest molecules, e.g. drugs, providing a prediction of the behaviour of potential future drug delivery liposomal platforms. [134] Furthermore, the combination of DSC with other methods, such as molecular dynamic simulations, Raman spectroscopy and X-ray scattering can reveal valuable information, such as the conformational changes of the molecule inserted in the core of the lipidic bilayers. [134-141]

DSC provides accurate information, quickly and easy, about both physical and energetic properties of a material. DSC measures the difference in heat flow between sample and related reference against time or temperature, while programming the sample temperature under specific atmosphere conditions. [142] There are two kinds of calorimetric technics, the first one is heat flux DSC, where sample and reference are heated in the same furnace and a difference of temperature (ΔT) is measured. Successively, the signal is converted to a power difference by the calorimetric sensitivity. The second one is power-compensated DSC, where both the sample and reference are heated in two independent heaters, while the electrical power ($\Delta P = d(\Delta Q/dt)$), requested to maintain close to zero the difference of temperature between sample and reference, is measured

in real time. [143] DSC measures the heat flow going into or being released by a material, that means that the heat capacity at constant pressure (C_p) can be calculated. Heat capacity units are $calº C^{-1}$ or $Jº C^{-1}$. It measures the amount of heat input (q) required to raise the temperature of a specimen by one degree Celsius while at constant pressure. Heat capacity is usually normalized by dividing the specimen heat capacity by the numbers of grams, to get the heat required to raise one gram of specimen by one degree Celsius. This corresponds then to the specific heat capacity C_p. If desired the heat capacity can be normalized by the number of moles. Heat capacity is defined by the equation below, where T is the temperature and q is the heat input. [133]

$$C_p = (\partial q / \partial T)_p$$

If the temperature changes from T_o to T_1, the enthalpy of reaction (ΔH) is

$$\Delta H = \int_{T_0}^{T_1} C_p dT$$

Usually, ΔT is small and C_p is independent of temperature between T_o and T_1. The integral thus reduces to

$$\Delta H = C_p(T_1 - T_o) = C_p \Delta T$$

Generally, the energy flux is associated with a transition or reaction and is graphed as a heat flow along the ordinate, while the temperature or time is the abscissa. In DSC curve, the endothermic peak is associated with absorption of energy, while the exothermic peak implies release of energy from the sample. The verse of the picks depends on the sign of the heat flow. [133, 143]

Phospholipids and especially glycerophospholipids, are a lipid group with a large variety of distinctive molecules. Phospholipid molecules have amphiphilic properties, since their structure consist of specific hydrophilic and hydrophobic regions, influencing greatly their physicochemical behaviour. They belong to the double-chain amphiphiles and are the building blocks of all biological membranes. The *sn*-1 and *sn*-2 positions of glycerol residue is esterified with fatty acids of varying degrees of unsaturation and numbers of carbon atoms. The *sn*-3 position of glycerol is etherified to the phosphate and the phosphate is also esterified to an alcohol that determines the phospholipid. [133, 144]

In aqueous media phospholipids can form a bilayer structure or lamella (L) resembling biological membranes therefore are used to study the thermotropic behaviour of such systems. Since they belong to the lyotropic liquid crystalline state, they exhibit extensive polymorphism. This polymorphism behaviour is related to the transition of biological membranes from gel to liquid crystalline phase, producing their functionality. The main transition of phospholipid bilayers when thermal energy is added occurs between the gel to fluid lamella (L) state i.e. ordered to disordered, affecting the van der Waals interactions between hydrocarbon chains, increasing their mobility. The provided amount of energy is associated with the phase transition of phospholipids and with the conformation properties of the phospholipids, which affect the stability of the system. The changes of enthalpy are associated with the thermal energy added, and the phase transitions of phospholipids formed bilayers from the gel to liquid crystalline state are related to the decrease of the hydrophobic van der Waals interactions between lipid acyl chains. The enthalpy of this transition is calculated using calorimetric techniques and measured as enthalpy per mol of phospholipid. [133]

DSC has been extensively used to study the thermotropic behaviour of phospholipid bilayers, which act as a model of biological membranes. [131] The reason for studying the transition changes of the phospholipid bilayers by measuring the changes of enthalpy (ΔH_{cal}) during the transition process is an extremely important issue for investigating not only biological phenomena but to rationally design lipid drug carries based on their thermal behaviour. These enthalpy changes correspond to changes of the heat capacity (C_{pmax}) of phospholipids during the transition process from gel to the liquid crystalline phase (see Figure 3.2). [133]

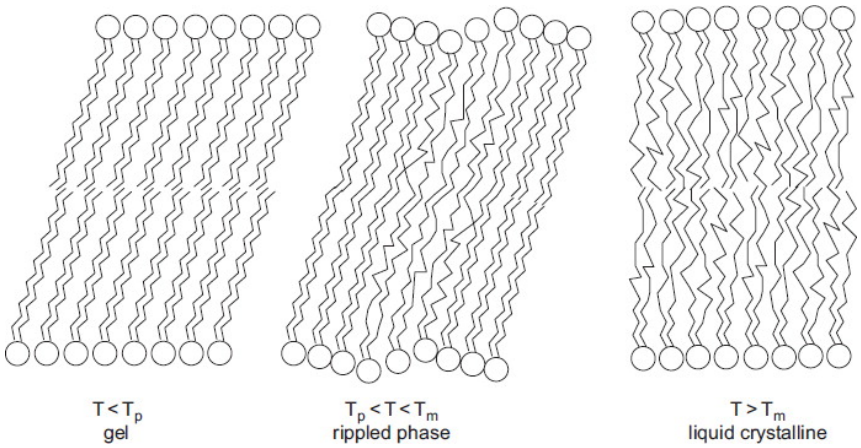

***Figure 3.2*:** Schematic presentation of the alignment of acyl chains in a saturated phospholipid such as DMPC to form a double layer of molecules. [133]

The cooperativity of the molecules during the transition process is crucial concerning the melting behaviour of the material. However, the phospholipid hydrocarbon acyl chain of DMPC is thermodynamically transit from an all trans conformation in the gel state to a disordered state that contains several *gauche* conformations resulting in a transition to a liquid crystalline phase. The van der Waals hydrophobic interactions of acyl chains of DMPC is reduced, due to the endothermic behaviour of the material, which increases the intramolecular and intermolecular lipid acyl chain motions. [131] The gel to liquid crystalline transition of pure phospholipids appears as a sharp peak, due to favourable van der Waals interactions of lipid acyl chain, resulting in high cooperativeness of the molecules (see Figure 3.3). [133]

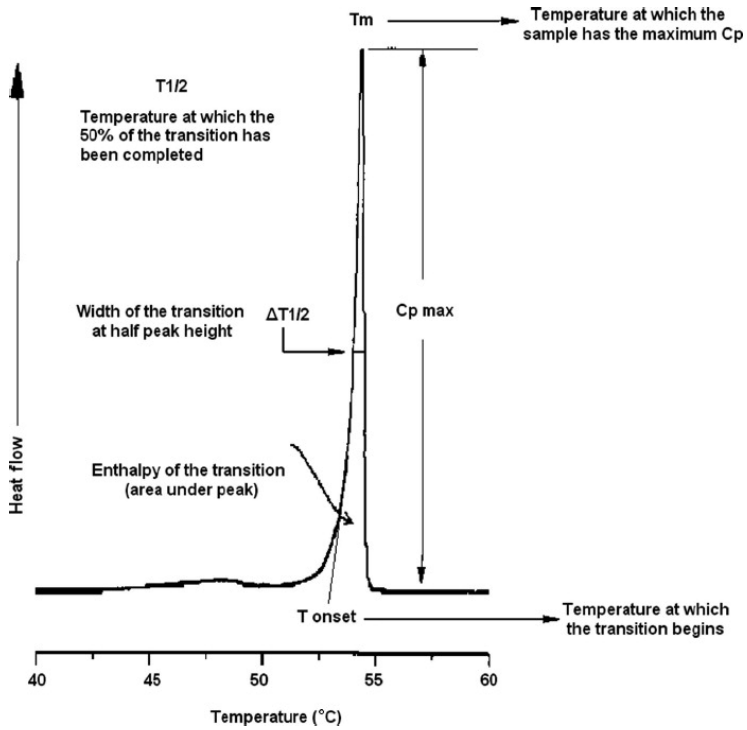

Figure 3.3: DSC thermogram with the characteristic thermodynamic parameters provided by the DSC technique. [133, 134]

There are several characteristic temperatures which can be used to describe DSC. The onset temperature (T_{onset}) is the temperature that is constructed by the intersection of the baseline tangent with the tangent of the leading edge of the endotherm or exotherm of a transition. The peak temperature (T_m) is the temperature represented by the apex of the peak. Where the peak transition returns to the baseline may be referred to as the recovery or endset temperature (T_{endset}). The temperature that corresponds to the half of the enthalpy change during the transition is $T_{1/2}$ while $\Delta T_{1/2}$ is the width of the transition at half peak height (see Figure 3.3). [133, 145] The phenomena that take place during heating process are the following: The glass transition or T_g is a transition that occurs in amorphous or semicrystalline materials. Around T_g, C_p undergoes a quasi-discontinuous change from a lower value to higher value i.e. it does not change sharply but happens over a broad range in temperature, depending on the molecular structure of the material. If an amorphous material tends to crystallize or a semicrystalline material does not crystalize to the limit of its ability when cooled, it is possible to see crystallization during the heating. Crystallization appears as an exothermic peak, with the crystallization temperature T_c always to

occur between T_g and melting temperature T_m. Crystallization only occurs in samples that can crystallize and in samples that are not already crystallized, but potentially can. The highest temperature peak in a DSC thermogram is often the melting transition. Melting is a first order endothermic peak, which means that it requires heat. For small molecules, the peak is very sharp, while for larger molecules such as polymers and lipid bilayers the melting transition is broad. The area under a melting transition curve is the total amount of heat absorbed during the melting process. Further peaks can be attributed to loss of solvent molecules, e.g., evaporation which is mostly endothermic, and to endothermic or exothermic chemical reactions, among them decomposition. [133]

The thermodynamic changes of lipid bilayers as a function of phase transitions after a drug is incorporated into lipid bilayers, and how these changes could be related to the interaction of the drug with the lipid carrier affecting the drug bioavailability, have been extensively studied. The modifications on the ordered lipidic structure of phospholipid bilayers, when they interact with a drug are observed. These are due to interactions either with the lipophilic part of a phospholipid, resulting in greater thermotropic changes in T_m, or with polar head region, resulting in an abolition of transition, i.e. pre-transition peak, at 13.3 ^{o}C when DMPC is used as the phospholipid. [146-148]

3.3 Small and wide-angle X-ray scattering

Small angle X-ray scattering (SAXS) is a well-established and versatile biophysical method for the analysis of nanoscale structures and dimensions and their shapes. The materials can be solid, or liquid and they can contain solid, liquid or gaseous domains of the same or another material in any combination. This makes it ideal for studying the overall shape and structural transitions of biological macromolecules in solution. The SAXS method is accurate, non-destructive and usually requires a minimum of sample preparation. Normally, X-rays are sent through the sample, i.e. transmission mode, and every particle that happens to be inside the beam will send out its signal. Thus, the average structure of all illuminated particles in the bulk material is measured. When combined with wide angle X-ray scattering (WAXS), complementary information about the atomic structure can be obtained. In principal nanoscale systems, e.g.,

membrane proteins inside lipid bilayers can be studied with real space imaging or reciprocal space scattering techniques. X-ray scattering makes use of the variation of a sample's electron density to generate contrast, providing reciprocal space data. A spatial variation of electron density at nanometer length scales will scatter an X-ray beam to low angles while in the atomic scale will scatter to high angles. SAXS is therefore a technique to study material structures at large distances or small angles. [149, 150]

At the individual practice level, SAXS is an immensely powerful tool to determine an object's size, size distribution, shape and surface structure. [149, 151, 152] The definition of particle in SAXS has a broad meaning, thus it has been used to study variety of particles such as aerosols, micelles, MLVs, minerals etc. [153, 154] The definition of a particle for SAXS can be unified under a broader concept of morphology, meaning that it is not the composition of the material but its structure that is used to classify particulate and nonparticulate systems. [149]

Only in two cases the SAXS method requires standards. The first one is when the sample to detector distance is not known. Then a reference sample of known structure is measured to calibrate the scattering angles. The second is when the density of a number of particles or their mean molecular weight must be determined. Then the experimental intensities must be scaled by the intensity from a standard sample, such as water.

SAXS beamlines are typically equipped with multiple types of detectors. This includes a two-dimensional (2D) area detector and at least two beam monitors, m_1 and m_2 (see Figure 3.4). The upstream beam monitor (m_1) is used to correct for any variation of incoming flux, while the downstream monitor (m_2) is typically mounted on the beamstop and is used to normalize the transmittance of the sample. The 2D area detector is used to collect the angle resolved SAXS signal that is elastically scattered i.e. that is without any change in wavelength, by the sample. Standard calibrants should be measured each time the setup is changed, including silver behenate to determine sample to detector distance, and glassy carbon or water to determine the absolute intensity. [149, 155-157]

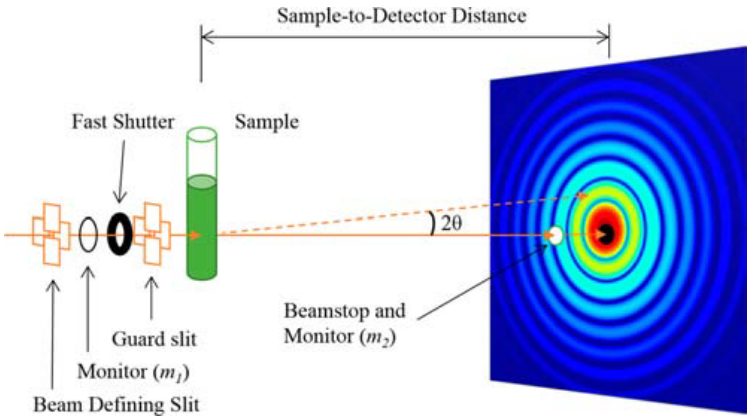

Figure 3.4: Schematic representation of the optical components of the 12ID-B SAXS beamline. [149]

Once the scattering signal is collected on the 2D detector, multiple data correction procedures may be performed, depending on the type of detector used e.g., dark current subtraction, image distortion, linearity correction and flat filed correction. Next, the position of each pixel on the SAXS image is converted into the scattering angle 2θ or the scattering vector q, where the modulus is $q = 4\pi \sin(\theta)/\lambda$, and λ is the wavelength of the X-ray, with the choice of an appropriate coordinate system. This conversion is accomplished using experimental parameters that include the sample to detector distance (SSD) and the pixel size of the detector. For an image that is isotropic along the azimuthal direction, polar coordinates are typically used. This is applicable to most nanoparticle systems in solution, as they are typically randomly oriented and therefore have isotropic scatterings. The 2D images are then azimuthally averaged to give a one dimensional (1D) scattering curve. When the image is no longer isotropic along the azimuthal direction, it may be represented in other coordination systems such as Cartesian or ellipsoidal polar, depending on the orientation of the nanostructures. [158, 159]

In SAXS experiments, the count value on a pixel of the 2D detector (J) or the 1D averaged data is typically normalized by the value of the second beam monitor (m_2) located downstream of the sample where counts on both detectors are collected for a given exposure time. The data I contains a background signal that originates primary from air, the beamline optics including the X-ray windows, and the sample cell. This contribution can be removed by subtracting the scattering

intensity of the empty container (I_{cell}) from that of the sample in the same container ($I_{sample/cell}$). [149]

$$\frac{J}{m_2} \equiv I$$

$$I_{\text{sample}} = I_{\text{sample/cell}} - I_{\text{cell}}$$

The units of *I* arbitrary, but it is a quantity proportional to the number of X-ray photons arriving at a particular pixel of the 2D detector. It is therefore possible to convert *I* into absolute intensity units by using a known absolute intensity calibration sample such as glassy carbon or water. [149, 155-157] When the background subtracted intensity *I* for a standard sample with thickness d_s at given scattering angle is I_s, and its precalibrated absolute intensity is $\frac{d\Sigma}{d\Omega_S}$, the intensity of a sample in absolute units, $\frac{d\Sigma}{d\Omega}$, is given by the equation below, where d is the thickness of the sample and the differential cross section $\frac{d\Sigma}{d\Omega}$ is given in units of cm^{-1}. This equation makes use of the value of the first monitor located upstream of the sample, m_1. In this case m_{1S} is the monitor value obtained when the standard sample is measured. When it is not necessary to describe scattering intensity in absolute units *I*(q) is used instead of $\frac{d\Sigma}{d\Omega}(q)$. [149]

$$\frac{d\Sigma}{d\Omega}(q) = \frac{d\Sigma}{d\Omega_S}\frac{d_S I(q) m_{1S}}{d I_S m_1}$$

The determination of the absolute scattering intensity of nanoparticle systems allows to obtain the concentration of nanoparticles. This information can be used in a variety of experiments such as determining molar extinction coefficients and the porosity of a sample. [149]

As it is known the functionality of biological membranes strongly depends on the geometrical and chemical properties of the amphiphilic molecules that constitute the membrane walls. Membrane parameters such as electron density profile or the flexibility are important parameters to know because the functionality of the membrane depends on them. The permeability or the tendency to reorganize into micelles, lamellar stacks or vesicles strongly depends on the internal arrangement of the molecules in the bilayers. The presence of pharmaceuticals or a change in the temperature can modify the inner structure of the membranes,

and therefore the investigation of membrane structure is important for creating drug delivery strategies. Phospholipid-bilayer membranes such as POPC, DPPC and DMPC can be studied with the SAXS method to obtain their electron density, thickness, repeat distance of lamella and stacks, number of layers, packing and flexibility parameters. [149]

3.4 Molecular dynamics simulations

3.4.1 Principles of the method

Molecular dynamics (MD) simulations are performed aiming at understanding the evolution of the system through time based on the intramolecular and intermolecular interactions of the studied system. Using MD simulations the position $r^N = (r_1,r_2,...r_N)$ and velocity $u^N = (u_1,u_2,...u_N)$ of each of the *N* atoms of the system through time can be calculated using a convenient potential $V(r^N)$ and integration of the Newtonian equations motion. [160]

$$m_i a_i = F_i(t) = \sum_{i \neq j}^{N} F_j$$

$$\frac{dp_i(t)}{dt} = -\frac{\partial V(r_i, \ldots, r_N)}{\partial r_i}$$

and the equation can be transformed to the following one

$$\frac{d^2 r_i(t)}{dt^2} = -\frac{1}{m_i}\frac{\partial V(r_i, \ldots, r_M)}{\partial r_i}$$

For this purpose, we calculate the forces $\mathbf{F}_i$ acting on each atom *i* from the other atoms *N*-1 atoms of the system using the applied potential of the system according to equation above. Numerical integration through a convenient integration algorithm leads to the complete set of momentums p^N or equally velocities u^N and positions r^N (3*N* atomic coordinates) *i.e.* the trajectory of the system (see Figure 3.5) after a time step Δ*t* if the velocities and positions and know in time *t*

$$r_1(t), \ldots, r_N(t) \rightarrow r_1(t + \Delta t), \ldots, r_N(t + \Delta t)$$
$$p_1(t), \ldots, p_N(t) \rightarrow p_1(t + \Delta t), \ldots, p_N(t + \Delta t)$$

At *t*=0 arbitrary velocities u^N can be assigned according to the temperature *T* of the system according to the equation below

$$\sum_{i=1}^{N} \frac{m_i v_i^2}{2} = \frac{3}{2} N k_B T \text{ or}$$

$$\Delta T = \frac{1}{2} \sum_{i=1}^{N} \frac{2}{3} \frac{m_i {v_i}^2}{N k_B}$$

and coordinates correspond to an experimental or potential energy minimized protein structure, using a steepest-descent or conjugate gradient algorithm. Time step or integration step Δ*t* is in the range of 1 fs = 10^{-14} s in atomistic simulations.

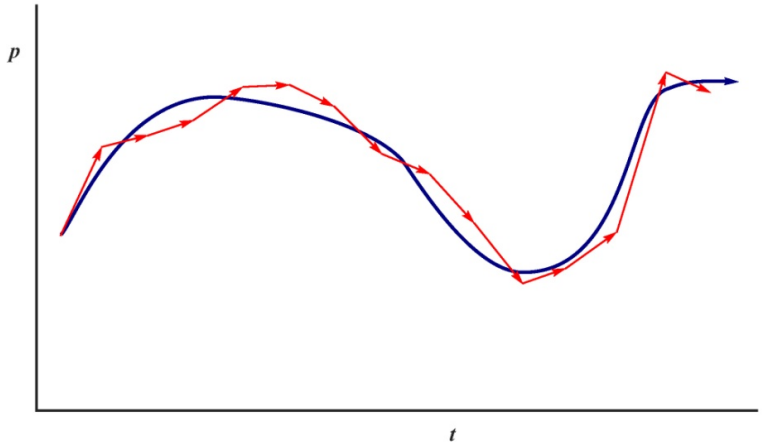

Figure 3.5: Accurate (in blue) trajectory of one atom of a *N*-atoms system and approximate trajectory (in red) the resulted after integration of the Newtonian equation of motions. Read arrows follow the accurate trajectory depending on the size of the time step and the accuracy of the potential energy $V(r^N)$ describing the forces between the atoms. Time step is always the same but the size Δp can be significantly changed after a time step.

A common integrator is the Verlet [160] algorithm which is based on the two equations below

$$r(t + \Delta t) = 2r(t) - r(t - \Delta t) + a(t)(\Delta t)^2$$

$$v(t) = \frac{r(t + \Delta t) - r(t - \Delta t)}{2\Delta t}$$

Periodic boundary conditions (PBCs) are a set of boundary conditions which are used for approximating a large (or infinite) system by using a small part called a unit cell. The geometry of the unit cell satisfies perfect two-dimensional tiling, and when an object passes through one side of the unit cell, it re-appears on the opposite side with the same velocity. The large systems approximated by PBCs consist of an infinite number of unit cells. In computer simulations, one of these is the original simulation box, and others are copies called images. During the simulation, only the properties of the original simulation box need to be recorded and propagated. The minimum-image convention is a common form of PBC particle book keeping in which each individual particle in the simulation interacts with the closest image of the remaining particles in the system. [160]

A flow scheme for MD simulations is presented in Figure 3.6.

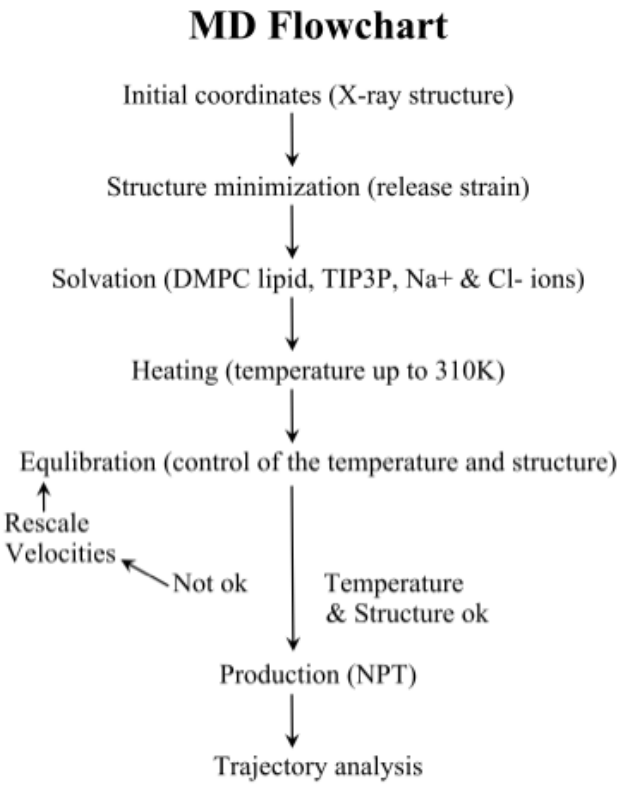

***Figure 3.6*:** The flow scheme for the molecular dynamics simulations applied.

3.4.2 The potential energy function and force fields

The potential energy function in MD simulations, is a set of equations that estimate the total potential energy of the system. It contains energetic terms that are associated with the angle values and the bond lengths deviation from their equilibrium values and terms that described the non-bonded interactions of the system (Coulomb and van der Waals interactions). Several parameters are used for the equilibrium values of bond lengths, angles, bond, angle and dihedral potential constants etc. and atom types that describe the connectivity of the atoms in the molecules. The set of equations, parameters and atom-types is known as force field. During the improvement of a force field the equations remain the same but the parameters set is changed. For example, the functional form of the OPLS 2005 and Amber force field are shown in equations below, respectively.

$$V_{MM} = V_{stretch} + V_{bend} + V_{torsn} + V_{vdW} + V_{el}$$

$$= \sum^{r\ bonds} U_r + \sum^{b\ angles} U_\theta + \sum^{t\ dihedrals} U_t + \sum_i^a \sum_j^b U_{non-bonded}$$

$$V_{MM}(\mathrm{OPLS}) = \sum^{r\ bonds} \frac{k_r}{2}(r - r_{\mathrm{eq}})^2 + \sum^{b\ angles} k_\theta(\theta - \theta_{\mathrm{eq}})^2$$

$$+ \sum^{t\ dihedrals} \left[\frac{V_1}{2}(1 + cos\,\varphi) + \frac{V_2}{2}(1 + cos\,2\,\varphi) + \frac{V_3}{2}(1 + cos\,3\,\varphi)\right.$$

$$\left. + \frac{V_4}{2}[(1 + cos\,4\,\varphi)\right] + \sum_i^a \sum_j^b \left[\frac{q_i q_j}{\varepsilon r_{ij}} + 4\varepsilon_{ij}\left(\frac{\sigma_{ij}^{12}}{r_{ij}^{12}} - \frac{\sigma_{ij}^{6}}{r_{ij}^{6}}\right)\right]$$

$$V_{MM}(\mathrm{Amber}) = \sum^{r\ bonds} \frac{k_r}{2}(r - r_{eq})^2 + \sum^{b\ angles} k_\theta(\theta - \theta_{eq})^2 + \sum^{t\ dihedrals} \frac{V_n}{2}[1 + \cos(n\varphi - \gamma)]$$

$$+ \sum_i^a \sum_j^b \left[\frac{q_i q_j}{\varepsilon r_{ij}} + 4\varepsilon_{ij}\left(\frac{\sigma_{ij}^{12}}{r_{ij}^{12}} - \frac{\sigma_{ij}^{6}}{r_{ij}^{6}}\right)\right]$$

3.4.3 Alchemical binding free energies calculated with free energy perturbation and bennett acceptance ratio method

The principle of the free energy perturbation (FEP) method [161] coupled with MD simulations for sampling has been well described in many references while

the calculation of relative protein-ligand binding free energy of alchemical transformations relies on the thermodynamic cycle and has also been explained in literature. [162, 163] In theory, the free energy is a state function, and thus the free energy difference between states is independent of the path that connects them. Briefly, a thermodynamic parameter λ that smoothly connects states 0 and 1 through a λ-dependent potential $U(r^N; \lambda)$, such that $U(r^N; 0) = U_0(r^N)$ and $U(r^N; 1) = U_1(r^N)$. The transformation is broken down into a series of M steps corresponding to a set of λ values $\lambda_1, \lambda_2, ..., \lambda_M$ ranging from 0 to 1, such that there is sufficient phase space overlap between neighboring intermediate λ states. For the sampling of λ states MD simulations are applied. FEP method computes the free energy change of transformation 0→1 from the following equation, known as the Zwanzig equation [164, 165].

$$\Delta G_{0\to1} = \langle G \rangle_1 - \langle G \rangle_0 = -k_B T \, ln\left\langle e^{-(V_1 - V_0)/k_B T} \right\rangle_0$$

The difference of ΔG between two λ values is according to equation below:

$$\langle G \rangle_{\lambda+d\lambda} - \langle G \rangle_\lambda = k_B T \, ln\left\langle e^{(V_{\lambda+d\lambda} - V_\lambda)/k_B T} \right\rangle_\lambda$$

A linear extrapolation between states can be applied for the construction of $V_1(r^N; \lambda)$

$$V(r^N; \lambda) = V_0(r^N; \lambda) + \lambda \Delta V(r^N; \lambda) = V_0 + \lambda(V_1 - V_0)$$

$$\Delta V(r^N; \lambda) = V(r^N; \lambda) - V_0 = \lambda(V_1 - V_0)$$

Softcore LJ and Coulomb term potentials [166] have also been described according to equations below in order to avoid penetration of atoms close to the end points 0,1.

$$U(r^N; \lambda) = U_0^{SC}(r^N; \lambda) + \lambda \Delta U_0^{SC}(r^N; \lambda)$$
$$= U_0^{SC}(r^N; \lambda) + \lambda \left(U_1^{SC}(r^N; 1 - \lambda) - U_0^{SC}(r^N; \lambda) \right)$$

Relative binding free energies between pairs of ligands $\Delta\Delta G_{\text{ligand } 0 \to 1}(\Delta G_{0,1})$ were calculated according to equation below based on ΔG obtained for the transformations of the ligands in the bound and the solvated state, respectively, $\Delta G_{\text{ligand},0\to1}$(b) and $\Delta G_{\text{ligand},0\to1}$(s) (see thermodynamic cycle in Figure 3.7)

$$\Delta\Delta G_{\text{ligand},0\to1} = \Delta G_0 - \Delta G_1 = \Delta G_{\text{ligand},0\to1}(b) - \Delta G_{\text{ligand},0\to1}(s)$$

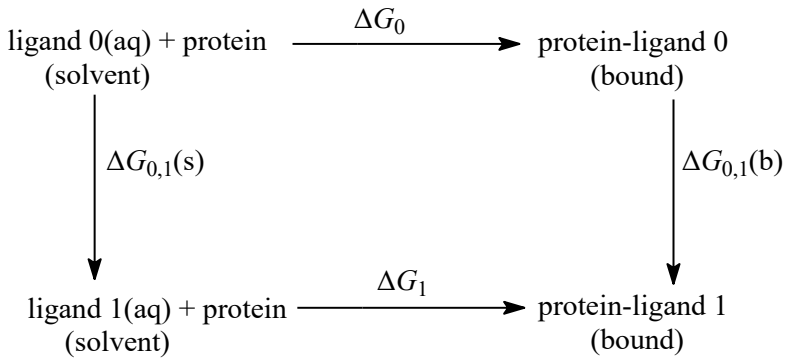

***Figure 3.7*:** Thermodynamic cycle for the calculation of relative free energies of binding applied to alchemical tranformations. ΔG_0, ΔG_1 are the free energies of transfer of 0 and 1 from the aqueous phase (unbound state) to the bound state, respectively. $\Delta G_{0,1}$(s) and $\Delta G_{0,1}$(b) are the free energy differences of the mutation of ligand 0 into ligand 1 in aqueous solution, and bound to the protein respectively.

BAR method calculates the free energy difference between neighboring intermediate states using equation below

$$\Delta G_{\lambda\to\lambda+1} = -\ln \frac{\langle w\exp(-\beta U_{\lambda+1})\rangle_{\lambda}}{\langle w\exp(-\beta U_{\lambda+1})\rangle_{\lambda+1}}$$

where w is a function of $G(\lambda)$ and $G(\lambda+1)$ and $\beta=k_B/T$. The equation is solved iteratively to give the free energy change of neighboring states $\Delta G(\lambda \rightarrow \lambda+1)$, which via combination yield the overall free energy change. BAR method has been shown to minimize the variance in the calculated free energies, by making more efficient use of the simulation data. [167, 168]

CHAPTER 4

Comparative Perturbation Effects Exerted by the Influenza M2 Protein Inhibitors Amantadine and the Spiro[pyrrolidine-2,2'-adamantane] Variant AK13 to Membrane Bilayers Studied Using Biophysical Methods and MD Simulations

4.1 Introduction

As it is established, binding of aminoadamantane derivatives [89, 94, 169, 170] inside the ion channel pore of the A/M2TM [34, 53, 58, 171] blocks proton conduction [17, 73] and in that way preventing a continuation of the viral life cycle and abrogating pathogenesis [12, 39]. Simulations and experimental biophysical studies for the *Aamt* - M2TM complexes [57, 58, 172-180] have been performed in a lipid environment for the investigation of the essential molecular interactions and conformational changes. It was found that DMPC is an optimal membrane bilayer for this system compared to other lipids or glycerophospholipids [85, 181].

The interaction of *Amt* with DMPC bilayers have also been studied by Li *et al.* using ssNMR and 12.6 ns MD simulations to *Amt* in DMPC bilayers [182] and showed that when the neutral *Amt* is incorporated in these bilayers it adopts a single preferred orientation and localization. The long axis of *Amt* is in an average parallel to the bilayer normal, the amine group interacts with glycerol backbone and much of the fatty acyl chain is wrapped underneath the drug, as indicated by the experimental and MD computational results. The lipid orientation changes upon drug binding as characterized by the anisotropy of ^{31}P chemical shielding and ^{14}N quadrupolar interactions and by the MD simulations [182]. Duff *et al.* applied neutron and X-ray diffraction experiments to study the interactions of *Amt* with 2-oleoyl-1-palmitoyl-*sn*-glycero-3-phosphocholine (POPC) bilayers. They found out that uncharged *Amt* had two populations, one that was nearly at the bilayer center and one at the water/bilayer interface [183]. Subczynski *et al.* performed EPR *studies* on DMPC, POPC and distearoylphosphatidylcholine (DSPC) liposomes, demonstrating that *Amt* distributes deep in the acyl chain equally in the gel and liquid crystalline lipid phases [184] simulation performed by a Potential of Mean Force (PMF). Chew *et al*. [185] using POPC bilayers concluded that *Amt* interacts considerably with head-groups and orients in such

way that the tricyclodecane moiety is in contact with the lipid acyl chains and the amine group with the glycerol oxygens. [186] Suwalsky *et al*. [187] used Differential Scanning Calorimetry (DSC), fluorescence and scanning electron microscopy (SEM) to study the effects of *Amt* on DMPC and dimyristoyl phosphatidylethanolamine (DMPE) as well as on human erythrocytes. DMPC bilayers were affected more considerably than DMPE bilayers, indicating that the charged amine [188-191] of *Amt* affects phosphate oxygens and its lipophilic part alters the acyl chain regions in both the gel and liquid crystalline phases. The morphological changes observed to erythrocytes were concentration dependent and attributed to the fact that *Amt* mostly interacts with DMPC which is located preferentially in the outer layer of the human erythrocyte membrane. [187]

Gu *et al.* found that, at biological pH 7.4, the *Amt* and *Rim* molecules are mostly protonated in water and at the lipid water interface, can bind favourably to lipid bilayers at the lipid-water interface. It has been calculated [192] that when lipophilic aminoadamantane drugs interact with the membrane bilayer their binding to the lipid-water interface is favoured with an energetic stabilization of -9 kcal/mol if the solvent-bound state is assigned to zero. The drugs may become easily deprotonated once inside the lipid bilayer, which would facilitate the transport of the drug molecules across membranes at exceptionally low energy cost. Based on their results as well as drug absorption and concentration studies i*n vivo*, it is believed that, once administered to the human body, the drugs may easily enter infected cells, such as the cells in the respiratory system, as shown by Hayden *et al.*, by crossing cell membranes to reach viral particles inside the cell.

To seek understanding experimentally the lipid bound state for two ligands, in this research project were examined the comparative effects of *Amt* and *AK13* on DMPC bilayers (see figure 4.1) using ssNMR, small-angle and wide-angle X-ray scattering (SAXS and WAXS), and DSC as well as MD simulations for 500 ns. Spiro[pyrrolidine-2,2'-adamantane] *AK13* is an A/M2 WT blocker [176] which includes an additional carbon adduct compared to *Amt*. *AK13* is more lipophilic compared to *Amt* and exhibits a higher affinity to A/M2TM according to the ITC results. The ITC experiments which were performed by titrating the receptor A/M2TM tetramer with aminoadamantane ligands in dodecyl phosphocholine

(DPC) solutions showed that K_d(*AK13*) is 0.62 μM and K_d(*Amt*) is 2.17 μM [174]. Compared to *Amt*, *AK13* exhibited similar or much higher antiviral efficacy against A/WSN/33-M2-N31S (H1N1) or Ishikawa [170] influenza A virus respectively.

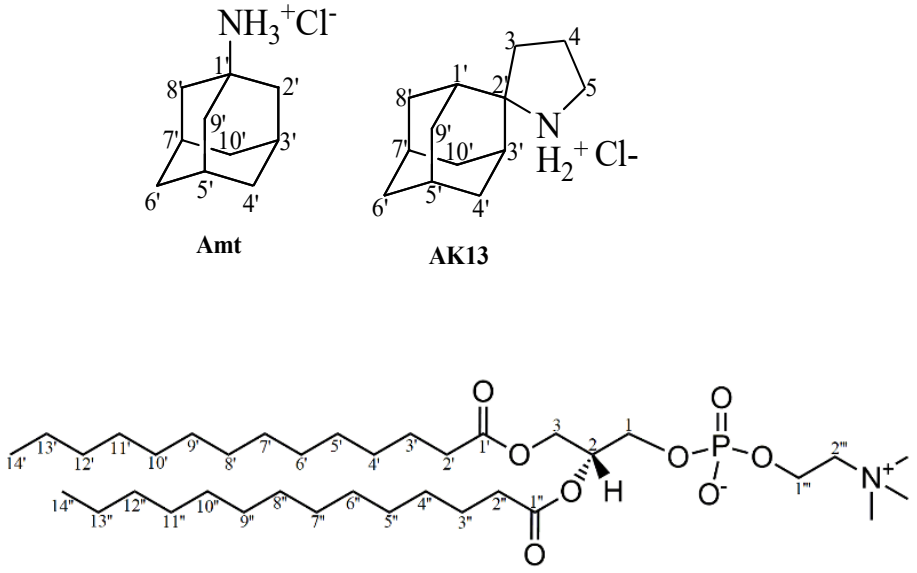

***Figure 4.1*:** Structures of *Amt* and the aminoadamantane derivative *AK13* and of DMPC phospholipid.

It is evident that drug action involved a system in lipid bilayers. For this reason details studies were initiated to seek drug:membrane perturbation information.

4.2 Material and methods

4.2.1 Materials

Amt (*Mw* = 187.7) was purchased from Merck Schuchardt OHG - Hohenbrunn, Germany and DMPC (Mw = 677.9) from Avanti Polar Lipids, Inc, Alabaster, Alabama, USA. *AK13* (*Mw* = 227.8) was re-synthesized in our lab according to a previously reported procedure [169].

4.2.2 Samples preparation

Samples were prepared by dissolving weighted amounts of dry DMPC lipid with *Amt* or *AK13* in methanol. The mixture was then evaporated at room temperature

under a gentle stream of argon and thereafter placed under vacuum for 24 hours to form a thin lipid film on the bottom of glass vials. The obtained mixtures were then fully hydrated at pH=7.8 with a buffer consisting of $Na_2HPO_4 \cdot 2H_2O$ and $NaH_2PO_4 \cdot H_2O$ to achieve multilamellar vesicles (MLVs). The drug concentration in the sample film was progressively increased to study the perturbation of drug and its presence in the lipid bilayers, both at low concentrations i.e., x=0.05 (5 mol%) and x=0.08 (8 mol%), as well as at high concentrations, i.e. x=0.20 (20 mol%) and x=0.50 (50 mol%).

4.2.3 Differential scanning calorimetry

DSC thermograms of the MLVs were obtained by utilizing a DSC822^e Mettler-Toledo calorimeter (Schwerzenbach, Switzerland), calibrated with pure indium (T_m=156.6°C). Sealed aluminum 40 μL crucibles were used as sample holders. The systems under investigation were MLVs composed of DMPC and *Amt* or *AK13* in various molar concentrations of drug as described above. Initially, around 5 mg of dried sample were weighted and placed in a crucible, followed by hydration with 5 μL of phosphate buffer, sealing of the crucible and subsequent 5-min vortexing. Then, each prepared sample was left to equilibrate for a 15-min period prior to measurement. The reference for the measurement of every sample was an empty aluminum crucible. Two heating-cooling cycles were performed until reproducibility of the sample was achieved. The temperature range used was from 10 to 40 °C and the scanning rate 2.5 °C/min. Before each cycle, the samples were equilibrated at a constant temperature of 10°C for 10 minutes. The calorimetric data obtained (characteristic transition temperatures $T_{onset,m/s}$ and $T_{m/s}$, enthalpy changes $\Delta H_{m/s}$ and widths at half peak height of the C_p profiles $\Delta T_{1/2,m/s}$) were analyzed using Mettler-Toledo STAR^e software. The transition enthalpy for DMPC is expressed as KJ/mol and is considered positive during an endothermic process.

4.2.4 Solid state ^{1}H MAS, ^{13}C CP/MAS and ^{31}P static NMR spectroscopy

^{1}H magic-angle spinning (^{1}H MAS), ^{13}C cross polarization/magic-angle spinning (^{13}C CP/MAS) and ^{31}P static ssNMR spectra were recorded on a Varian 600 MHz

VNMRS spectrometer equipped with a 3.2 mm HX MAS probe. Larmor frequencies for ^{1}H, ^{13}C, and ^{31}P nuclei were 599.53, 150.77, and 242.70 MHz, respectively. In the ^{1}H MAS NMR experiment samples were spun with rotation frequency of 5 kHz, protons were excited with a 90-degree pulse of 2.3 ms, repetition delay was 5 s, and 4 scans were co-added. In the ^{13}C CP/MAS experiment the polarization was transferred from protons to carbon nuclei in a 5 ms CP block (using RAMP on the proton channel), repetition delay between scans was 2 s, and number of scans was 2000. Static ^{31}P Hahn-echo NMR spectra were obtained using a 90-degree pulse of 1.8 ms, a 180-degree pulse of 3.6 ms, and an inter-pulse delay of 50 ms. Repetition delay was 5 s and 1000 scans were co-added. During acquisition of the ^{13}C CP/MAS and ^{31}P static signals, high-power proton decoupling was employed. The ^{1}H and ^{13}C chemical shift axes were referenced to tetramethylsilane, and the ^{31}P chemical shifts were reported relative to the phosphorus signal of 85% H_3PO_4.

4.2.5 X-ray diffraction

SAXS experiments were carried out at the Austrian SAXS beamline (Elettra Sincrotrone Trieste, Italy). [186] Two-dimensional Pilatus3 1M and Pilatus 100k detectors (Dectris Ltd, Baden, Switzerland) were used to collect SAXS and WAXS scattering pattern, respectively. For SAXS, the sample to detector distance was 1048 mm. The X-ray wavelength was 0.154 nm at a photon energy of 8 keV, covering a q-range between 0.095 to 7.74 nm^{-1}, where q is the length of the scattering vector defined by $q = 4\pi/\lambda \sin(\theta/2)$, with λ the wavelength and 2θ the scattering angle. For WAXS, the covered angular range corresponded to a q-spacing between 8.7 and 18.7 nm^{-1}. Silver behenate $CH_3(CH_2)_{20}COOAg$, with a d-spacing value of 5.838 nm and p-bromobenzoic acid were used as calibration standards to obtain respectively the angular scale of the SAXS and WAXS measured intensity. The 2D images were integrated to 1D scattering functions with Fit2D [193], and analyzed with IGOR pro (Wavemetrics, Inc., Lake Oswego, OR) to calculate when possible the characteristic lattice distance. The samples were loaded in a dedicated sample holder specially designed for gel samples and thermostated with a water bath (temperature stability ±0.1 °C, Unistat CC, Huber, Offenburg, Germany). The static measurements were done at 15 °C and 35 °C,

acquiring 15 frames of 20 s, with 2 s delay between each frame. The samples were equilibrated for few minutes before exposure. The bilayer model used and its applications was recently presented [194, 195].

4.2.6 Molecular dynamics (MD)

4.2.6.1 GROMACS

All MD simulations were performed with package GROMACS 5.1.4 package [196]. A bilayer of 256 DMPC molecules was placed in an orthorhombic box and was simulated in the full-atom representation using the CHARMM 36 force field [197, 198], in contact with a water phase of 7271 and 7259 water molecules for *Amt* and *AK13* systems respectively, described by the TIP3P model. [199] The water phase extends to approximately 14 Å alongside each side of the membrane. Periodic boundary conditions were applied (90.6 x 90.6 x 74.0 $Å^3$). The equilibrated structure of the DMPC bilayer was constructed through the CHARM-GUI program [200], a web-based graphical user interface to generate various molecular simulation systems and input files to facilitate and standardize the usage of common and advanced simulation techniques. The topologies of both *Amt* and *AK13* were acquired by the SwissParam server program [201] that provides topology files in GROMACS format, based on Merck molecular force field (MMFF) [202] in a functional form that is in compatibility with the CHARMM force field. All simulations were performed in the NP_zAT ensemble with a constant area per lipid, A, equal to 0.64 nm^2/lipid, whereas the equations of motion were integrated using the leap-frog algorithm, with a time step equal to 2 fs. Temperature was kept constant at 323 K using the Berendsen thermostat [203] with a coupling time constant equal to 0.1 ps whereas the Berendsen barostat [203] was used in order to maintain the pressure at 1 bar. The temperature of 323 K was used in MD simulations in order to ensure that the membrane state is above the phase transition temperature of 297 K for DMPC lipids [204]. Long-range electrostatic interactions were treated with the particle mesh Ewald (PME) method [205, 206] while Coulomb and Lennard–Jones interactions were calculated using a 10 Å cut-off radius. The system was initially energy-minimized using the steepest descent method and after that the MD simulation was started, since the membrane was pre-equilibrated through the CHARM-GUI module

[200]. Two systems were created where the ligand, *Amt* or *AK13*, in its neutral form, that has been suggested to be the permeant form [182] within lipid bilayers, was randomly positioned in the water phase in order to examine its trajectory and distribution over the aqueous and lipid phases.

4.2.6.2 AMBER

The MD simulations of the *Amt* and *AK13* with DMPC lipid bilayers were conducted with Amber 12 package [207, 208] according to the following procedure. The aminoadamantanes were embedded in the center of DMPC lipid bilayers including 60 lipid molecules in an orthorhombic box. Each bilayer was then solvated in a 30 Å layer of TIP3P water model [199]. To neutralize each system Na^+ and Cl^- ions were added in the water layer and also to reach the experimental salt concentration of 0.150 M NaCl. Each system's number of atoms was approximately 20000. The bilayers as well as their solvation were constructed using "System Builder" panel of Desmond software package [209] and converted to pdb format compatible to Lipid14. Subsequently, the systems were processed with the LEaP program of the AmberTools14 [210] package, to prepare Amber parameter topology file and initial coordinate files for each system. Amber ff14SB forcefield parameters [211] were applied to the protein, lipid14 [212] to the lipids and TIP3P to the water molecules. For the ligands, the atomic charges, were calculated using PARM10 parameters [213], and the standard AMBER RESP protocol generated the partial charges. After a short energy minimization and a 10 ns equilibration in the NVT ensemble, 500 ns NPT simulations was performed on the ligand-membrane systems using the CPU implementation of the AMBER 12 code [210]. In particular, 5000 steps of energy minimization using the steepest descent method were followed by 5000 steps of minimization using the conjugate gradient method [214]. The system was heated at constant volume for 10 ps from 0 K to 100 K using the Langevin dynamics [215] and applying restraints on the lipid with a force constant of 10 kcal/mol$Å^2$. The restraints were removed and the temperature was smoothly raised to 310 K during 100 ps with a Langevin collision frequency of γ = 1.0 ps^{-1}, and anisotropic Berendsen regulation [203], with constant pressure of 1 atm and time of 2 ps. The same weak restraint of 10 kcal/mol$Å^2$ was maintained on lipid bilayers. The

above-mentioned equilibration was followed by 500 ns NPT simulation, with constant pressure of 1 atm and periodic boundary conditions in three dimensions were applied. The SHAKE algorithm [216] constrained all bonds involving hydrogen and for the integration of equations of motion a time step of 2 fs was applied. Structural data was recorded every 5 ps. The particle mesh Ewald method (PME) was employed to treat all electrostatic interactions with a real space cutoff of 8 Å. Long-range analytical dispersion correction was applied to the energy and pressure. Langevin thermostat [215] was utilized to maintain constant temperature, with a collision frequency of γ = 1.0 ps^{-1}. Pressure was regulated with anisotropic Berendsen method [203], with constant value at 1 atm and relaxation time of 1.0 ps. For structural analyses, snapshots of the two systems were created with VMD [217]. The analysis of the trajectories were accomplished with PTRAJ and CPPTRAJ [218]. As in the GROMACS MD simulations, both systems had the aminoadamantane molecules in their permeant neutral form [182].

4.3 Results and discussion

4.3.1 DSC results

The effect of increasing molar concentrations of *Amt* on the thermotropic behaviour of DMPC MLVs is depicted in Figure 4.2 (*left*), while in Table 4.1 the values of the respective thermodynamic parameters for the thermal transitions are listed. DMPC bilayers alone exhibit a sharp high-enthalpy transition centered at 23.4 °C and a broad low-enthalpy transition centered at 13.3 °C. These values, as well as their respective transition enthalpies are in agreement with previous studies [204]. The membrane incorporation of various amounts of *Amt* up to x=0.2 molar concentration resulted in the following effects. The secondary gel-to-rippled phase transition did not appear, which indicates the interaction of the drug molecules with the phospholipid polar heads, affecting their mobility. The main transition temperature was found significantly lower (*ca* 3 °C), while the peak width increased to twice the initial value. However, the transition enthalpy remained unaffected or even increased, which means that the transition effectiveness of the lipids is nevertheless the same. These results indicate fluidization, or increase of *trans:gauche* isomerization, of the membrane and loss

of cooperativity between the phospholipids, where the formation of domains with different transition temperatures close to the peak temperature is evident (especially in the cooling runs that are not presented herein) [219]. In the case of *Amt x*=0.5, the thermodynamic parameters of the main transition remain closer to those of neat DMPC bilayers, compared with the lower molar ratios, with the exception of the enthalpy value, which was found considerably increased. As T_m is decreased and $\Delta T_{1/2,m}$ is increased in respect to DMPC bilayers the ΔH increase may reflect the strong *Amt* interactions with lipid bilayers or a possible induced partial interdigitation. Such effects can organize the system and explain the higher amount of energy required for the transition to the liquid crystalline state as reflected by the increased enthalpy. The interactions of *Amt* with DMPC polar head groups are expected, since the amino group (pK_a = 10.17) is protonated. In the study of Suwalsky et al., the effect of *Amt* on DMPC and DMPE MLVs and especially on the polar head groups of the bilayers were not as profound. This may due to the fact that the drug was added to the suspension post preparation, while in the present study, the drug was present during the evaporation of methanol and phospholipid self-assembly [187]. As a result, the packing and orientation of the molecule inside the lipid membrane varies significantly between the two cases. In the latter case *Amt* effects an enhanced packing of the phospholipids and has stronger interactions with the polar head groups.

The effects of *AK13* on the thermotropic behaviour of DMPC MLVs, is presented in Figure 4.2 (*right*), and the corresponding transition parameter values are given in Table 4.1. The thermal effects of *AK13* resemble those of *Amt*, except for *x*=0.5 molar concentration. At this high concentration, *AK13* showed a complicated broad peak which clearly contains more components. This more profound thermal effect may be explained by the formation of different domains. On top of these pronounced effects, the *ΔH* value, which is the amount of energy required for transition and is related with the membrane interchain interactions, resembles the case of *Amt x*=0.5. This means that while the organization of the membrane is altered, affected by the presence of new drug-induced domains, the amount of energy required for DMPC phase to transit has been distributed to these various domains [220].

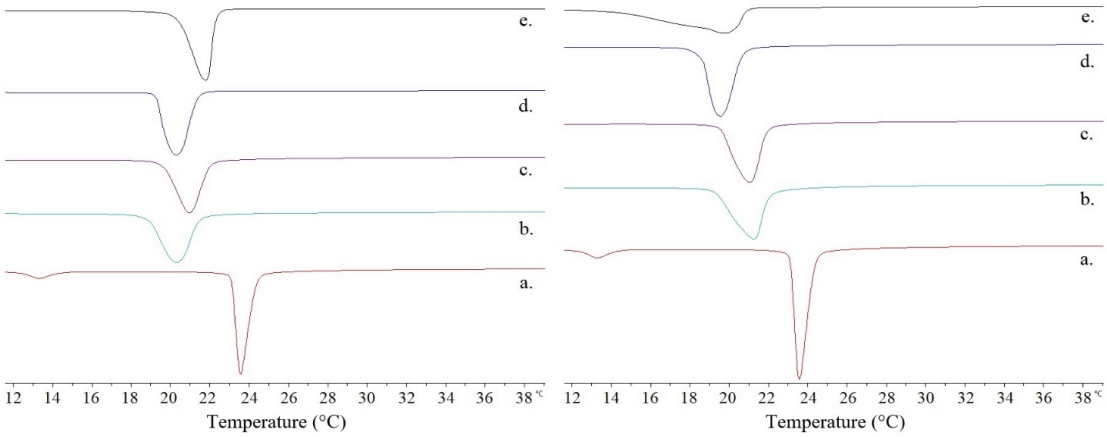

***Figure 4.2*: DSC heating curves of DMPC: *Amt* (*left*) and DMPC : *AK13* (*right*) MLVs with different drug molar concentration: (a) *x*=0.0 (b) *x*=0.05, (c) *x*=0.08, (d) *x*=0.2 and (e) *x*=0.5.

4.3.2 Solid state NMR results

4.3.2.1 Gel phase

^{1}H MAS: The gel, ripple and liquid crystalline phases of DMPC fully hydrated bilayers are well established in the literature [221]. The ^{1}H NMR high-resolution spectrum of DMPC fully hydrated bilayers shows that at 15 ºC DMPC exists in the gel phase and includes only eminent peaks around 3.0 and 4.5 ppm attributed to the hydrogens of the head-group (see Figure 4.3, *bottom*).

The effects of *Amt* in DMPC bilayers at the gel phase (15 ºC) using four concentrations are shown in Figure 4.3 (*left*). When a low concentration of the drug is incorporated (*x*=0.05), the peak of DMPC bilayers attributed to $N(CH_3)_3$ is shifted to the lower field by 0.1 ppm (see Table 4.2). This difference will be considered as real; all through the ssNMR experiments as it is repeatable. Increase of *Amt* concentration (*x*=0.2) results in the appearance of new peaks in the region 3.3-3.7 ppm and a broad peak covering the region 0.0-2.6 ppm. Such peaks are evident in DMPC bilayers alone at high temperature of 30 ºC (see Figure 4.6) and are attributed to the alkyl chains and head-group regions. It is evident that *Amt* causes fluidization at this concentration. This result is in a perfect agreement to DSC data reported by Suwalsky *et al.* [187]. The authors found that upon the addition of *Amt*, the thermotropic phase behaviour of DMPC bilayers

changed; they observed a gradual diminishing of the pre-transition phase temperature peak and both pre-transition and phase transition temperatures shifted to the lower ones [187] at *ca* 3.1 ppm. Such thermal behaviour was also shown in our described results. Interesting, the two peak the spectrum of DMPC bilayers alone present the two possible conformations of the headgroups leading to two conformational isomers [221]. The presence of the *Amt* provides preference to only one isomer. This result is also in agreement with DSC data (Figure 4.2) which showed that *Amt* abolished the pre-transition which is associated with head-group effects.

At the highest concentration used (x=0.5), a complex pattern of peaks in the region 1.0-2.5 ppm is observed. As this pattern at the highest temperature of DMPC bilayers is not identical, it signifies that some of the peaks can be attributed to the drug. Indeed, the high resolution ^{1}H NMR spectrum of *Amt* shows peaks in this region (see Table 4.2). Thus, at this high concentration, the drug molecule shows its appearance, as enough concentration is added to fall in the sensitivity of the NMR spectrometer. The overly broad peak ranging in the region 1.0-2.5 ppm may indicate that drug is immobilized in lipid bilayers due to its strong exerting interactions. At this highest concentration, the complex peak of DMPC bilayers at 3.1 ppm is shifted and appears as a broad peak at the lower field (3.4 ppm).

The effects of *AK13* in DMPC bilayers at the gel phase (15 ºC) using four concentrations is shown in Figure 4.3 (*right*) for comparison reasons. As it can be observed, *AK13* affects similarly the DMPC bilayers, thus increasing the fluidization of DMPC bilayers and shifting the peaks at lower field by 0.2-0.3 ppm. Indeed, similarly to *Amt*, at the highest concentration, *AK13* ^{1}H NMR peaks are observable in the region 1.0-2.5 ppm (see Table 4.3). The only difference in the spectra of DMPC:*AK13* in respect to DMPC:*Amt* is that the former does not show identical chemical shifts of the head-group protons at x=0.2 (see Table 4.3) but resonates at lower field, i.e. 3.3 ppm vs 3.1 ppm in DMPC bilayers alone or DMPC:*Amt* (x=0.2), suggesting possibly the higher perturbation of *AK13* to DMPC bilayers.

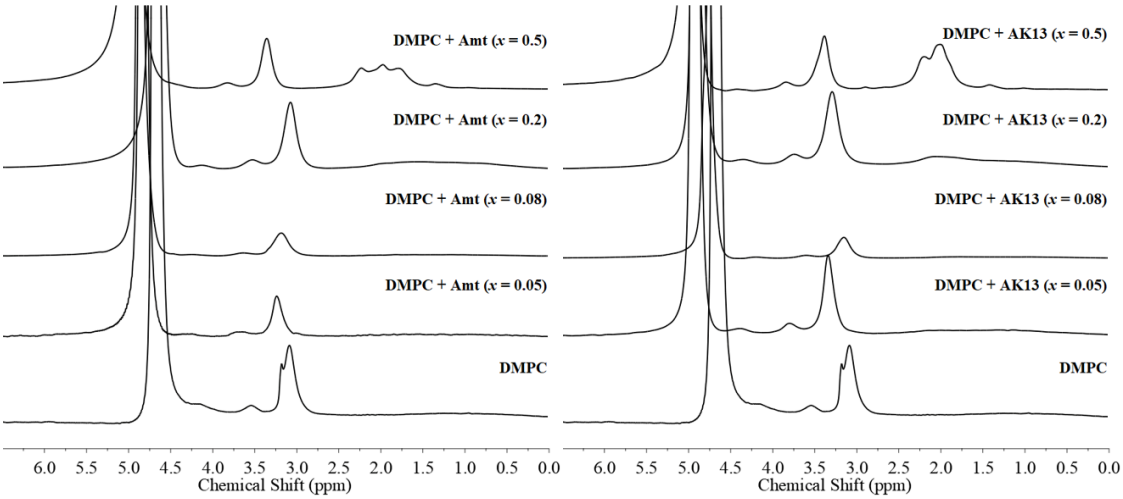

Figure 4.3: ^{1}H MAS NMR spectra of DMPC bilayers with and without the *Amt* (*left*) or *AK13* (*right*) at 15 ºC.

^{13}C CP-MAS: The ^{13}C CP-MAS NMR spectra showing the effects of *Amt* in DMPC bilayers at the gel phase (15 ºC) using four concentrations are depicted in Figure 4.4 (upper eight spectra). At the lowest concentration and in accordance with ^{1}H NMR spectra, *Amt* only causes shift changes of the DMPC bilayers towards lower field (see Table 4.4). When the concentration is increased (x=0.20) not only a further shift towards the lower field [187] of the resonances is observed, but also three additional new peaks were observed, attributed to *Amt* (see Table 4.5) in accordance to its ^{13}C high resolution spectrum. Of special interest is the observed peak of DMPC at ~ 60.1 ppm which decreases significantly in intensity when *Amt* (x=0.2) is present. Similarly, the carbonyl peak of DMPC at ~ 174 ppm decreases in intensity when *Amt* is present. This is evidence that *Amt* affects lipids glycerol backbone and polar head. Indeed, MD simulations reported in the literature showed that this is possible [185]. This result was also confiremed with MD simulations for 500 ns which will be discussed in the next session. Using the highest concentration of x=0.5, peaks attributed to *Amt* are of higher intensity signifying further incorporation of the drug.

AK13 exerted similar effects at high concentrations as *Amt* and new peaks appeared at a concentration x=0.08 due to the presence of the drug (see Table 4.5). A different effect between *Amt* and AK13, which is only observable in ^{13}C NMR spectra, is localized at the carbonyl. Incorporation of *Amt* shifts the DMPC bilayers carbonyl peaks to the lower field as it is shown with the three lowest

concentrations. When its highest concentration is incorporated, the chemical shift of DMPC bilayers containing *Amt* lowers and approaches that of DMPC bilayers alone. In contrast, *AK13* shifts the DMPC bilayers peaks at lower field at all concentrations. At the higher concentrations of x=0.08 and 0.2, the chemical shift of DMPC bilayers with *AK13* decreases and is almost identical to that of DMPC bilayers alone. At the highest concentration of x=0.5 the chemical shift again increases. This signifies that the two molecules perturb the carbonyl region significantly.

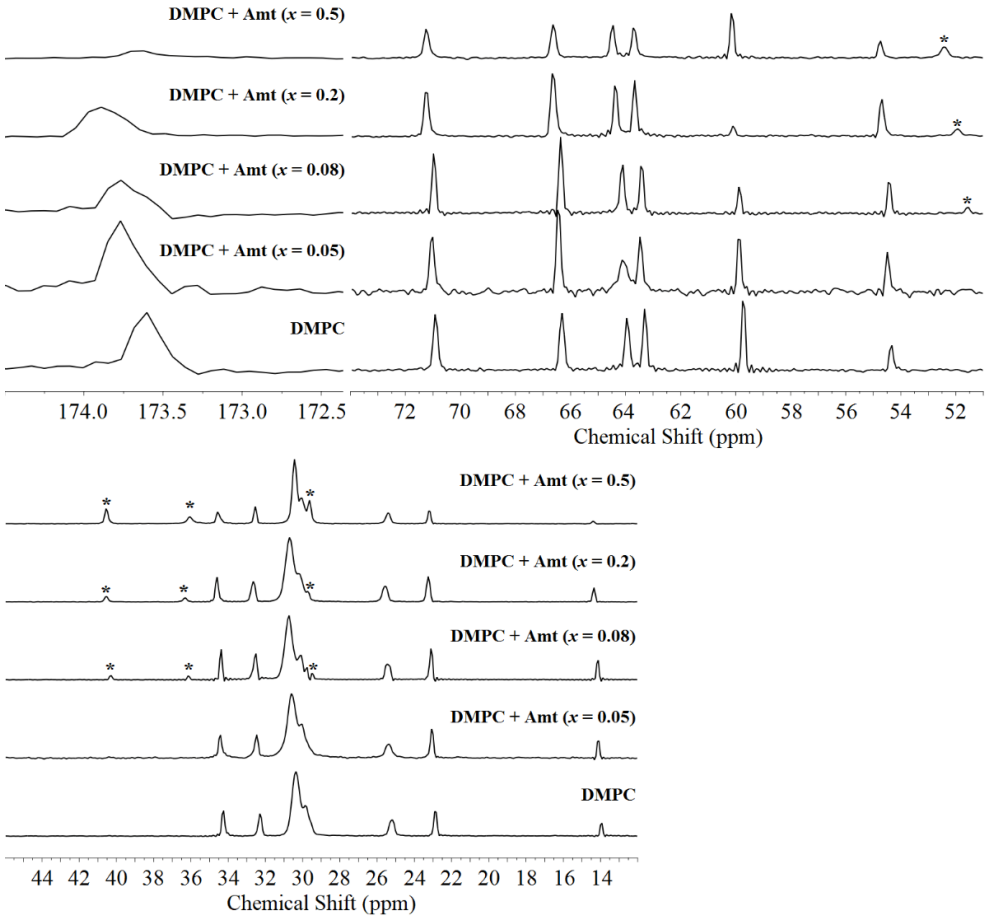

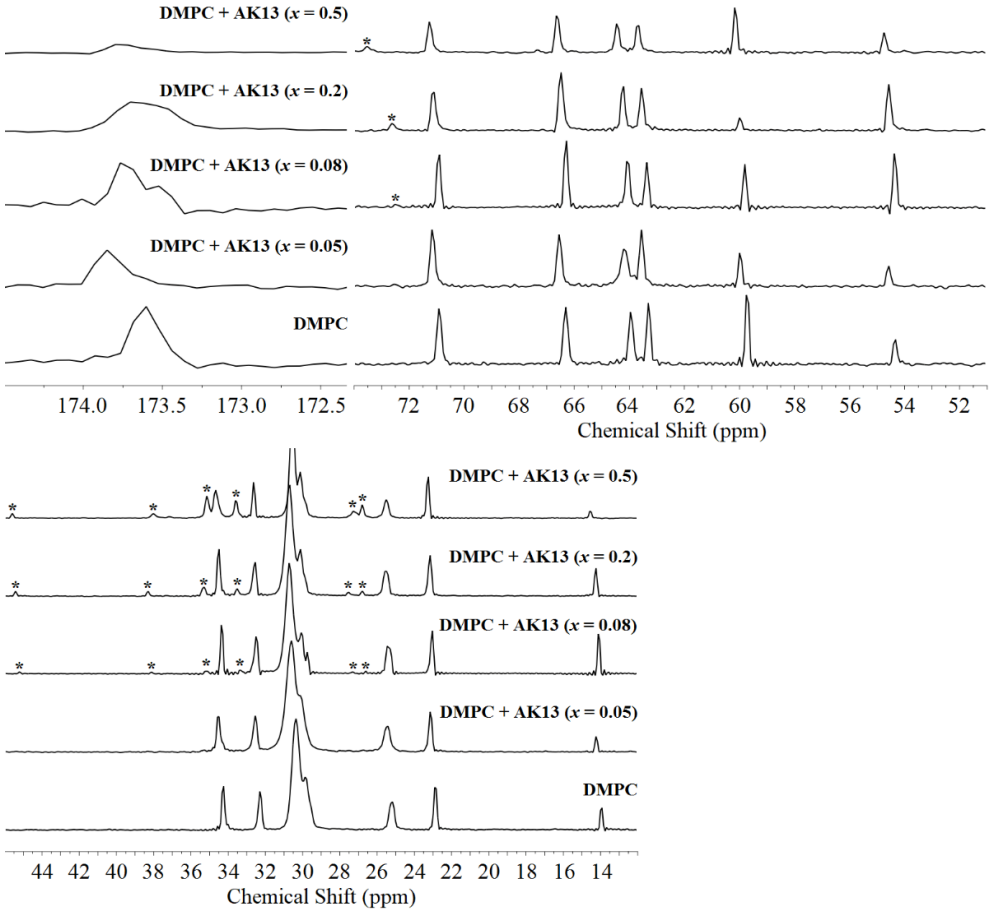

Figure 4.4: ^{13}C CP-MAS NMR spectra of DMPC bilayers without and with *Amt* (*upper two parts*) or *AK13* (*lower two parts)* at 15 ^{o}C. Peaks attributed to the drugs are marked with an asterisk.

Of paramount importance is the fact that at the highest concentration *Amt* almost abolishes the carbonyl peak and *AK13* completely indicating a strong fluidization effect at this region. As will be analysed in the next section, this is in accordance with MD simulations.

^{31}P: The effects of *Amt* and *AK13* incorporated in DMPC bilayers on the phosphate group resonance at ~ -20 ppm are shown in the static ^{31}P powder spectra (Figure 4.5). The narrow peaks in the ^{31}P spectra between 0-10 ppm correspond to the phosphate groups of the buffer solution. It is evident that the two molecules at x>0.05 cause increase in the difference in the components of the shielding tensor σ_{II}-σ_{I} values. Especially, at the highest concentration of x=0.5 both molecules significantly affect the head group of the lipids as they increase considerably the σ_{II}-σ_{I} value of DMPC bilayers. This may signify a different distribution of the two molecules in the lipid bilayers as the concentration of the

drug increases. Thus, at the low concentrations, the molecules are mostly embedded deep in the lipid bilayers, but as the concentration is increased, the lipophilic host segment is saturated more drug molecules are oriented and positioned at the phosphate group. Some reports for *Amt* suggest that it is localized in the phosphate region [185]. The obtained data do agree with these findings if high concentration of drug is considered.

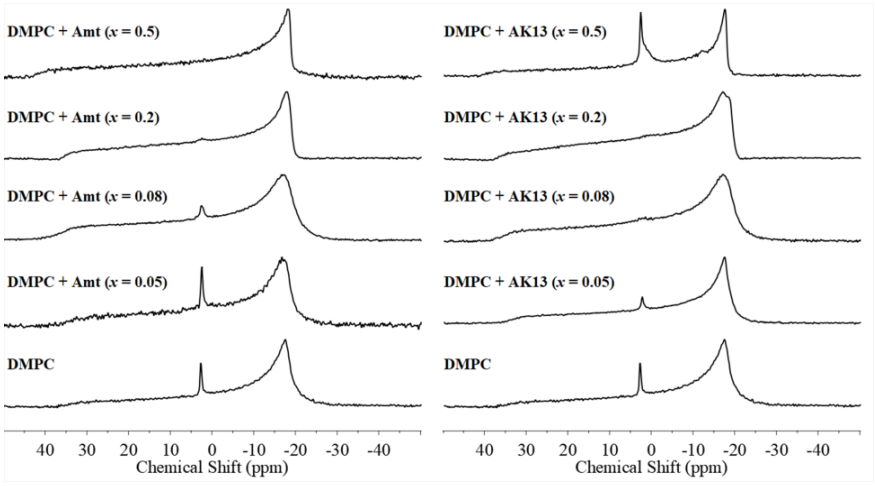

Figure 4.5: ^{31}P NMR spectra of DMPC bilayers without and with the *Amt* (*left*) or *AK13* (*right*) at 15 ºC.

4.3.2.2 Liquid crystalline phase

^{1}H MAS NMR: The effects of *Amt* in DMPC bilayers at the liquid crystalline phase (35 ºC) using the same four concentrations as in the gel phase are shown in ^{1}H MAS NMR spectra (see Figure 4.6, *left*). Identical effects of the molecule as in the gel phase are observed also in the liquid crystalline phase. In summary, at low concentration *Amt* causes only chemical shift changes to lower field (Table 4.7). At higher concentrations not only further chemical shift changes to lower field are observed but also the presence of drug is eminent. The same effects are observed also with *AK13* (see Figure 4.6, *right*) but noteworthy when the highest concentration of *AK13* is used, overly broad peaks are observed showing that drug is intercalated strongly in DMPC bilayers causing immobilization.

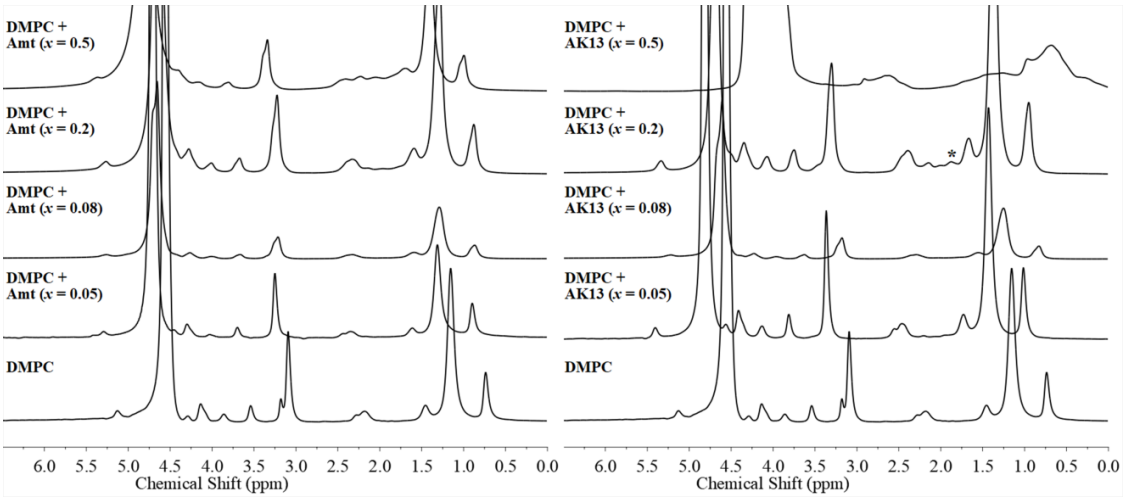

Figure 4.6: ^{1}H MAS NMR spectra of DMPC bilayers without and with *Amt* (*left*) or *AK13* (*right*) at 35 ^{o}C. Peak attributed to the drug is marked with an asterisk.

^{13}C CP-MAS: The same emerging picture is observed with ^{13}C CP-MAS data (Figure 4.7) confirming that the two molecules are intercalated in the polar region of the lipid bilayers independently of the lipid mesophase state. Thus, they are equally well distributed at low and high temperatures in the lipid bilayers and exert their fluidizing effect. Only, when the highest concentration of AK13 is used, very broad peaks are observed, showing that drug is intercalated strongly in DMPC bilayers causing immobilization; this effect was already observed at the gel phase but in the liquid crystalline phase it is more pronounced. In addition, at this highest concentration, upfield shifts are observed for all peaks of DMPC bilayers (Table 4.8). As with the gel phase, the highest concentration of *Amt* almost abolishes the carbonyl peak and *AK13* completely indicating a strong fluidization effect at this region. As will be explained in the next section this is in accordance with MD simulations.

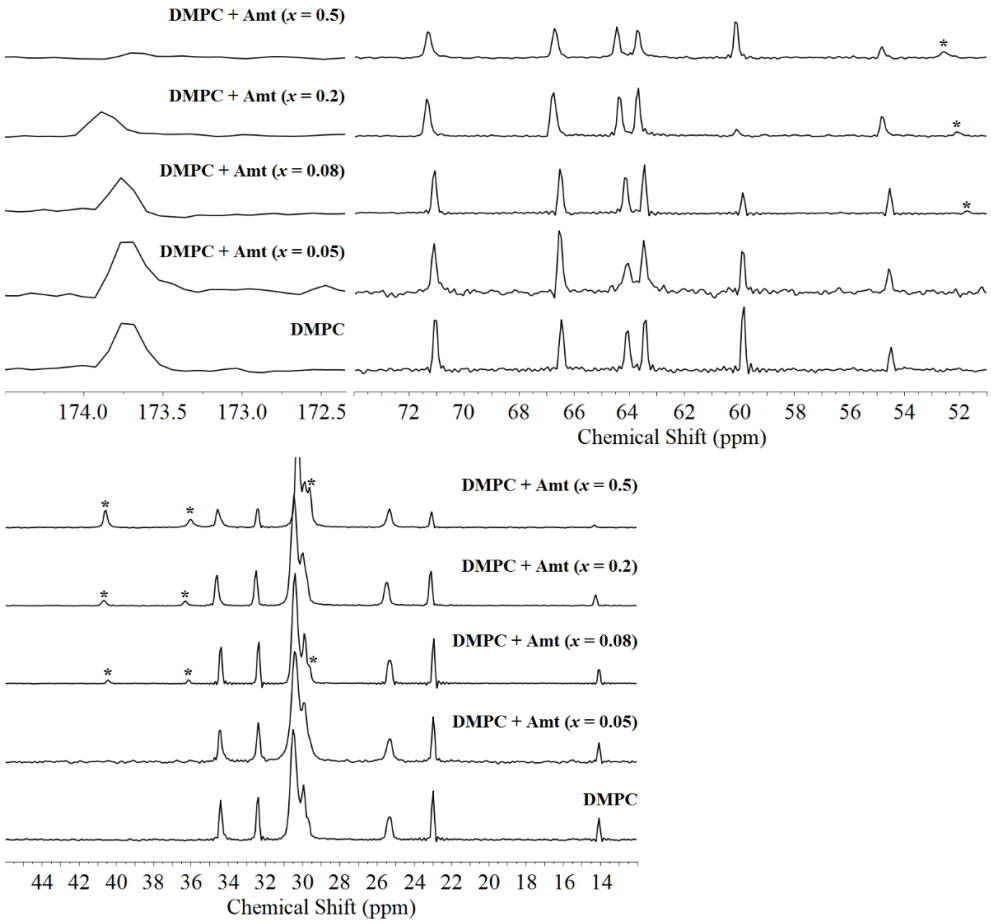
DMPC + Amt (x = 0.5)
DMPC + Amt (x = 0.2)
DMPC + Amt (x = 0.08)
DMPC + Amt (x = 0.05)
DMPC
174.0 173.5 173.0 172.5
72 70 68 66 64 62 60 58 56 54 52
Chemical Shift (ppm)
DMPC + Amt (x = 0.5)
DMPC + Amt (x = 0.2)
DMPC + Amt (x = 0.08)
DMPC + Amt (x = 0.05)
DMPC
44 42 40 38 36 34 32 30 28 26 24 22 20 18 16 14
Chemical Shift (ppm)

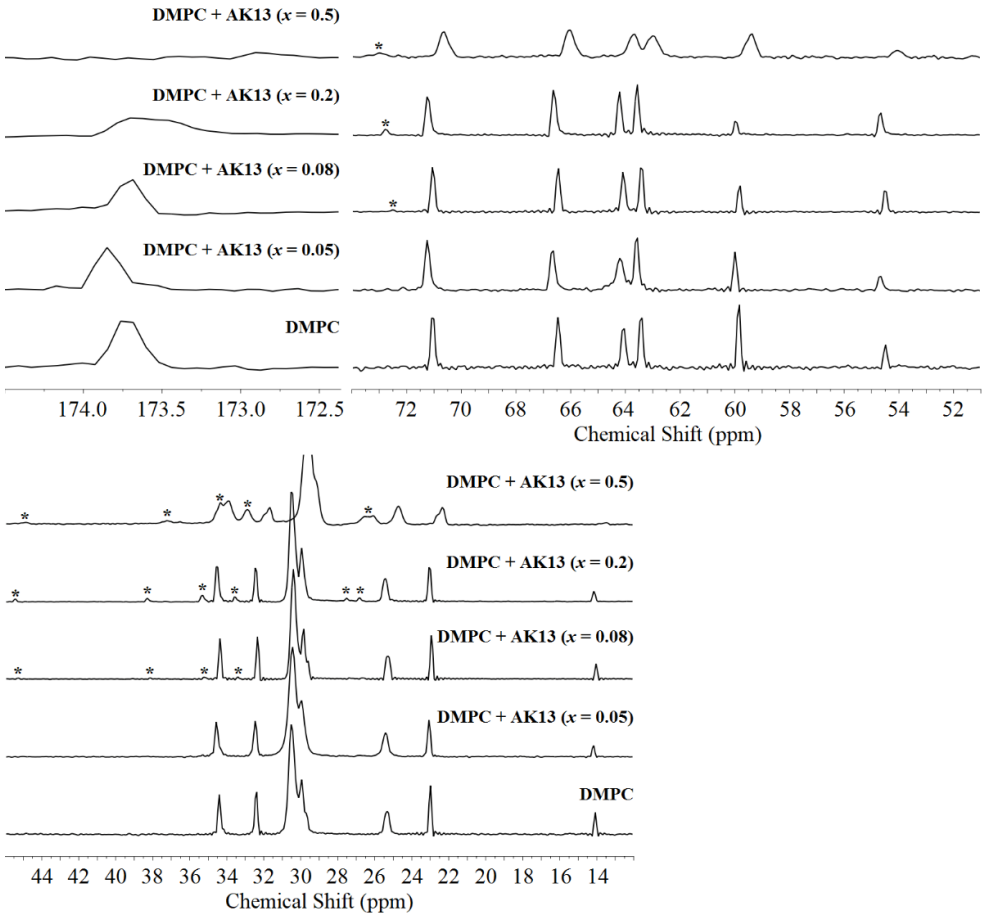

Figure 4.7: ^{13}C CP-MAS NMR spectra of DMPC bilayers without and with (*upper two parts*) *Amt* or *AK13* (*lower two parts*) at 35 ^{o}C. Peaks attributed to the drugs are marked with an asterisk.

^{31}P: ^{31}P spectra of *Amt* or *AK13* incorporated in DMPC bilayers at 35 ^{o}C are shown in Figure 4.8. As expected σ_{II}-σ_{I} values are smaller than those recorded at 15 ^{o}C, as expected, since lipid bilayers are in the liquid crystalline phase. The ^{31}P spectra at liquid crystalline phase show that drugs affect this region by increasing the breadth (σ_{II}-σ_{I}) at all concentrations (Table 4.6). This increase is pronounced at the highest concentration in accordance with gel phase. These results show that at liquid crystalline phase the drugs are localized in the upper segment of the lipid bilayers exerting amphipathic interactions, in agreement with the MD simulations, as it will be described below.

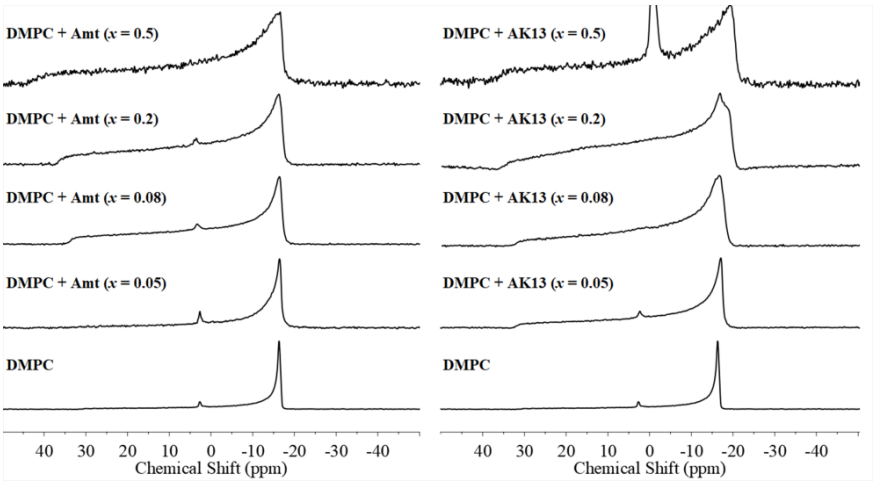

Figure 4.8: ^{31}P NMR spectra of DMPC bilayers without and with *Amt* (*left*) or *AK13* (*right*) at 35 ºC. Peaks attributed to the drugs are marked with an asterisk.

4.3.3 X-ray diffraction results

4.3.3.1 Gel phase

SAXS patterns of DMPC bilayers without and with *Amt* at 15 ºC (gel phase) are shown in Figure 4.9 (*left*). D-spacing of DMPC bilayers is calculated to be 66.4 Å, close to the value 64.9 Å reported by Janiak *et al.* at 20 ºC [222]. As it can be observed at low drug concentrations up to (x=0.09) membrane bilayers are disordered as shown by the increase of the FWHM of the diffraction peaks. D-spacing is increased probably due to the water absorption by the amine group of the drug [188-191]. At higher concentrations (x=0.4 and x=0.5) the periodicity of the membranes is lost, meaning that the bilayers are not regularly stacked anymore, and probably form unilamellar vesicles. Similar conclusions can be derived with *AK13* at the same conditions (Figure 4.9, *right*). Such behaviour is also induced by the highly lipophilic cannabinoid analogue AMG3 [223].

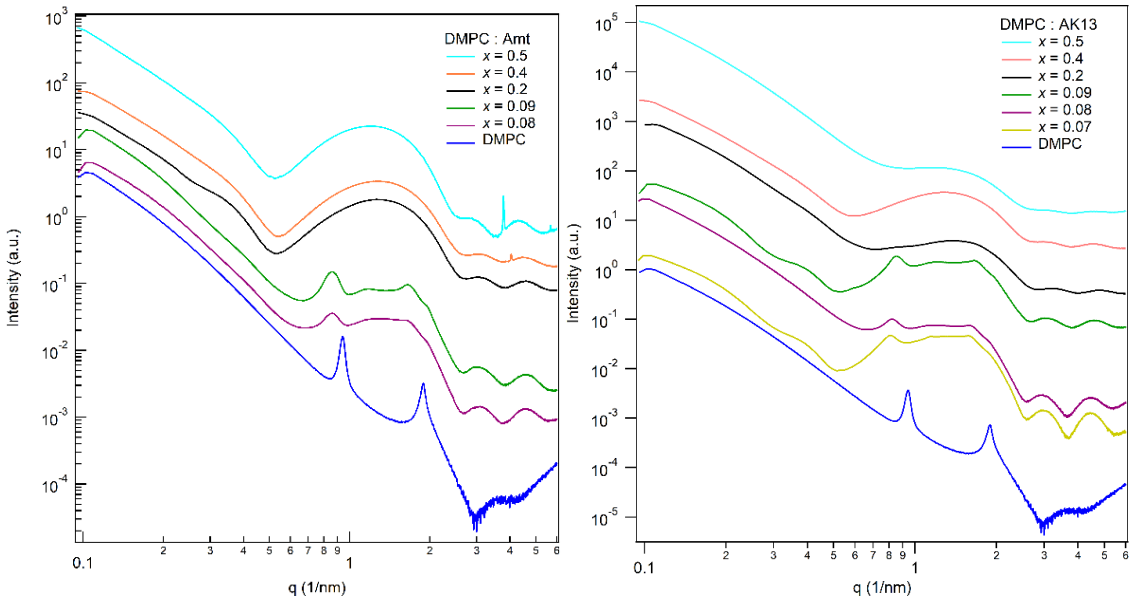

Figure 4.9: SAXS patterns collected at 15 °C from DMPC pure, and in presence of increasing concentrations of *Amt* (*left*) and *AK13* (*right*). Drug concentrations increase from bottom to top in the graphics. Data were shifted vertically for clarity.

The corresponding WAXS patterns collected from DMPC bilayers without and with *Amt* are shown in Figure 4.10 (*left*). The chain packing d-spacing for the various preparations shows only small deviations (4.23-4.20 Å) from that of DMPC bilayers (4.23 Å) [222]. This indicates that lipid bilayers exist in the gel phase. At the higher concentration of *Amt* (x=0.4) few peaks which correspond to the crystalline state of *Amt* become visible, indicating that at 15 °C there is a saturation limit of the drug in the lipid bilayers. The crystallization of *Amt* is even more evident when the DMPC to *Amt* ratio is increased to x=0.5. Such behaviour is also observed with the highly hydrophobic irbesartan [224].

WAXS data collected from DMPC without and with *AK13* are shown in Figure 4.10 (*right*). Similarly, to what was observed in the presence of *Amt*, the chain packing d-spacing shows only small deviations (4.23-4.21 Å) from that of DMPC bilayers (4.23 Å). No peak due to the drug crystallization was visible even at x=0.5 lipid to drug molar ratio, indicating that lipid bilayers can accommodate higher concentrations of this more lipophilic analogue.

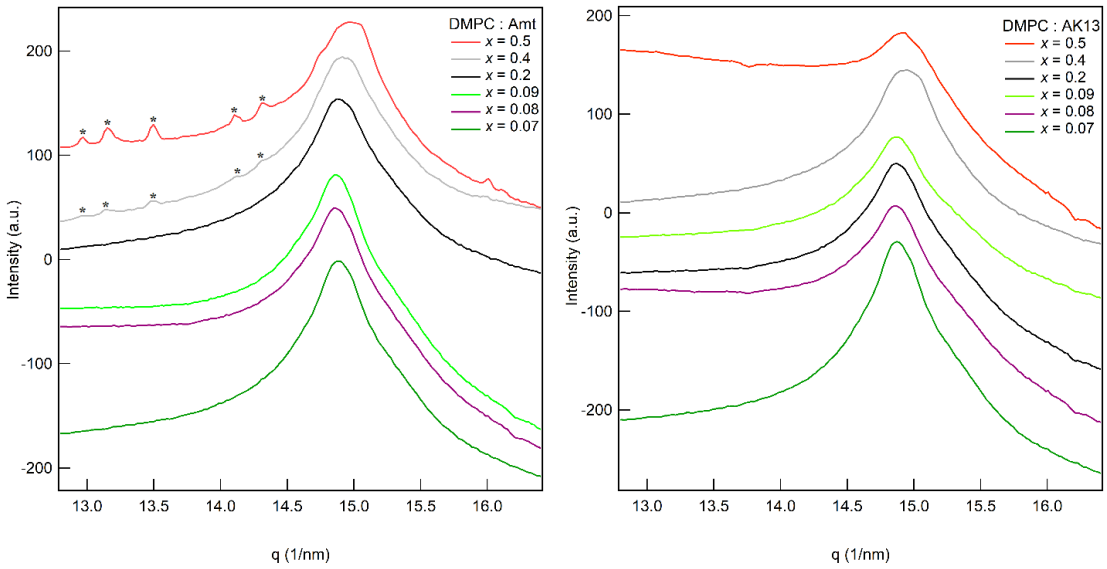

Figure 4.10: WAXS patterns of DMPC without and with *Amt (left)* and *AK13 (right),* collected at 15 °C. Drug concentration increase bottom to top in the graphics. Data are shifted vertically for clarity. Peaks with an asterisk indicate crystallization.

4.3.3.2 Liquid crystalline phase

Similar behaviour of *Amt* was observed regarding the SAXS patterns at 35 °C in the liquid crystalline phase, as shown in Figure 4.11, (*left*). The only difference in these spectra is that when the drug is incorporated in lipid bilayers a d-spacing of DMPC bilayers decrease is observed. This is eminent that *Amt* enhances *trans:gauche* isomerisation, a result that is in accordance with DSC data. *AK13* behaves similarly in the liquid crystalline state, as shown in the SAXS experiments (Figure 4.11, *right*).

The only difference between the two samples is that *AK13* did not decrease the d-spacing of DMPC bilayers but rather increased it as in the gel phase. This may indicate that amino group of *AK13* absorbs also in the liquid crystalline phase water and consequently this probably hides the observed increase of *trans:gauche* isomerization and expected decrease of d-spacing.

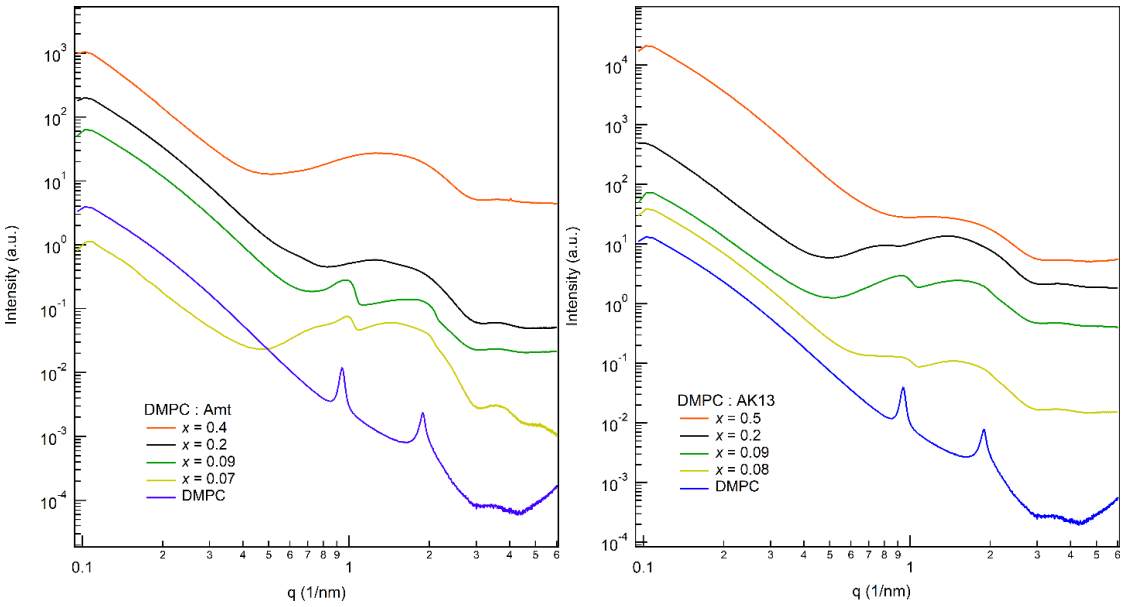

Figure 4.11: SAXS patterns collected at 35 °C from DMPC pure, and in presence of increasing concentrations of *Amt* (*left*) and *AK13* (*right*). Drugs concentration increase bottom to top in the graphics. Data were shifted vertically for clarity.

WAXS experiments of DMPC with and without *Amt* (x=0-0.5) at the liquid crystalline state were also obtained (data not shown). At 35 ºC the lateral d-spacing of few samples ranges between 4.5-4.4 Å. The lateral d-spacing shows that at liquid crystalline phase preparations differ from that of DMPC which shows not such lateral d-spacing at this temperature. At the two highest concentrations *Amt* is crystallized as in the gel phase. This shows that crystallization is not temperature but rather concentration dependent. The WAXS experiments of DMPC with and without *AK13* (x=0-0.5) in the liquid crystalline state at 35 ºC show that the lateral d-spacings range between 4.5-4.4 Å. No crystallization is observed also in the liquid crystalline phase as in the gel phase.

4.3.4 MD simulations

4.3.4.1 GROMACS

The 500 ns MD simulations provide, at first, a clear view on the drug molecules orientation and topological site inside the DMPC bilayer, which is in good agreement with the PMF calculations earlier performed by Chew *et al.* [185] for *Amt*. Both drug molecules were placed initially in the water phase and after a

short period of time (*ca* 20 ns) entered the lipid bilayer as expected (Figure 4.12), since they are both hydrophobic neutral amines form. Particularly, as depicted in Figure 4.16 the density profiles clearly demonstrate that *Amt* and *AK13* are located *ca* 10 Å away from the bilayer's center and *ca* 5 Å apart the DMPC's phosphorus atom for both drug molecules. With regards to the preferred orientation, the angle between the vector consisting of the Ca carbon and N atom of the adamantane derivative versus the canonical axis of the DMPC bilayer was calculated. Our results show that *Amt* is oriented with a tilt of C-N bond axis circa 40º toward the z-axis whereas the *AK13* resides itself with a 50º angle in average (Figure 4.13). Furthermore, as expected, the hydrophobic part of the drug molecule is most of the time tilted towards the DMPC bilayer, whether it's in the water phase or inside the membrane, whereas the amine is tilted towards the polar lipid headgroups, as demonstrated in Figure 4.14

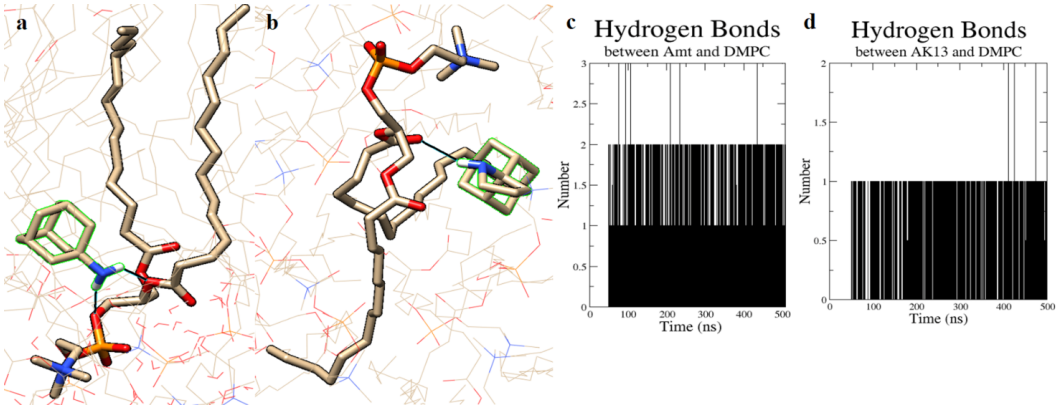

Figure 4.12: Screenshot of the hydrogen bonds with DMPC molecules and *Amt* (*a*) or *AK13* (*b*). Number of hydrogen bonds vs time for *Amt* (*c*) and *AK13* (*d*).

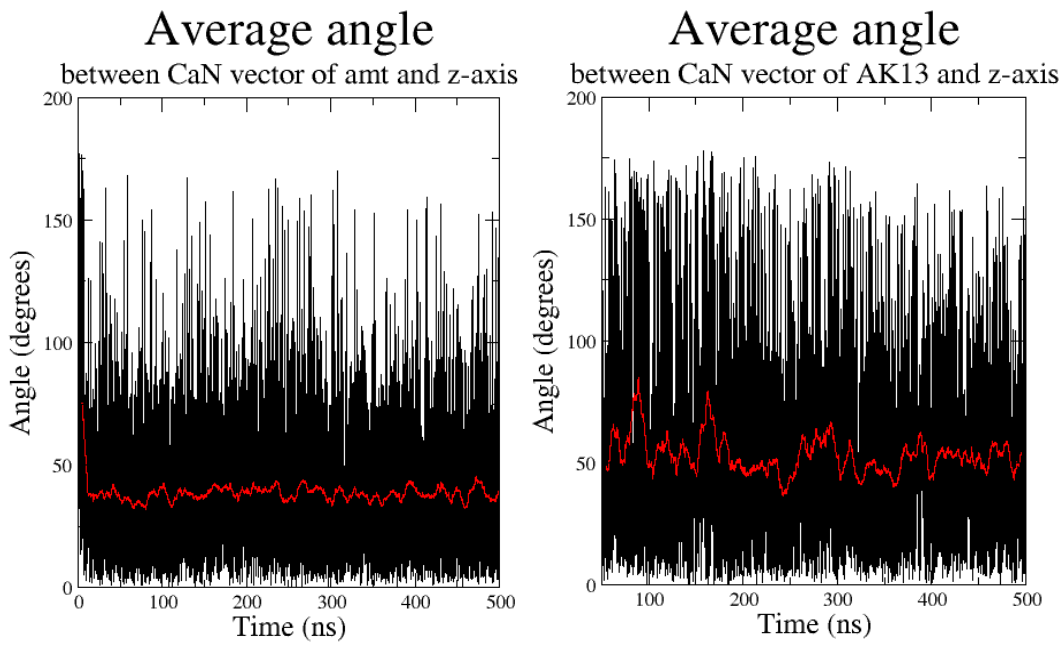

Figure 4.13: Average angle of C_a-N vector vs the z-axis, showing the orientation of (*left*) *Amt* and (*right*) *AK13*

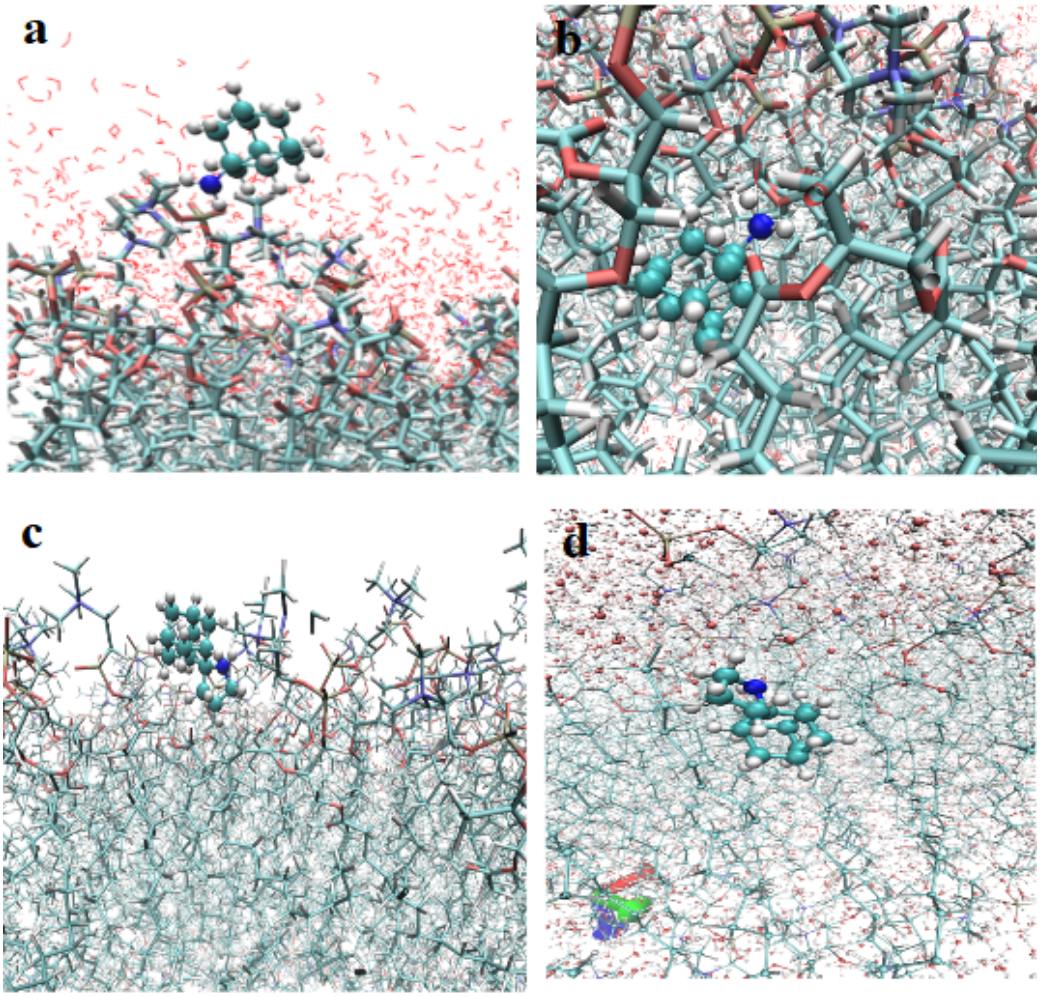

Figure 4.14: Orientation of *Amt* (*a, b*) and *AK13* (*c, d*) in the water phase (*a, c*) and inside lipid bilayers (*b, d*).

The MD simulations confirmed the observations from the NMR spectra, indicating that indeed both drugs strongly interact with the carbonyl or polar head region of DMPC molecules. More specifically, *Amt* forms two hydrogen bonds as a primary amine donor with the polar neighbouring DMPC molecules and *AK13* forms one as a secondary amine donor, Figure 4.12. Both molecules exhibit hydrogen bonding which can be considered moderate, mostly electrostatic, as proposed by Jeffrey *et al.* [225] but *Amt* interacts slightly stronger than *AK13 i.e.* average hydrogen bond distance of 2.9 Å versus 3.1 Å respectively, as presented in Figure 4.15. Moreover, our MD simulations demonstrate that the presence of the adamantane derivatives strongly affect the orientation of the DMPC molecules that reside in close proximity with the drug. Although, in average, the P to N vector of the DMPC molecules is perpendicular to the canonical axis of the membrane, in Figure 4.17, it is clearly shown that this angle is tilted to *ca* 70° within 20 Å of *Amt* and *AK13*.

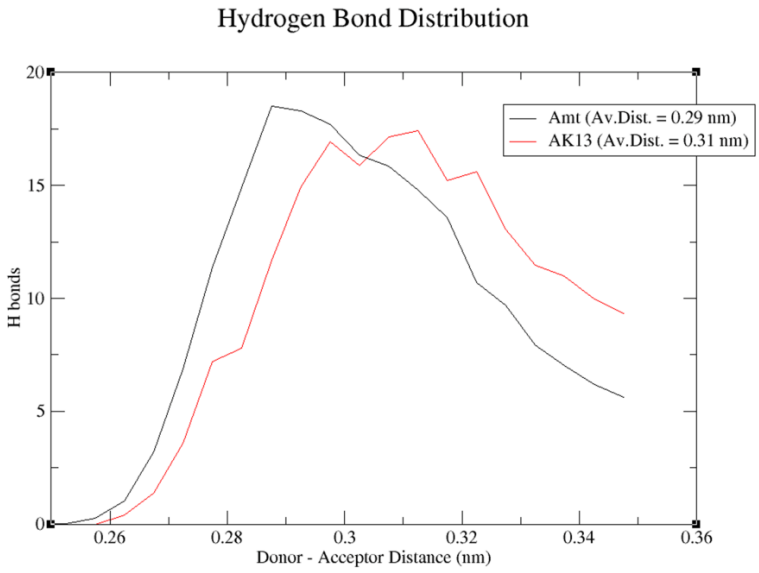

Figure 4.15: Average hydrogen bond distance for *Amt* (*black*) and *AK13* (*red*).

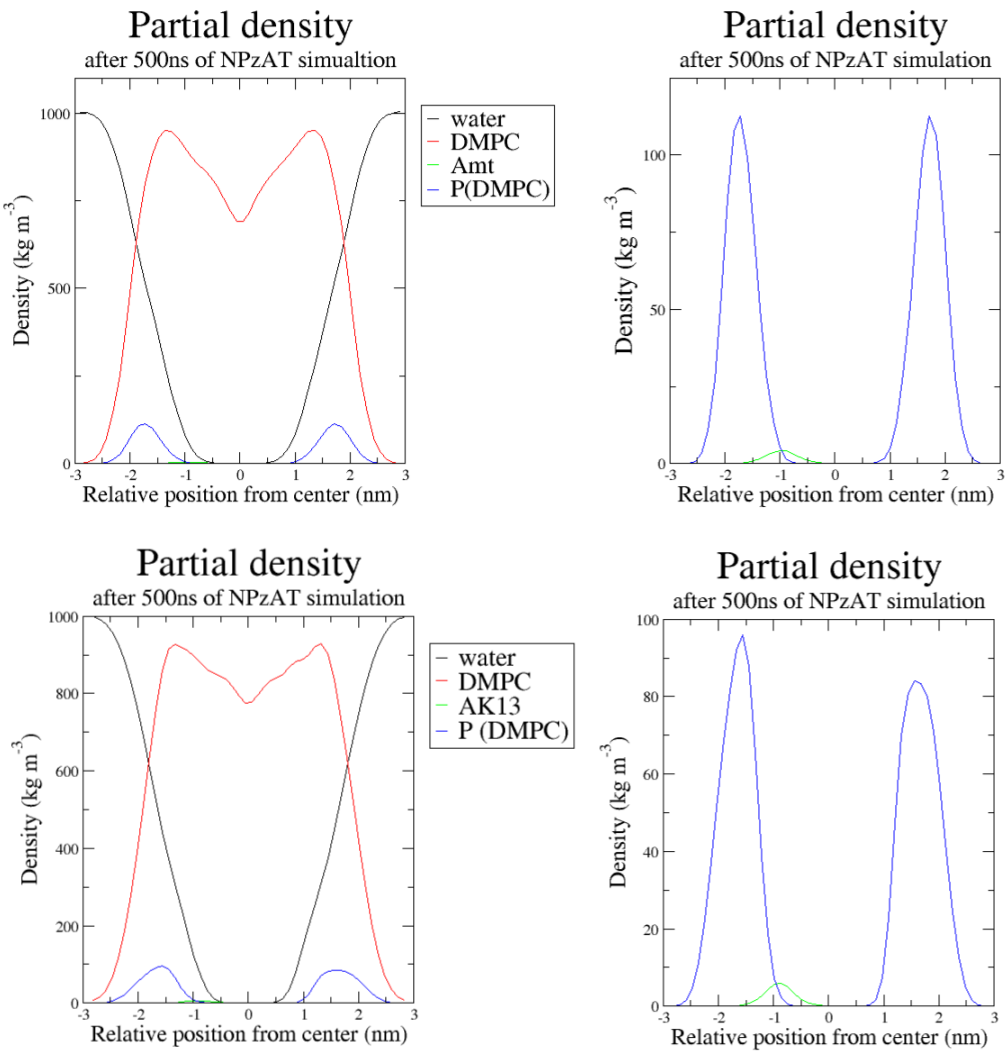

Figure 4.16: (*up left*) Partial density profiles after 500 ns of NP_zAT ensemble illustrating the relevant positions of water (black), DMPC (red), the phosphorus atom of the lipid polar head (blue) and *Amt* (green). (*up right*) The partial density profile of *Amt* and P atom clearly showing that it is most of the time located ~ 1 nm from the center of the DMPC bilayer. (*down left*) Partial density profiles after 500 ns of NP_zAT ensemble illustrating the relevant positions of water (black), DMPC (red), the phosphorus atom of the lipid polar head (blue) and *AK13* (green). (*down right*) The partial density profile of *AK13* and P atom clearly showing that it is most of the time located ~1 nm from the center of the DMPC bilayer.

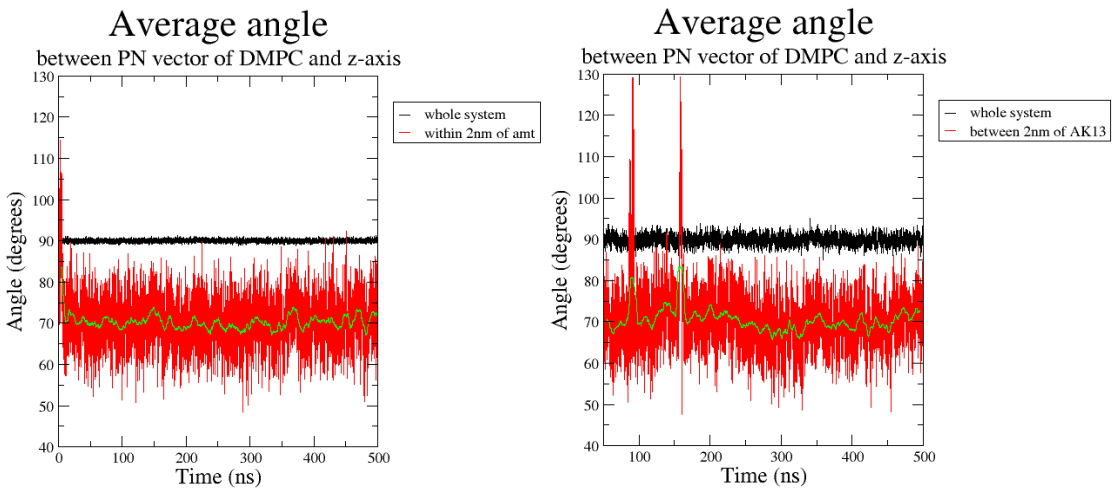

Figure 4.17: Average Angle of P-N vector of the DMPC molecules vs the z-axis (green line) showing the re-orientation caused by the drug molecule, within a radius of 2 nm from the ligand, for *Amt* (*left*) and *AK13* (*right*).

4.3.4.2 AMBER

The results from MD simulations using the Amber package are in good agreement with both the previous PMF calculations performed by Chew *et al.* [185] for *Amt* and complementary to the GROMACS MD simulations. In this experiment the aminoadamantane molecules were placed in the center of lipid bilayer and in a short period of time, during equilibration, both molecules moved and approached lipid interface with their amino group oriented toward hydrophilic polar head. Notably, the *Amt* and *AK13* location within the lipid bilayers is 10 Å (Figure 4.18), furthermore it is evident that the two molecules cross easily the center of the bilayer heading from one to the other lipid leaflet which is consistent with PMF results by Chew *et al.* [185]. The more lipophilic *AK13* remains for longer period inside center bilayer (Figure 4.18, *right*). Thus, the two MD simulations showed that independently of the initial position the aminoamantadanes thermodynamically reside in the interface of the lipid bilayers in an attempt to maximize their amphipathic interactions.

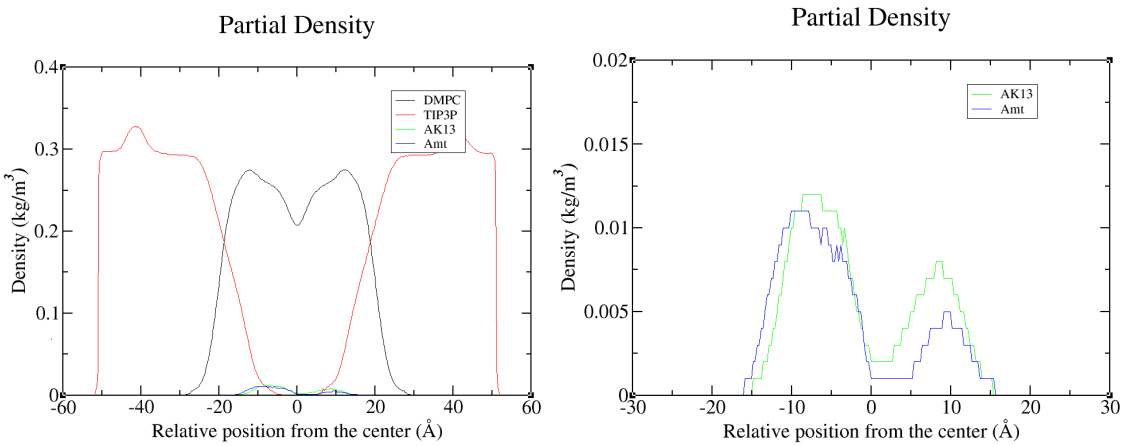

Figure 4.18: (*left*) Partial density profiles after 500 ns of NPT ensemble illustrating the relevant positions of water, DMPC, *Amt* and *AK13*. (*right*) Partial density profiles illustrating the relevant positions of *Amt* and *AK13*.

4.4 Conclusions

The investigation of how and how much aminoadantane drugs of different structure induced changes of the membrane properties has not been investigated. A different perturbation of the membrane bilayers may influence the function of embedded A/M2 membrane protein. Second, drug-membrane interactions, where the drug binds to the membrane, effectively reduce the available free drug, and thus make the treatment potentially less efficient. Thus, probing the membrane role in aminoadamantane drug interactions is critical to a complete understanding.

DSC results clearly show that both *Amt* and *AK13* molecules perturb DMPC bilayers in the same way. Thus, they decrease T_m, and broaden DMPC bilayers half-width and increase ΔH only at the highest concentration of x=0.5. In addition, they abolish the pretransition signifying a perturbing effect on the head-group. At high concentration *AK13* is far more perturbing and creates domains. ^{1}H and ^{13}C NMR experiments confirmed those results of DSC and provided additional molecular details. The two molecules affect glycerol backbone and carbonyl region as well as the headgroup region. The amine drugs distribution from 500 ns MD simulations suggested that *Amt* and *AK13* are mainly positioned ~ 10 Å from the center of the bilayer which is consistent with their anchoring with glycerol

moiety. X-ray diffraction data confirmed the bilayer disorder induced by the two drugs and showed evidence that at the highest concentrations *Amt* is crystallized in lipid bilayers. This effect is not observed with *AK13*, which suggests that higher amounts of this compound can be accommodated in lipid bilayers with respect to *Amt*. This information may have pharmacological consequences in the formulations of the two molecules. MD density profiles show precisely that *Amt* and *AK13* are located ca 10 Å away from the bilayers center and ca 5 Å apart the DMPC's phosphorous atom for both drug molecules. The amines are mainly stabilized at the lipid surface through hydrogen bonding formation. *Amt* and *AK13* are oriented with a tilt between C-N bond axis and membrane normal of ~ 50^o and *70^o towards z-axis* and thus and affect the orientation of DMPC bilayers by changing the tilt of P to N vector from 90^o to 70^o. Based on the MD simulations, it was postulated that *Amt* forms two hydrogen bonds with the neighbouring DMPC bilayers or water molecules, while only one bond is formed by *AK13*. These strong interactions of the two molecules clearly explain the strong perturbation effect depicted in DSC, ssNMR and X-ray diffraction. No significant differences were observed between *Amt* and *AK13* as regards their affinity to DMPC lipids and provide useful insight en route to our efforts to understand the important contributors resulting to the final affinity to the membrane A/M2 protein [192].

4.5 Tables

***Table 4.1*:** Calorimetric profiles of DMPC:*Amt* and DMPC:*AK13* MLVs in PBS (pH=7.8).

Sample	**Drug Molar %**	**$T_{onset,m}$ (°C)**	**T_m (°C)**	**$\Delta T_{1/2,m}$ (°C)**	**ΔH_m (kJ/mol)**	**$T_{onset,s}$ (°C)**	**T_s (°C)**	**$\Delta T_{1/2,s}$ (°C)**	**ΔH_m (kJ/mol)**
DMPC	-	23.07	23.43	0.71	29.44	12.32	13.27	1.14	3.11
DMPC:Amt	0.05	18.80	20.18	1.62	31.50	-	-	-	-
DMPC:Amt	0.08	19.56	20.77	1.39	29.80	-	-	-	-
DMPC:Amt	0.2	19.20	20.12	1.38	34.01	-	-	-	-
DMPC:Amt	0.5	20.35	21.62	1.13	41.79	-	-	-	-
DMPC:AK13	0.05	19.21	21.16	1.66	27.44	-	-	-	-
DMPC:AK13	0.08	19.48	20.90	1.48	26.98	-	-	-	-
DMPC:AK13	0.2	18.53	19.40	1.34	31.33	-	-	-	-
DMPC:AK13	0.5	16.27	19.69	3.93	38.05	-	-	-	-

***Table 4.2*:** Chemical shifts observed in ^{1}H MAS NMR spectra of DMPC bilayers with and without *Amt* or *AK13* at 15 °C.

Sample Constitution	**H-(4'-13'), H-(4''-13'')**	**H-14', H-14''**	**$N(CH_3)_3$**	**H-2'''**	**H-1'''**
DMPC			2.6-3.3	3.6	4.2
DMPC + Amt x=0.05			3.2	3.7	4.3
DMPC + Amt x=0.08			3.2	3.6	4.3
DMPC + Amt x=0.2	0.0-2.6	0.0-2.6	3.1	3.5	4.1
DMPC + Amt x=0.5	0.8-2.8	0.8-2.8	3.4	3.8	
DMPC + AK13 x=0.05			3.3	3.8	4.4
DMPC + AK13 x=0.08			3.2	3.6	4.2
DMPC + AK13 x=0.2	0.0-2.7	0.0-2.7	3.3	3.7	4.4
DMPC + AK13 x=0.5	0.9-3.0	0.9-3.0	3.4	3.8	4.4

***Table 4.3*:** Comparative chemical shifts of *Amt* and *AK13* observed in high resolution ^{1}H NMR spectra for liquid and solid samples in gel and liquid states (35 ºC).

Sample Constitution	**^{1}H NMR of Amt and AK13 salts in D_2O**	**Identification**	**15 ºC ^{1}H MAS NMR**	**35 ºC ^{1}H MAS NMR**
DMPC + Amt x=0.05	2.1 1.7 1.6 1.5	3',5',7' 4', 6', 10' 2', 8', 9' $-NH_2$	-	-
DMPC + Amt x=0.08	2.1 1.7 1.6 1.5	3',5',7' 4', 6', 10' 2', 8', 9' $-NH_2$	-	-

DMPC + Amt x=0.2	2.1 1.7 1.6 1.5	3',5',7' 4', 6', 10' 2', 8', 9' $-NH_2$	1.4-2.8	1.6-2.3
DMPC + Amt x=0.5	2.1 1.7 1.6 1.5	3',5',7' 4', 6', 10' 2', 8', 9' $-NH_2$	1.3-2.2	1.6-2.2
DMPC + AK13 x=0.05	2.9 (t) 2.1 (bd) 1.9 1.7 1.6 1.4 (bd)	5 $4'_{ax}$, $9'_{ax}$ 5', 7' $10'_{ax}$, $8'_{ax}$,4,6' 1',3',3,$10'_{eq}$,$8'_{eq,}$ $4'_{eq}$, $9'_{eq}$	-	-
DMPC + AK13 x=0.08	2.9 (t) 2.1 (bd) 1.9 1.7 1.6 1.4 (bd)	5 $4'_{ax}$, $9'_{ax}$ 5', 7' $10'_{ax}$, $8'_{ax}$,4,6' 1',3',3,$10'_{eq}$,$8'_{eq,}$ $4'_{eq}$, $9'_{eq}$	-	-
DMPC + AK13 x=0.2	2.9 (t) 2.1 (bd) 1.9 1.7 1.6 1.4 (bd)	5 $4'_{ax}$, $9'_{ax}$ 5', 7' $10'_{ax}$, $8'_{ax}$,4,6' 1',3',3,$10'_{eq}$,$8'_{eq,}$ $4'_{eq}$, $9'_{eq}$	0.0-2.7	1.5-2.0
DMPC + AK13 x=0.5	2.9 (t) 2.1 (bd) 1.9 1.7 1.6 1.4 (bd)	5 $4'_{ax}$, $9'_{ax}$ 5', 7' $10'_{ax}$, $8'_{ax}$,4,6' 1',3',3,$10'_{eq}$,$8'_{eq,}$ $4'_{eq}$, $9'_{eq}$	1.5-3.0	*

*Observed peaks were very broad and the chemical shifts are not resolved.

Table 4.4: Chemical shifts observed in ^{13}C CP-MAS NMR spectra of DMPC bilayers with and without the *Amt* or *AK13* at 15 ^{o}C.

Sample Constitution	**C-1**	**C-2**	**C-3**	**C-1', C-1"**	**C-2', C-2"**	**C-3', C-3"**	**C-(4'-11'), C-(4"-11")**	**C-12', C-12"**	**C-13', C-13"**	**C-14', C-14"**	**$N(CH_3)_3$**	**C-2"'**	**C-1"'**
DMPC	63.3	70.9	64.0	173.6	34.3	25.2	29.0-31.3	32.3	22.9	14.0	54.4	66.3	59.7

DMPC + Amt x=0.05	63.5	71.0	64.1	173.8	34.4	25.4	29.1-31.6	32.5	23.1	14.1	54.5	66.4	59.9
DMPC + Amt x=0.08	63.4	71.0	64.1	173.8	34.4	25.5	29.6-31.5	32.5	23.1	14.2	54.4	66.4	59.9
DMPC + Amt x=0.2	63.7	71.2	64.4	173.9	34.6	25.6	29.8-31.7	32.6	23.3	14.4	54.7	66.6	60.1
DMPC + Amt x=0.5	63.7	71.2	64.5	173.7	34.6	25.4	29.8-31.5	32.5	23.2	14.4	54.8	66.6	60.1
DMPC + AK13 x=0.05	63.6	71.2	64.2	173.9	34.5	25.5	28.9-31.9	32.5	23.1	14.2	54.6	66.6	60.0
DMPC + AK13 x=0.08	63.4	70.9	64.1	173.7	34.4	25.4	31.6-29.6	32.5	23.0	14.1	54.4	66.3	59.8
DMPC + AK13 x=0.2	63.6	71.1	64.2	173.7	34.5	25.5	29.5-31.6	32.6	23.2	14.3	54.6	66.5	60.0
DMPC + AK13 x=0.5	63.7	71.3	64.5	173.8	34.7	25.5	29.3-31.4	32.6	23.3	14.6	54.7	66.6	60.2

Table 4.5: Comparative chemical shifts of *Amt* and *AK13* observed in ^{13}C NMR spectra for liquid and solid samples.

Sample Constitution	**^{13}C NMR, of Amt and AK13 salts in D_2O**	**Identification**	**15 ºC ^{13}C-CP MAS NMR**	**35 ºC ^{13}C-CP MAS NMR**
DMPC + Amt x=0.05	52.9 40.0 34.8 28.7	1’ 2’, 8’, 9 4’, 6’, 10’ 3’, 5’, 7’	-	-
DMPC + Amt x=0.08	52.9 40.0 34.8 28.7	1’ 2’, 8’, 9 4’, 6’, 10’ 3’, 5’, 7’	51.6 40.3 36.1 29.5	51.7 40.5 36.1
DMPC + Amt x=0.2	52.9 40.0 34.8 28.7	1’ 2’, 8’, 9’ 4’, 6’, 10’ 3’, 5’, 7’	51.9 40.6 36.3 29.7	52.1 40.7 36.3
DMPC + Amt x=0.5	52.9 40.0 34.8 28.7	1’ 2’, 8’, 9 4’, 6’, 10’ 3’, 5’, 7’	52.4 40.5 36.0 29.6	52.6 40.6 36.0 29.6
DMPC + AK13 x=0.05	73.9 44.6	2’ 5	-	-

	36.7	6’		
	34.3	1’, 3’		
	34.2	3		
	34.0	8’, 10’		
	32.8	4’, 9’		
	26.1	5’		
	25.9	7’		
	22.6	4		
	73.9	2’	72.5	72.5
	44.6	5	45.2	45.3
	36.7	6’	38.1	38.1
	34.3	1’, 3’		
DMPC +	34.2	3		
AK13 x=0.08	34.0	8’, 10’	35.1	35.2
	32.8	4’, 9’	33.4	33.4
	26.1	5’	27.3	27.4
	25.9	7’	26.6	26.7
	22.6	4		
	73.9	2’	72.6	72.8
	44.6	5	45.4	45.4
	36.7	6’	38.3	38.3
	34.3	1’, 3’		
DMPC +	34.2	3		
AK13 x=0.2	34.0	8’, 10’	35.3	35.3
	32.8	4’, 9’	33.5	33.6
	26.1	5’	27.5	27.5
	25.9	7’	26.8	26.8
	22.6	4		
	73.9	2’	73.5	73.0
	44.6	5	45.6	44.9
	36.7	6’	38.0	37.2
	34.3	1’, 3’		
DMPC +	34.2	3		36.5
AK13 x=0.5	34.0	8’, 10’	35.1	34.3
	32.8	4’, 9’	33.6	32.9
	26.1	5’	27.3	26.5
	25.9	7’	26.8	26.1
	22.6	4		

***Table 4.6*:** Components of the ^{31}P chemical shielding tensors of DMPC bilayers without and with *Amt* or *AK13* at 15 or 35 °C.

Sample Constitution	**σ_{II}-σ_{I}**	
	15 °C	**35 °C**
DMPC	56	48
DMPC + Amt x=0.05	55	52
DMPC + Amt x=0.08	60	52
DMPC + Amt x=0.2	55	54
DMPC + Amt x=0.5	62	62
DMPC + AK13 x=0.05	55	51
DMPC + AK13 x=0.08	60	51
DMPC + AK13 x=0.2	55	54
DMPC + AK13 x=0.5	59	60

***Table 4.7*:** Chemical shifts observed in ^{1}H MAS NMR spectra of DMPC bilayers without and with *Amt* or *AK13* at 35 °C.

Sample Constitution	**H-1**	**H-2**	**H-3**	**H-2', H-2''**	**H-3', H-3''**	**H-(4'-13'), H-(4''-13'')**	**H-14', H-14''**	**$N(CH_3)_3$**	**H-2'''**	**H-1'''**
DMPC	3.9	5.1	4.3	2.2	1.5	1.2	0.7	2.9-3.3	3.5	4.1
DMPC + Amt x=0.05	4.0	5.3	4.5	2.3	1.8-0.8	1.8-0.8	1.8-0.8	3.3	3.7	4.3
DMPC + Amt x=0.08	4.0	5.3	4.4	2.3	1.6	1.3	0.9	3.2	3.7	4.3
DMPC + Amt x=0.2	4.0	5.3		2.3	2.2-0.6	2.2-0.6	2.2-0.6	3.2	3.7	4.3
DMPC + Amt x=0.5	4.2	5.4		3.0-0.7	3.0-0.7	3.0-0.7	3.0-0.7	3.3	3.8	4.4
DMPC + AK13 x=0.05	4.1	5.4	4.6	2.8-0.5	2.8-0.5	2.8-0.5	2.8-0.5	3.4	3.8	4.4
DMPC + AK13 x=0.08	4.0	5.2	4.4	2.3	1.6	1.3	0.8	3.2	3.6	4.2
DMPC + AK13 x=0.2	4.1	5.3	4.5	2.7-0.5	2.7-0.5	2.7-0.5	2.7-0.5	3.3	3.8	4.4
****DMPC + AK13 x=0.5***										

*Observed peaks were very broad and the chemical shifts are not resolved.

Table 4.8: Chemical shifts observed in ^{13}C CP-MAS NMR spectra of DMPC bilayers with and without the *Amt* or *AK13* at 35 °C.

Sample Constitution	**C-1**	**C-2**	**C-3**	**C-1', C-1"**	**C-2', C-2"**	**C-3', C-3"**	**C-(4'-11'), C-(4"-11")**	**C-12', C-12"**	**C-13', C-13"**	**C-14', C-14"**	**$N(CH_3)_3$**	**C-2"'**	**C-1"'**
DMPC	63.4	71.1	64.1	173.7	34.4	25.3	29.3-31.2	32.4	23.0	14.1	54.5	66.5	59.9
DMPC + Amt x=0.05	63.5	71.1	64.1	173.7	34.4	25.3	28.8-31.6	32.4	23.0	14.1	54.6	66.5	59.9
DMPC + Amt x=0.08	63.5	71.1	64.1	173.8	34.4	25.3	30.9-29.3	32.4	23.0	14.1	54.6	66.5	59.9
DMPC + Amt x=0.2	63.7	71.3	64.4	173.9	34.6	25.5	29.2-31.3	32.5	23.1	14.3	54.8	66.8	60.1
DMPC + Amt x=0.5	63.7	71.3	64.5	173.7	34.6	25.3	29.7-30.9	32.4	23.1	14.3	54.8	66.7	60.1
DMPC + AK13 x=0.05	63.6	71.2	64.2	173.9	34.6	25.4	28.9-31.6	32.5	23.1	14.2	54.7	66.8	60.0
DMPC + AK13 x=0.08	63.4	71.0	64.1	173.7	34.4	25.3	30.9-29.4	32.3	22.9	14.0	54.5	66.5	59.8
DMPC + AK13 x=0.2	63.6	71.2	64.2	173.7	34.5	25.4	29.3-31.2	32.4	23.0	14.2	54.7	66.6	60.0
DMPC + AK13 x=0.5	63.0	70.7	63.7	172.9	33.9	24.7	28.6-30.8	31.7	22.3	13.5	54.1	66.0	59.4

CHAPTER 5

The Boundary Lipid around DMPC-Spanning Influenza A M2 Transmembrane Domain Channels: Its Structure and Potential for Drug Accommodation

5.1 Introduction

The homotetrameric influenza A/M2 protein is one of the simplest protein ion channels under investigation (Figure 5.1). The A/M2TM monomer is a lipophilic peptide with most of its lipophilic amino acid side chains oriented toward either the hydrophobic core of the lipid bilayers or between adjacent helices. [29, 34, 57, 58, 61, 87, 174, 176] As it is known aminoadamantane ligands bind inside the A/M2TM pore and block proton conduction, thereby preventing a continuation of the viral life cycle and abrogating pathogenesis when applied at low micromolar concentrations. [73] State-of-the-art ssNMR, X-rays, [29, 34, 57, 58, 61, 85, 87, 92, 93, 104, 174, 176, 226-228], MD simulations [61, 174, 176] and other biophysical studies [227, 229] have been performed to investigate the A/M2 protein structure needed for full biological function, along with its complexes with *Amt*, *Rim*, and other aminoadamantane derivatives. The effects of drugs [230] and the lipid environment on the conformation and function of A/M2 protein have been carefully studied. [85, 93, 226, 231] Among the lipid bilayers studied, DMPC is a convenient membrane bilayer, and it was found optimal for the detection of the drug bound to A/M2 compared to other glycerophospholipids. [16, 85, 93, 226, 230, 231]

In addition to the virus-uncoating process, another pivotal role of influenza A virus M2 protein is the host's cell membrane bending, which produces viral budding from cells and scission. [47] This complex process requires the organized deformation of the cellular membrane and necessarily involves localized regions of high membrane curvature and, presumably, localized high A/M2 density around the periphery of the raft, which gives rise to the budding virion. The effect of the A/M2 protein on the membrane required for virus budding is under investigation and is thought to include changes in the mobility and packing of the lipids and the curvature of the lipid bilayers. [227, 232, 233] Membrane lipids have profound impacts on the structure and function of membrane-bound proteins and

peptides. [234] Even a small difference in bilayer composition can cause an experimentally detectable membrane perturbation. [147] Membrane proteins such as A/M2 ion channel form extensive clusters at high concentrations inside lipid bilayers, suggesting a role of protein-protein interactions in the function and regulation of the A/M2 tetramer. [235]

DSC, SAXS and WAXS, ^{1}H, ^{13}C, ^{31}P ssNMR, and MD simulations were applied to systems including M2TM tetramers with or without an excess of *Amt* or the synthetic *AK13* (Figure 5.1) in DMPC bilayers at pH 8.0, in which M2TM forms tetramers. [33] The aim is to investigate if the above common biophysical methods can be used to identify DMPC membrane perturbation after incorporation of the M2TM tetramer. In the above chapter, the effects of *Amt* and *AK13* in DMPC bilayers were investigated using the same methods [147].

In particular, the perturbation of the DMPC bilayer caused by: (a) small changes in micromolar-range concentration of M2TM; (b) small changes in micromolar-range concentration of the aminoadamantane M2 WT channel blocker *Amt* or *AK13*; and (c) modification of the aminoadamantane ligand structure from *Amt* to *AK13* was studied. Increasing drug lipophilicity in *AK13* may increase the local concentration in lipids around the protein target, [236] and it has been shown that *AK13* has six-fold higher affinity for M2TM than *Amt*. [174]

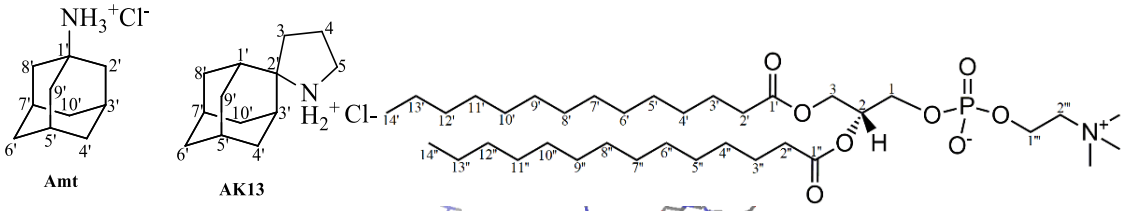

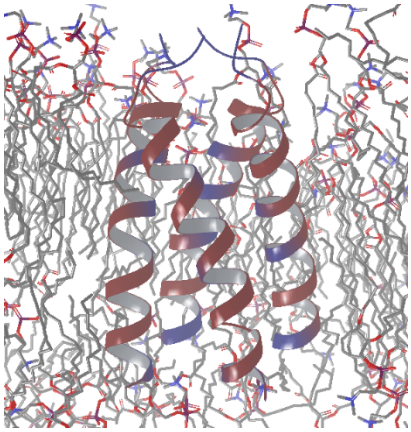

***Figure 5.1*:** (*up*) Structures of *Amt*, *AK13*, and DMPC phospholipid; (*down*) a ribbon model of an M2TM tetramer inside a DMPC bilayer (shown in sticks).

5.2 Materials and methods

5.2.1 Materials

Amt (*MW*=187.7; amantadine hydrochloride) was purchased from Merck Schuchardt OHG-Hohenbrunn, Germany, and DMPC (MW=677.9) from Avanti Polar Lipids, Inc., from Alabaster, Alabama, USA. *AK13* (*MW*=227.8; hydrochloride) was resynthesized in our lab according to a previously reported procedure. [169] The resin and Fmoc (9-fluorenylmethyloxycarboxyl) protected amino acids were obtained from Chemical and Biopharmaceutical Laboratories, Patras (BLP), Greece. All solvents and other reagents were purchased from Merck & Co., Inc. (Kenilworth, New Jersey, USA), Sigma-Aldrich Corp. (Saint Louis, Missouri, USA) and Fluka (Honeywell Research Chemicals, Bucharest, Romania).

5.2.2 M2TM peptide synthesis

The linear M2TM C-terminally amidated peptide, SSDPLVVAASIIGILHLILWILDRL-$CONH_2$, corresponding to residues 22-46 of the A/Udorn/72 wild type sequence of influenza A M2 protein, was synthesized on 2-chlorotrityl chloride resin conjugated with the Rink Amide linker using the Fmoc/tBu solid-phase methodology and a standard synthetic protocol by Professor Theodore Tselios group. [237-241] The first N^{α} Fmoc-protected ring amide linker [4-[(2,4-Dimethoxyphenyl)(Fmoc-amino)methyl]phenoxyacetic acid] was esterified to the resin in the presence of *N,N*-diisopropylethylamine (DIEA) in dichloromethane (DCM). The protected peptide was synthesized on the resin by sequential couplings of the appropriate Fmoc-protected amino acids in the presence of *N,N'*-diisopropylcarbodiimide (DIC) and 1-hydroxybenzotriazole (HOBT) in *N,N*-dimethylformamide (DMF). Fmoc deprotection was achieved using 25% piperidine solution in *N,N*-dimethylformamide. The cleavage of the final protected peptide from the resin was carried out using dichloromethane /

2,2,2-trifluoroethanol (7 / 3) solution. Trifluoroacetic acid (TFA) in dichloromethane (DCM) solution in the presence of scavengers (anisole, 1,2-ethanedithiole) was used for the final deprotection of the side-chain-protecting groups. The final unprotected crude M2TM peptide was purified by semipreparative reverse phase high performance liquid chromatography with a Nucleosil C-18 reversed phase analytical column (250 × 10 mm with 7 µm packing material) using a procedure previously described [179]. A Waters system equipped with a 600E controller and a Waters 996 photodiode array UV detector were used, while the analysis was controlled by a Millenium 2.1 operating system. The peptide purity, which was higher than 95%, was assessed by analytical RP-HPLC (1260 Infinity, Quaternary Pump VL Agilent, Waldbronn, Germany) using an Agilent ZORBAX Eclipse Plus C18 column (100 × 4.6 mm with 3.5 µm packing material), and the identification of the M2TM peptide was achieved by ESI-MS (*MW*=2727.3). Electron spray ionization mass spectrometry (ESI-MS) analysis was performed on a TSQ 7000 spectrometer (Electrospray Platform LC of Micromass) coupled to a MassLynx NT 2.3 data system.

5.2.3 Sample preparation

Samples were prepared by dissolving weighed amounts of dry DMPC lipid with M2TM peptide, and *Amt* or *AK13* in methanol. The mixture was then evaporated at room temperature under a gentle stream of argon and thereafter placed under vacuum for 24 hours in order to form a thin lipid film on the bottom of the glass vial (see Supporting Information and ref. [184]). The mixtures obtained were then fully hydrated at pH 8.0 with an aqueous buffer solution consisting of $Na_2HPO_4 \cdot 2H_2O$ and $NaH_2PO_4 \cdot H_2O$ and vortexed to form multilamellar vesicles (MLVs) (Table 5.1). The samples hydration ratio differs depending on the requirements of each biophysical method, i.e. the hydration ratio for DSC thermograms and ssNMR spectra was 1:1 of dried sample:phosphate buffer but for SAXS/WAXS scattering patterns was 1:19 of dried sample:phosphate buffer. The samples were studied at two mole fractions of M2TM monomer per DMPC molecule, x=0.03 or x=0.06. These two samples correspond to M2TM monomer : DMPC molar ratios of 1:30 and 1:16 and M2TM tetramer : DMPC molar ratios of 1:120 and 1:64, respectively. Two mole ratios of drug were used, x=0.05 drug

: 0.03 M2TM monomer : 1 DMPC molecule and *x*=0.08 drug : 0.06 M2TM monomer : 1 DMPC molecule, corresponding to ratios of M2TM tetramer : drug (*Amt* or *AK13*) of 3:20 (dilute peptide) or 3:16 (more concentrated peptide), i.e., both ~1:6.

5.2.4 DSC

DSC thermograms of the MLVs were obtained by utilizing a DSC822^e Mettler-Toledo calorimeter (Schwerzenbach, Switzerland) calibrated with pure indium (T_m=156.6°C). Sealed aluminum 40-μL crucibles were used as sample holders. The systems under investigation were MLVs composed of DMPC and M2TM without or with *Amt* or *AK13*. Initially, around 5 mg of dried sample was weighted and placed in a crucible, followed by hydration with 5 μL of phosphate buffer. The crucible was sealed and vortexed for 5 min. Then, the sample was left to equilibrate for a 15 min period prior to measurement. The reference for the measurement of every sample was an empty aluminum crucible. Heating-cooling cycles were performed repeatedly until reproducibility of the sample was achieved. The temperature range used was 10-40^{o}C and the scanning rate was 2.5^{o}C min^{-1}. Before each cycle, the samples were equilibrated at a constant temperature of 10°C for 10 min. The calorimetric data were obtained (Table 5.2), i.e., the characteristic transition temperatures $T_{onset,m/s}$ and $T_{m/s}$, the enthalpy changes $\Delta H_{m/s}$, and the widths at half peak height of the C_p profiles $\Delta T_{1/2,m/s}$ were analyzed using Mettler-Toledo STAR^e software. The transition enthalpy for DMPC is expressed in units of kJ mol^{-1} and is considered positive during an endothermic process.

5.2.5 Solid state ^{1}H MAS, ^{13}C CP/MAS, and ^{31}P static NMR spectroscopy

^{1}H magic-angle spinning (MAS), ^{13}C cross polarization/magic-angle spinning (^{13}C CP/MAS), and ^{31}P static ssNMR spectra were recorded on a Varian 600 MHz VNMRS spectrometer equipped with a 3.2 mm HX MAS probe. Larmor frequencies for ^{1}H, ^{13}C, and ^{31}P nuclei were 599.53, 150.77, and 242.70 MHz, respectively. In the ^{1}H MAS NMR experiment, samples were spun with rotation frequency of 5 kHz, protons were excited with a 90-degree pulse of 2.3 μs,

repetition delay was 5 s, and 4 scans were coadded. In the ^{13}C CP/MAS experiment, the polarization was transferred from protons to carbon nuclei in a 5-ms CP block using Ramped-Amplitude on the proton channel, the repetition delay between scans was 2 s, and the number of scans was 2000. Static ^{31}P Hahn-echo NMR spectra were obtained using a 90-degree pulse of 1.8 µs, a 180-degree pulse of 3.6 µs, and an inter-pulse delay of 50 µs. Repetition delay was 5 s and 1000 scans were coadded. During acquisition of the ^{13}C CP/MAS and static ^{31}P signals, high-power proton-decoupling was employed. The ^{1}H and ^{13}C chemical shift changes were referenced to tetramethylsilane, and the ^{31}P chemical shifts were reported relative to the phosphorus signal of 85% H_3PO_4. [136, 224]

5.2.6 X-ray scattering

SAXS experiments were carried out at the Austrian SAXS beamline (Elettra Sincrotrone, Trieste, Italy) [186]. Two-dimensional Pilatus3 1M and Pilatus 100k detectors (Dectris Ltd., Baden, Switzerland) were used to collect SAXS and WAXS scattering patterns, respectively. For SAXS, the sample to detector distance was 1048 mm. The X-ray wavelength was 0.154 nm at a photon energy of 8 keV, covering a q-range between 0.095 nm^{-1} to 7.54 nm^{-1}, where q is the magnitude of the scattering vector defined by $q=4\pi/\lambda \sin(\theta/2)$, with λ the wavelength and 2θ the scattering angle. For WAXS, the angular range covered corresponded to a q- regime between 11.7 nm^{-1} and 21.2 nm^{-1}. The angular scale of the SAXS- and WAXS-measured intensity was obtained using silver behenate ($CH_3(CH_2)_{20}COOAg$), with a d-spacing value of 5.838 nm, and p-bromobenzoic acid as calibration standards, respectively. The 2D images were integrated to 1D scattering functions with Fit2D, [193] and analyzed with IGOR Pro (Wavemetrics, Inc., Lake Oswego, Oregon) to calculate, when possible, the characteristic lattice distance. The samples were loaded in a glass capillary and inserted in a dedicated sample holder with a water bath, having a temperature stability of ±0.1°C (Unistat CC, Huber, Offenburg, Germany). The static measurements were done at 20°C and 30°C, acquiring 4 frames of 30 s, with 2 s delay between each frame. The samples were equilibrated for a few minutes at each temperature

before exposure. The bilayer model used and its applications were recently presented. [194, 195]

5.2.7 MD Simulations

The MD simulations were conducted with Desmond. The M2TM tetramer in complex with *Amt* or *AK13* and an additional five molecules of the *Aamt* ligand, set up to resemble the ratio of the constituents used in the biophysical studies, were embedded in DMPC lipid bilayers. The *Aamt* ligand is in its ammonium form at pH 8.0. The DMPC lipid molecules represent the optimal membrane mimetic system in this case [85, 231] for observing the *Aamt* binding process compared to other glycerophospholipids. Thus, DMPC lipid bilayers have been used for structure determination of M2TM-*Amt* complex (PDB ID 2KQT). [58] The DMPC lipid bilayer extended 20 Å beyond the solutes in the x and y directions, resulting in a system of 120 lipid molecules. The bilayer was solvated using a 20-Å thick layer of TIP3P waters [199] for each leaflet. Na^+ and Cl^- ions were placed in the water phase to neutralize the systems and to represent the experimental salt concentration of 0.150 M NaCl, for a total of ~50,000 atoms in the system. Membrane creation and system solvation were carried out with the “System Builder” utility of Desmond (Schrodinger, Cambridge, Massachusetts) [242, 243]. For modeling the interactions, MD simulations were performed with either the OPLS 2005 force field [244-246] or the Amber ff99SB [247] force field applied using the Viparr module of Desmond. Calculation of long-range electrostatic interactions utilized the particle mesh Ewald method [205, 206], with a grid spacing of 0.8 Å. Van der Waals and short-range electrostatic interactions were smoothly truncated at 9.0 Å. A constant temperature was maintaned in all simulations using the Nosé-Hoover thermostat, and the Martyna-Tobias-Klein method was employed to control the pressure [248]. Periodic boundary conditions were applied using a simulation box of 95×70×81 $Å^3$. The multistep RESPA integrator [249] was used to integrate the equations of motion with an inner time step of 2 fs for bonded interactions within a cutoff of 9 Å; an outer time step of 6.0 fs was used for nonbonded interactions beyond the cutoff. The default protocol provided by Desmond was modified in order to perform the MD simulations. The equilibration protocol consists of a series of restrained

minimizations and MD simulations designed to relax the system, while not deviating substantially from the initial coordinates. Initially, two rounds of steepest descent minimization with a maximum of 2,000 steps and harmonic restraints of 50 kcal mol^{-1} $Å^{-2}$ were applied on all solute atoms, followed by 10,000 steps of minimization without restraints. The first simulation was run for 200 ps at a temperature of 10K in the NVT ensemble with solute heavy atoms restrained with a force constant of 50 kcal mol^{-1} $Å^{-2}$. The temperature was then raised during a 200-ps MD simulation to 325K in the NVT ensemble with the force constant retained. The temperature of 325K was used in the MD simulations in order to ensure that the membrane state is above the melting temperature state of 297K for DMPC lipid. [204] The heating was followed by equilibration runs. Three stages of NPT equilibration (1 atm) with restraints were performed, first with the heavy atoms of the system restrained for 1 ns and second with solvent and lipid molecules restrained harmonically with a force constant of 10 kcal/mol/$Å^2$ for 10 ns. In the third stage, the C_α atoms of M2TM were harmonically restrained with a force constant of 2 kcal/mol/$Å^2$ for 1 ns. The above-mentioned was followed by a 200-ns NPT simulation without restraints. Within this time, the total energy, system dimensions, and the RMSD reached a plateau, and the systems were considered equilibrated. For structural analyses, snapshots of the different systems were visualized with VMD [217] or Maestro. [250] Trajectories were analysed with Maestro, Gromacs, [196, 251] and VMD. Measurements were done with Gromacs tools. For the calculation of hydrogen bonds, a cutoff angle of 30 degrees deviation from 180^o between the donor-hydrogen-acceptor atoms and a cutoff distance of 3.5 Å between the donor and acceptor atoms were applied. The definition of boundary and nonboundary lipids was realized by the application of an algorithm that uses Voronoi cells around protein atoms for the partition of the system. [252]

5.3 Results

5.3.1 DSC results

At the two concentrations of M2TM in fully hydrated DMPC at pH 8.0 used in this research, x=0.03 and x=0.06 corresponding to M2TM tetramer: lipid molecule ratios of 1:120 and 1:64, respectively, M2TM quantitatively forms tetramers. [231]

The concentration drugs in the samples used are in the physiological relevant range, i.e., the micromolar regime where *Aamt* drugs exhibited their biological activity. The thermal effects of the M2TM tetramer at these concentrations and in presence of a six-molar excess of *Amt* or *AK13* were studied. The calorimetric data for pure DMPC bilayers are in accordance with the previous findings. [204] In particular, there is a main sharp peak centered at 23.43°C, exhibiting a high-enthalpy transition, accompanied by a broad low-enthalpy pretransition centered at 13.27°C (Figure 5.2a), which signals the onset of the ripple phase during heating [253] and is more sensitive to disruption than the main transition. A thermal scan of the binary system DMPC + M2TM (x=0.03) (Figure 5.2b), is lacking the pretransition but is still composed of two distinct peaks. The first domain (domain I) is a very broad, small endothermic event centered approximately at 23°C (Figure 5.2b, Table 5.2). The second major domain (domain II) also contains a broadened peak with T_m=20.60^{o}C, about 3^{o}C lower from that observed by DMPC bilayers alone. The formation of the two domains was studied systematically with time and was found to be persistent, although with some modifications in their intensities. Shifting and broadening of lipid phase transitions, as well as elimination of pretransitions, are commonly observed upon membrane-insertion of proteins, e.g., mellitin, defensins, and gramicidin S. [132, 233, 254, 255]

Adding *Amt* or *AK13* (x=0.05) in the mixture of DMPC + M2TM (x=0.03) affects both domains (Figure DMPC + M2TM (x=0.03)). Compounds *Amt* and *AK13* do not differ appreciably in their effects at this concentration. Both molecules further decrease the T_m and ΔH_m for the two domains. Interestingly, the presence of either drug results in decreasing the breadth of domain II and shifting the T_m of both domains to lower temperatures. The sample composition for Figures 2 (DMPC + M2TM (x=0.03) + *Amt* or *AK13* (x=0.05)) corresponds to one equivalent M2TM tetramer + six equivalents *Amt* or *AK13* with 120 DMPC lipid molecules. It has been previously shown that when the sample composition is one equivalent M2TM tetramer + four equivalents *Amt,* one equivalent of the drug binds inside the high-affinity binding site of the M2TM tetramer pore. [85, 92]

In the denser binary mixture DMPC + M2TM (x=0.06), which corresponds to a sample composition including the M2TM tetramer in 64 DMPC lipids, a very broad

peak is observed at T_m=22.8°C that is very close to that of the pure DMPC bilayers, but with ΔH_m highly decreased and $\Delta T_{1/2}$ highly increased (Figure 5.2e) and the second domain disappears. Interestingly, the two drugs in this lipid bilayer containing high-density M2TM cause different effects. In the ternary mixture DMPC + M2TM (x=0.06) + *Amt* (x=0.08), the DSC scan still may include two domains (or, alternatively, reinstates the pretransition shifted up to ~15.2°C (Figure 5.2f). But if so, domain II is now almost absent or at least less prominent compared to the lower concentration sample M2TM (x=0.03) + *Amt* (x=0.05) (Figure 5.2c). In fact, when the *Aamt* ligand is *AK13*, the DSC scan results in only one domain (Figure 5.2g), similar to the single domain I of DMPC + M2TM (x=0.06) (Figure 5.2e), suggesting that the M2TM-*AK13* complex and the excess *AK13* constituents are uniformly distributed in the lipid bilayer. Thus, the sample including five equivalents *AK13*, one equivalent M2TM-*AK13* complex, and 64 lipid molecules does not produce a second domain compared to *Amt*; it only affects domain I significantly by increasing $\Delta T_{1/2}$ and lowering ΔH_{cal}.

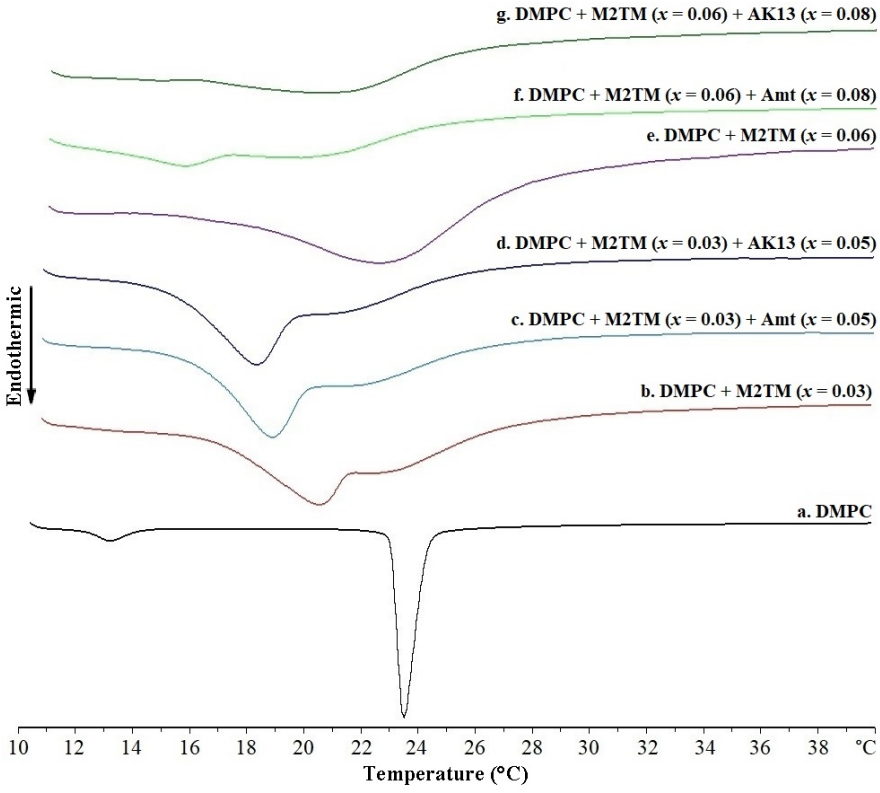

Figure 5.2: DSC heating scans (endothermic) of DMPC bilayers, fully hydrated in phosphate buffer at pH 8.0, including M2TM tetramer and six-fold excess of the *Aamt* ligand. The range for the calculation of thermotropic parameters is from 10°C to 40°C.

5.3.2 Solid state NMR spectroscopy

5.3.2.1 1H MAS NMR in the gel phase

The high resolution ^{1}H MAS NMR spectrum of DMPC fully hydrated bilayers at pH 8.0 shows only eminent peaks at ca 3.0 ppm, [221] which are assigned to the N-methyl hydrogens of the lipid polar head-group (Figure 5.3, Table 5.3). The presence of M2TM (x=0.03) at 15^{o}C causes fluidization of DMPC bilayers at pH 8.0, as became evident from the appearance of peaks attributed to the alkyl chains (0.5-1.7 ppm) in Figure 5.3 (left). Increasing the concentration of M2TM (x=0.06) causes further fluidization of DMPC bilayers at pH 8.0, as the alkyl chain-region covers a broader range (0.0-2.7 ppm), while a systematic shift of the peaks in the lower field is also observed (Table 5.3).

The spectrum of the sample DMPC + M2TM (x=0.03) + *Amt* (x=0.05) or *AK13* (x=0.05) (Figure 5.3, right) is similar to that of DMPC + *Amt* (x=0.05) or *AK13* (x=0.05) (data shown in ref. [231]). Therefore, the drugs mask the effects of M2TM at 0.5-1.7 ppm in the NMR spectrum. Additionally, it has been reported that *Aamt* drugs bound to the M2TM pore reduce its conformational plasticity [256], which is in agreement with the observed limited protein's effect on DMPC fluidization. When higher *Amt* or *AK13* (x=0.08) and M2TM (x=0.06) concentrations are used (Figure 5.3, right), the spectrum at pH 8.0 appears similar to that of DMPC + M2TM (x=0.03) (Figure 5.3, left), but the peaks' intensities are increased, suggesting instead a higher fluidization of DMPC acyl chains in this case.

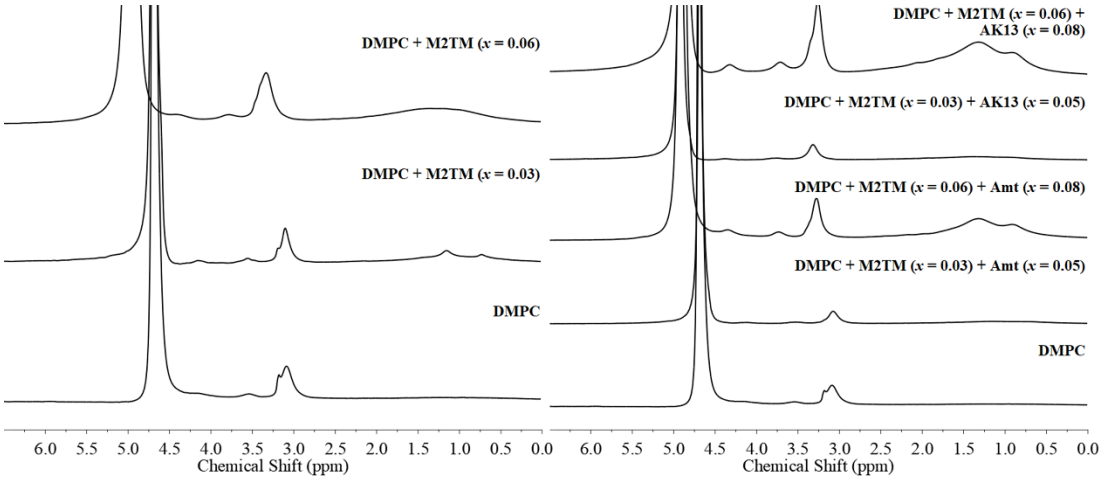

Figure 5.3: ^{1}H MAS NMR spectra of DMPC bilayers with M2TM (*left*) and with M2TM and *Amt* or *AK13* (*right*) at 15ºC and fully hydrated in phosphate buffer at pH 8.0.

5.3.2.2 ^{13}C CP/MAS NMR at gel phase

M2TM at concentration *x*=0.03 does not modify the chemical shifts and intensities of the DMPC bilayer peaks acquired at pH 8.0; instead it raises them by 0-0.4 ppm at lower fields for the higher concentration of *x*=0.06 (Figure 5.4, upper traces). The methyl group of the DMPC resonance at *δ*=14.4 ppm in the same sample increases in intensity through cross polarization. When *Amt* or *AK13* is incorporated at the lower concentration *x*=0.05 (Figure 5.4, lower traces), the peaks from DMPC at ca 14 ppm and 54 ppm, which are susceptible to cross polarization effects, show modified intensities. At higher drug concentrations of *x*=0.08, the chemical shifts of the drug move by 0.2 ppm, most often toward the lower field (Table 5.4). The peaks from the drug (see asterisks in Figure 5.4; Table 5.4) are already observed at the lower concentration of *x*=0.05 but are more eminent at the higher concentration of *x*=0.08. It has been observed that when a stoichiometric amount of *Amt* with M2TM tetramer is present, the spectrum resembles the lipid-only spectrum. [58] Thus, the peaks in the bottom traces of Figure 5.4 are due to the excess of drug molecule not bound with M2TM distributed in the DMPC bilayers. These peaks of the drug show chemical shift changes that ranged between 0.4 and 1.4 ppm compared to the solution resonances, suggesting an interaction of the drug with the membrane system (Table 5.5).

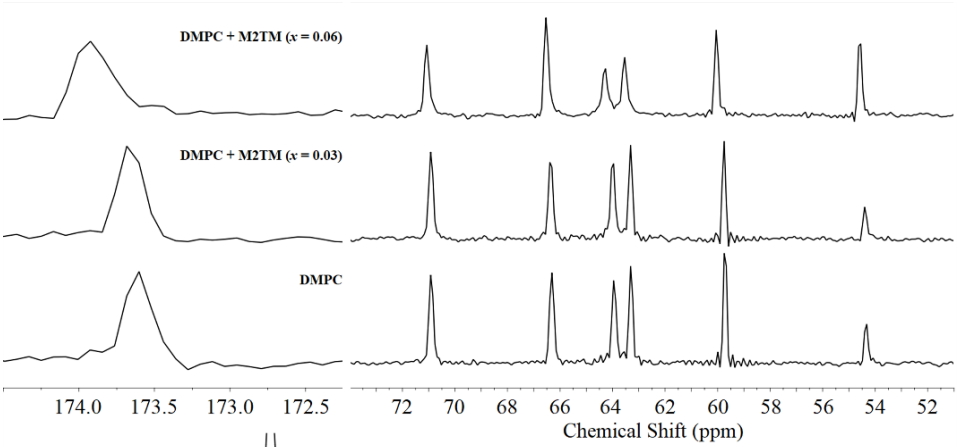
DMPC + M2TM (x = 0.06)
DMPC + M2TM (x = 0.03)
DMPC
174.0 173.5 173.0 172.5
72 70 68 66 64 62 60 58 56 54 52
Chemical Shift (ppm)

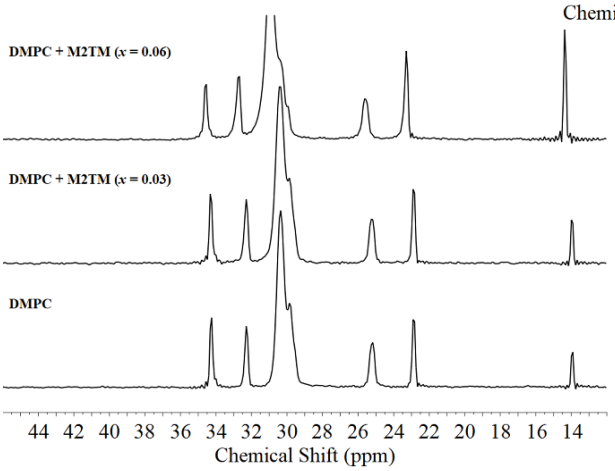
DMPC + M2TM (x = 0.06)
DMPC + M2TM (x = 0.03)
DMPC
44 42 40 38 36 34 32 30 28 26 24 22 20 18 16 14
Chemical Shift (ppm)

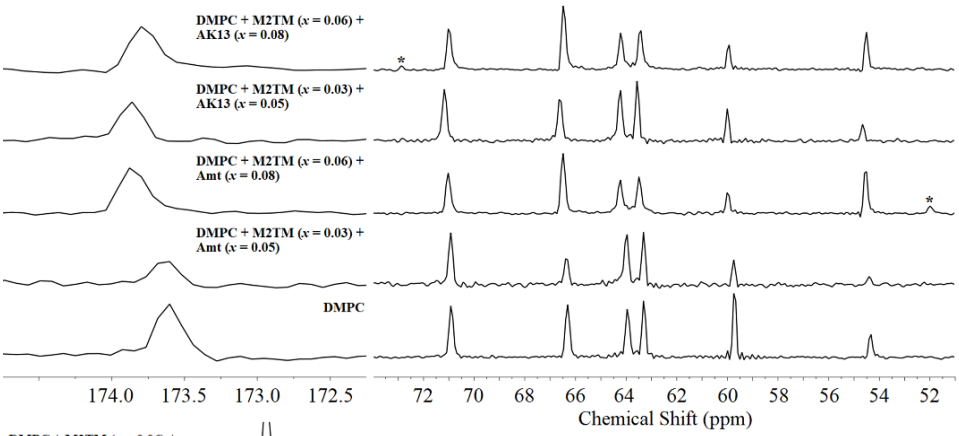
DMPC + M2TM (x = 0.06) + AK13 (x = 0.08)
DMPC + M2TM (x = 0.03) + AK13 (x = 0.05)
DMPC + M2TM (x = 0.06) + Amt (x = 0.08)
DMPC + M2TM (x = 0.03) + Amt (x = 0.05)
DMPC
174.0 173.5 173.0 172.5
72 70 68 66 64 62 60 58 56 54 52
Chemical Shift (ppm)

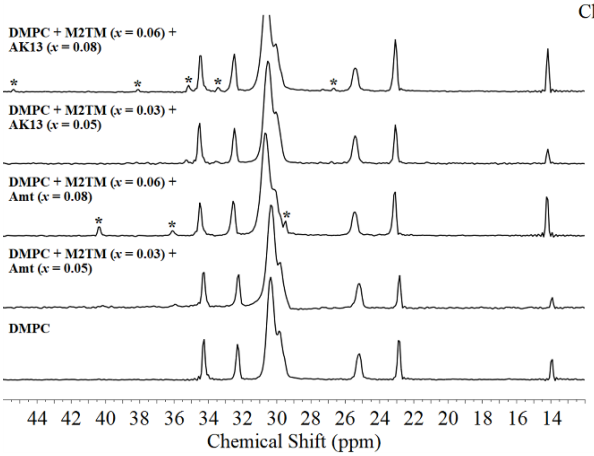
DMPC + M2TM (x = 0.06) + AK13 (x = 0.08)
DMPC + M2TM (x = 0.03) + AK13 (x = 0.05)
DMPC + M2TM (x = 0.06) + Amt (x = 0.08)
DMPC + M2TM (x = 0.03) + Amt (x = 0.05)
DMPC
44 42 40 38 36 34 32 30 28 26 24 22 20 18 16 14
Chemical Shift (ppm)

Figure 5.4: ^{13}C CP-MAS NMR spectra of DMPC bilayers with M2TM (*upper traces*) and with M2TM and *Amt* or *AK13* (*lower traces*) at 15ºC and fully hydrated in phosphate buffer at pH 8.0.

5.3.2.3 ^{31}P static NMR spectroscopy at gel phase

The effects of M2TM incorporated in DMPC bilayers at pH 8.0 on the phosphate group resonance at *ca* -20 ppm are shown in the static ^{31}P powder spectra (Figure 5.5). The narrow peaks in the ^{31}P spectra between 0 and 10 ppm correspond to the phosphate groups of the buffer solution. It is evident that M2TM at x=0.03 causes a decrease in the difference in the components of the shielding tensor $\sigma_{II}-\sigma_{I}$ value by *ca* 10 ppm (Table 5.6). At the highest concentration of x=0.06, the $\sigma_{II}-\sigma_{I}$ value decreases further by 4 ppm. According to ^{31}P NMR spectra, the ternary system DMPC + M2TM (x=0.03) + *Amt* (x=0.05) or *AK13* (x=0.05) produces σ_{I}-σ_{II} values almost identical to those of DMPC + M2TM (x=0.03) at the gel phase, indicating that *Amt* and *AK13* at concentration x=0.05 do not further perturb the phosphate group region in the presence of M2TM. This is consistent with results from our previous paper [147] showing that at these concentrations the drugs do not change the $\sigma_{II}-\sigma_{I}$ value compared to pure DMPC. Only when the concentration of the drug was x=0.08 in the DMPC + *Aamt* system did the σ_{I}-σ_{II} value increase by 4 ppm, compared to the pure DMPC. [147] The ternary system DMPC + M2TM (x=0.06) + *Amt* (x=0.08) or *AK13* (x=0.08) gives σ_{I}-σ_{II} values increased by ca 3 ppm, compared to those of DMPC + M2TM (x=0.06) at the gel phase temperature of 15ºC.

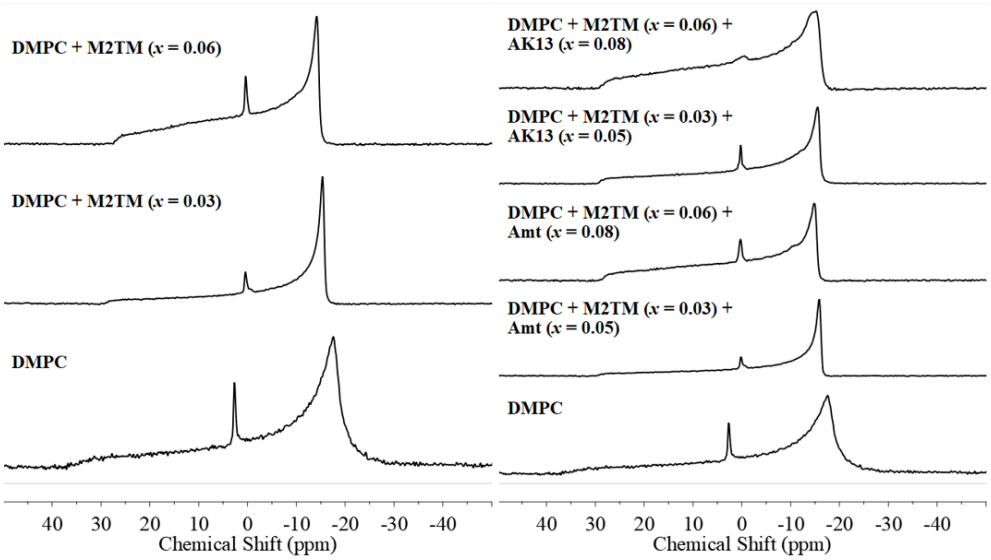

Figure 5.5: ^{31}P NMR spectra of DMPC bilayers with M2TM (*left*) and with M2TM and *Amt* or *AK13* (*right*) at 15ºC and fully hydrated in phosphate buffer at pH 8.0.

5.3.2.4 ^{1}H MAS NMR at liquid crystalline phase

The effects of M2TM in DMPC bilayers in the liquid crystalline phase (35°C) at pH 8.0, using the same two concentrations as in the gel phase, are shown in Figure 5.6 (left). At *x*=0.03, M2TM has no observable effect on the DMPC bilayers spectrum, suggesting that the protein is embedded in the lipid bilayer and does not significantly affect its dynamics. At the higher concentration of *x*=0.06, the intensities of the peaks grow, and the resonances are shifted to the lower field (Table 5.7). The preparations DMPC + M2TM (*x*=0.03) + *Amt* (*x*=0.05) or *AK13* (*x*=0.05) and DMPC + M2TM (*x*=0.06)+ *Amt* (*x*=0.08) or *AK13* (*x*=0.08) resemble those of DMPC + M2TM (*x*=0.03) and DMPC + M2TM (*x*=0.06), correspondingly. In these two preparations, the *Aamt* drug is inserted in the M2TM pore and the excess of drug molecules is distributed mainly in the bilayers. The observance of peaks with identical linewidths as those reported in our previous publication [147] where drugs perturbed DMPC bilayers not containing M2TM, is an indication that *Aamt* drugs insert into and affect the lipid bilayer (see asterisks in Figure 5.6; Table 5.8).

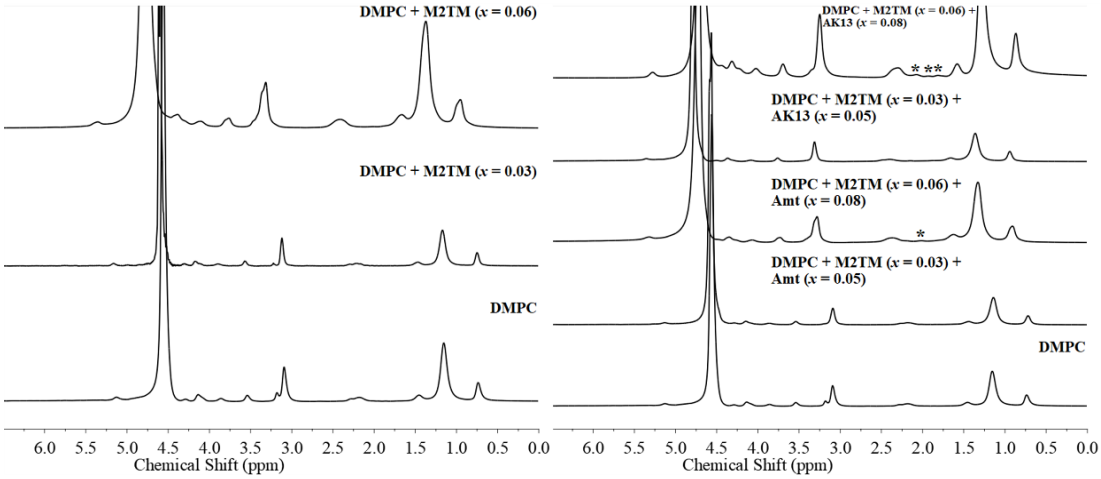

Figure 5.6: ^{1}H MAS NMR spectra of DMPC bilayers with M2TM (*left*) and with M2TM and *Amt* or *AK13* (*right*) at 35ºC and fully hydrated in phosphate buffer at pH 8.0.

5.3.2.5 ^{13}C CP/MAS NMR at liquid crystalline phase

At 35ºC and pH 8.0, M2TM at concentration *x*=0.03 did not modify the chemical shifts and intensities of DMPC bilayer peaks, and only at the higher concentration *x*=0.06 does M2TM produce a change of the chemical shifts of DMPC bilayers at the lower field (Table 5.9). These are identical to the effects that *Amt* and *AK13* caused in the gel phase temperature of 15ºC (Figure 5.7, Table 5.9).

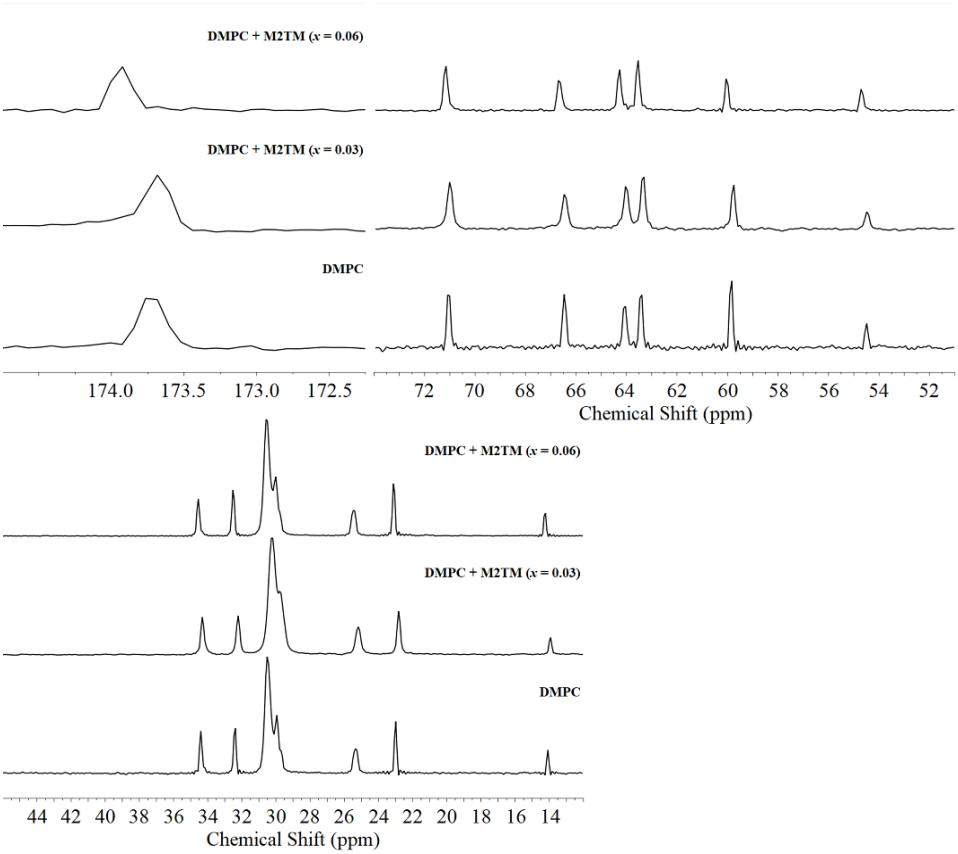
DMPC + M2TM (x = 0.06)
DMPC + M2TM (x = 0.03)
DMPC
174.0 173.5 173.0 172.5
72 70 68 66 64 62 60 58 56 54 52
Chemical Shift (ppm)
DMPC + M2TM (x = 0.06)
DMPC + M2TM (x = 0.03)
DMPC
44 42 40 38 36 34 32 30 28 26 24 22 20 18 16 14
Chemical Shift (ppm)

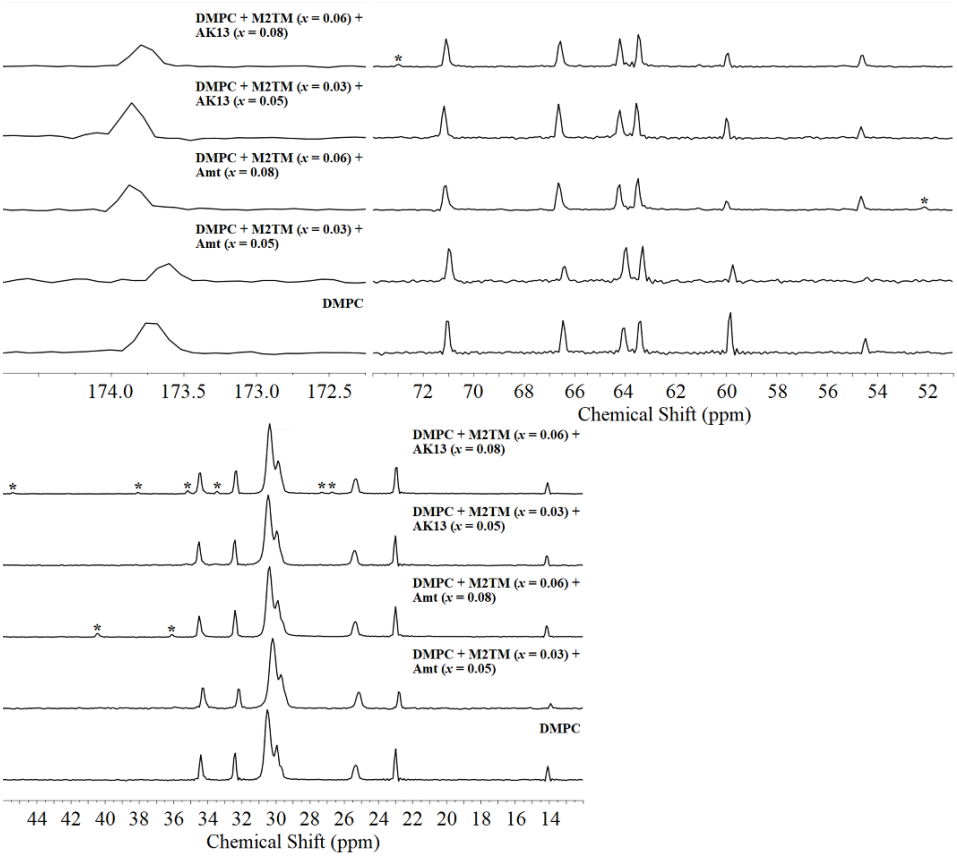
DMPC + M2TM (x = 0.06) + AK13 (x = 0.08)
DMPC + M2TM (x = 0.03) + AK13 (x = 0.05)
DMPC + M2TM (x = 0.06) + Amt (x = 0.08)
DMPC + M2TM (x = 0.03) + Amt (x = 0.05)
DMPC
174.0 173.5 173.0 172.5
72 70 68 66 64 62 60 58 56 54 52
Chemical Shift (ppm)
DMPC + M2TM (x = 0.06) + AK13 (x = 0.08)
DMPC + M2TM (x = 0.03) + AK13 (x = 0.05)
DMPC + M2TM (x = 0.06) + Amt (x = 0.08)
DMPC + M2TM (x = 0.03) + Amt (x = 0.05)
DMPC
44 42 40 38 36 34 32 30 28 26 24 22 20 18 16 14
Chemical Shift (ppm)

Figure 5.7: ^{13}C CP-MAS NMR spectra of DMPC bilayers with M2TM (*upper traces*) and with M2TM and *Amt* or *AK13* (*bottom traces*) at 35ºC and fully hydrated in phosphate buffer at pH 8.0.

5.3.2.6 ^{31}P NMR spectra in the liquid crystalline phase

Similar effects are observed with ^{31}P NMR spectra in the liquid crystalline phase (Figure 5.8, Table 5.6). This is not surprising as similar effects are also observed in the ^{1}H and ^{13}C NMR spectra for the gel and liquid crystalline phase.

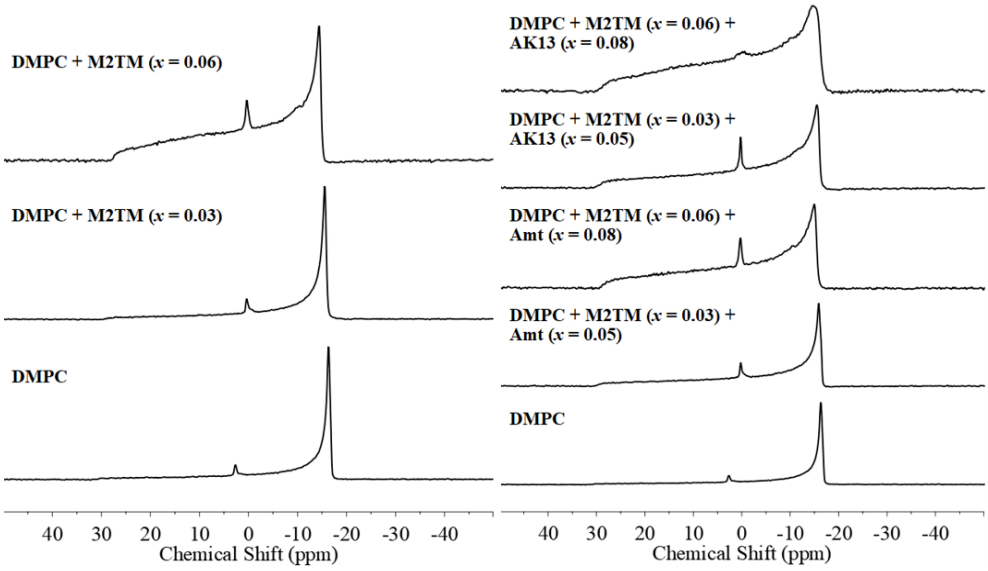

Figure 5.8: ^{31}P NMR spectra of DMPC bilayers with M2TM (*left*) and with M2TM and *Amt* or *AK13* (*right*) at 35ºC and fully hydrated in phosphate buffer at pH 8.0.

5.3.3 X-ray scattering

X-ray scattering patterns of DMPC + M2TM (x=0.03) in absence or presence of *Amt* or *AK13* at concentration x=0.05 at 20°C (A) and 30°C (B) at pH 8.0 are shown in Figure 5.9. The corresponding WAXS peaks arising from the lipids chain-packing are shown in the insets.

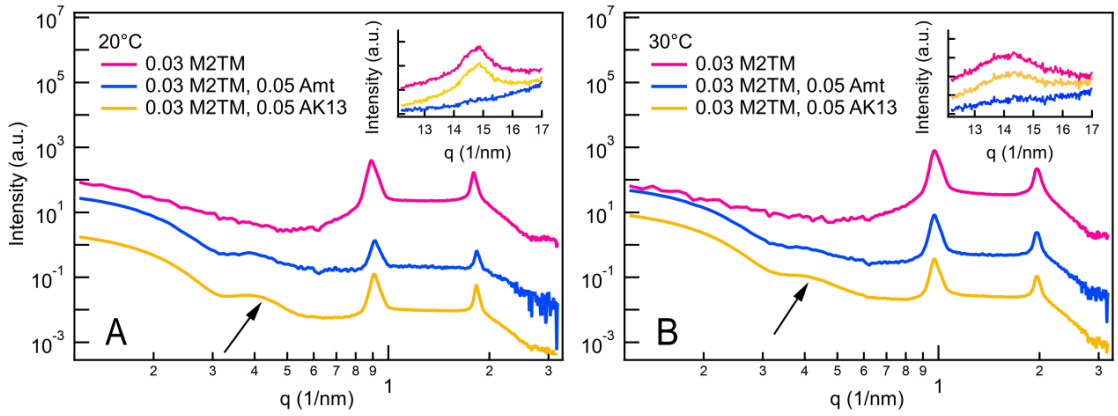

Figure 5.9: X-ray scattering curves of DMPC + M2TM (*x*=0.03) in the absence or presence of *Amt* or *AK13* at concentration *x*=0.05 at 20°C (*A*) and 30°C (*B*) and fully hydrated in phosphate buffer at pH 8.0. Insets show the WAXS peak arising from the lipids chain-packing. Traces were vertically shifted for clarity. The broad shoulder is indicated with an arrow.

At 20°C, a typical pattern of a bilayer is observed in DMPC + M2TM (*x*=0.03). Adding the drug molecules, the formation of a broad shoulder is observed, and this scattering pattern is consistent with DSC results suggesting the presence of two lipid domains. In the SAXS patterns, drug molecules do not modify the d-spacing of DMPC + M2TM (*x*=0.03) bilayers substantially (Table 5.10). However, in WAXS spectra, *Amt* exerts a significant disordering of the chain-packing, more so than *AK13*, as no peak is evident at this temperature. At 30°C, the same conclusions can be drawn, implying that *Amt* is acting more effectively in both mesomorphic states. The only difference is that, at liquid crystalline temperatures, *Amt* significantly expands the d-spacing of the lipid bilayers, i.e., to 69.16 Å at *x*=0.05 (Table 5.10). The ordering of the bilayers (peak width) is unaffected by the change of temperature.

For high drug concentrations, i.e., DMPC + M2TM (*x*=0.06), X-ray scattering patterns in the absence or presence of *Amt* or *AK13* (*x*=0.08) at 20°C (A) and 30°C (B) are shown in Figure 5.10. It is evident from the spectra at 20°C that the broad component observed with lower peptide concentrations is absent. These results are again in harmony with DSC results showing the presence of only one lipid domain. Interestingly, in SAXS experiments, all three samples at 20°C or

30°C show a very similar d-spacing, which is again consistent with the DSC results showing one domain of lipids uniformly occupied by M2TM and the *Aamt* ligand (Table 5.10). At both temperatures, the peak width of *Amt* is larger than the others, indicating stronger activity for the side chain-disorder. However, in the liquid crystalline phase at 30°C, the SAXS sample DMPC + M2TM (x=0.06) + *Amt* (x=0.08) does not show any peaks, i.e., the formation of unilamellar vesicles, indicating a drastic modification of the lamellar structure of the lipid bilayers. In contrast, DMPC + M2TM (x=0.06) and DMPC + M2TM (x=0.06) + *AK13* (x=0.08) samples show similar d-spacing results. This is again in agreement with DSC results in which, at this concentration of the sample, *Amt* appears to cause the most significant effect. However, in ref. [147], which uses DMPC lipid with only *Amt* at the same concentration, more ordered bilayers are observed, resulting in Bragg peaks in SAXS and WAXS experiments. This highlights a discrepancy between the results.

The activity of *Amt* is generally visible by comparing the WAXS peak data for all temperatures and concentrations (Table 5.10). Here a general trend is seen that higher drug concentrations cause increased side chain-packing, which is evidenced by the smaller d-spacings and smaller peak widths in the WAXS regime.

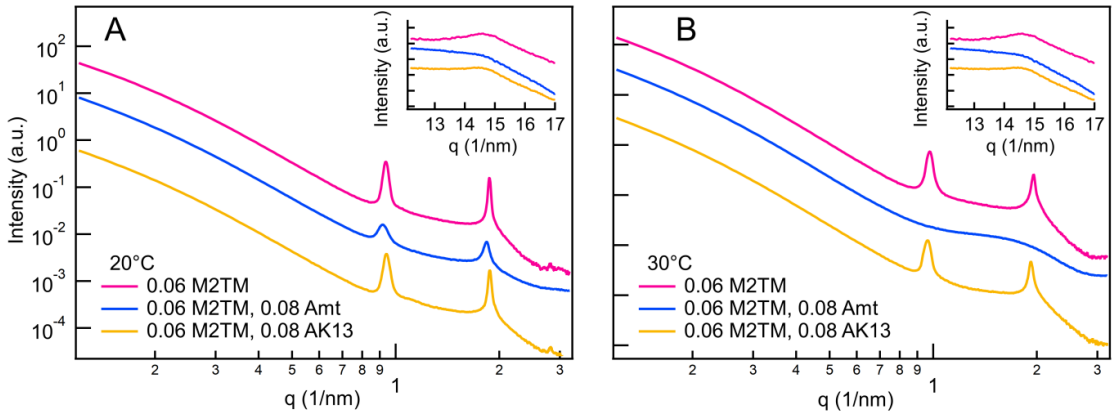

Figure 5.10: X-ray scattering curves of DMPC + M2TM (x=0.06) in absence or presence of *Amt* or *AK13* at high concentration x=0.08, 20°C (*A*) and 30°C (*B*) and fully hydrated in phosphate buffer at pH 8.0. Insets show the WAXS peak due to the lipids chain-packing. Traces were vertically shifted for clarity.

5.3.4 MD simulations

For the 120 DMPC molecule system, the area-per-lipid for the M2TM boundary lipid region is calculated as ca 47 Å^2. The definition of the boundary lipids is based on the Voronoi cells being close to the protein atoms. [252] These values are significantly lower than the calculated area-per-lipid for the bulk lipid domain, ca 63 Å^2. The experimental value for DMPC is ca 60 Å^2, as determined by SAXS. [257] The M2TM boundary lipids are volume constricted because of their more oriented structure around M2TM. MD simulations were performed for systems including M2TM-*Aamt* complex and five molecules of *Aamt* in 120 DMPC lipids that resemble experimental samples. The simulations results show that the five *Aamt* drug molecules are associated with the polar head area of the bilayer by forming ionic hydrogen bonding interactions between ammonium group of the drug and lipid phosphate groups. These drug molecules may also in contact with through adamantane ring with hydrophobic residues of M2TM. This hydrophobic interaction with M2TM is more frequent for *AK13* than for *Amt*. This is consistent with the radial distribution plots that describe the distance of *Aamt* molecule from the center of mass of G34. These plots suggest more frequent contacts of *AK13* than of *Amt* with the M2TM pore (Figure 5.12). This preference of *AK13* to remain closer to M2TM may have important consequences, leaving *Amt* to more efficiently perturb the DMPC bilayer.

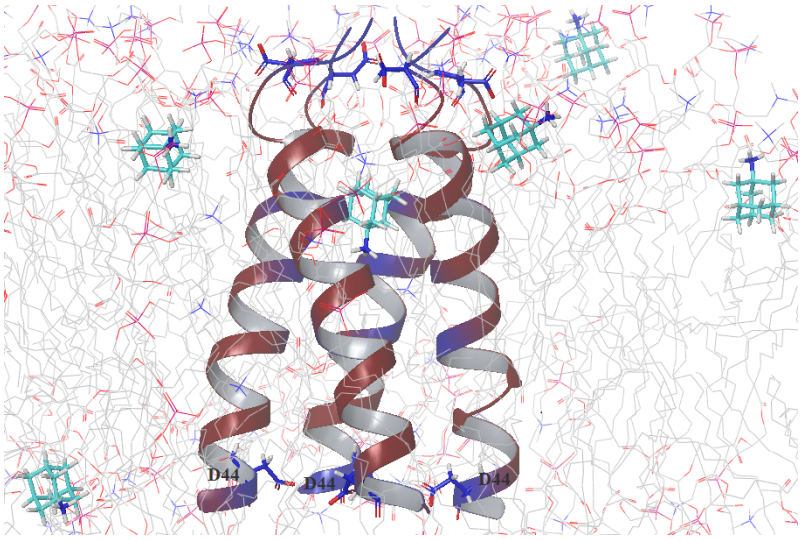

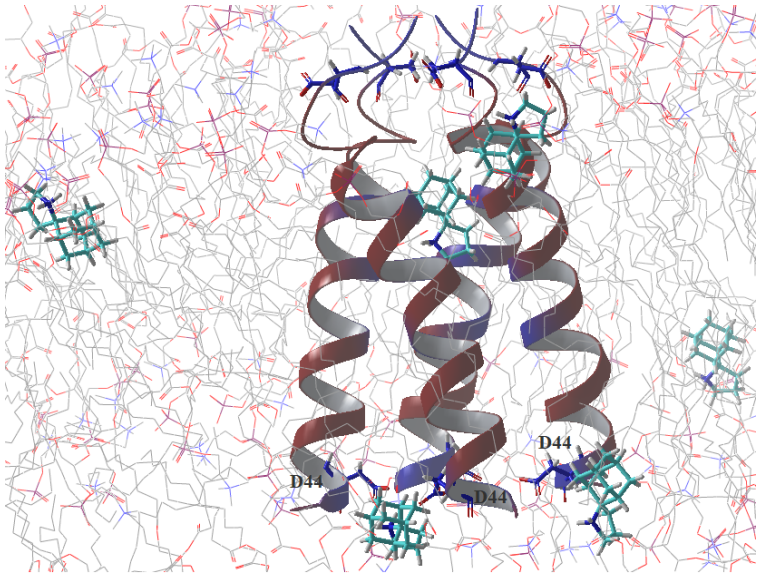

Figure 5.11: Screenshot from a 200 ns MD simulation of the system including: (*upper*) the M2TM tetramer-*Amt* complex with five *Amt* molecules or (*lower*) the M2TM tetramer-*AK13* complex with five *AK13* molecules in DMPC bilayers at pH 8.0.

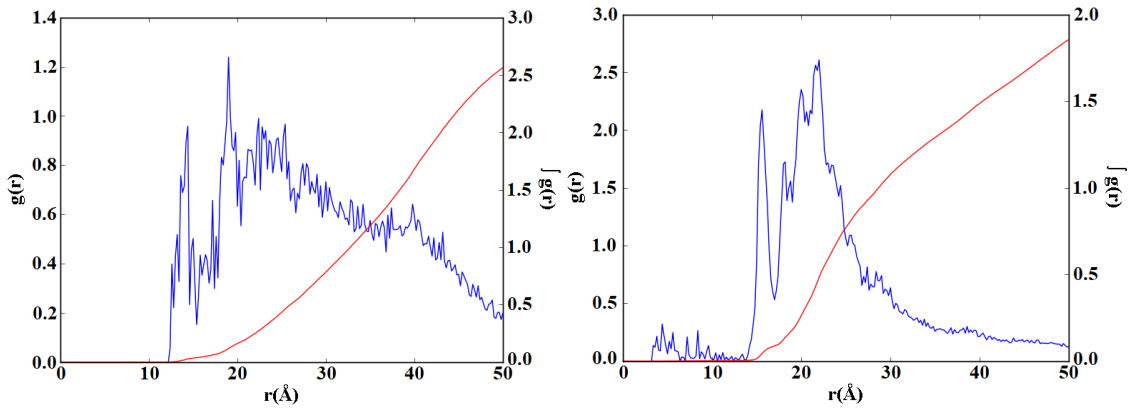

Figure 5.12: Radial distribution function of the center of mass of: (*left*) *Amt* and (*right*) *AK13* from the center of mass of Gly34.

5.4 Discussion

M2 plays an important role in the induction of membrane curvature and/or in the scission process whereby the envelope is cut upon virion release. Here, the interaction of two concentrations of M2TM is investigated in *apo* or *Aamt*-bound form with a variety of biophysical methods to evaluate their ability to identify lipid perturbations affected by small changes in M2TM and *Aamt* concentration and in *Aamt's* structure. The M2TM homotetramer doesn't comprise of the amphipathic helixes of the C-terminal, which are the primary region of ion channel responsible

for generating curative and scission in the host cell. Nevertheless, the understanding the of importance M2TM region on the confirmation and dynamics of the membrane is crucial since the TM domain is functioning as ion channel and involved in clustering of the M2 tetrameric channel through intertetramer interactions of the transmembrane helixes. [235]

M2TM spans the membrane thickness and, according to ^{31}P ssNMR evidence and MD simulations, exerts strong interactions with phosphate groups of the polar head surface. In addition, the pretransition seen in DSC is ablated by M2TM without drugs, indicating that, like the drugs, the high-peptide density (x=0.06, 64 lipid molecules per tetramer which corresponds to 32 lipids in each leaflet) and even the low-peptide density (x=0.03, 120 lipid molecules per tetramer which corresponds to 60 lipids in each leaflet) perturb the head groups or hydrocarbon chain-tilts.

The DSC scans suggests the presence of two domains, as it is shown in Figure 5.13, at the low concentration of embedded M2TM protein (x=0.03) in the DMPC bilayers (Figure 5.2b) in the absence or presence of the *Aamt* drug (Figure 5.2c,d). It may be suggested that the low-T_m domain (II) corresponds to bulk DMPC lipids with a strongly cooperative phase transition but also that M2TM contributes to the destabilization of the gel phase through long-range interactions. Domain I corresponds to lipids bound to M2TM tetramers, which constitute essentially all of the lipids at high-peptide density (x=0.06) (Figure 5.2e). These findings are confirmed by SAXS experiments. This system becomes uniform when M2TM protein is increased in concentration in the bilayer (x=0.06). The second domain disappears, indicating that the M2TM is distributed uniformly in the lipid bilayers, such that at this density all lipid molecules behave as boundary lipids. The presence of an excess of the drug as regards M2TM in the membrane system affects the DSC profiles, indicating a clear perturbation of the lipid properties in the M2TM-containing bilayers.

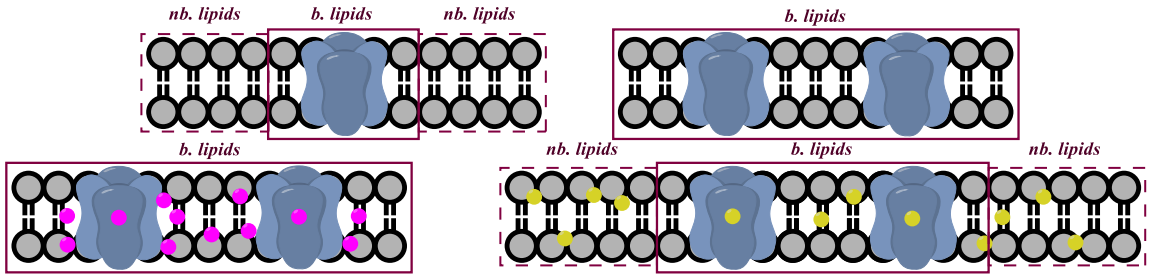

Figure 5.13: At the low concentration of embedded M2TM protein (shown as tetrameric surface) two domains appeared, one that corresponds to bulk lipids (lipids are shown as head with two tails) and one to lipids bound to M2TM tetramers, which constitute essentially all of the lipids at high peptide density. The second domain disappears indicating that the M2TM is distributed uniformly in the lipid bilayers, such that at this density all lipid molecules behave as boundary lipids. The excess *Amt* (shown as yellow spheres) not bound to the protein pore, anchors through its ammonium to the lipid polar head region in contrast, to the excess of the more lipophilic *AK13* (shown in pink spheres) which interacts more with the lateral surfaces of M2TM and not with the lipid polar head region. The stronger effect of *Amt* to the bilayers compared to the more lipophilic *AK13*, when M2TM is present, results in the two lipid domains observed in the DSC scans (***b. lipids***: boundary lipids; ***nb. lipids***: non boundary lipids which are the bulk lipids).

According to WAXS experiments, *Amt* induces a significant chain-stacking disordering, in contrast to *AK13*, which shows only milder effect. It is thus evident that the membrane-perturbing effects of these drugs are different in the system containing M2TM protein compared to the effects of these drugs alone. It has been previously observed using DSC [147] that *Amt* and *AK13* similarly perturb the DMPC bilayers when x=0.05, and the two molecules affect the glycerol backbone and the carbonyl region of the headgroup region in their amine form, or the phosphate groups in their ammonium form according to ^{13}C or ^{31}P ssNMR, respectively, and MD simulations. The changes in the shape of the ^{1}H NMR ssNMR spectrum in the studied M2TM protein systems are consistent with the fluidization of the bilayers and the changes in the chemical shifts of ^{13}C signals of the drug, which are clearly observed at a concentration higher than x=0.05, suggesting interactions of the drug with the lipid bilayer. The MD simulations show that the excess *Amt*, not bound to the protein pore, anchors through its ammonium to the lipid polar head region due to the strong ionic interactions of the *Amt* ammonium group with phosphate groups. In contrast, the excess of the more lipophilic *AK13 i.e.* logP 2.07 interacts more with the lateral surfaces of

M2TM and not with the lipid polar head region, due to the buried secondary ammonium group. Indeed, it has been previously shown using 500 ns MD simulations in DMPC-*Aamt* systems that, although *AK13* is also mainly localized in the polar head region, it can move easily between the two leaflets of the bilayer. [147] The stronger effect of *Amt* to the bilayers when M2TM is present, compared to the more lipophilic *AK13*, results in the two lipid domains observed in the DSC scans.

The lipid bilayer may serve as a reservoir for lipophilic/amphiphilic ligands, which in turn helps to concentrate the ligands near the binding site of the receptor, thereby affecting the observed association rate without necessarily changing interactions with binding-site residues. We showed previously that *AK13* is tolerated in lipid bilayers at very high concentrations, while *Amt* crystallizes. [147] The higher M2TM binding affinity of *AK13* compared to *Amt* may be associated with its higher concentration in the lipid bilayers close to M2 transmembrane helices around the binding area. [174]

5.5 Conclusions

The homotetrameric influenza A M2 protein is one of the simplest protein ion channels under investigation, and the applied techniques here correspond to common biophysical methods used for membrane systems.

We have investigated the interactions of influenza A M2TM with membrane bilayers due to the significance of M2 protein in affecting membrane bending and virus budding in a host cell. We have shown that (a) DSC and SAXS are useful methods to detect changes in membrane organization caused by small changes in M2TM or *Aamt* concentration and *Aamt* structure and (b) that WAXS and MD can suggest details of ligand topology. In particular, DSC and SAXS show that at a low M2TM micromolar concentration in DPMC bilayers, two lipid domains are observed, which likely correspond to M2TM boundary lipids and bulklike lipids. At higher M2TM concentrations, one domain only is identified, which constitutes essentially all of the lipid molecules behaving as boundary lipids. According to SAXS, WAXS, and DSC in the absence of M2TM, both *Aamt* drugs exert a similar perturbing effect on the bilayer at low concentrations, i.e., x=0.05-0.08. [147] At

the same concentrations of the drug when M2TM is present, the *Amt* and, to a lesser extent, *AK13* cause, according to WAXS, a significant disordering of chain-stacking, which also leads to the formation of two lipid domains. This effect is likely due, according to MD simulations, to the preference of the more lipophilic *AK13* (logP 2.07) to locate closer to the lateral surfaces of M2TM when compared to *Amt* (logP 1.17), which forms stronger ionic interactions with phosphate groups. The preference of *AK13* to concentrate inside the lipid bilayer close to the exterior of the hydrophobic M2TM helices may contribute to its higher binding affinity compared to *Amt*. It may be possible that the receptor binding of *AK13* occurs through lipid pathways via the transmembrane helices; but this possibility warrants further investigation.

5.6 Tables

***Table 5.1*:** Samples preparation details.

Sample	**DMPC (mg)**	**M2TM (mg)**	***Amt* (mg)**	***AK13* (mg)**
DMPC	37.3	-	-	-
DMPC + M2TM (x=0.03)	37.3	5.0	-	-
DMPC + M2TM (x=0.03) + Amt (x=0.05)	37.3	5.0	0.5	-
DMPC + M2TM (x=0.03) + AK13 (x=0.05)	37.3	5.0	-	0.6
DMPC + M2TM (x=0.06)	37.3	10.0	-	-
DMPC + M2TM (x=0.06) + Amt (x=0.08)	37.3	10.0	1.0	-
DMPC + M2TM (x=0.06) + AK13 (x=0.08)	37.3	10.0	-	1.2

*The drugs were not added after lipids were hydrated since this would cause unequal distribution to the bilayers. This was also mentioned in the study of Suwalsky et al. [see ref. 40 in the main text] that dealt with the effect of *Amt* on DMPC and DMPE MLVs. In the Suwalsky et al. study, the drug was added to the suspension post-preparation. In the present study, the drug was present during the evaporation of methanol and phospholipid self-assembly. The packing and orientation of the molecule inside the lipid membrane varies significantly between the two cases. In our case, the drug affects an enhanced packing of the phospholipids and has stronger interactions with the polar head groups, as has been observed in our previous publication. Thus, here the appearance

and detection of bound M2 lipid and bulk lipid domains using DSC and SAXS is due to different molecular interactions between lipids and different concentrations of M2TM without or with drugs.

***Table 5.2*:** Calorimetric heating profiles of DMPC + M2TM without or with *Amt* or *AK13*. The DMPC bilayers were fully hydrated in phosphate buffer at pH 8.0.

Sample	$T_{onset,m}$ (°C)	T_m (°C)	$\Delta T_{1/2,m}$ (°C)	ΔH_m (kJ mol^{-1})	$T_{onset,s}$ (°C)	T_s (°C)	$\Delta T_{1/2,s}$ (°C)	ΔH_s (kJ mol^{-1})
DMPC	23.07	23.43	0.71	29.44	12.32	13.27	1.14	3.11
DMPC + M2TM (x=0.03)	16.76	20.60	5.56	19.81	-	-	-	-
DMPC + M2TM (x=0.03) + Amt (x=0.05)	16.17	18.91	2.73	19.79	-	-	-	-
DMPC + M2TM (x=0.03) + AK13 (x=0.05)	15.40	18.37	2.99	19.44	-	-	-	-
DMPC + M2TM (x=0.06)	16.94	22.77	6.20	11.23	-	-	-	-
DMPC + M2TM (x=0.06) + Amt (x=0.08)	11.07	15.88	9.23	14.36	-	-	-	-
DMPC + M2TM (x=0.06) + AK13 (x=0.08)	14.78	21.34	6.37	10.24	-	-	-	-

*T_{onset}: temperature at which the thermal event starts; T: temperature at which heat capacity ΔC_p at constant pressure is maximum; $\Delta T_{1/2}$: half width at half peak height of the transition; ΔH: transition enthalpy normalized per mol of lipid. Subscript m: main transition; subscript s: secondary transition (i.e., pretransition).

***Table 5.3*:** Chemical shifts observed in ^{1}H MAS NMR spectra of DMPC bilayers with M2TM in absence and presence of the *Amt* or *AK13* at 15ºC and fully hydrated in phosphate buffer at pH 8.0.

Sample	**H3**	**H(4'-13'), H(4"-13")**	**H14', H14"**	**$N(CH_3)_3$**	**H2'"**	**H1'"**
DMPC				2.6-3.3	3.6	4.2
DMPC + M2TM (x=0.03)		1.2	0.7	2.7-3.4	3.6	4.2
DMPC + M2TM (x=0.06)	4.4	0.1-2.7	0.1-2.7	3.3	3.8	
DMPC + M2TM (x=0.03) + Amt (x=0.05)		0.1-2.3	0.1-2.3	3.1	3.5	4.1
DMPC + M2TM (x=0.06) + Amt (x=0.08)	4.4	1.3	0.9	3.3	3.7	
DMPC + M2TM (x=0.03) + AK13 (x=0.05)		0.1-2.8	0.1-2.8	3.3	3.8	4.4

DMPC + M2TM (x=0.06) + AK13 (x=0.08)	4.3	1.3	0.9	3.3	3.7	

***Table 5.4*:** Chemical shifts observed in ^{13}C CP-MAS NMR spectra of DMPC bilayers with M2TM in absence and presence of *Amt* or *AK13* at 15ºC and fully hydrated in phosphate buffer at pH 8.0.

Sample	C1	C2	C3	C1', C1''	C2', C2''	C3', C3''	C(4'-11'), C(4''-11'')	C12', C12''	C13', C13''	C14', C14''	$N(CH_3)_3$	C2'''	C1'''
DMPC	63.3	70.9	64.0	173.6	34.3	25.2	29.0-31.3	32.3	22.9	14.0	54.4	66.3	59.7
DMPC + M2TM (x=0.03)	63.3	70.9	64.0	173.7	34.3	25.2	28.8-31.7	32.3	22.9	14.0	54.4	66.4	59.8
DMPC + M2TM (x=0.06)	63.5	71.1	64.3	173.9	34.6	25.6	29.4-32.3	32.7	23.3	14.4	54.6	66.5	60.1
DMPC + M2TM (x=0.03) + Amt (x=0.05)	63.3	70.9	64.0	173.6	34.3	25.2	29.2-31.8	32.2	22.8	13.9	54.4	66.4	59.8
DMPC + M2TM (x=0.06) + Amt (x=0.08)	63.5	71.0	64.2	173.9	34.5	25.5	29.6-31.7	32.5	23.1	14.2	54.5	66.5	60.0
DMPC + M2TM (x=0.03) + AK13 (x=0.05)	63.6	71.2	64.2	173.9	34.5	25.4	29.2-31.8	32.5	23.1	14.2	54.7	66.6	60.0
DMPC + M2TM (x=0.06) + AK13 (x=0.08)	63.4	71.0	64.2	173.8	34.5	25.4	28.7-31.7	32.5	23.1	14.2	54.5	66.5	60.0

***Table 5.5*:** Chemical shifts of *Amt* and *AK13* observed in ^{13}C NMR high-resolution spectra at 15ºC and 35ºC and fully hydrated in phosphate buffer at pH 8.0.

Sample	^{13}C NMR of *Amt* and *AK13* salts in D_2O	Identification	15 ºC ^{13}C-CP MAS NMR	35 ºC ^{13}C-CP MAS NMR
DMPC + M2TM (x=0.03)	-	-	-	-
DMPC + M2TM (x=0.06)	-	-	-	-
DMPC + M2TM (x=0.03) + Amt (x=0.05)	52.9 40.0 34.8 28.7	1' 2', 8', 9 4', 6', 10' 3', 5', 7'	35.9	35.9
DMPC + M2TM (x=0.06) + Amt (x=0.08)	52.9 40.0 34.8 28.7	1' 2', 8', 9 4', 6', 10' 3', 5', 7'	52.0 40.4 36.1 29.5	52.2 40.5 36.1
DMPC + M2TM (x=0.03) + AK13 (x=0.05)	73.9 44.6 36.7	2' 5 6'		

	34.3	1', 3'	35.3	35.2
	34.2	3		
	34.0	8', 10'	33.6	33.6
	32.8	4', 9'		
	26.1	5'	27.5	
	25.9	7'	26.8	
	22.6	4		
	73.9	2'	72.9,63.7	73.0
	44.6	5	45.4	45.4
	36.7	6'	38.1	38.1
	34.3	1', 3'	35.2	
DMPC + M2TM (x=0.06) +	34.2	3		
AK13 (x=0.08)	34.0	8', 10'		35.2
	32.8	4', 9'	33.4	33.5
	26.1	5'	27.3	27.3
	25.9	7'	26.7	26.7
	22.6	4	22.8	

Table 5.6**:** Components of the ^{31}P chemical shielding tensors of DMPC bilayers with M2TM in absence and presence of *Amt* or *AK13* at 15ºC or 35ºC and fully hydrated in phosphate buffer at pH 8.0.

Sample	**σ_{II}-σ_{I}**	
	15ºC	**35ºC**
DMPC	55.5	48.5
DMPC + M2TM (x=0.03)	45.7	45.6
DMPC + M2TM (x=0.06)	41.7	42.7
DMPC + M2TM (x=0.03) + Amt (x=0.05)	46.0	46.8
DMPC + M2TM (x=0.06) + Amt (x=0.08)	44.6	44.9
DMPC + M2TM (x=0.03) + AK13 (x=0.05)	45.4	46.3
DMPC + M2TM (x=0.06) + AK13 (x=0.08)	44.8	45.1

Table 5.7**:** Chemical shifts observed in ^{1}H MAS NMR spectra of DMPC bilayers with M2TM in absence and presence of *Amt* or *AK13* at 35ºC and fully hydrated in phosphate buffer at pH 8.0.

Sample	H1	H2	H3	H2', H2''	H3', H3''	H(4'-13'), H(4''-13'')	H14', H14''	$N(CH_3)_3$	H1'''	H2'''
DMPC	3.9	5.1	4.3	2.0-2.4	1.5	1.2	0.7	2.9-3.3	4.1	3.5
DMPC + M2TM (x=0.03)	3.9	5.2	4.3	2.1-2.4	1.5	1.2	0.8	3.0-3.3	4.2	3.6
DMPC + M2TM (x=0.06)	4.1	5.4	4.4	2.4	1.7	1.4	1.0	3.3	4.4	3.8
DMPC + M2TM (x=0.03) + Amt (x=0.05)	3.9	5.1	4.3	2.1-2.4	1.5	1.1	0.7	3.1	4.1	3.5
DMPC + M2TM (x=0.06) + Amt (x=0.08)	4.1	5.3	4.4	2.4	1.6	1.3	0.9	3.3	4.4	3.7
DMPC + M2TM (x=0.03) + AK13 (x=0.05)	4.1	5.4	4.5	2.4	1.7	1.4	0.9	3.3	4.4	3.8
DMPC + M2TM (x=0.06) + AK13 (x=0.08)	4.0	5.3	4.5	2.3	1.6	1.3	0.9	3.3	4.3	3.7

Table 5.8: Chemical shifts of *Amt* and *AK13* observed in ^{1}H NMR high-resolution spectra at 15ºC and 35ºC, and fully hydrated in phosphate buffer at pH 8.0.

Sample	^{1}H NMR of *Amt* and *AK13* salts in D_2O	Identification	15ºC ^{1}H MAS NMR	35ºC ^{1}H MAS NMR
DMPC + M2TM (x=0.03)	-	-	-	-
DMPC + M2TM (x=0.06)	-	-	-	-
DMPC + M2TM (x=0.03) + Amt (x=0.05)	2.1 1.7 1.6 1.5	3',5',7' 4', 6', 10' 2', 8', 9' $-NH_2$	-	-
DMPC + M2TM (x=0.06) + Amt (x=0.08)	2.1 1.7 1.6 1.5	3',5',7' 4', 6', 10' 2', 8', 9' $-NH_2$	-	2.0
DMPC + M2TM (x=0.03) + AK13 (x=0.05)	2.9 (t) 2.1 (bd) 1.9 1.7 1.6 1.4 (bd)	5 $4'_{ax}$, $9'_{ax}$ 5', 7' $10'_{ax}$, $8'_{ax}$,4,6' 1',3',3,$10'_{eq}$,$8'_{eq,}$ $4'_{eq}$, $9'_{eq}$	-	2.2
DMPC + M2TM (x=0.06) + AK13 (x=0.08)	2.9 (t) 2.1 (bd) 1.9	5 $4'_{ax}$, $9'_{ax}$ 5', 7'	-	2.1 1.9

	1.7 1.6 1.4 (bd)	10'$_{ax}$, 8'$_{ax}$,4,6' 1',3',3,10'$_{eq}$,8'$_{eq,}$ 4'$_{eq}$, 9'$_{eq}$		1.8

***Table 5.9*:** Chemical shifts observed in ^{13}C CP-MAS NMR spectra of DMPC bilayers with M2TM in absence and presence of *Amt* or *AK13* at 35°C and fully hydrated in phosphate buffer at pH 8.0.

Sample	C1	C2	C3	C1', C1''	C2', C2''	C3', C3''	C(4'-11'), C(4''-11'')	C12', C12''	C13', C13''	C14', C14''	$N(CH_3)_3$	C1'''	C2'''
DMPC	63.4	71.1	64.1	173.7	34.4	25.3	29.3-31.2	32.4	23.0	14.1	54.5	59.9	66.5
DMPC + M2TM (x=0.03)	63.3	71.0	64.0	173.7	34.3	25.2	28.7-31.3	32.2	22.8	13.9	54.5	59.8	66.5
DMPC + M2TM (x=0.06)	63.6	71.2	64.3	173.9	34.6	25.4	29.4-31.3	32.5	23.1	14.3	54.7	60.0	66.7
DMPC + M2TM (x=0.03) + Amt (x=0.05)	63.3	71.0	64.0	173.6	34.3	25.2	29.0-31.2	32.2	22.8	13.9	54.4	59.7	66.4
DMPC + M2TM (x=0.06) + Amt (x=0.08)	63.5	71.1	64.3	173.9	34.5	25.4	28.8-31.1	32.4	23.0	14.2	54.7	60.0	66.6
DMPC + M2TM (x=0.03) + AK13 (x=0.05)	63.6	71.2	64.2	173.9	34.5	25.4	29.3-31.4	32.4	23.0	14.1	54.7	60.0	66.6
DMPC + M2TM (x=0.06) + AK13 (x=0.08)	63.5	71.1	64.2	173.8	34.5	25.3	29.2-31.3	32.4	23.0	14.1	54.6	60.0	66.6

***Table 5.10*:** Values of d-spacing and peak width of the lowest order reflections $fwhm_q$ of SAXS and WAXS data of DMPC + M2TM (*x*=0.03) in absence and presence of *Amt* or *AK13* at concentration *x*=0.05 and DMPC + M2TM (*x*=0.06) in absence and presence of *Amt* or *AK13* at concentration *x*=0.08 at 20°C (*top panel*) and 30°C (*bottom panel*), fully hydrated in phosphate buffer at pH 8.0.

Sample	SAXS		WAXS	
20°C	**d-spacing (Å)**	**$fwhm_q$ (1/Å)**	**d-spacing (Å)**	**$fwhm_q$ (1/Å)**
DMPC + M2TM (x=0.03)	70.41(3)	0.221(7)	4.26(1)	5.706(94)
DMPC + M2TM (x=0.06)	67.12(2)	0.154(5)	4.26(1)	3.887(76)
DMPC + M2TM (x=0.03) + Amt (x=0.05)	68.12(5)	0.228(9)	no peak	no peak
DMPC + M2TM (x=0.06) + Amt (x=0.08)	68.38(4)	0.292(10)	4.27(1)	5.638(159)
DMPC + M2TM (x=0.03) + AK13 (x=0.05)	69.16(3)	0.204(6)	4.35(2)	5.392(112)
DMPC + M2TM (x=0.06) + AK13 (x=0.08)	66.81(2)	0.177(5)	4.28(1)	3.94(75)

Sample	SAXS		WAXS	
30°C	**d-spacing (Å)**	**fwhm$_q$ (1/Å)**	**d-spacing (Å)**	**fwhm$_q$ (1/Å)**
DMPC + M2TM (x=0.03)	64.36(3)	0.258(8)	4.46(5)	13.50(42)
DMPC + M2TM (x=0.06)	64.35(2)	0.199(5)	4.25(1)	9.79(15)
DMPC + M2TM (x=0.03) + Amt (x=0.05)	69.16(5)	0.239(6)	no peak	no peak
DMPC + M2TM (x=0.06) + Amt (x=0.08)	unilamellar bilayer	unilamellar bilayer	4.12(4)	17.43(47)
DMPC + M2TM (x=0.03) + AK13 (x=0.05)	64.5(6)	0.23(6)	4.46(6)	11.6(5)
DMPC + M2TM (x=0.06) + AK13 (x=0.08)	65.3(3)	0.211(8)	4.27(1)	12.35(24)

CHAPTER 6

Inhibitors of the M2 Proton Channel Engage and Disrupt Transmembrane Networks of Hydrogen-Bonded Waters

6.1 Introduction

Protein channels and water-filled pores present a particularly challenging target for drug design. Typically, drugs bind their targets at extended allosteric or substrate-binding sites, lined with multiple functional groups capable of forming numerous protein-small molecule interactions. Often structural and functional water molecules play critical roles in drug interactions. [105, 106] Water is also an important component in channels, but these proteins often have very constricted cavities with only sparse polar functionality available for drug design. The natural substrate in such cases can be as small as a single proton. Nevertheless, potent inhibitors of channels can still be achieved, possibly by targeting water molecules that serve to hydrate charged groups during ion conduction. Examples of this include channel-blockers such as the chloride channel blocker, picrotoxin, [258] or the adamantyl-amine class of influenza A virus matrix 2 (M2) proton channel inhibitors (see Figure 6.1). [12, 73] These compounds achieve high affinity, ligand efficiency, and biologically useful specificity, despite their relatively small size and low molecular weights (e.g., the M.W. of amantadine is 151 g/mol). Here we use X-ray crystallography to show the role of water in the binding and the mechanism of action of the adamantyl-amine class of M2 inhibitors. The hydrophobic groups of these molecules displace waters from the portion of the pore that faces the viral interior, while the drug's positively charged ammonium group locks into water networks that normally hydrate and stabilize protons as they diffuse through the pore. Intriguingly, the α-helical pore-lining carbonyl groups are physicochemical chameleons that are easily dehydrated to hydrophobically stabilize the binding of apolar groups from M2 inhibitors in the drug-bound form, and yet are also able to form stabilizing interactions with cations through water-mediated polar interactions in the drug-free form. We also elucidate several features of adamantane, which explain its increasingly successful use in drug design. [259]

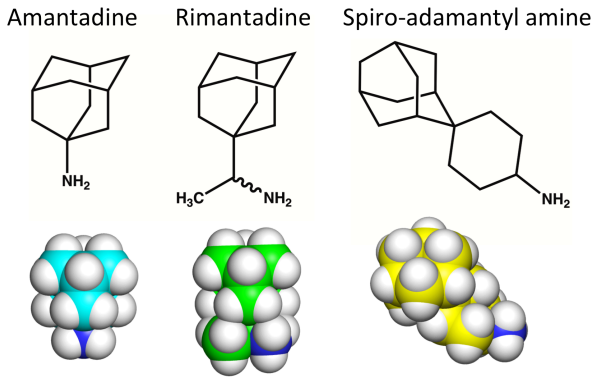

Figure 6.1: Chemical structures and space-filling models of amantadine (cyan), rimantadine (green), and spiro-adamantyl amine (yellow).

Influenza virus infections are perennial problems. The 2017-2018 influenza season is a timely reminder of the devastating impact of influenza: between October 1, 2017 and April 30, 2018, 30,451 laboratory-confirmed influenza-associated hospitalizations have been reported in the United States. [260] Moreover, 2018 marks the 100-year anniversary of the 1918 Spanish Flu, which infected an estimated one-third of the human population and killed approximately 50 million people. [261] In recent years, resistance to the adamantyl-amine class of drugs has become widespread, leaving the neuraminidase inhibitor oseltamivir (Tamiflu) as the sole orally bioavailable anti-influenza medication. [262] Thus, elucidating the structural mechanism of inhibition of adamantyl-amines has specific relevance to the design of new compounds to target drug-resistant influenza infections, as well as general relevance to the design of drugs that bind to the water-filled pores of channel proteins.

The M2 protein is a homotetrameric channel that serves several different functions during the life cycle of the virus, [17-21] which enters the cell via receptor-mediated endocytosis. The transmembrane (TM) domain (residues 23-46) transports protons from the low pH conditions of the endosome into the viral interior. The resulting drop in the intra-viral pH triggers the dissociation of viral ribonucleoproteins (RNPs) from the matrix 1 protein. [263] M2's extracellular domain (residues 1-22) aids incorporation of M2 into the virion, but this domain is absent in influenza B viruses. [25] An amphiphilic helix in the cytosolic tail of M2 (residues 46-60) assists viral budding and membrane scission, and a disordered domain at the C-terminus is involved in virus assembly through

interactions with M1. [263] The TM domain is the minimal construct needed for selective proton transport and amantadine binding. [29, 32-34] The rate of conductance of the M2 TM domain and its ability to be inhibited by amantadine are nearly identical to the full-length protein when the proteins are expressed in frog oocytes or reconstituted in phospholipid vesicles. [29, 35, 51] In fact, the conductance rate differences between different-length constructs (when expressed or reconstituted under identical conditions) are smaller than those seen between point mutants found in different strains of the virus. [264] Thus, much crystallographic work has focused on the TM domain, because the extra-membrane domains appear to impede crystallization.

The structure of M2 has been studied using solution NMR, solid state NMR (ssNMR), and X-ray crystallography. Two conformational states of the conductance domain have been observed, in which the C-terminus is either largely closed or open to the viral interior ($Inward_{closed}$ and $Inward_{open}$, respectively). In both states, His37 is directed towards the center of the channels, where it serves as a selectivity filter and proton shuttle that imbues M2 with its strong proton-selectivity. [23, 265] The $Inward_{closed}$ state has been characterized through solution NMR, [50, 89] ssNMR, [30, 90] and X-ray crystallography. [43] The $Inward_{open}$ state has been characterized primarily through X-ray crystallography, [34, 40, 41, 266] with conformational equilibria between the multiple states at low pH resulting in peak broadening in NMR studies. [50, 89, 91] The various crystallographic structures of the $Inward_{open}$ state are in good agreement with molecular dynamics simulations that quantitatively explain experimental conductance curves. [103] The conductance mechanism involves a transporter-like cycling between different protonation states and the two conformations. [107] Although the degree of protonation of His37 near the C-terminal region of the pore defines the stability of the $Inward_{open}$ and $Inward_{closed}$ states, the energetic difference between the two is not large, which assures dynamic switching between states during the transport mechanism. Thus, it is possible to isolate both conformational states in a variety of pH ranges using crystallography.

Previously, structure-based approaches have been used to inform the design of M2 inhibitors that are effective against wild type and amantadine-resistant strains

of the virus. [267-269] However, high-resolution structural studies of M2 bound to inhibitors, and with high enough resolution to examine the critical role of water in drug binding, have been lacking. The only previous drug-bound structures were obtained at relatively low resolution by solution or solid state NMR, [58, 76] and the sole crystal structure was solved at a diffraction limit of 3.5 Å. [34] These studies have been sufficient to locate the drug's general location, but not its engagement of the pore-lining residues and water molecules in the channel. Here, we report crystallographic structures of rimantadine bound to both the $Inward_{open}$ and $Inward_{closed}$ states of the wild-type (WT) M2 channel. We also determined structures of amantadine and a novel spiro-adamantyl amine inhibitor (see Figure 6.1) bound to the $Inward_{closed}$ states of WT M2 channel. These drug-bound structures describe the mechanism of binding and inhibition and inform the future design of drugs that interact with and disrupt the networks of hydrogen bonded waters that are widely utilized throughout nature to facilitate proton diffusion within proteins. [270]

6.2 Materials and methods

6.2.1 Structural biology and X-ray crystallography

The construct of M2 used in this study was Influenza A/Udorn/1972 M2 wild-type, residues 22-46. The peptide was chemically synthesized and purified as previously described, [40, 266] with acetylation of the N-terminus and amidation of the C-terminus:

Ace-SSDPLVVAASIIGILHLILWILDRL-NH2

The peptide sample was reconstituted into the lipid cubic phase (LCP) with some modifications to Caffrey and Cherezov's protocol. [102] Dry peptide was dissolved in ethanol and added directly to monoolein powder. Excess ethanol was blown off with nitrogen gas, and the sample was left under vacuum (<100 mTorr) overnight to remove the remaining solvent.

The drugs and inhibiting compounds used in this study were amantadine (1-adamantylamine HCl, Aldrich), rimantadine (1-(1-adamantyl)ethylamine HCl, Aldrich), and spiro adamantyl amine "Compound 9" from Wang et al. 2011. [94]

Amantadine, rimantadine, and spiro-adamantyl amine [94] were co-crystallized with M2TM (see Figure 6.2).

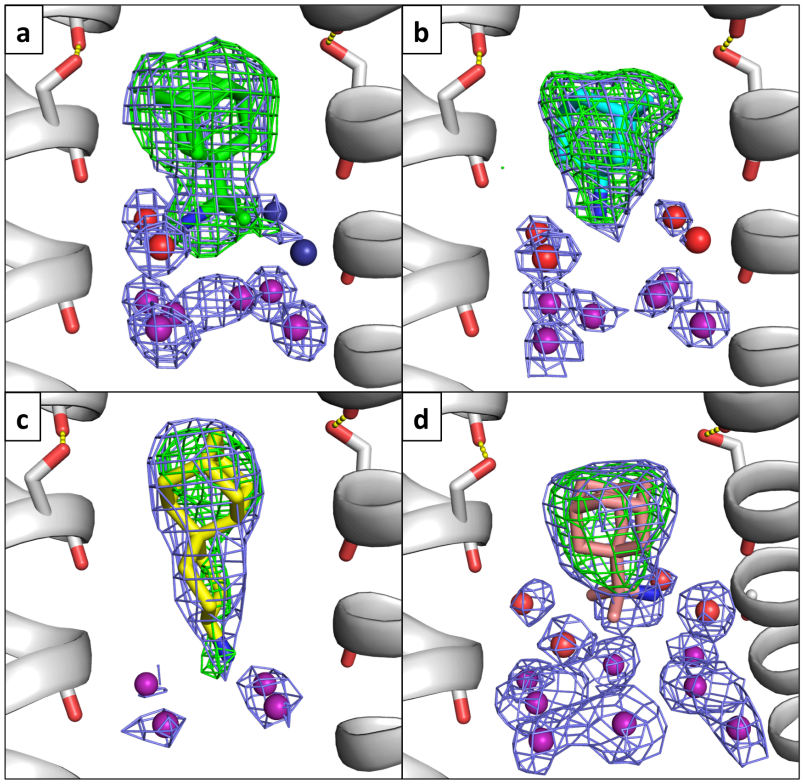

Figure 6.2: Electron density in channel pore above the gating His37 residues: blue mesh is 2Fo-Fc density shown at a contour of 1 σ, green mesh is a polder omit map [271] shown to a contour of 3 σ. Ala30 water layer is shown as red spheres, Gly34 water layer is shown as purple spheres. Partial occupancy waters are shown as dark blue spheres. The hydrogen bond between Ser31 and the Val27 carbonyl is shown. a. Rimantadine-bound $Inward_{closed}$ state (green, 6BKL, monomers F and H). b. Amantadine-bound $Inward_{closed}$ state (cyan, 6BKK, monomers B and D). c. Spiro-adamantyl amine-bound $Inward_{closed}$ state (yellow, 6BMZ, monomers B and D). d. Rimantadine-bound $Inward_{open}$ state (pink, 6BOC, monomers B and D). Note that, in the rimantadine-bound structures (a,d), the bound rimantadine has been modeled as a superposition of the R and S enantiomers. with both at half occupancy. In the rimantadine-bound $Inward_{closed}$ structure, two of the waters in the Ala30 layer have been also been modeled as half-occupancy due to steric clashes with the rimantadine methyl group. Also note the difference in the shape of 2Fo-Fc electron density corresponding to bridging waters in the Gly34 layer in the amantadine- and rimantadine- bound $Inward_{closed}$ state structures (a, b); these waters are two clearly defined spheres when amantadine binds to one of the tetramers (monomers A,B,C,D), though this density consists of just one water in the second tetramer within the asymmetric unit (monomers E,F,G,H); the bridging water density is elongated when

rimantadine binds. This is likely caused by a racemic mixture of rimantadine enantiomers resulting in two water structures that are averaged in the electron density.

Crystallization conditions were tested in plastic 96-well LCP trays (Laminex) using a LCP crystallization robot (TTP Labtech). Trays were screened using visible light and UV images (see Figure 6.3). Crystals were harvested from the 96-well sandwich trays then frozen in liquid nitrogen. Data were collected at Advanced Light Source (ALS) beam 8.3.1 at 100 K. Data collection, processing are presented in Table 6.2, model building, refinement in Table 6.3.

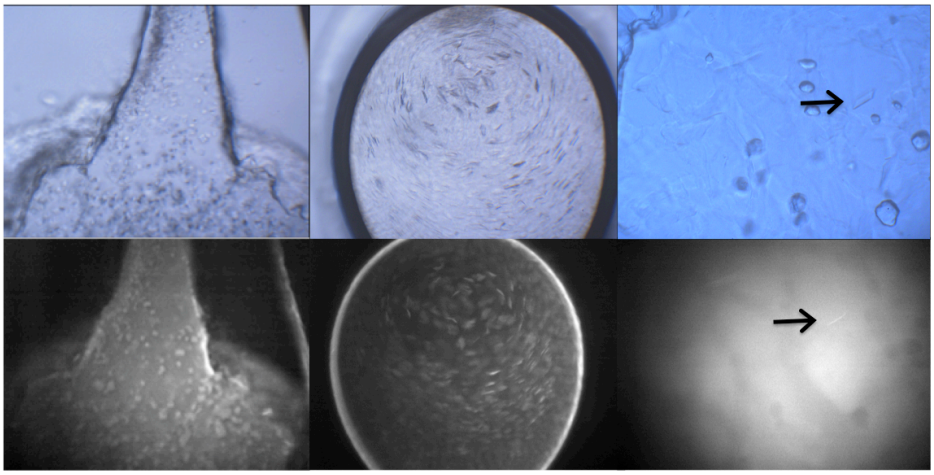

Figure 6.3: Visible light (top) and UV (bottom) images of M2 crystals. Square-shaped plates of M2TM bound to drugs and inhibitors form in the lipid cubic phase.

The lipid cubic phase was made by mixing 30 mg of peptide/monoolein sample with 20 µL of 50 mM detergent solution. The detergent used in this study was decyl maltose neopentyl glycol (DMNG, MW = 949.08); MNG detergents have been observed to stabilize membrane proteins for crystallization trials. [272, 273] DMNG detergent was synthesized by the Pil Seok Chae group (Hanyang University, Seoul, South Korea). In other crystallographic studies, Plastic 96-well LCP sandwich trays (Laminex, 200 micron base) containing drops of LCP plus precipitant solution were used to screen crystallization conditions using a LCP crystallization robot (TTP Labtech). Trays were screened using visible-light and

UV imaging. Crystals were harvested from 96-well trays and frozen in liquid nitrogen for transport and data collection.

The crystals formed by these conditions were thin, square-shaped plates. Though a detergent amphiphile was present in the crystallization conditions, the protein-containing lipid cubic phase remained separate from the precipitant solution and did not swell into the sponge phase. The crystallization conditions yielding the deposited PDB structures are as follows:

***6BKK*:** 100 nL LCP + 1 µL precipitant solution. LCP: 60 mg monoolein, 1.6 x 10^{-6} moles M2TM (EtOH stock), 6.4 x 10^{-6} amantadine (EtOH stock) (4:1 ratio of amantadine:M2 monomer); 40 µL of 50 mM DMNG detergent in water. Precipitant solution: 0.1 M NaCl, 0.02 M sodium citrate pH 5.6, 11% w/v PEG 3350. Crystals grew at 20 ˚C. Thin square plates formed after 9 months and grew to 100 µm in size.

***6BKL*:** 100 nL LCP + 0.5 µL precipitant solution. LCP: 60 mg monoolein, 1.6 x 10^{-6} moles M2TM (EtOH stock), 6.4 x 10^{-6} moles rimantadine (EtOH stock) (4:1 ratio of rimantadine:M2 monomer); 40 µL of 50 mM DMNG detergent in water. Precipitant solution: 0.2 M $MgCl_2$, 0.1 M sodium acetate / acetic acid pH 4.5, 20% w/v PEG 8000. Plates were incubated at 20 ˚C. Thin square plates formed after 1 month and grew to 75 µm in size.

***6BMZ*:** 100 nL LCP + 0.5 µL precipitant solution. LCP: 60 mg monoolein, 1.6 x 10^{-6} moles M2TM (EtOH stock), 6.4 x 10^{-6} moles spiro-adamantyl amine (EtOH stock) (4:1 ratio of inhibitor:M2 monomer); 40 µL of 50 mM DMNG detergent in water. Precipitant solution: 0.1 M HEPES pH 7.0, 30% v/v PEG 400. Plates were incubated at 20 ˚C. Thin square plates formed after 1 week and grew to 50 µm in size.

***6BOC*:** 100 nL LCP + 0.5 µL precipitant solution. LCP: 2.4 x 10^{-6} moles M2TM (EtOH stock), 9.6 x 10^{-6} moles rimantadine (EtOH stock) (4:1 ratio of rimantadine:M2 monomer); 40 µL of 50 mM DMNG detergent in water. Precipitant solution: 0.18 M LiSO4, 4% v/v (±)-1,3-butanediol, 0.09 M sodium citrate pH 3.5 (adjusted w/ HCl), 25.2% v/v PEG 400. Thin square plates formed after 2 weeks and grew to 300 µm in size.

Data were collected at Advanced Light Source (ALS) beam 8.3.1. 6BKK, 6BKL, and 6BMZ were collected using a Q315 detector. 6BOC was collected using a Pilatus 6M detector. Data collection parameters were as follows:

***6BKK*:** E = 11111 eV, d = 250 mm, oscillation = 1˚, t = 2 s, 115 frames.

***6BKL*:** E = 11111 eV, d = 250 mm, oscillation = 1˚, t = 1 s, 360 frames.

***6BMZ*:** E = 11111 eV, d = 350 mm, oscillation = 1˚, t = 1 s, 200 frames.

***6BOC*:** E = 11111 eV, d= 300 mm, oscillation = 0.7˚, t = 0.2 s, 300 frames.

Indexing and integration were carried out in MOSFLM, [274] and the data were scaled and merged using Aimless [275] in the CCP4 suite. [276, 277] Molecular replacement was done using Phaser [278] with previously solved structures as search models (3LBW [43] for the $Inward_{closed}$ state, 4QK7 [40] for the $Inward_{open}$ state). Zanuda [279] was used to aid in space group determination. Refinement was carried out in PHENIX, [280] with model building in Coot [281] and PyMOL. [282]

The tilts of amantadine and rimantadine adamantyl groups relative to the channel's central axis for structures 6BKK and 6BKL were calculated as the angle between two vectors: the channel central axis vector, and the adamantyl 3-fold axis vector. The channel central axis vector consists of the averaged Cα coordinates for all four monomers of the tetramer at two different residues, Leu26 and His37. The adamantyl 3-fold axis vector consists of the averaged coordinates of three symmetrically equivalent adamantyl carbons (atom names C2, C4, and C6 for amantadine, and atom names CG1, CG2, and CG3 for rimantadine), and the coordinates of an atom at the center of the 3-fold axis (atom name C10 for amantadine, and atom name CD for rimantadine).

Use of the LCP crystallization robot was made possible by National Center for Research Resources Grant 1S10RR027234-01. Beamline 8.3.1 at the Advanced Light Source is operated by the University of California Office of the President, Multicampus Research Programs and Initiatives grant MR-15-328599 and NIGMS grants P30 GM124169 and R01 GM124149.

6.2.2 Molecular dynamics

6.2.2.1 Protein setup and molecular dynamics simulations protocol

The $M2TM_{WT}$ complexes or $M2TM_{S31N}$ complexes were embedded in a POPC lipid bilayer extending 30 Å beyond the solutes. The number of lipids added were ~ 200. The bilayer was then solvated by a 30-Å-thick layer of waters. Na^+ and Cl^- ions were placed in the water phase to neutralize the systems and to reach the experimental salt concentration of 0.150 M NaCl. The total number was ~ 80000. Membrane creation and system solvation were conducted with the "System Builder" utility of Desmond. The OPLS 2005 force field [244-246] was used to model all protein and ligand interactions, and the TIP3P [199] model was used for water. The particle mesh Ewald method (PME) [205, 206] was employed to calculate long-range electrostatic interactions with a grid spacing of 0.8 Å. Van der Waals and short range electrostatic interactions were smoothly truncated at 9.0 Å. The Nosé-Hoover thermostat [248] was utilized to maintain a constant temperature in all simulations, and the Martyna-Tobias-Klein method [248] was used to control the pressure. Periodic boundary conditions were applied $(90\times90\times105)Å^3$. The equations of motion were integrated using the multistep RESPA integrator with an inner time step of 2 fs for bonded interactions and non-bonded interactions within a cutoff of 9 Å. An outer time step of 6.0 fs was used for non-bonded interactions beyond the cut-off. Each system was equilibrated in MD simulations with a modification of the default protocol provided in Desmond, which consists of a series of restrained minimizations and MD simulations designed to relax the system, while not deviating substantially from the initial coordinates. First, two rounds of steepest descent minimization were performed with a maximum of 2000 steps with harmonic restraints of 50 kcal mol^{-1} $Å^{-2}$ applied on all solute atoms, followed by 10000 steps of minimization without restraints. The first simulation was run for 200 ps at a temperature of 10 K in the NVT ensemble with solute heavy atoms restrained with a force constant of 50 kcal mol^{-1} $Å^{-2}$. The temperature was then raised during a 200 ps MD simulation to 310 K in the NVT ensemble with the force constant retained. The heating was followed by equilibration runs. First, two stages of NPT equilibration were performed, one with the heavy atoms of the system restrained for 1 ns and one for solvent and lipids for 10 ns, with a force constant of 10 kcal/mol/$Å^2$ for the

harmonic constraints, respectively. A NPT simulation followed with the C_α atoms restrained for 1ns with a force constant of 2 kcal/mol/Å^2. The above-mentioned equilibration was followed by a 250ns NPT simulation without restraints. Within this time, the total energy and the RMSD reached a plateau (see Figure 6.4), and the systems were considered equilibrated. For structural analyses, snapshots of the different systems were created with VMD [217] or Maestro [250] or Chimera [283]. Trajectories were analyzed with Maestro, Gromacs [196, 251], and VMD. Measures were done with Gromacs tools. For the calculation of hydrogen bonds, a cut-off angle of 30° deviation from 180° between the donor-hydrogen-acceptor atoms and a cut-off distance of 3.5 Å between the donor and acceptor atoms were applied.

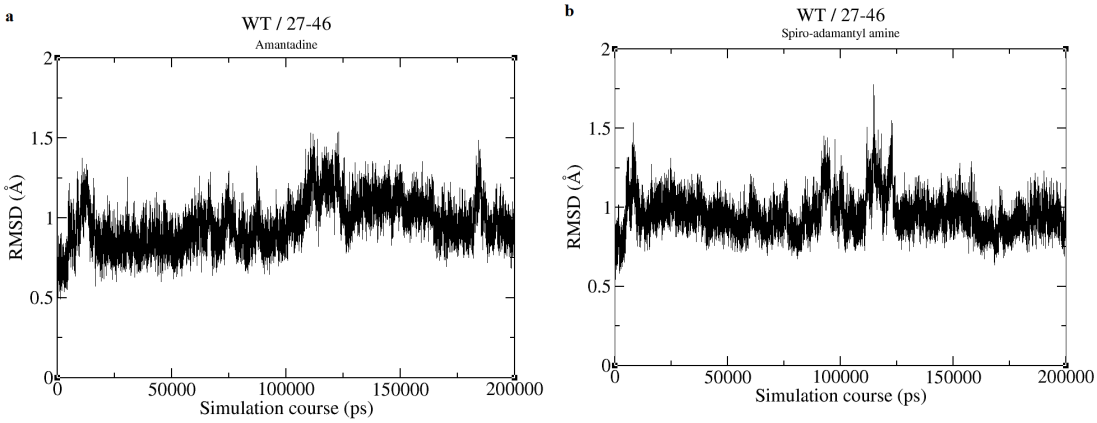

***Figure 6.4*:** Root-mean-square deviation (RMSD) for Cα atoms of M2TM relative to the initial structure for amantadine and spiro-adamantyl amine (PDB IDs: 6BKK and 6BMZ respectively) after root-mean-square fitting of Cα atoms of M2TM; in Å. The X-ray of the tetramer structure was maintained for all 200 ns of simulation time.

6.2.2.2 Molecular dynamics Analysis

We analyzed snapshots at 5 ps intervals of the 100 ns trajectory. Snapshots were aligned to the M2 crystal structure via CA atoms of residues 26-42.

Autocorrelation

Autocorrelation functions of Figure 6.5 were calculated by equation below

$$C(t) = (\langle A(0)A(t) \rangle - \langle A \rangle^2) / (\langle A^2 \rangle - \langle A \rangle^2)$$

where A is the variable of interest, and were fit to a mono- or bi-exponential decay function. For angular data, we fit the autocorrelation of the cosine of the angle.

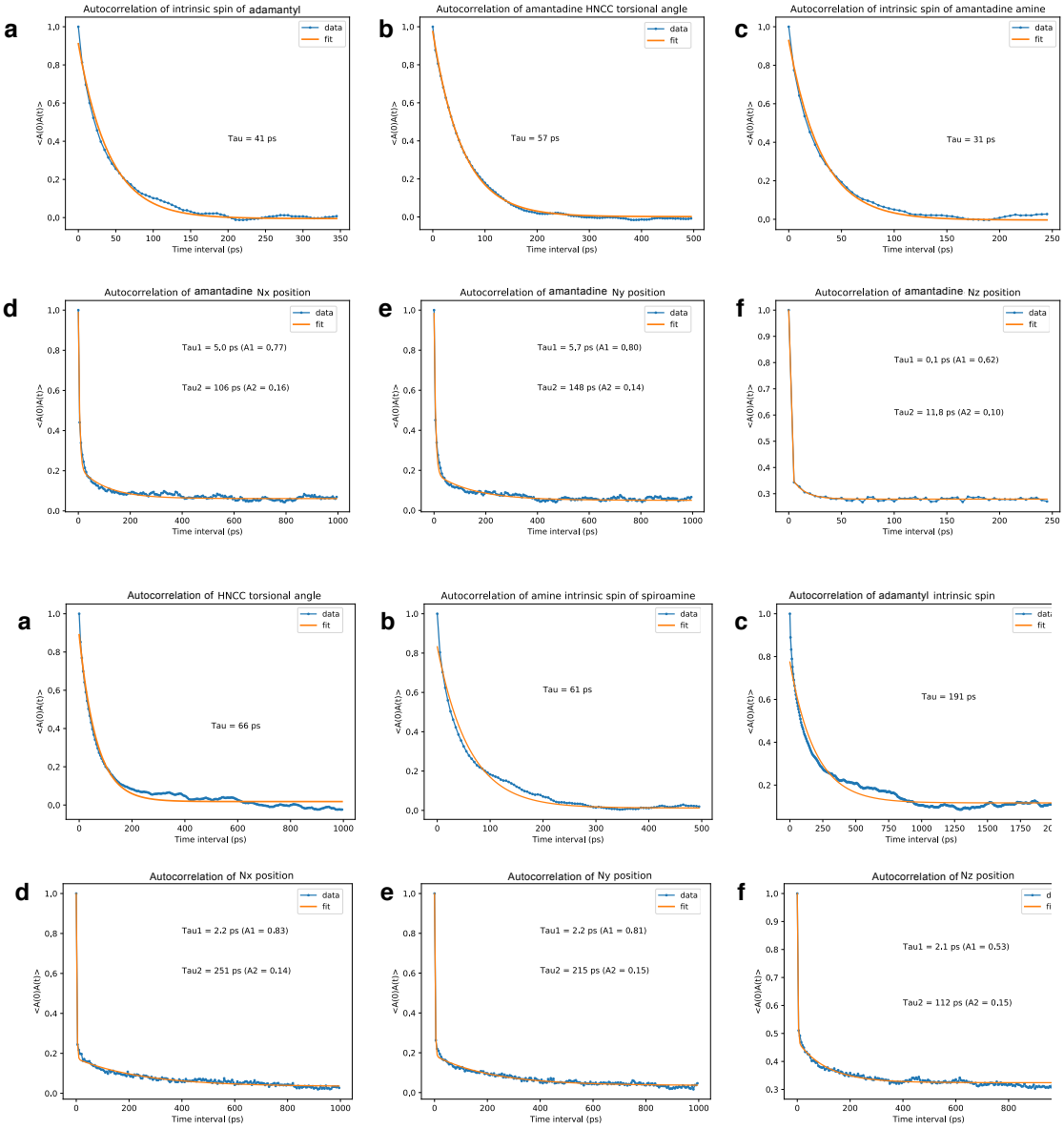

Figure 6.5: Autocorrelation of (A) amantadine rotation and spiro-adamantyl (B) amine rotation and displacement. Correlation decay times are labeled in the insets, with corresponding amplitudes for bi-exponential fits.

Intrinsic spin

Intrinsic spin was calculated by the following procedure: An internal reference frame of the drug was rotated about the X and Y axes of the bundle (see Figure 6.6). The intrinsic spin is the final rotation about the Z axis (long axis of the bundle) to align the drug internal reference frame with the reference frame of the bundle. For intrinsic spin of the amine, the internal reference frame was taken as the following (normalized) vectors:

Amine of amantadine:

origin = center of mass of amine hydrogens

z-axis = C1 – origin

x-axis = H1A – origin

y-axis = z $\otimes$ x

Amine of spiro-adamantyl amine:

origin = center of mass of amine hydrogens

z-axis = C10 – origin

x-axis = HN1 – origin

y-axis = z $\otimes$ x

Adamantane of amantadine:

origin = center of mass of C7, C8, C9

z-axis = N1 – origin

x-axis = C8 – origin

y-axis = z $\otimes$ x

Adamantane of Spiro-adamantyl amine:

origin = center of mass of C8, C10, C14, C15

z-axis = C4 – origin

x-axis = C8 – origin

y-axis = z $\otimes$ x

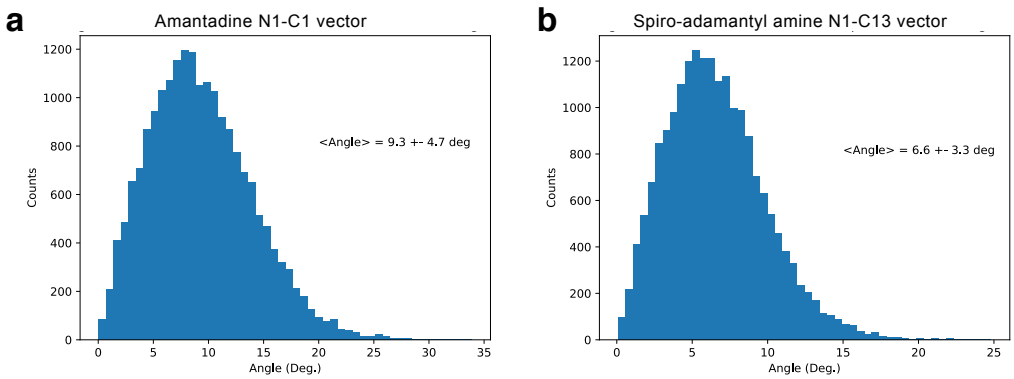

Figure 6.6: Histograms from 20,000 MD snapshots (5ps intervals) of tilt angle relative to bundle long axis.

Clustering of MD snapshots by amine position

After superposition of the snapshots onto the crystal structure as described above, we used a greedy clustering method (see Daura et al. [284]) to cluster the MD snapshots by position of the amine, including hydrogens. No further manipulation of the amine coordinates was taken. Atoms used in the RMSD calculation were C10, N1, HN1, HN1A, and HN1B for amantadine and C1, N1, H1A, H1B, and HIC for spiro-adamantyl amine. The amines were clustered with a 0.6 Å RMSD. At this cutoff, greater than 50% of the MD snapshots were placed into the top 2 (amantadine) or 3 (spiro-adamantyl amine) clusters. All permutations of the hydrogens were considered in the clustering. The positions of the waters from these top clusters are shown in the water density figures.

6.3 Results and discussion

The adamantane groups of rimantadine and amantadine disrupt networks of hydrogen bonded waters, while the ammonium group engages the remaining water networks in the $Inward_{closed}$ state

Using lipid cubic phase (LCP) crystallization techniques, [102] we have solved X-ray crystal structures of the M2 TM domain (residues 22-46) (M2TM) in the $Inward_{closed}$ state bound to rimantadine (PDB code 6BKL, 2.00 Å resolution) and amantadine (PDB code 6BKK, 2.00 Å resolution) at a resolution of 2.00 Å (see Figure 6.7a,b). In both structures, the electron density (see Figure 6.2)

unambiguously defines the positions of the drug and surrounding water molecules. Crystals containing drug-bound M2 complexes formed at acidic pH (pH 5.6 for amantadine-bound structure 6BKK, pH 4.5 for rimantadine-bound structure 6BKL). A DMNG detergent additive was used in crystallization trials to stabilize the $Inward_{closed}$ state. The binding of adamantane drugs also stabilizes this conformation and lowers the pKa of His37. [80]

A Polder omit map, [271] which is calculated by removing the drug and solvent from the model, shows good density for the drugs at a contour of 3 σ (see Figure 6.2, green mesh). For each complex, the hydrophobic adamantane moiety points upward towards the N-terminus on the exterior of the virus, while the ammonium group is directed downwards in the aqueous pore towards His37. The adamantane is bound in a predominantly hydrophobic pocket, lined by the sidechains and mainchains of Val27, Ala30, and Ser31. The hydroxyl of Ser31 forms an internal hydrogen bond to a mainchain carbonyl of Val27, increasing the effective hydrophobicity of the environment. Rimantadine is a racemic drug, and the ligand electron density strongly suggests that the bound drug consists of an equimolar mixture of both the R and S enantiomers, which were hence each modeled at half occupancy. Indeed, the two enantiomers have been shown to have equal potency in *in vitro* electrophysiology and cellular antiviral plaque assays. [285]

In previous high-resolution crystallographic and molecular dynamics investigations of M2's TM domain in the drug-free form, ordered waters form continuous hydrogen bonding networks that span the pore from the exterior vestibule near Val27 to His37. [40, 41] The carbonyl groups of Val27, Ala30, and Gly34 form hydrogen bonds to successive layers of waters. Additional "bridging" waters bridge the carbonyl-associated waters to form continuous hydrogen bonding networks from the Val27 to His37 (see Figure 6.7e). In both the amantadine- and rimantadine-bound structures, the adamantane cage fits snugly into the top of the pore, displacing the layer of waters near Val27 (see Figure 6.8a,d). Thus, the drug dehydrates the upper portion of the pore, snipping the continuous hydrogen bonding network seen in the drug-free state.

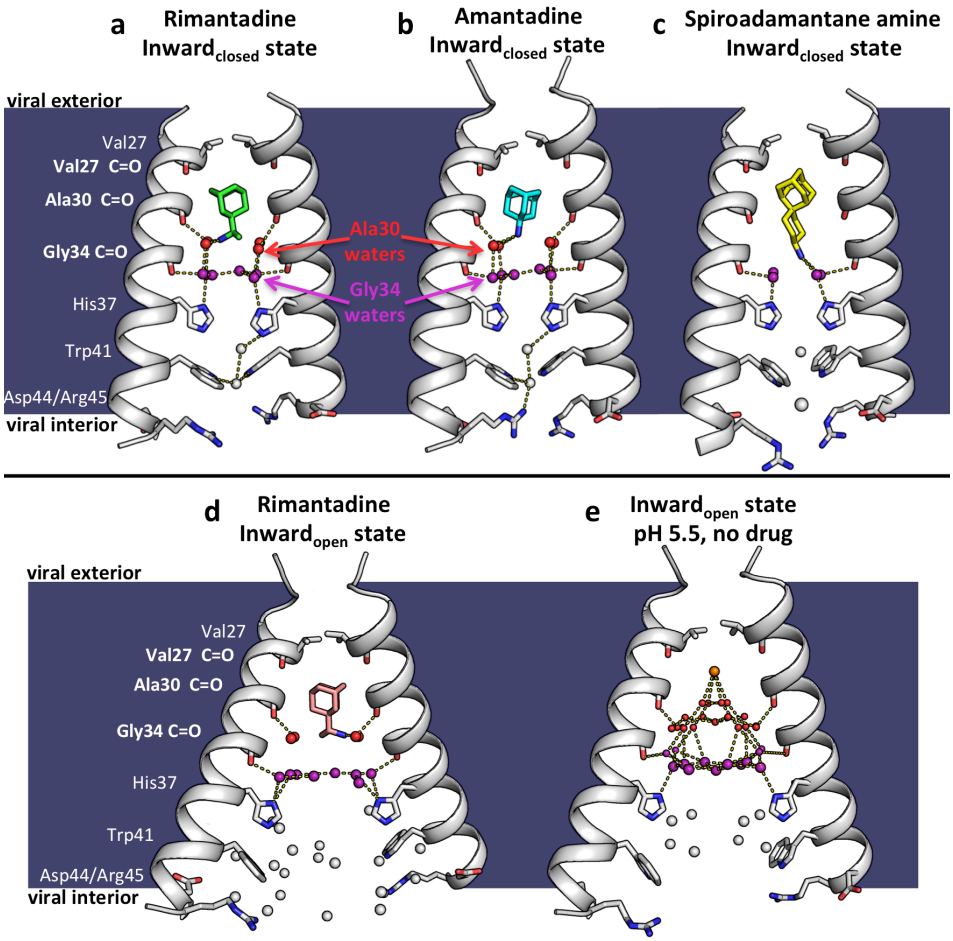

***Figure 6.7*:** X-ray crystal structures of the M2 proton channel bound to drugs and inhibitors. The channel is a homotetramer, but here the front and back monomers have been removed to show the contents of the channel pore. Hydrogen bonds are shown as yellow dashes. The layer of waters forming H-bonds to Ala30 carbonyls ("Ala30 layer") is shown as red spheres; the layer of waters forming H-bonds to Gly34 carbonyls ("Gly34 layer") is shown as purple spheres. Top, left to right: a. M2 bound to rimantadine in the Inward$_{closed}$ state; PDB code 6BKL, 2.00 Å resolution, monomer subunits F and H; b. M2 bound to amantadine in the Inward$_{closed}$ state; 6BKK, 2.00 Å resolution, monomers B and D; c. M2 bound to spiro-adamantyl amine in the Inward$_{closed}$ state; 6BMZ, 2.63 Å resolution, monomers B and D. Bottom, left to right: d. M2 bound to rimantadine in the Inward$_{open}$ state; 6BOC, 2.25 Å resolution, monomers B and D; e. Previously solved structure of M2 in the Inward$_{open}$ state at pH 5.0 in the absence of bound drug, [41] 5JOO, 1.41 Å resolution.

In contrast to the disruption of the waters adjacent to Val27, the lower two water layers remain similar to the drug-free state. [43] The ammonium group is positioned proximal to the four waters comprising the Ala30 layer (see Figure 6.8b,e), followed by the Gly34 water layer consisting of four carbonyl-associated

and two bridging water molecules (see Figure 6.8c,f). The B-factors of the waters bound directly to Ala30 and Gly34 backbone carbonyls are generally similar to those of the backbone atoms, indicating that they are tightly associated, while the bridging waters show greater disorder. The overall water arrangement is strikingly similar to that observed in the crystal structure of the $Inward_{closed}$ conformation of M2TM in the absence of drug (3LBW), indicating that the water structure that stabilizes the ammonium group is largely pre-organized. This same pathway would appear ideally oriented for stabilizing and facilitating proton transfer and diffusion through this region of the channel in the absence of inhibitor. This arrangement is also in good agreement with earlier MD simulations of the water in a model of the amantadine complex based on the structure of the drug-free structure (PDB: 3LBW). [43]

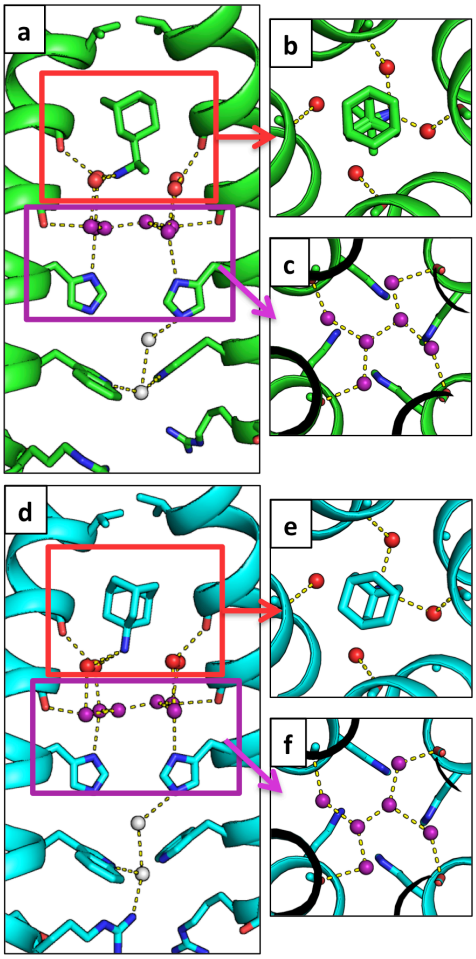

***Figure 6.8*:** Water-mediated hydrogen bonds facilitate the binding of rimantadine and amantadine to the M2 pore. In both the rimantadine-bound (6BKL, green) and amantadine-bound (6BKK, cyan) structures of the Inward$_{closed}$ conformation, the drug ammonium group is positioned to H-bond with two of the four waters in the Ala30 water layer, shown as red spheres. The Gly34 water layer is shown as purple spheres. H-bonds are shown as yellow dashes. Amantadine and rimantadine bind asymmetrically and form hydrogen bonds with two of the four waters in the top solvent layer. a,d: Side view of rimantadine (a, monomer subunits F and H) and amantadine (d, monomers B and D) binding. b,e: Top-down view of rimantadine (b, monomers E,F,G,H) and amantadine (e, monomers A,B,C,D) binding to the Ala30 water layer in the pore of the M2 channel. c,f: Top-down view of the Gly34 water layer.

While the overall structure of the tetramer and pore waters is largely symmetrical, the placement of the drug within the pore deviates slightly from four-fold rotational symmetry. The rimantadine- and amantadine-bound M2 crystals presented here belong to the $P2_1$ space group, with two crystallographically distinct tetramers per asymmetric unit. Both drugs adopt in similar asymmetric orientations in each of the two amantadine and rimantadine complexes. Their alkyl ammonium groups have three hydrogen-bond donating protons, which cannot form symmetrical interactions with each of the four Ala30 waters without breaking symmetry. Thus, the drugs tilt slightly within the site, displacing the ammonium group away from the central axis towards two of the Ala30 waters. The angle of tilt of the adamantyl 3-fold axis of symmetry relative to the channel's four-fold axis of symmetry is 11.3˚ ± 0.7 for the amantadine-bound structure and 11˚ ± 3 for the rimantadine bound structure, in good agreement with the value of 13˚ measured by SSNMR for amanatadine. [58]

The spiro-adamantyl amine inhibitor additionally displaces a second layer of water molecules in the Inward$_{closed}$ state

Spiro-adamantyl amine derivatives are excellent inhibitors of the wild-type M2 channel and also the V27A drug-resistant mutants as assessed by antiviral plaque assay and electrophysiological assays. [94, 286] Moreover, these compounds have also been shown to rescue mice from lethal influenza infection. [287] The more extended scaffold of the spiro-adamantyl amine (see Figure 6.1) was designed to exclude more water from the channel and to bind with their

ammonium groups deeper in the wild-type channel relative to the ammonium position of amantadine. [94] The X-ray crystal structure of spiro-adamantyl amine bound to the $Inward_{closed}$ conformation (see Figure 6.7c) solved here at a resolution of 2.63 Å (PDB code 6BMZ) shows that the drug indeed projects more deeply into the channel. The longer spiro-adamantyl amine compound displaces the waters of the Ala30 water layer (see Figure 6.9a,b) previously observed in the amantadine- and rimantadine-bound structures, and the ammonium group of the spiro-adamantyl amine is positioned to form H-bonds with the four carbonyl-associated waters in the Gly34 solvent layer.

Interestingly, the adamantane groups are oriented differently in the channel in the spiro-adamantyl amine versus the amantadine and rimantadine complexes. The adamantyl group projects one of its methylene groups along its own pseudo- two-fold symmetry axis towards the top of the channel in the spiro-adamantyl amine complex. By contrast, a tertiary center along the three-fold axis of adamantane projects upward in the amantadine and rimantadine complexes (see Figure 6.9a-c). This result highlights the near-spherical nature of the adamantane group and helps explain its versatility in drug design. [259]

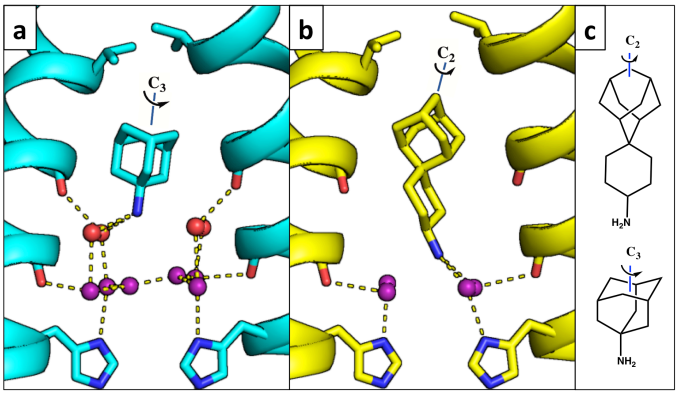

Figure 6.9: Binding of spiro-adamantyl amine to the $Inward_{closed}$ state. Hydrogen bonds are shown as yellow dashes. a,b: Side view of (*a*) amantadine-bound $Inward_{closed}$ M2 structure (6BKK, cyan, monomers B and D) and (*b*) the spiro-adamantyl amine-bound $Inward_{closed}$ M2 structure (6BMZ, yellow, monomers B and D). The spiro-adamantyl amine inhibitor binds with its ammonium group deeper in the channel. The Ala30 water layer (red) is completely displaced, and the inhibitor ammonium group is within H-bonding distance of the Gly34 water layer (purple). (*c*) Chemical structures of spiro-adamantyl amine (top) and amantadine (bottom), showing adamantyl C2 and C3 symmetry axes.

Structure of rimantadine bound to M2 in the Inward$_{open}$ state

Effective blockers of M2 inhibit proton conductance at both high and low pH with the same or only slight reductions in potency (less than two-fold) at lower pH. [29, 73] This versatility is likely an important property for drugs that need to remain bound as the pH of the endosome decreases prior to fusion of the viral and endosomal membranes. Nevertheless, this finding runs contrary to early biophysical studies, which appeared to show that amantadine bound the channel only under conditions in which the His residues are in the neutral state [33, 57] and that the amantadine dissociated at lower pH. However, these early studies focused on spectroscopic signatures of only the Inward$_{closed}$ state suggesting that the drug must also bind to another conformational form at low pH. Thus, it was important to determine structures of drugs bound to the Inward$_{open}$ state in addition to the Inward$_{closed}$ conformational state.

We solved the structure of rimantadine bound to the Inward$_{open}$ state of the M2 channel (see Figure 6.7d) to a resolution of 2.25 Å (PDB code 5BOC). The helices, which bend slightly at Gly34 in the Inward$_{closed}$ rimantadine complex (see Figure 6.7a), straighten in the Inward$_{open}$ rimantadine complex. This conformational change increases the diameter of the bottom of the channel while slightly constricting the upper portion of the channel. The newly solved structure of rimantadine bound to the Inward$_{open}$ state is in good agreement with a previously solved low-resolution (3.5 Å) structure of the Inward$_{open}$ amantadine complex (3C9J) [34] (Cα RMSD = 0.98 Å). The adamantane drugs are observed to bind to the same position in both structures (see Figure 6.10). However, the water molecules, which were not resolved in the low-resolution amantadine complex (3C9J), are now well defined in the current rimantadine complex (5BOC).

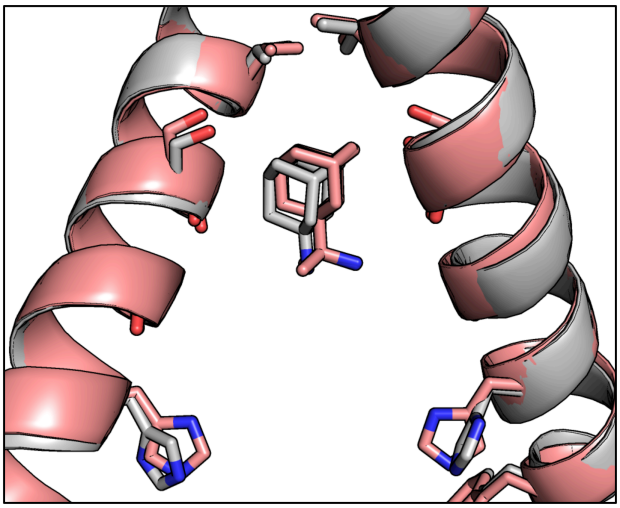

Figure 6.10: Aligned rimantadine-bound $Inward_{open}$ (6BOC, pink) and amantadine-bound $Inward_{open}$ (3C9J, gray) structures. The position of the bound rimantadine group is in good agreement with the previously observed binding position of amantadine. Note that the His37 rotamers in structure 3C9J are not meaningfully different, as these side chains were fit to 3.5 Å resolution electron density.

Hydrogen-bonded networks of water molecules play a similar role in stabilizing the $Inward_{open}$ and $Inward_{closed}$ rimantadine complexes (see Figure 6.7a,d). In both complexes, the ammonium group is proximal to the four Ala30 carbonyl-associated water molecules, and the Gly34 waters are retained. However, the increased radius of the channel near the C-terminus of the $Inward_{open}$ complex leads to an increase in the number of the bridging waters in the Gly34 layer, and a progressive opening of a channel from His37 downward. The structures of the $Inward_{open}$ and $Inward_{closed}$ complexes are consistent with the known pH-independent binding of the drugs to the channel, which now can be understood in terms of the affinity of the individual conformational forms for drugs at a given pH (see Figure 6.11). The $Inward_{closed}$ drug-bound conformation is stable at high pH where the overall charge on His37 is 0 or at most +1. At lower pH, His37 residues are protonated, leading to repulsion between the imidazolium cations as well as the ammonium group of the drug in the highly restricted environment of the channel. However, at low pH, charge repulsions between protonated His37 groups as well as their interaction with the drug ammonium group would be more easily electrostatically screened in the solvent-exposed end of the $Inward_{closed}$ conformation. Also, water molecules are well suited to stabilizing charge changes

by switching back and forth from donors to acceptors. Thus, the structures of the $Inward_{open}$ and $Inward_{closed}$ complexes explain how the drugs can inhibit over a wide range of pH with similar affinity. [29, 73]

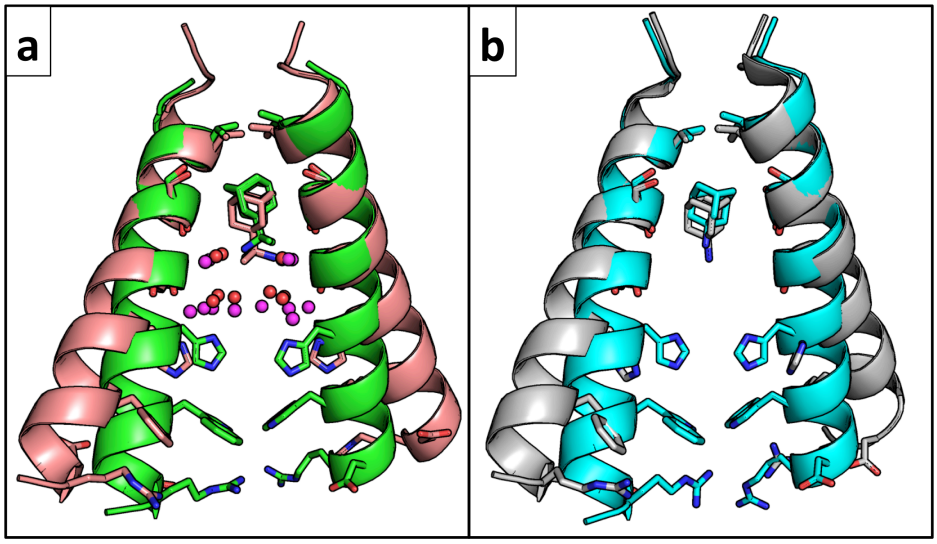

Figure 6.11: Alignment of $Inward_{open}$ and $Inward_{closed}$ structures showing amantadine and rimantadine binding. (*a*) Rimantadine-bound $Inward_{open}$ (6BOC. pink with waters shown as magenta spheres) and $Inward_{closed}$ (6BKL, green with waters shown as red spheres) structures. (*b*) Previously solved amantadine-bound $Inward_{open}$ (3C9J, gray) [34] and $Inward_{closed}$ (6BKK, cyan) structures. In the $Inward_{open}$ conformation, the adamantane drugs bind slightly deeper in the channel pore.

Structural mechanism of drug-binding and channel inhibition

The binding of the adamantane drugs to M2 presents particularly interesting problems for understanding the mechanism of drug action against channels in general as well as the design of drugs to address drug resistance in strains of M2 in particular. We hypothesize that amantadine acts as a *mechanism-based inhibitor*. The amantadine ammonium group exploits the channel's essential capability of stabilizing an excess hydrated proton. Thus, the ammonium groups do not form H-bonds with pore-facing carbonyl groups; instead they are hydronium mimics that interact with functional water networks connected directly to the proton-shuttling and gating residue, His37. This hypothesis is consistent with the fact that replacing the ammonium group of amantadine with hydroxyl strongly decreases antiviral activity. [288] Moreover, the large adamantane

displaces loosely bound waters near the top of the pore, thereby stabilizing the complex through hydrophobic van der Waals interactions, while also inhibiting conduction by occluding entry of protons into the pore. The more extended spiro-adamantyl amine places its ammonium group further down the channel into a lower site lined by four water molecules that simultaneously receive hydrogen bonds from both the carbonyl of Gly34 and the imidazole of His37.

Interestingly, our structures show that the pore-lining carbonyl groups act as physicochemical chameleons that stabilize hydrated cations through polar interactions in some complexes (e.g. the Ala30 carbonyls in structures 6BKL, 6BKK), but hydrophobically stabilize apolar aliphatic groups in others (e.g. the Ala30 carbonyls in structure 6BMZ). This behavior is consistent with the known tendency of the carbonyl groups of helices to form a single strong helical hydrogen bond with an amide at position *i-4* when in the hydrophobic core of a protein, but to form an additional hydrogen bond to water molecules when exposed to water. [289] The ability to switch between these two states offers intriguing and potentially generalizable possibilities for small molecule drug design.

Explaining the effectiveness of adamantane as a substituent for drug design

Adamantane derivatives are commonly used in drugs that treat influenza (amantadine, rimantadine), Alzheimer's disease (memantine), and diabetes (saxagliptin, vildagliptin), among other uses. [259, 290] The adamantyl group has been referred to as a "liphophilic bullet" [259] that can be added onto drugs to increase their hydrophobicity and structural stability. The adamantane drugs are hydrophobic, though less so than one would expect based on the number of carbons they contain. Adamantane has ten carbons contained within four inter-connected cyclohexane rings that form a cage with a greatly reduced apolar surface area when compared to the corresponding unbranched alkane. In fact, the hydrophobicity of adamantane (LogP = 3.98) is far smaller than that of n-decane (LogP = 5.98), and instead is similar to n-hexane (LogP = 3.87). [291] The decreased hydrophobicity of adamantane is a simple consequence of its highly compact, highly cross-linked structure. For example, the solvent

accessible surface area of adamantane is 262 $Å^2$ while that of n-decane in an extended conformation 361 $Å^2$.

A second attractive feature of adamantane is that it has no rotatable bonds and hence it loses very little conformational entropy when it binds into a protein pocket. By comparison, an alkane of similar hydrophobicity such as n-pentane could lose up to 2.6 kcal/mol ($\Delta S = 4 \times RT \ln(3)$) associated with the three rotamers of each of its four rotatable bonds) when immobilized in a receptor-binding site. Moreover, adamantane has a very smooth surface (see Figure 6.1), which allows it to rotate extremely rapidly about its C3 axis, even in the crystalline state at room temperature. [292] Due to this rapid rotational averaging adamantane effectively has a smooth ellipsoidal shape with a round cross-section that belies its jagged appearance when drawn as a stick figure in two dimensions. Thus, the apparent mismatch between the C3 structural symmetry of amantadine and the M2 tetramer is an artifact of considering the complex as a static object. The smooth cross-section of the adamantane ring also assures a low torsional barrier for rotation of the amantadine C1-N bond, which again contributes to minimal loss in configurational entropy of binding. In summary, adamantane is a highly rigid group with a hydrophobicity similar to n-hexane, which can contribute to binding with a greatly lower conformational entropy loss than an unbranched alkane.

Molecular dynamics confirm the structural mechanism of drug binding and inhibition

To test and further refine these conclusions we turned to all-atom molecular dynamics simulations of the M2 channel in a POPC (200 lipid molecules) bilayer (see Methods). We examined the amantadine and spiro-adamantyl amine complexes in the neutral $Inward_{closed}$ conformation to allow a comparison of the two distinct drug classes in the same conformation of the channel. The simulated complexes were structurally stable and showed no large conformational changes over 200 nsec (Cα RMSD to the crystallographic structures $\leq$ 1 Å, Table 6.1, Figure 6.3). In accord with SSNMR measurements, [58] amantadine undergoes rapid rotation about its major axis (correlation, t_c = 40 psec) (see Figure 6.4). Torsional averaging about the C1-NH_2 bond of the drug also occurs with t_c = 30

psec. Also in agreement with ssNMR, the main axis of the drug undergoes rapid motion within a cone (mean tilt = 9 ± 5°, Figure 6.5) rather than being fixed in one single orientation. Thus, the fixed asymmetric orientation seen in the cryo-cooled crystal structure represents a single snapshot of the time-averaged structure seen by SSNMR and MD simulations.

Table 6.1: Structural and dynamic measures from 250 ns MD trajectories of M2TM-ligand complexes in POPC bilayer at high pH.

	RMSD				
Ligand	**(Cα 27-46) [1]**	**Achain (Cα 27-46) [2]**	**Bchain (27-46) [3]**	**Cchain (27-46) [4]**	**Dchain (27-46) [5]**
Amt	0.90 ± 0.2	0.76 ± 0.1	0.75 ± 0.1	0.64 ± 0.1	0.62 ± 0.1
Rim-R	0.97 ± 0.2	0.60 ± 0.1	0.53 ± 0.1	0.66 ± 0.1	1.03 ± 0.2
Rim-S	0.77 ± 0.2	0.61 ± 0.1	0.56 ± 0.1	0.64 ± 0.1	0.55 ± 0.1
Spiro-adamantyl amine	0.96 ± 0.2	0.60 ± 0.1	0.62 ± 0.1	0.58 ± 0.1	0.93 ± 0.2

Ligand	**Ligand tilt**	**V27-Ad [8]**	**A30-Ad [9]**	**G34-Ad [10]**	**H-bonds [11]**	**Cl-N distance [12]**
Amt	11.5 ± 6.1 [6]	4.5 ± 0.3	0.7 ± 0.3	5.2 ± 0.3	2.8 ± 0.4	51.0 ± 10.7
Rim-R	21.7 ± 7.7 [6]	4.2 ± 0.3	1.1 ± 0.3	5.7 ± 0.3	3.0 ± 1.1	47.2 ± 10.1
Rim-S	17.4 ± 5.7 [6]	4.3 ± 0.3	1.0 ± 0.3	5.5 ± 0.3	2.9 ± 1.1	47.1 ± 10.4
Spiro-adamantyl amine	8.2 ± 4.1 [7]	4.3 ± 0.3	1.0 ± 0.3	5.4 ± 0.3	2.7 ± 0.5	49.0 ± 10.6

[1] Root-mean-square deviation (RMSD) for Cα atoms of M2TM tetramer, residues 27-46, relative to the initial structure (PDB entry: 5TP7, 5TP8, 6BMZ respectively) after root-mean-square fitting of Cα atoms; in Å.

[2-5] Root-mean-square deviation (RMSD) for Cα atoms of M2TM helix A-D, residues 27-46, relative to the initial structure (PDB entry: 5TP7, 5TP8, 6BMZ respectively) after root-mean-square fitting of Cα atoms; in Å.

[6] Angle between the adamantane C3 symmetry axis vector and the normal to the membrane; in degrees.

[7] Angle between the adamantane C2 symmetry axis vector and the normal to the membrane; in degrees.

[8] Mean distance between center of mass of V27 and centers of mass of adamantane calculated using Gromacs tools; in Å.

[9] Mean distance between center of mass of A30 and centers of mass of adamantane calculated using Gromacs tools; in Å.

[10] Mean distance between center of mass of G34 and centers of mass of adamantane calculated using Gromacs tools; in Å.

[11] Mean number of H-bonds between ligand's ammonium group and waters.

[12] Mean distance in Å between the ligand N and the nearest Cl^-.

Although the water molecules undergo rapid motions in the channel, their average positions are in excellent (< 1 Å) agreement with the positions seen in the crystal structure of the corresponding amantadine complex. As in the crystallographic structure, the waters form tight clusters within hydrogen-bonding distance of the Ala30 and Gly34 carbonyls, with more diffuse density in the region bridging between the four Gly34 waters (see Figures. 6.2 and 6.12).

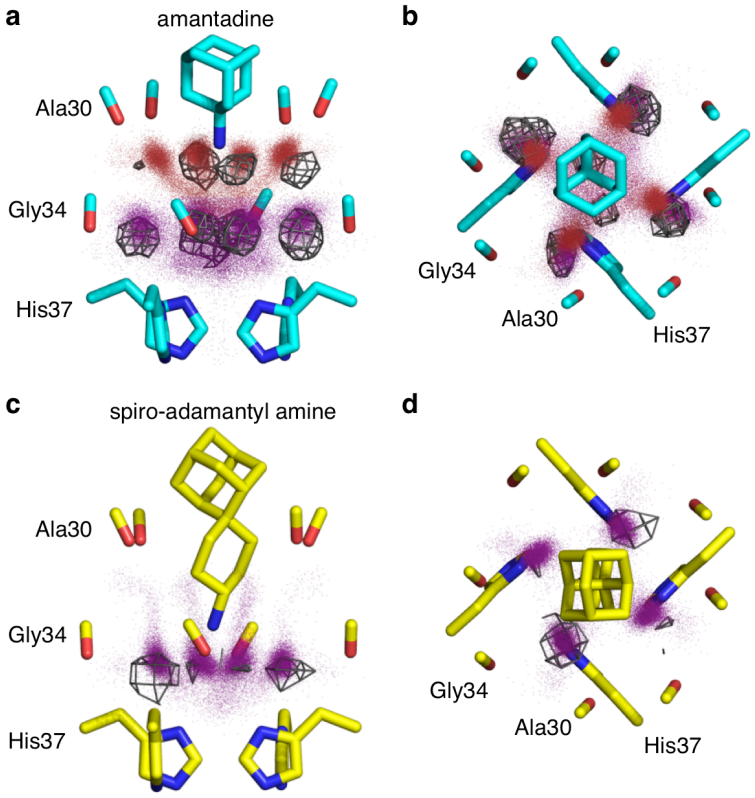

Figure 6.12: Molecular dynamics simulations reproduce the positions of the crystallographic waters. X-ray crystal structures are shown as sticks. Red and purple dots are water oxygen positions from 20,000 MD simulations snapshots of the largest amine clusters. Gray wireframe

shows 1σ contours of water electron density from the X-ray crystal structure. a,c: Side views. b,d: Top views. See supplement for details of the simulations and treatment of the data.

Examination of the probability density function for the amine-water interaction (see Figure 6.13), showed that, on average, three to four waters are within hydrogen-bonding distance of the amine, and that other features of the water are in quantitative agreement with the crystallographic structure. In summary, the MD simulations of the amantadine $Inward_{closed}$ complex are in excellent agreement with experimental results and confirm the expectation that the complex is entropically stabilized by rapid axial rotation and torsional motions of the bound amantadine.

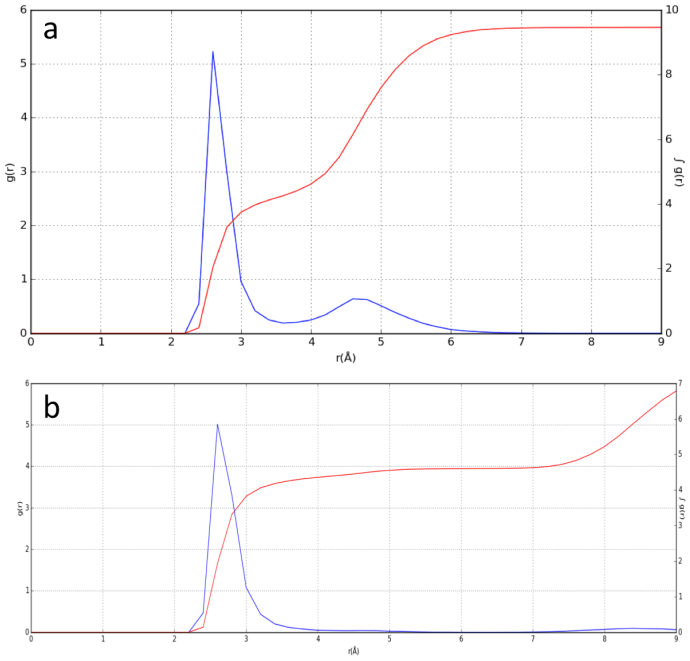

Figure 6.13: (*a*) Radial distribution function (RDF) between amantadine amino group and water oxygen atoms, extracted from a 200 ns simulation. a. The RDF g(r) function (right axis) shows a strong peak near 2.7 Å, associated with waters forming hydrogen bonds to the ammonium group. The cumulative integrated intensity (Sg(r), right axis) indicates that 3.5 to 4 waters are associated with the ammonium, on average. The second broad peak near 4.8 Å represents the bridging and Gly34 waters, and integrate to approximately five to six waters, in good agreement with the crystallographic structure. (*b*) RDF between Spiro-adamantyl amine amino group and water oxygens, extracted from a 200 ns simulation. Four waters are observed associated with the ammonium group, in agreement with the crystal structure. The second peak near 8 Å reflect more distant waters between His37 and Trp41 of the channel.

Simulations of the spiro-adamantyl amine complex were similarly in good agreement with ssNMR [94] and the crystallographic structures. The drug undergoes rapid rigid-body and torsional rotations about its pseudo-C2 axis (t_c = 190 and 70 psec, respectively) (see Figure 6.5), similar to the rotation of amantadine about its C3 axis. The water density obtained from the ensemble-averaged structures also matches the crystallographic structure (see Figures 6.2, 6.12), with dense clusters of water seen near the carbonyls of Gly34. Throughout the simulations of both M2 bound to amantadine and M2 bound to the spiro-adamantyl amine, the ammonium group remained near the center of the channel, within 1 Å of its position in the starting crystallographic structures (see Figure 6.14).

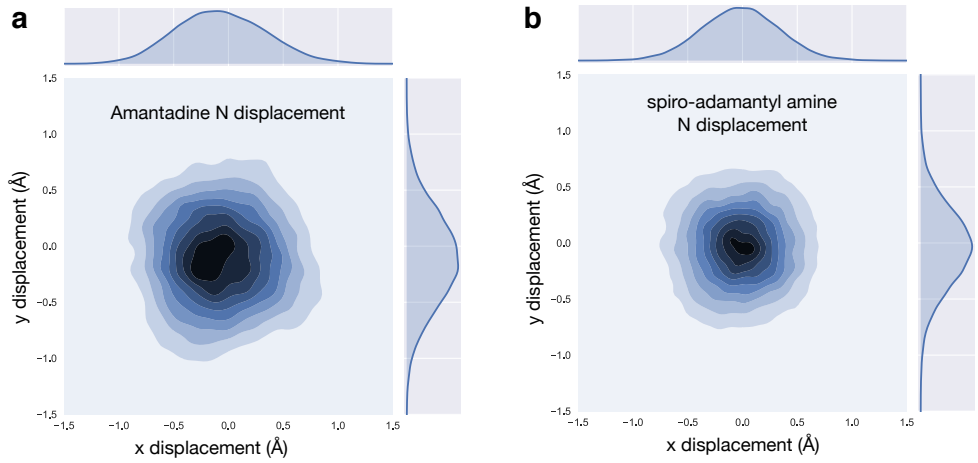

***Figure 6.14*:** Kernel density estimate (KDE) of the amine N displacement of amantadine (a) and spiro-adamantyl amine (b) in the x-y plane (orthogonal to bundle long-axis). Darker shading means higher density, e.g., near (-0.3, -0.3) in (a) showing the amine N spends a substantial amount of time off-center. KDEs are derived from 20,000 snapshots (5 ps intervals) of a molecular dynamics simulation.

6.4 Conclusions

Implications for the design of drugs that target influenza A virus

M2 undergoes changes in conformation and the protonation state of the gating His37 tetrad as the pH of the endosome gradually decreases. Thus, a successful drug must inhibit the channel over a wide range of pH and conformational states.

If drugs such as amantadine and rimantadine bound exclusively to the $Inward_{closed}$ state, then one would expect that the drug would dissociate as the pH was lowered below the pKa of the His37 residues (Ie Chatlier's principle). However, the affinity of amantadine is relatively invariant with pH between neutral pH and acidic endosomal pH, as assessed by electrophysiological measurements at pH as low as 5.5. [29, 73] It was therefore important to define the mode of inhibition of drugs when bound to the $Inward_{open}$ form of the channel, which is the more stable form in native membranes at low pH. [107] The crystal structures shown here define similar modes of drug binding in both forms, with the ammonium group engaged in hydrogen bonds with ordered waters lower in the channel and the adamantane cage displacing water from the hydrophobic region near Val27. Thus, the ability of drugs to bind over a range of pH and conformational states appears to be important for viral inhibition. Along these lines, it is noteworthy that a series of inhibitors that appear to bind the S31N variant of M2's TM domain exclusively in the $Inward_{open}$ state (with a straight helix lacking the kink that allows formation of the inwardly closed state) are very weak inhibitors of this protein's proton channel activity, and they are also inactive in antiviral assays. [176]

The structures presented here should also inform the design of compounds that inhibit M2 mutants from amantadine- and rimantadine-resistant forms of the virus. These mutants cluster in the upper portion of the channel between residues 26-31, disrupting the hydrophobic adamantane-binding site, while the pore-lining residues that are important for water-mediated conduction (Ala30, Gly34, His37) remain unchanged in more than 99% of the virus identified in humans, pigs and animals to date. [293] Here, we show that inhibitors can be designed by either hydrogen-bonding to the Ala30-associated waters in the amantadine and rimantadine complexes, or by displacing these same water molecules in the spiro-adamantyl amine complex. The structures presented here will provide critical information to aid in the design of inhibitors that also displace waters that associate with the absolutely conserved His37 imidazole and Gly34 carbonyls. Such compounds might be able to bind lower in the channel, avoiding the more resistance-prone upper region of the pore altogether.

***Table 6.2*:** Data processing statistics for M2 bound to amantadine (6BKK), rimantadine (6BKL), and spiro-adamantyl amine (6BMZ) in the $Inward_{closed}$ conformation, and M2 bound to rimantadine (6BOC) in the $Inward_{open}$ conformation. Data processing was carried out in Aimless, [275] with space group validation in Zanuda. [279]

Structure	**6BKK**	**6BKL**	**6BMZ**	**6BOC**
Space group	$P2_1$	$P2_1$	$P2_12_12_1$	P2
Cell dimensions (Å)				
a,b,c (Å)	44.22, 52.05, 48.72	36.46, 47.84, 48.53	49.62, 72.59, 99.25	34.05, 34.02, 72.09
	90.00, 108.2, 90.00	90.00, 96.76, 90.00	90.00, 90.00, 90.00	90.00, 90.23, 90.00
Resolution (Å)	52.05 - 2.00 (2.05 - 2.00)	48.19 - 2.00 (2.05 - 2.00)	72.59 - 2.63 (2.76 - 2.63)	36.04 - 2.25 (2.32 - 2.25)
Completeness (%)	93.5 (88.8)	93.3 (90.8)	99.3 (98.9)	98.3 (96.3)
Number of unique reflections	13454 (942)	10589 (754)	11007 (1442)	7894 (695)
Average redundancy	2.2 (2.1)	4.8 (4.5)	7.0 (6.9)	3.2 (3.3)
Rmerge	0.164 (0.808)	0.114 (0.348)	0.154 (0.608)	0.203 (0.463)
CC(1/2)	0.974 (0.508)	0.994 (0.959)	0.997 (0.920)	0.957 (0.791)
Average I/sigI	4.6 (2.2)	7.1 (2.9)	8.7 (3.0)	4.2 (2.1)

***Table 6.3*:** Refinement statistics for M2 bound to amantadine (6BKK), rimantadine (6BKL), and spiro-adamantyl amine (6BMZ) in the $Inward_{closed}$ conformation, and M2 bound to rimantadine in the $Inward_{open}$ conformation (6BOC). Refinement was carried out in PHENIX.refine [280] with model-building in Coot [281] and PyMOL. [282]

Structure	**6BKK**	**6BKL**	**6BMZ**	**6BOC**
Resolution (Å)	46.29 - 1.995 (2.066 - 1.995)	48.19 - 1.995 (2.066 - 1.995)	44.38 - 2.634 (2.728 - 2.634)	34.05 - 2.25 (2.33 - 2.25)
Number of reflections refined against	13419 (1269)	10543 (1022)	10945 (1075)	7886 (747)
Completeness (working + test) (%)	92.83 (89.05)	92.24 (89.81)	98.49 (98.53)	97.74 (95.77)
Rwork	0.2271 (0.2443)	0.1863 (0.2019)	0.2255 (0.2608)	0.2600 (0.2785)
Rfree	0.2703 (0.3112)	0.2439 (0.2892)	0.2767 (0.3376)	0.2815 (0.4070)

Number of non-hydrogen atoms	1680	1538	3115	849
Macromolecules	1536	1452	2964	768
Ligands	39	52	84	44
Water	105	34	67	37
Ramachandran favored (%)	100	100	99.14	100
RMS(bonds)	0.001	0.007	0.002	0.015
RMS(angles)	0.33	0.75	0.44	1.23
Average B-factor	15.95	28.49	29.20	32.96
Macromolecules	14.99	28.41	28.83	31.85
Ligands	21.01	26.92	32.62	42.70
Water	28.14	34.42	41.39	44.62

CHAPTER 7

X-ray Crystal Structures of the Influenza M2 Proton Channel Drug-Resistant V27A Mutant Bound to a Spiro-Adamantyl Amine Inhibitor Reveal the Mechanism of Adamantane Resistance

7.1 Introduction

Influenza A M2 is a multifunctional viral protein whose domains play several roles during the viral lifecycle. It is a homotetramer that contains monomers made up of 97 amino acids. The N-terminal domain (residues 1-22) is well-conserved and plays a role in incorporation of M2 into the virion. [25] The transmembrane (TM) domain (22-46) forms a unidirectional, proton-selective channel [17, 294] that acidifies the viral interior after the virus is endocytosed into the host cell. This allows viral ribonucleoproteins (vRNPs) to dissociate from the matrix 1 (M1) protein; when proton conductance through M2 is blocked by the adamantane drugs (see Figure 7.1), this dissociation is prevented and the virus is no longer able to replicate. [263] The proton channel function of M2 also serves a secondary role in the de-acidification of the Golgi apparatus so that acid-sensitive hemagglutinin is not prematurely activated before the virus assembles and buds. [295] The minimal construct needed for selective, unidirectional proton transport is the TM domain (residues 22-46). [29, 32] The TM domain is relatively well-conserved compared to the rest of the channel, and only a small number of mutants retain conductance rates similar to the WT. [264] The cytosolic helix of M2 induces membrane curvature and is involved in viral budding and scission, [47, 227] and the C-terminal tail interacts with the M1 protein. [27]

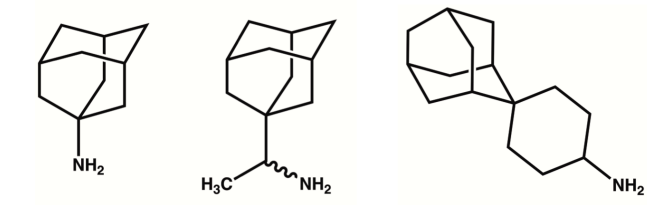

***Figure 7.1*:** Chemical structures of the adamantane drugs (amantadine, rimantadine) and spiro-adamantyl amine.

In recent years, adamantane drug-resistant mutants have become prevalent in circulating viruses. Some viruses are resistant to the adamantanes and neuraminidase inhibitors, [296-298] thus highlighting the need to develop new influenza antivirals. The two most prevalent drug-resistant mutants are S31N and V27A. [299] While the S31N mutation was present in populations of influenza before the introduction of the adamantane drugs, V27A has become enriched by selection pressure. [300], Double mutants containing both S31N and V27A mutations have been observed. [293, 301] The percent of influenza viruses containing the V27A mutation varies widely depending on the viral strain and season, with some studies reporting incidence as high as 7-10%. [302, 303] Overall, the V27A mutation is becoming more prevalent in circulating populations of influenza, [293] so there has been interest in designing drugs to target it. [88, 94, 287, 304-306]

Here we present X-ray crystal structures of the drug-resistant V27A mutant of M2 bound to a spiro-adamantyl amine inhibitor, using both M2(22-46) and M2(21-61) constructs for crystallization trials. Spiro-adamantyl amine was developed by molecular dynamics simulation-directed design and was able to inhibit the conductance of protons in both the V27A mutant and the WT channel in two electrode voltage clamp (TEVC) assays using *Xenopus* oocytes, with an IC_{50} of 0.3 μM against the V27A channel and an IC_{50} of 18.7 μM against the WT channel (compare to IC_{50} = 15.7 μM for amantadine against the WT channel). [94] Spiro-adamantyl amine was further shown to have both in vitro and in vivo antiviral activity against influenza A M2 V27A mutant virus. [287] Therefore, spiro-adamantyl amine appears to represent a promising antiviral drug candidate that warrants further characterization. In this study, we focus on understanding the mechanism of action of spiro-adamantyl amine in inhibiting the M2 V27A mutant by solving high-resolution X-ray crystal structures. It was found that when Val27 is mutated to Ala, the diameter of the channel pore at the drug binding site increases and the hydrophobic interactions that stabilize the binding of adamantanes to the WT channel are removed. This widening of the pore at the channel's N-terminus allows the spiro-adamantyl amine compound to bind with its adamantyl group higher in the channel relative to previous structures of drug-

bound M2 WT. The inhibitor binds with its ammonium group pointed down the channel pore, in the direction of the gating His37 residues. The inhibitor ammonium group interacts indirectly with the gating His37 residues through two intervening water layers, compared to one water layer in the M2 WT complex with the same spiro-adamantyl amine inhibitor. This interrupts hydrogen bonded water networks leading down to the His37 gate and prevents proton conduction through the channel. In the structure of M2(21-61) V27A bound to spiro-adamantyl amine, we observe tight packing at the channel's C-terminus, particularly at residue Arg45.

7.2 Material and methods

7.2.1 M2 peptide synthesis and purification

The sequence of the M2(22-46) V27A construct used in this study is as follows:

Ac-SSDPLAVAASIIGILHLILWILDRL-NH_2

The sequence of the M2(21-61) V27A construct used in this study is as follows:

Ac-DSSDPLAVAASIIGILHLILWILDRLFFKSIYRFFEHGLKR-NH_2

M2(22-46) V27A and M2(21-61) V27A were synthesized using Fmoc chemistry with an optimized solid phase synthesis protocol and purified using reverse phase HPLC. [40, 266] Coupling reagents were 5 equiv. amino acid, 5 equiv. HCTU (O-(6-Chlorobenzotriazol-1-yl)-N,N,N′,N′-tetramethyluronium hexafluorophosphate), 10 equiv. DIEA (N,N-Diisopropylethylamine) in NMP (N-Methyl-2-pyrrolidone). Several factors were taken into consideration when synthesizing this peptide. [40] First, hydrophilic PEG (polyethylene glycol) based Chemmatrix Rink Amide resin was used in order to minimize peptide aggregation. Second, coupling and Fmoc deprotection for each residue were performed at 75 ^{o}C for 5 minutes to achieve high yield, except H37 and H57 which were coupled at 20 ˚C for 30 minutes to minimize racemization. Third, a solution of 5% piperazine + 0.1 M HOBt (hydroxybenzotriazole) was used for Fmoc deprotection instead of 20% piperidine. This is to suppress a major side reaction of aspartimide formation between D44 and R45. Fourth, all three arginines (R45, R53, and R61) and the residues immediately following them (D44, Y52, and K60) were double coupled.

The peptide was cleaved from the resin using 95% TFA (trifluoroacetic acid), 2.5% Tris, 2.5% H_2O and precipitated from ether after removal of TFA. Ether was decanted after centrifugation and the peptide was washed with cold ether again. Crude peptides were dissolved in a solution consisting 50% B' buffer (59.9% isopropanol, 30% acetonitrile, 10% H_2O, and 0.1% TFA) and 50% A buffer (99.9% H_2O, 0.1% TFA) and purified by preparative C4 reverse phase HPLC with a linear gradient of 70% B' to 85% B'. M2(21-61)-V27A was eluted at around 80% B'. Purity and identity of the peptide were confirmed by analytical HPLC and MALDI-MS.

7.2.2 Crystallization

The peptides were reconstituted into the lipid cubic phase with modifications to the protocol described by Caffrey and Cherezov, [102] as previously described. [61, 307, 308] The V27A peptides were dissolved in ethanol and added directly to dry monoolein powder (1-oleoyl-rac-glycerol, Sigma-Aldrich) along with an ethanol stock of spiro-adamantyl amine and the sample was vortexed, then the excess ethanol was removed using a stream of nitrogen and was then lyophilized overnight to remove excess ethanol (<100 mTorr). [40, 307, 308] The cubic phase was formed by melting the peptide/inhibitor/monoolein sample at 40 ˚C and mixing with an aqueous solution containing MNG-3-C8 detergent, [272, 273] which in previous crystallization trials and solution NMR studies has been shown to stabilize the $Inward_{closed}$ conformation of the M2 channe, [61, 309] transferred to a glass Hamilton syringe, then the lipid cubic phase was formed after addition of aqueous solution at a ratio of 20 µL aqueous per 30 mg sample. Crystallization conditions were screened in plastic 96-well sandwich trays (Laminex, 200 micron) using a LCP Mosquito crystallization robot (TTP Labtech).

The crystallization conditions for the structure of M2(22-46) V27A bound to spiroadamantyl amine (PDB code 6NV1) were as follows: 100 nL LCP plus 500 nL precipitant solution. LCP composition: 30 mg monoolein (Sigma-Aldrich), 1.2 x 10^{-6} moles M2(22-46) V27A peptide, 4.8 x 10^{-6} moles spiroadamantyl amine inhibitor (4-fold excess over M2 monomer), mixed with 20 µL of 50 mM MNG-3-C8 ($C_{43}H_{80}O_{22}$, MW = 949.08) in water using a syringe coupler at 20˚C. Precipitant solution composition: 0.045 M HEPES pH 7.5, 19.8% (w/v) PEG 4000,

0.01 M L-proline. Crystals formed as 25 μm rectangular plates after two weeks of incubation at 20 ˚C.

The crystallization conditions for the structure of M2(21-61) V27A bound to spiroadamantyl amine (PDB code 6OUG) were as follows:

100 nL LCP plus 1000 nL precipitant solution. LCP: 30 mg monoolein (Sigma-Aldrich), 8 x 10^{-7} moles M2(21-61) V27A peptide, 4.8 x 10^{-6} moles adamantyl amine inhibitor (6-fold excess over M2 monomer), mixed with 20 μL of 50 mM MNG-3-C8 in water using a syringe coupler at 20˚C. Precipitant solution: 0.04 M sodium chloride, 0.04 M Tris pH 8.0, 27% v/v PEG 350 MME. Crystals formed as 20 μm cubes after 3 weeks of incubation at 20 ˚C (see Figures 7.10 and 7.11).

Crystals were diffracted at the Advanced Light Source (Berkeley, USA) on beam 8.3.1 using a Dectris Pilatus3 S 6M detector. Data were collected at 100 K. Data indexing, integration and scaling were carried out using XDS. [310] Anisotropic scaling was used for one of the datasets (PDB ID 6OUG). [311] Both structures were solved by molecular replacement using Phaser [278] in the CCP4 suite, [277] with a single tetramer (PDB ID 6BMZ) as a search model. [61] Refinement was carried out in Phenix [280] with model building in Coot. [281] Polder maps were calculated using Phenix. [271] Pore diameters were calculated using CHUNNEL. [312]

Use of the LCP crystallization robot was made possible by National Center for Research Resources Grant 1S10RR027234-01. The authors thank Pil Seok Chae (Hanyang University, Seoul, South Korea) for providing MNG detergent for crystallization trials. J.T. and M.C. thank David Aragão and Valerie Pye for help with diffraction measurements and structure determination using first ever crystals of the M2-V27A TM domain. Data collection was carried out at ALS 8.3.1. Beamline 8.3.1 at the Advanced Light Source is operated by the University of California Office of the President, Multicampus Research Programs and Initiatives grant MR-15-328599 and NIGMS grants P30 GM124169 and R01 GM124149. The authors thank George Meigs and James Holton at ALS 8.3.1 for support during data collection.

7.2.3 Data collection

Crystals were harvested from the LCP plates and snap cooled in liquid nitrogen with no added cryoprotectant. Data collection was carried out at the Advanced Light Source (Berkeley, USA) using a Dectris Pilatus3 S 6M detector. Crystals were diffracted at 100 K.

Data collection parameters for the structure of M2(22-46) V27A bound to spiroadamantyl amine (6NV1) were as follows: detector distance = 300 mm, oscillation = 1˚, exposure time = 0.5 s, energy = 11.111 keV, 360 frames. The crystal diffracted to 2.5 Å with a P 21 21 21 space group and unit cell dimensions a, b, c (Å) = 49.81, 49.95, 75.03; α, β, γ (˚) = 90, 90, 90.

Data collection parameters for the structure of M2(21-61) V27A bound to spiroadamantyl amine (6OUG) were as follows: detector distance = 300 mm, oscillation = 0.25˚, exposure time = 0.3 s, energy = 11.111 keV, 1480 frames. The crystal diffracted to 3.0 Å with a P 21 21 2 space group and unit cell dimensions a, b, c (Å) = 49.42, 49.38, 122.38; α, β, γ (˚) = 90, 90, 90.

7.2.4 Data processing

Data indexing, integration and scaling were carried out using XDS. [310] For the 6OUG dataset, the resolution cutoff was made generously because of strong anisotropy, which later was corrected by anisotropic scaling. [311] Statistics for data processing and refinement are shown in Table 7.4.

7.2.5 Refinement and modeling

Both structures were solved by molecular replacement using Phaser [278] in the CCP4 suite, [277] with a single M2(22-46) tetramer as a search model (PDB code: 6BMZ). [61] For both structures, two tetramers were observed in the asymmetric unit. Refinement was carried out using Phenix.refine. [280] Rigid body refinements were performed using single helices as rigid body domains. In the early stages of refinement, simulated annealing was applied to remove model bias.

Models were built with Coot. [281] For the structure of M2(22-46) V27A bound to spiroadamantyl amine (6NV1), eight monoolein molecules (one per monomer helix) were modeled based on difference maps. The TLS domains for refinement were defined down to single monomer helices. For the structure of M2(21-61) V27A bound to spiroadamantyl amine (6OUG), residues at the C-terminus were modeled based on omit maps. Twinning was observed, and data were refined using the twin law k, h, -l. For TLS refinement, each helix was split into two TLS domains between residues L46 and F47, as the C-terminal cytosolic helix was observed to be more flexible than the TM domain. Polder omit maps were calculated in Phenix. [271]

7.2.6 Molecular dynamics simulations

The X-ray crystal structure of M2(22-46) WT in complex with spiro-adamantylamine molecule (PDB ID 6BMZ) [61] was used as the starting structure after mutating Val27 to Ala. The M2(22-46) V27A - spiro-adamantylamine complex was embedded in a hydrated POPC lipid bilayer. The complexes was simulated in the neutral Inwardclosed conformation at pH 8.0 with a protonated ammonium group for the spiro-adamantyl amine ligand. and the system was subjected to all-atom MD simulations using Desmond. [61, 242, 243] The POPC lipid bilayer extended 30 Å beyond the protein, resulting in a system including ca 200 lipid molecules to allow the formation of two layers without interdigitation (see Figure 7.2). The TIP3P [199] model was used for water. The bilayer was solvated using a 30 Å thick layer of TIP3P waters Na+ and Cl- ions were placed in the water phase to neutralize the systems and to represent the experimental salt concentration of 0.150 M NaCl. The total number of atoms in the system reached ca 80000. Membrane creation and system solvation were conducted with the “System Builder” utility of Desmond (Schrodinger, Cambridge, MA). [242, 243] Protein-ligand interactions were modelled using OPLS 2005. [244-246] This setup resulted in a simulation box of 88×88×105 $Å^3$ dimensions and ca 19000 water molecules.

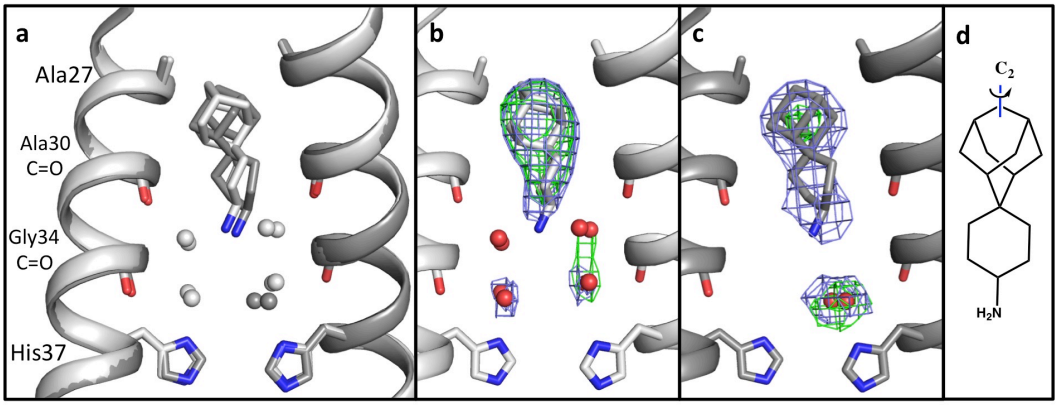

***Figure 7.2*:** Spiro-adamantyl amine binding site for structures of M2(22-46) V27A (PDB code 6NV1, light gray) and M2(21-61) V27A (PDB code 6OUG, dark gray). Front and back monomer helices have been removed so the contents of the pore can be clearly viewed. (*a*) Alignment of structures 6NV1 (monomer chains B and D) and 6OUG (chains B and D). The bound spiro-adamantyl amine localizes to the same position in the pore in both M2 constructs. The compound's adamantyl cage interacts with the four mutant Ala27 residues at the N-terminus the homotetrameric channel. (*b*) and (*c*) 2Fo-Fc maps at a contour of 1 σ (blue net) and Polder omit maps [271] to a contour of 3 σ (green net) for M2(22-46) V27A (6NV1) (*b*) and M2(21-61) V27A (6OUG) (*c*) In structure 6NV1, Polder map density at 3 σ shows both the adamantyl cage and cyclohexyl group of the bound spiroadamantyl amine inhibitor. However, in structure 6OUG, only the adamantyl cage of the channel is observed at this contour level. (*d*) Chemical structure of spiro-adamantyl amine, showing the adamantyl C2 symmetry axis.

Calculation of long-range electrostatic interactions was carried out using the particle mesh Ewald method with a grid spacing of 0.8 Å. [205, 206] Van der Waals and short-range electrostatic interactions were smoothly truncated at 9.0 Å. A constant temperature was maintaned in all simulations using Nosé-Hoover thermostat, and the Martyna-Tobias-Klein method was employed to control the pressure. [248] Multistep RESPA integrator [313] was used to integrate the equations of motion with an inner time step of 2 fs for bonded interactions and non-bonded interactions within a cut-off of 9 Å. An outer time step of 6.0 fs was used for non-bonded interactions beyond the cut-off. The equilibration protocol consisted of a series of restrained minimizations and MD simulations designed to relax the system, while not deviating substantially from the initial coordinates. Initially, two rounds of steepest descent minimization with a maximum of 2000 steps and harmonic restraints of 50 kcal mol-1 Å-2 were applied on all solute atoms, followed by 10000 steps of minimization without restraints. The first

simulation was run for 200 ps at a temperature of 10 K in the NVT ensemble with solute heavy atoms restrained with a force constant of 50 kcal mol-1 Å-2. The temperature was then raised during a 200 ps MD simulation to 310 K in the NVT ensemble with the force constant retained. A temperature of 310 K was used in the MD simulations to ensure that the membrane state was above the chain order/disorder transition temperature of 271 K for fully hydrated POPC lipids. [204] The heating was followed by equilibration runs. Three stages of NPT equilibration (1 Atmosphere) with restraints were performed, first with the heavy atoms of the system restrained for 1 ns, then with solvent and lipid molecules restrained harmonically with a force constant of 10 kcal/mol/Å2 for 10 ns. In the third stage of equilibration, the Cα atoms of M2(22-46) V27A were harmonically restrained with a force constant of 2 kcal/mol/Å2 for 1 ns. The above-mentioned was followed by a 300 ns NPT simulation without restraints. Within this time, the total energy, system dimensions, and the RMSD reached a plateau, and the systems were considered equilibrated. For Figures 7.12 and 7.13 the MD trajectory was converted to Gromacs format xtc using VMD software, for further analysis using Gromacs 2016 tools. Water molecules were selected from the section of all water molecules within 6Å radius from His37 and 6Å radius from ligand. Distances between ligand's nitrogen and each water's oxygen molecule were calculated based on their position on Z-axis. A 300 ns NPT simulation without restraints was performed. Within this time, the RMSD of C_α carbons of the protein reached a plateau, and the systems were considered to be equilibrated. For structural analyses, snapshots of the different systems were created with VMD [217] or Maestro. [250] Trajectories were analyzed with Maestro, Gromacs, [196, 251] and VMD. Measurements were carried out with Gromacs tools. For the calculation of hydrogen bonds, a cut-off angle of 30^o of deviation from 180^o between the donor-hydrogen-acceptor atoms and a cut-off distance of 3.5 Å between the donor and acceptor atoms were applied.

7.3 Results and discussion

7.3.1 X-ray crystal structures of spiro-adamantyl amine bound to M2(22-46) V27A and M2(21-61) V27A

We have used LCP crystallization techniques [102] to solve two X-ray crystal structures of the adamantane-resistant M2 V27A mutant: one 2.5 Å structure of M2(22-46) V27A in complex with spiro-adamantyl amine (PDB ID 6NV1), and one 3.0 Å structure of M2(21-61) V27A in complex with spiro-adamantyl amine (PDB ID 6OUG). The binding site of the spiro-adamantyl amine inhibitor is nearly identical in the two structures (see Figure 7.3).

Co-crystallization with a maltose neopentyl glycol (MNG) detergent additive appears to have stabilized M2 in its tetrameric form; in the absence of this detergent, the protein crystallized as an antiparallel dimer. The asymmetric unit of each structure contains two tetramers of M2 in the $Inward_{closed}$ conformation. The C-terminus of the channel is tightly packed and each monomer helix is slightly kinked at residue Gly34. In the structure of the M2(22-46) V27A construct (6NV1), we observe a total of eight ordered monoolein molecules in the asymmetric unit interacting with the hydrophobic face of each monomer helix.

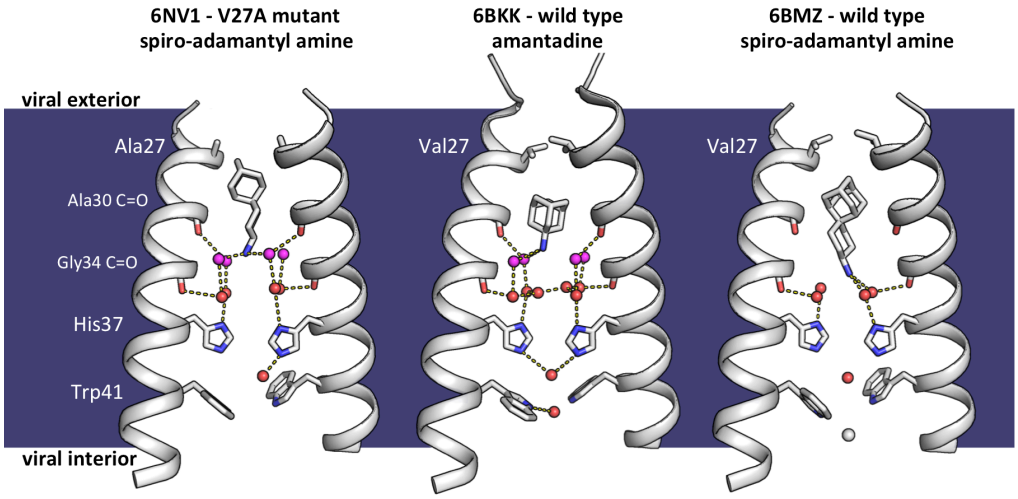

Figure 7.3: Mechanism of adamantane drug resistance in the V27A mutant channel, and mechanism of dual inhibition by spiro-adamantyl amine. Front and back monomer helices have been removed to clearly show the contents of the channel pore. Pink spheres correspond to waters that form hydrogen bonds with the Ala30 carbonyl, and red spheres correspond to waters forming hydrogen bonds with Gly34 carbonyl. Left to right: Newly solved structure of M2(22-46) V27A bound to a spiro-adamantyl amine inhibitor (6NV1, monomer chains B and D),

M2(22-46) WT bound to amantadine (6BKK, chains B and D), [61] and M2(22-46) WT bound to spiro-adamantyl amine (6BMZ, chains B and D). [61] When spiro-adamantyl amine binds to the V27A channel (6NV1), the ammonium group of the inhibitor localizes to the same position as the ammonium of amantadine in the WT structure (6BKK). The adamantyl group is positioned higher in the channel pore, occupying the extra space created by the Val27 to Ala mutation. In the previously solved structure of spiro-adamantyl amine inhibitor bound to the WT channel (6BMZ), the adamantyl group of the inhibitor binds lower in the channel pore, and the four waters in the Ala30 layer are displaced. For the spiro-adamantyl amine bound structures, a network of one or two layers of hydrogen-bonded waters is formed depending whether Val or Ala is present at position 27.

Consistent with previous X-ray crystal structures of the WT and S31N mutant M2 channel, here we observe ordered water molecules above the channel's gating His37 residues (see Figure 7.4b,c). [34, 40, 43, 61, 266] In the 2.5 Å resolution structure of M2(22-46) V27A (6NV1), four ordered water molecules are within hydrogen bonding distance of Ala30 carbonyls ("Ala30 layer") and spiro-adamantyl amine, and four waters are observed forming hydrogen bonds to Gly34 carbonyls ("Gly34 layer"). The Gly34 layer waters also form hydrogen bonds with the channel's gating His37 residues (see Figure 7.3). In the 3.0 Å resolution structure of M2(21-61) (6OUG), we only observe electron density corresponding to two waters in the Gly34 layer. This is likely a result of increased molecular motion within the channel pore in this lower resolution structure. In the following discussion of adamantane resistance in the V27A mutant and the spiro-adamantyl amine binding mechanism, we will focus on the structure of the M2(22-46) V27A construct (6NV1) because it was solved to higher resolution and shows the contents of the channel pore in greater detail.

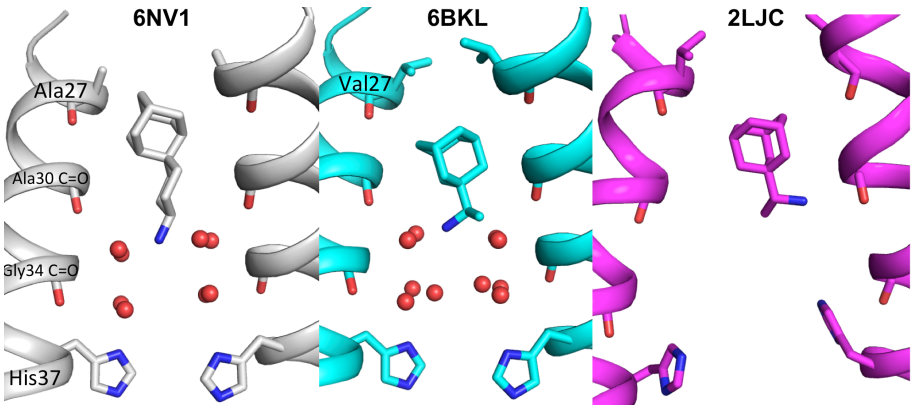

***Figure 7.4*:** Crystal structure of spiroadamantyl amine inhibitor bound to the M2(22-46) V27A mutant (6NV1) compared to the crystal structure of rimantadine bound to M2(22-46) WT (6BKL) [61] and the NMR structure of rimantadine bound to an AM2-BM2 chimera (2LJC). [60]

7.3.2 Mechanism of amantadine and rimantadine resistance in the V27A mutant

The Val27 to Ala mutation at the N-terminus of M2 widens the channel pore at the adamantane binding site. In the M2 WT channel, four symmetry related Val27 residues form a valve that completely occludes the N-terminus of the channel in the $Inward_{closed}$ conformation. [43, 61] Breathing motions of this Val27 gate are predicted to allow water, ions, and drugs/inhibitors to enter the N-terminus of the WT channel. [314, 315] The adamantyl group of the bound adamantane drugs interacts with the hydrophobic surface formed by the Val27 residues. [34, 61] When residue 27 is mutated from Val to Ala, these hydrophobic contacts are removed and the adamantanes (amantadine and rimantadine) can no longer inhibit the channel. In the crystal structure of M2(22-46) V27A bound to spiro-adamantyl amine, we observe that the width of the channel pore is 3.0 Å at residue Ala27. For comparison, in the structure of M2(22-46) WT bound to amantadine (6BKK), the diameter at Val27 is 0.7 Å. [312] This widening of the N-terminal channel pore is consistent with a previous solution NMR model of M2(18-60) V27A in DHPC micelles. [316] The V27A mutant M2 channel conducts protons at an increased rate relative to the WT channel. [264, 316] This could be explained by the widened N-terminal pore, as water and hydronium ions would have greater access to the region of the pore above the His37 gate. Though rimantadine is slightly longer than amantadine, the length of the compound is not sufficient to allow for the drug ammonium group to form hydrogen bonds with Ala30 layer waters while also allowing the adamantyl group to engage in hydrophobic contacts with the N-terminal portion of the pore near residue 27, and so rimantadine is not able to inhibit the V27A channel.

7.3.3 Spiro-adamantyl amine shifts its binding position depending on which residue is present at position 27

Though mutation of Val27 to Ala prevents amantadine and rimantadine from inhibiting the channel, longer and bulkier inhibitors such as spiro-adamantyl amine can bind to the wider N-terminal pore of V27A mutant and inhibit its proton conduction (see Figure 7.3). In the structure of the spiro-adamantyl amine complex with V27A (6NV1), we observe that the ammonium group of the spiro-adamantyl amine inhibitor localizes to approximately the same position as the ammonium group of amantadine in complex with M2(22-46) WT (6BKK) from our previous work. [61] When the two structures are aligned, the position of the ammonium groups are nearly identical (0.9 Å) when comparing the WT-amantadine vs. V27A-spiro-adamantyl amine complexes. In both structures there are ordered waters in the Ala30 and Gly34 solvent layers, and the ammonium group of the bound drug/inhibitor forms hydrogen bonds with two waters in the Ala30 layer. The hydrogen bonds formed between the inhibitor nitrogen and pore waters are short (2.4-2.6 Å), which supports the ionization state we have chosen for the ligand. The binding of the spiro-adamantyl amine inhibitor to the top of this hydrogen-bonded water network blocks protons from being transported down through these water wires to the gating His37 residue. The tautomer we have assigned for the His37 residues is as previously observed in ssNMR experiments. [42]

In our previous work, [61] we characterized the binding of this same spiro-adamantyl amine inhibitor to the M2(22-46) WT channel (6BMZ). When spiro-adamantyl amine binds to the WT channel, the inhibitor's adamantyl group occupies approximately the same position in the pore as the adamantyl group of bound amantadine or rimantadine in M2 WT. However, the longer hydrophobic scaffold of the inhibitor completely displaces the four waters in the Ala30 layer (see Figure 7.3), such that its ammonium group binds deeper in the channel pore and forms hydrogen bonds with waters in the Gly34 solvent layer. Thus, the spiro-adamantyl amine inhibitor blocks proton conductance in both the WT and the adamantane-resistant V27A M2 channel by shifting its binding position depending on which residue is present at position 27. This dual inhibitor exploits

the M2 channel's functionally essential ability to stabilize positive charges at multiple sites within the channel pore. [94]

7.3.4 Crystal structure of the M2(21-61) V27A construct in complex with spiro-adamantyl amine

The TM domain of M2 is the minimum construct needed for selective, unidirectional proton transport. [317, 318] However, truncation of the C-terminus and cytosolic helix (residues 46-60) has minor effects on the proton conduction properties relative to the full length channel. [51] More importantly, the cyto helix also has functional importance for budding and membrane scission. [47, 227, 319] Constructs including the cytosolic helix were more difficult to crystallize relative to the TM construct, presumably because of the conformational mobility of this domain. Nevertheless, after much optimization, we were able to grow crystals of M2(21-61) V27A in complex with spiro-adamantyl amine and solve a structure to 3.0 Å resolution (6OUG).

In structure 6OUG, we observe electron density for residues 22-56. The structural features of the TM domain (22-46) are similar for both the M2(22-46) and the M2(21-61) constructs, with Cα RMSD = 0.25 Å. The binding site of the spiro-adamantyl amine inhibitor is nearly identical, although in structure 6OUG there are fewer ordered waters visible in the channel pore between the inhibitor ammonium group and the gating His37 residues (likely a result of the lower resolution of this structure). Residues 47-56 form an α-helix that extends straight down from the TM helix. We observe tighter packing of the tetrameric bundle at the C-terminus relative to structures that include only the TM domain (see Figure 7.5b,c). At residue Arg45, the minimum pore diameter is 2.8 Å in the structure of M2(22-46) V27A and 1.0 Å in the structure of M2(21-61) V27A. [312] All four Asp44 and Arg45 residues in the structure of M2(21-61) V27A face the aqueous pore. Residue Phe48 faces the channel pore and is well-positioned for the stabilization of the positive charge on Arg45 through cation-π interactions. In the native M2 protein, Cys50 is palmitoylated. [320] Here, Cys50 has been mutated to Ser to facilitate peptide synthesis and purification and to prevent oligomerization through the formation of disulfide bonds. We observe that the Ser50 side chain faces away from the aqueous pore and toward the lipid bilayer.

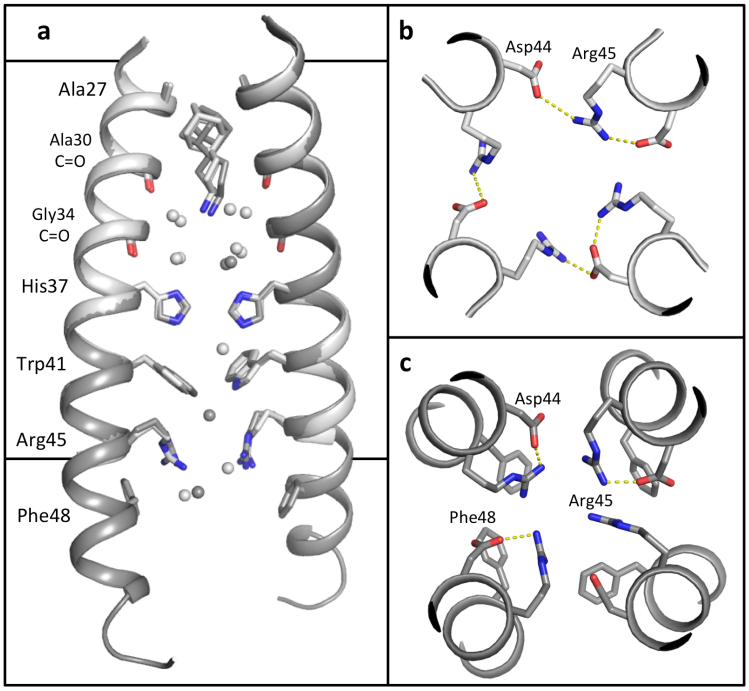

Figure 7.5: Structural differences between M2(22-46) V27A (6NV1, light gray) and M2(21-61) V27A (6OUG, dark gray). (*a*) Alignment of 6NV1 and 6OUG. Two monomer helices are shown here (chains B and D). The binding site of the spiro-adamantyl amine inhibitor is nearly identical in the two structures, though fewer ordered waters are observed in the channel pore in structure 6OUG. Residues 47-55 of M2(21-61) form an α-helix that extends straight downward from the TM helix; the conformational state we observe here is potentially influenced by crystal contacts or choice of lipid mimetic. (*b*) Top-down view of residues Asp44 and Arg45 in the structure of M2(22-46). (*c*) Top-down view of residues Asp44, Arg45, and Phe48 in the structure of M2(21-60). The packing of the channel at the C-terminus is tighter in the longer construct of M2.

Several NMR studies predict that the cytosolic helix of M2 has α-helical secondary structure, with either a turn or a disordered region connecting the cyto helix to the TM domain. In these NMR structures, the TM helix ends and the turn / disordered region begins at either residue Leu46 (2KWX, 2RLF, 2KIH) [50, 316, 321] or residue Phe48 (2L0J, 2N70). [30, 119] The conformation of the channel's C-terminus that we observe in the X-ray crystal structure here differs from solution and solid state NMR structures. Solution NMR studies have shown that the conformation of the juxta-membrane domain connecting the TM and cytosolic helices is sensitive to solubilizing environments. [322] Thus, the conformation of the monomer helices from residue 47 to 56 is possibly influenced by crystal contacts at the channel's C-terminus or choice of lipid mimetic. We include

structure 6OUG here as a comparison to the shorter M2(22-46) V27A construct and also because structural information about the helical turn immediately below residue 46 may prove useful for understanding proton conduction through the C-terminus of the channel.

7.3.5 Molecular dynamics simulations of M2(22-46) V27A in complex with spiro-adamantyl amine

The contents of the M2 channel pore differ in the two crystal structures described here; fewer waters are observed in the structure of M2(21-61) V27A in complex with spiro-adamantyl amine. We carried out molecular dynamics simulations in bilayers (see Figure 7.6) to examine the ordering of water within the pore at room temperature.

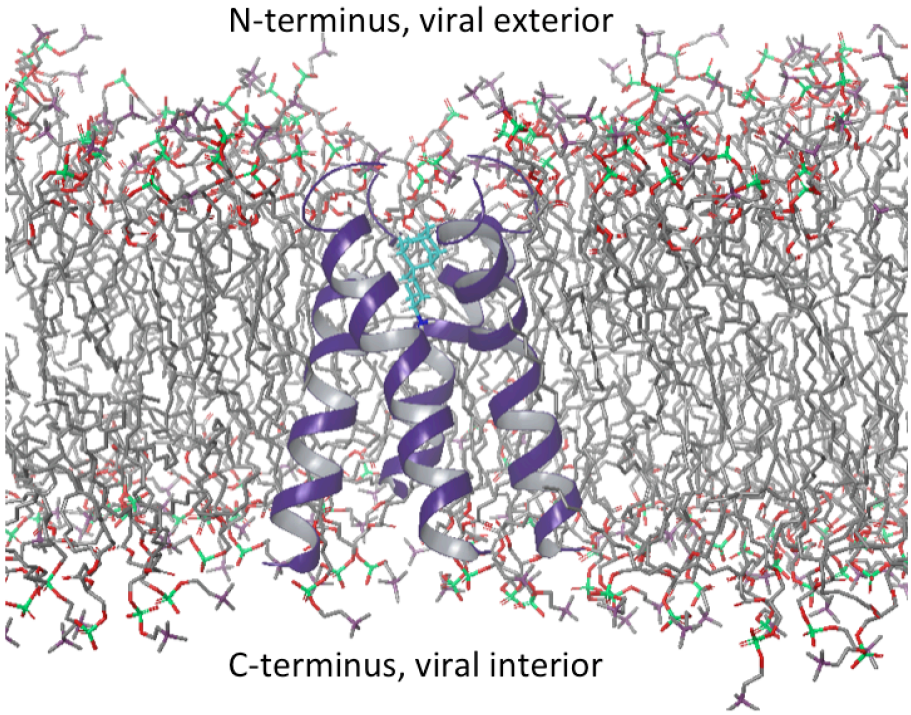

***Figure 7.6*:** Screenshot of the last snapshot of 300 ns MD simulation of M2 (22-46) V27A - spiro-adamantyl amine complex in POPC bilayer. Waters, hydrogen atoms, and ions have been removed for clarity. M2(22-46) V27A helices are shown as purple ribbons, ligand are shown as cyan sticks, lipid hydrocarbon chains in grey, phosphorus in light green, oxygen in red and nitrogen in blue purple.

M2(22-46) was simulated in the Inward$_{closed}$ conformation at pH 8.0 with a neutral form assigned for all four His37 residues and a protonated ammonium group for the ligand. The starting structure was produced after applying the V27A mutation to the structure of spiro-adamantyl amine in complex with M2(22-46) WT in the Inward$_{closed}$ state (6BMZ). The spiro-adamantyl amine - M2(22-46) V27A protein complex was subjected to MD simulations in a POPC bilayer for 300 ns. The simulated M2(22-46) V27A - ligand complex was stable, and in all cases the M2(22-46) V27A tetramer showed no large conformational changes in the course of the simulations, as demonstrated by RMSDs smaller than 1.5 Å for M2 (22-46) C_{α}-carbons with respect to the starting structure (see Figure 7.7). Also, the individual chains of the tetramer did not deviate from the starting structure, with RMSDs ≤ 1.1 Å for M2 (27-46) Cα carbons and no changes observed in selected torsion angles of each chain (see Tables 7.1-7.3).

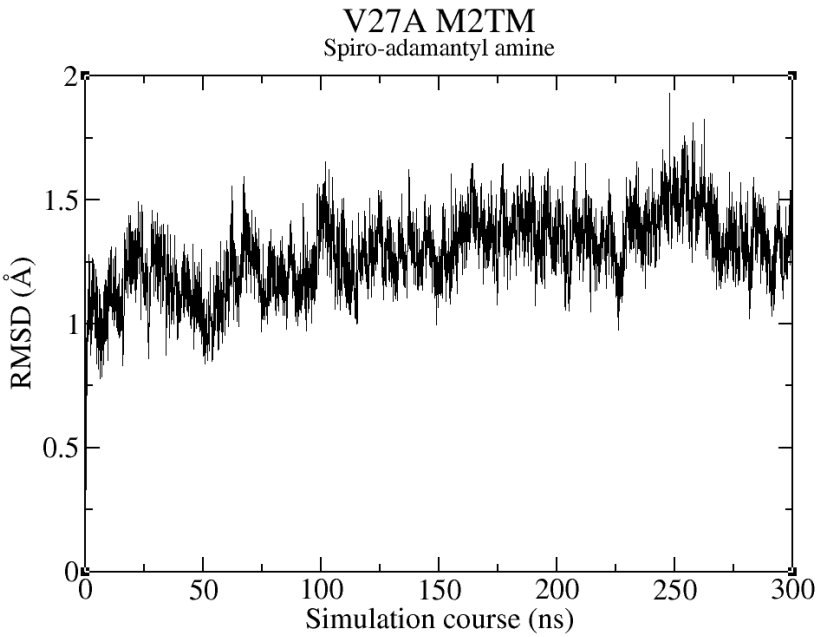

Figure 7.7: RMSD for Cα atoms of M2(22-46) V27A during the 300 ns MD simulation of M2 (22-46) V27A - spiro-adamantyl amine complex in POPC bilayer.

Tables 7.1-3: Structural and dynamic measures from 300 ns MD simulation of M2 (22-46) V27A - spiro-adamantyl amine complex in POPC bilayer at high pH.

Table 1

Complex	RMSD (C_α) [1]	Angle vector (C2'-C1) [2]	V27A-Ad [3]	H-bonds [4]	RMSF ligand [5]
Spiro-adamantyl amine - M2(22-46) WT	1.3 ± 0.2	8.2 ± 4.1	4.3 ± 0.3	2.7 ± 0.5	0.2
Spiro-adamantyl amine - M2(22-46) V27A	1.1 ± 0.1	11.2 ± 5.5	1.9 ± 0.03	2.8 ± 0.5	0.2

Table 2

Complex	RMSD (27-46) [6]	RMSD Achain (27-46) [7]	RMSD Bchain (27-46) [8]	RMSD Cchain (27-46) [9]	RMSD Dchain (27-46) [10]
Spiro-adamantyl amine - M2(22-46) WT	0.96	0.60	0.62	0.58	0.93
Spiro-adamantyl amine - M2(22-46) V27A	1.08	0.73	0.95	0.69	0.88

[1] Maximum root-mean-square deviation (RMSD) for C_α atoms of M2(22-46) V27A tetramer relative to the initial structure after root-mean-square fitting of C_α atoms of M2(22-46) V27A; in Å.
[2] Angle between the adamantane C2' carbon and hexylamine C1 carbon symmetry axis vector and the normal to the membrane; in degrees.
[3] Mean distance between center of mass of V27 or A27 and centers of mass of adamantane calculated using Gromacs tools; in Å.
[4] Mean number of H-bonds between ligand's ammonium group and waters.
[5] Maximum root-mean-square fluctuation (RMSF) for the ligand.
[6] Root-mean-square deviation (RMSD) for C_α atoms of M2(22-46) V27A tetramer, residues 27-46, relative to the initial structure after root-mean-square fitting of C_α atoms; in Å.
[7-10] Root-mean-square deviation (RMSD) for C_α atoms of M2(22-46) V27A helix A-D, residues 27-46, relative to the initial structure after root-mean-square fitting of C_α atoms; in Å.

Table 3

Torsion Angles (Mean / std dev.)

	Chain	φ	ψ
Ala30	A	-65.67 ± 9.78	-29.50 ± 9.58

	B	-65.24 ± 9.79	-29.54 ± 9.50
	C	-66.27 ± 9.62	-28.61 ± 9.68
	D	-64.87 ± 9.50	-30.25 ± 9.34
Ser31	A	-70.54 ± 10.08	-45.50 ± 10.21
	B	-71.43 ± 10.02	-43.49 ± 11.07
	C	-71.84 ± 10.25	-43.76 ± 10.60
	D	-70.53 ± 10.05	-43.65 ± 10.65
Ile32	A	-64.15 ± 11.01	-48.52 ± 8.79
	B	-66.20 ± 11.88	-49.21 ± 8.47
	C	-64.96 ± 11.37	-49.85 ± 8.50
	D	-65.18 ± 11.21	-48.14 ± 8.68
Ile33	A	-63.46 ± 9.99	-33.79 ± 9.31
	B	-61.72 ± 9.80	-34.83 ± 9.16
	C	-63.36 ± 10.07	-34.66 ± 9.39
	D	-59.66 ± 9.88	-36.70 ± 9.02
Gly34	A	-68.20 ± 10.36	-33.44 ± 12.38
	B	-67.33 ± 10.19	-27.97 ± 14.44
	C	-68.06 ± 10.43	-29.32 ± 14.99
	D	-67.37 ± 10.30	-29.59 ± 14.47
Ile35	A	-75.04 ± 12.89	-44.22 ± 8.87
	B	-82.51 ± 15.87	-44.68 ± 9.02
	C	-82.07 ± 16.39	-42.07 ± 12.04
	D	-82.57 ± 15.86	-44.33 ± 8.87
Leu36	A	-61.74 ± 10.28	-38.92 ± 9.45
	B	-63.26 ± 11.48	-36.77 ± 9.75
	C	-64.87 ± 15.66	-38.49 ± 9.86
	D	-61.18 ± 10.83	-38.61 ± 9.42
His37	A	-61.50 ± 9.65	-39.74 ± 9.59
	B	-60.05 ± 9.85	-40.08 ± 10.55
	C	-60.65 ± 9.81	-39.56 ± 10.09
	D	-62.09 ± 9.58	-35.75 ± 10.16

Leu38	A	-67.37 ± 9.76	-42.55 ± 9.00
	B	-67.32 ± 10.54	-42.13 ± 10.13
	C	-66.61 ± 10.08	-44.28 ± 9.12
	D	-68.34 ± 9.89	-41.75 ± 9.20

In agreement with the crystal structure, the spiro-adamantyl amine moved towards the N-terminus by *ca*. 2 Å within the first 50 ns of the simulation. The average angle between the central axis of the pore and the adamantane symmetry axis was ca 8° (see Table 7.1), i.e., the ammonium group of the spiro-adamantylamine compound oriented towards the C-terminus, and the adamantyl cage localized between Ala27 and Ser31. The ligand's ammonium group forms hydrogen bonds with water molecules between the ligand and the His37 residues. We observe two layers of water molecules inside the pore, which are stabilized by extensive hydrogen-bonding interactions. These two layers of waters can be seen in the radial distribution density plotted for the distance between the spiro-adamantyl amine ammonium group and the oxygen atoms from water (see Figure 7.8).

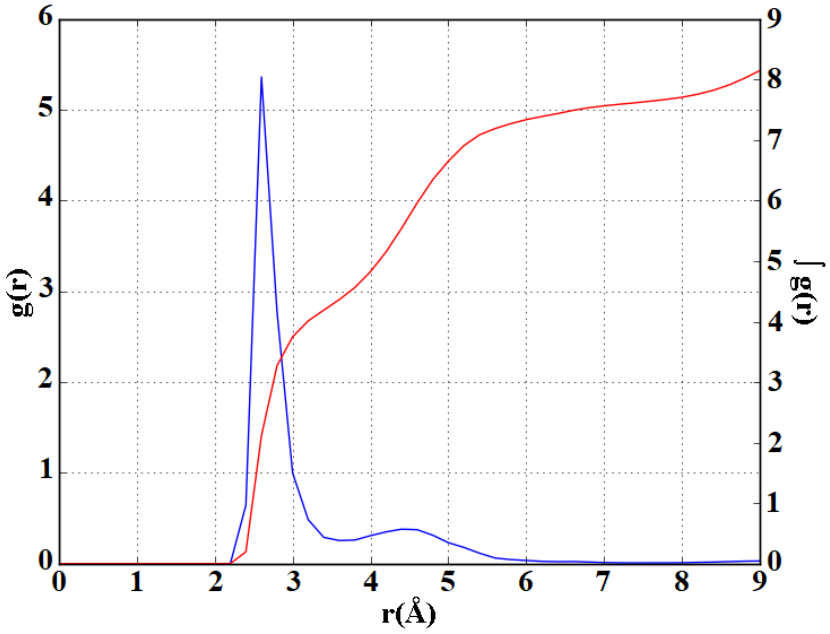

Figure 7.8: Radial distribution function plot for the distance between spiro-adamantyl ammonium group and water oxygen atoms, extracted from a 300 ns MD simulation of M2 (22-46) V27A - spiro-adamantyl amine complex in a hydrated POPC bilayer; the integration at ~ 2.7

and 4.6 Å corresponds to the two layers of waters, with four waters each between the ligand and His37.

The top layer consists of four water molecules that form hydrogen bonds with the ligand's ammonium group and the Ala30 carbonyls. The lower layer of four water molecules is stabilized by hydrogen-bonding interactions involving the carbonyls of Gly34 as well as the His37 side chain. Cl^- ions were present in the simulation to reduce the electrostatic potential created by positively charged groups. No Cl^- ions entered the pore, as indicated by the average Cl-N distance (see Table 7.1).

Previous works [323-325] mention the presence of a Cl^- ion close to His37 because the His37 residues were charged. In our experimental structure and MD simulations, a Cl^- anion was found in the vicinity of Trp41. This is not unexpected because the spiro-adamantyl ligand is in the ammonium form. The spiro-adamantyl amine - M2(22-46) V27A complex in the X-ray structure was perfectly superimposed with the structure from the 300 ns MD simulation, with the RMSD of the ligand being less than 1 Å (see Figure 7.9).

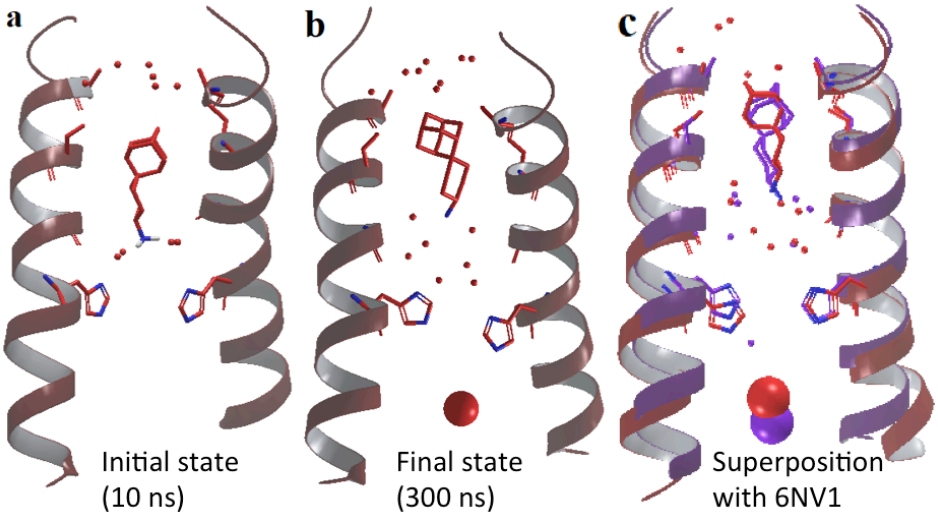

Figure 7.9: (*a*) Initial state after 10 ns of MD simulation of M2 (22-46) V27A - spiro-adamantyl amine complex in a hydrated POPC bilayer. (*b*) Final state after 300 ns of MD simulation. Superposition of spiro-adamantyl amine - M2 (22-46) V27A complexes from X-ray structure (in purple) and 300 ns MD simulation (in red). The chloride ion at the C-terminus of the channel is shown as a sphere.

We have analyzed the trajectories of the MD simulation to determine whether the waters in the channel pore remain tightly bound or if they are exchanged during the simulation. A total of 31 water molecules are observed to be in exchange with the waters in Ala30 and Gly34 water layers (see Figure 7.12), i.e. from the inhibitor ammonium to His37, which is a distance of 7 Å. The two layers are formed and the ligand position converges after 85 ns. Out of the 31 total waters, 13 have low occupancy. The remaining 18 water molecules in Figure 7.13 are located inside the binding cavity for 40 ns. Only water molecule 2087 first remained inside the cavity for 10 ns then was re-positioned after 40 ns for the last 30 ns.

7.4 Conclusions

These X-ray crystal structures reveal the mechanism of adamantane resistance in the V27A channel. Hydrophobic contacts critical for drug binding are removed when Val27 is mutated to Ala. We also observe that the spiro-adamantyl amine inhibitor blocks proton conduction in both the WT and V27A mutant M2 channels by shifting its binding site depending on whether Val or Ala are present at position 27, and that a network of either one or two layers of hydrogen-bonded waters is formed. MD simulations in POPC hydrated bilayers accurately predict the X-ray M2 V27A structure (6NV1).

These findings are consistent with MD simulations in which positive charges within the M2 pore are predicted to be stabilized at multiple positions within the channel. [94] The structural characterization of this dual inhibition mechanism is intriguing from the perspective of molecular recognition and drug design. Though there are a limited number of M2 mutants that retain the electrophysiological properties necessary for viral replication, circulating populations of the influenza virus often contain a mix of M2 sequences. The design of drugs to target more than one sequence could be a successful strategy for targets such as M2. Structural information about adamantane-resistant mutants can guide this process.

7.5 Supporting information

Tables 7.4**:** *Data* processing and refinement statistics for structures of M2(22-46) bound to spiroadamantyl amine (PDB code 6NV1) and M2(21-61) V27A bound to spiroadamantyl amine (PDB code 6OUG). Values in parentheses refer to statistics for the highest resolution bin.

Structure	**6NV1**	**6OUG**
Space group	P 21 21 21	P 21 21 2
Cell dimensions		
a, b, c (Å)	49.81, 49.95, 75.03	49.42, 49.38, 122.38
α, β, γ (˚)	90, 90, 90	90, 90, 90
Wavelength (Å)	1.11583	1.11583
Resolution (Å)	41.58 - 2.5 (2.589 - 2.5)	122.4 - 3.00 (3.118 - 3.00)
Total reflections	70475 (6775)	80149 (12047)
Unique reflections	6840 (653)	6417 (992)
Completeness (%)	99.25 (98.93)	99.8 (99.5)
Multiplicity	10.3 (10.4)	12.5 (12.1)
R_{merge}	0.1262 (0.7294)	0.457 (2.736)
I/σI	13.27 (3.52)	5.79 (1.24)
Wilson B-factor	40.04	56.62
CC(1/2)	1.000 (0.941)	0.997 (0.465)
Refinement		
R_{work}	0.2213 (0.2665)	0.2840 (0.2744)
R_{free}	0.2548 (0.3367)	0.2973 (0.4859)
Number of non-hydrogen atoms	1696	2037
Protein	1424	1998
Ligands	242	32
Water	30	7
RMSD Bond Lengths (Å)	0.008	0.003
RMSD Bond Angles (˚)	0.96	0.62
Ramachandran favored (%)	100	100
Average B factor	42.05	45.64
Protein	39.04	45.79
Ligands	59.14	38.87
Solvent	47.1	34.76

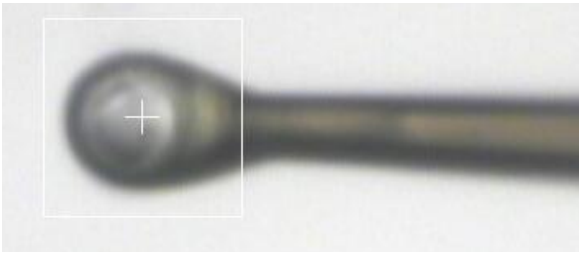

***Figure 7.10*:** Crystal of M2(22-46) V27A during data collection. Loop diameter is 35 µm; crystal is visible as a thin rectangular plate inside the loop.

***Figure 7.11*:** Crystal of M2(21-61) V27A during data collection. Loop diameter is 50 µm; crystal is visible as a small cube sitting atop the upper left portion of the loop.

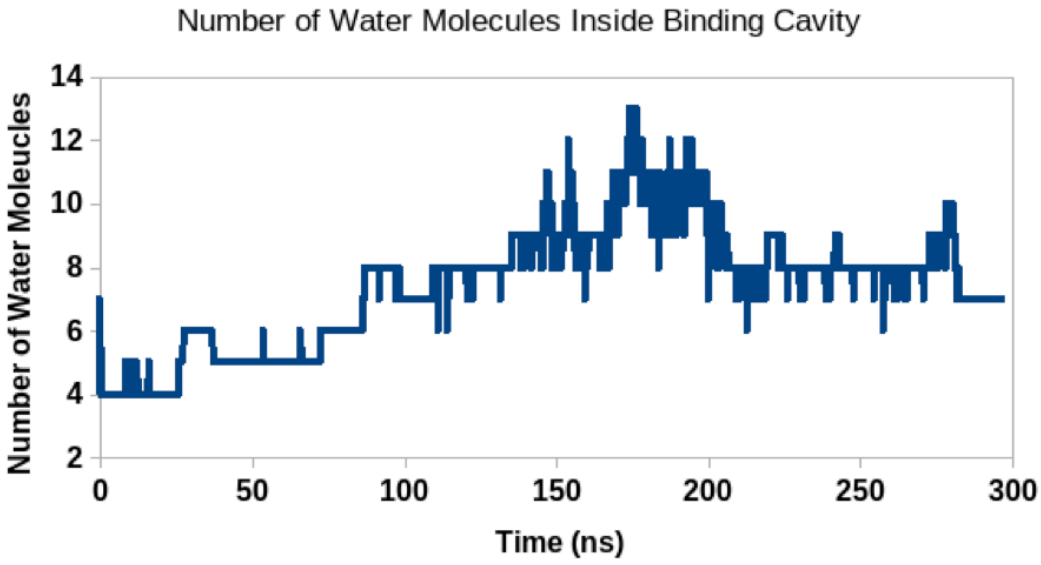

***Figure 7.12*:** Total number of waters inside binding cavity. At 85 ns 6 waters are defined and after 85ns, 2 layers of water molecules are formed.

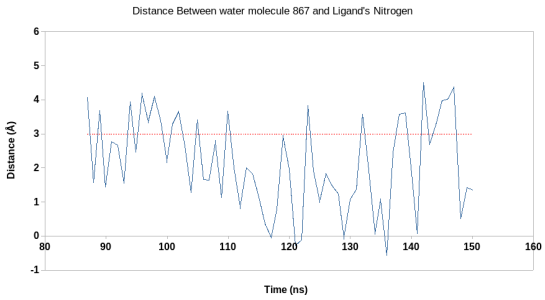
Distance Between water molecule 867 and Ligand's Nitrogen
Distance (Å)
Time (ns)

A

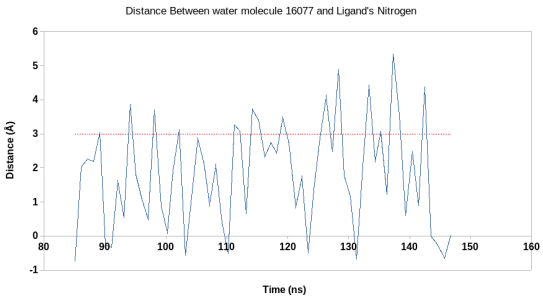
Distance Between water molecule 16077 and Ligand's Nitrogen
Distance (Å)
Time (ns)

B

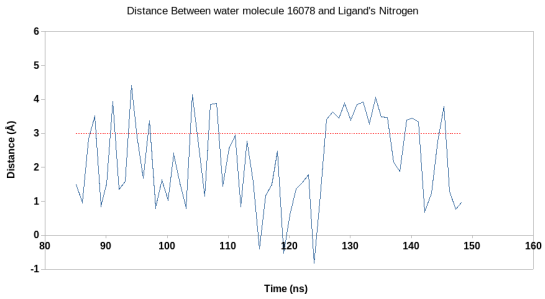
Distance Between water molecule 16078 and Ligand's Nitrogen
Distance (Å)
Time (ns)

C

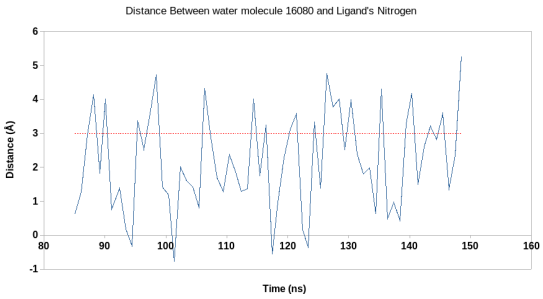
Distance Between water molecule 16080 and Ligand's Nitrogen
Distance (Å)
Time (ns)

D

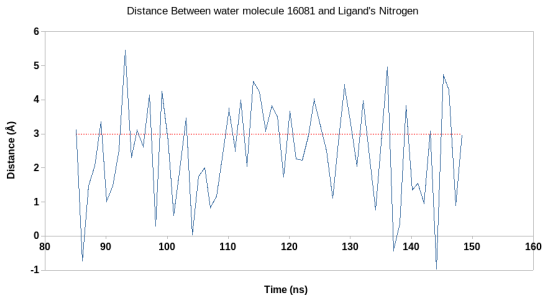
Distance Between water molecule 16081 and Ligand's Nitrogen
Distance (Å)
Time (ns)

E

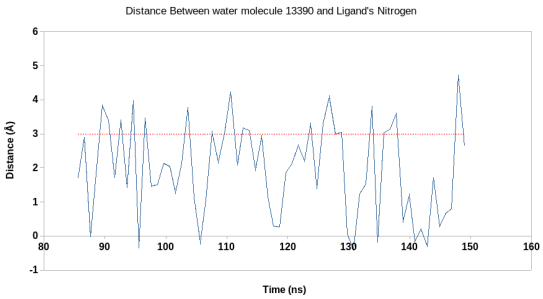
Distance Between water molecule 13390 and Ligand's Nitrogen
Distance (Å)
Time (ns)

F

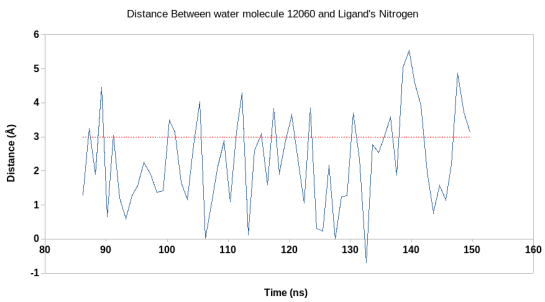
Distance Between water molecule 12060 and Ligand's Nitrogen
Distance (Å)
Time (ns)

G

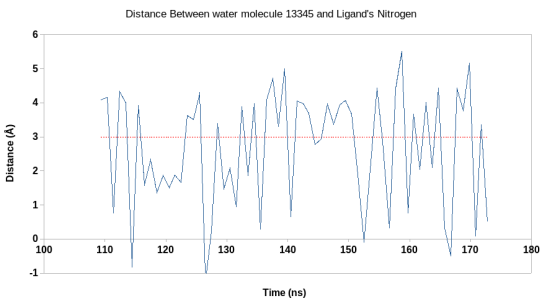
Distance Between water molecule 13345 and Ligand's Nitrogen
Distance (Å)
Time (ns)

H

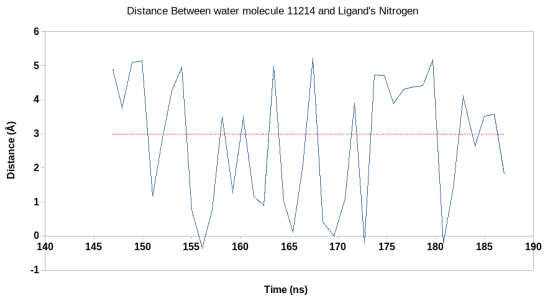
Distance Between water molecule 11214 and Ligand's Nitrogen
Distance (Å)
Time (ns)

I

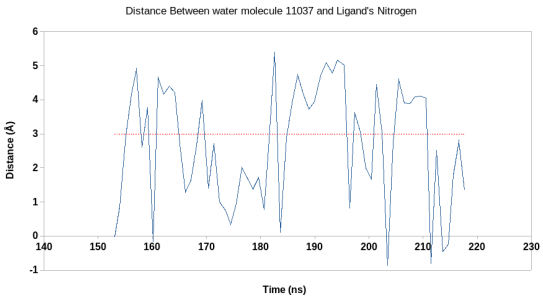
Distance Between water molecule 11037 and Ligand's Nitrogen
Distance (Å)
Time (ns)

J

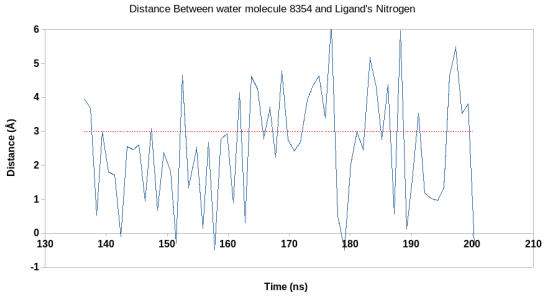
Distance Between water molecule 8354 and Ligand's Nitrogen
Distance (Å)
Time (ns)

K

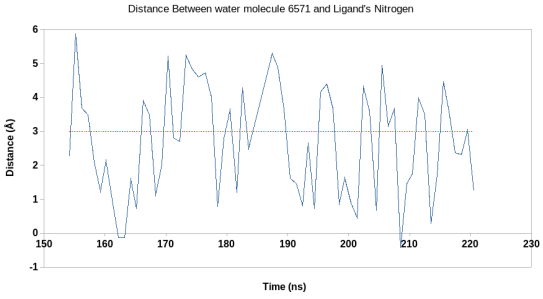
Distance Between water molecule 6571 and Ligand's Nitrogen
Distance (Å)
Time (ns)

L

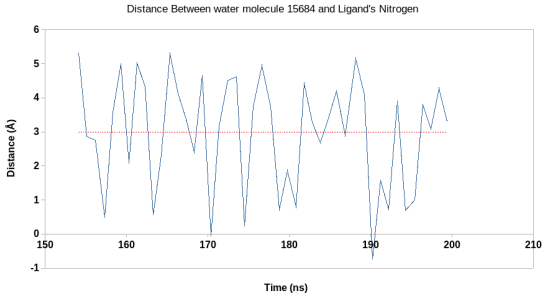
Distance Between water molecule 15684 and Ligand's Nitrogen
Distance (Å)
Time (ns)

M

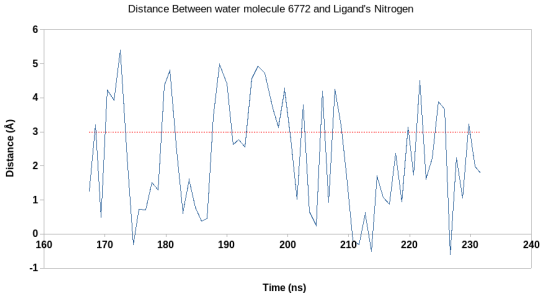
Distance Between water molecule 6772 and Ligand's Nitrogen
Distance (Å)
Time (ns)

N

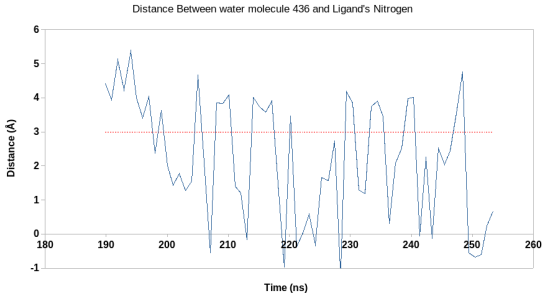
Distance Between water molecule 436 and Ligand's Nitrogen
Distance (Å)
Time (ns)

O

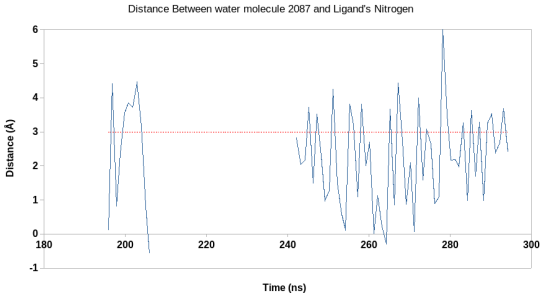
Distance Between water molecule 2087 and Ligand's Nitrogen
Distance (Å)
Time (ns)

P

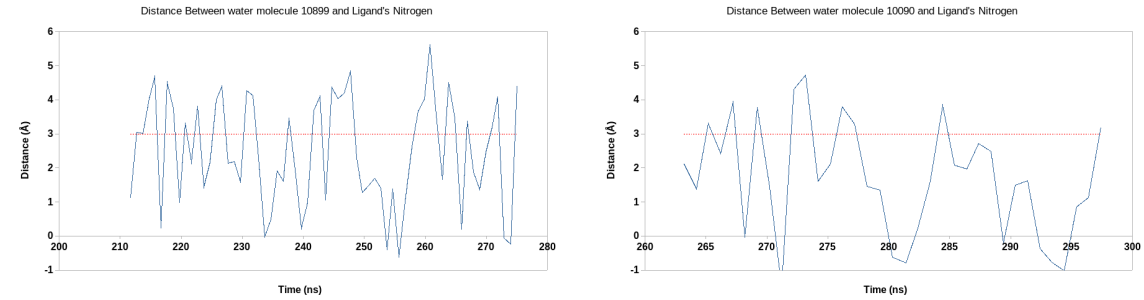

Q R

Figure 7.13**:** A - R: Distance between the position along the pore axis of each of 18 water molecules, and the corresponding position of nitrogen atom of the spiro amine. Water molecules that locate within 6 Å radius of His37 and 6Å radius of ligand were selected for analysis. Distances between ligand's nitrogen and each water's oxygen molecule were calculated based on their position on Z-axis (helical bundle axis) of the channel. Red dashed line separates the two layers of water molecules indicated after the first 85ns when the ligand is equilibrated inside binding cavity. A dotted red line is used to describe the two layers. One water molecule (water molecule 2087, panel P) entered into this region of the pore for 10 ns, followed by exiting for 40 ns, and then re-entering for the last 30 ns.

CHAPTER 8

Rimantadine Binds to and Inhibits the Influenza A M2 Proton Channel without Enantiomeric Specificity

8.1 Introduction

The influenza A matrix 2 (M2) protein is the most extensively studied viroporin, and is currently considered the most well-validated viroporin antiviral drug target. [326] It is an attractive target for anti-influenza medications because it mutates less frequently than other proteins within the virus. [299] However, though the M2 channel mutates infrequently, drug-resistant mutations have become prevalent since the early 2000s and currently this class of drugs is no longer recommended for treatment of influenza infections. [327, 328] The rise of adamantane-resistant influenza necessitates an in-depth understanding of the stereochemical requirements for M2 channel blockers so that new drugs can be developed.

The M2 protein is a homotetrameric proton channel [294, 329-331] whose minimally functional transmembrane core consists of residues 22-46. [317, 318] The gating residues involved in proton conductance are His37 and Trp41. [332, 333] After an influenza virus particle is endocytosed by the host cell, proton transport through the M2 channel lowers the pH within the viral envelope and allows viral ribonucleoproteins (RNPs) to unpack from M1. [263] Blocking proton transport through the M2 wild type (WT) channel using adamantanes [334, 335] prevents this dissociation from happening and thus prevents viral replication from occurring. [336-338] The proton transport function of M2 plays a second role in the viral life cycle; M2 inhibits the acidification of the trans Golgi compartment, thereby preventing premature activation of the acid-sensitive hemagglutinin protein. [339, 340]

Solid state NMR (ssNMR) spectra using deuterium-labeled (*R*)- and (*S*)-rimantadine showed differences in chemical shifts when the two enantiomers bind to full-length M2 WT. [341] These spectral differences were considered to arise from differences in potency and affinity of the isomers. However, electrophysiological (EP), isothermal titration calorimetry (ITC), and antiviral assays carried out using enantiomerically pure rimantadine indicated that the two enantiomers have equal potency against M2 WT. [336, 342] Additionally, *in vivo*

experiments in mice have shown similar antiviral activity for both enantiomers. [343] One possible explanation for the difference in ssNMR chemical shifts for the two rimantadine enantiomers might relate to differences in the kinetics of binding, which are particularly important for the potency of M2 inhibitors. In the earlier EP study examining rimantadine enantiomer binding to M2 WT, [344] the time traces were not recorded for sufficient time to allow accurate measurement of k_{off}. Here we perform a more stringent kinetic study by recording both the binding and washing curves so that we can more accurately measure k_{off}. Using this improved methodology, we did not observe any difference in binding kinetics between the (*R*)- and (*S*)- enantiomers, as shown by similar values for k_{on}, k_{off} and K_d in EP assays. We also tested the potency of the two enantiomers against an amantadine-sensitive strain of influenza in an antiviral plaque assay and found that the EC_{50} values are indistinguishable.

We also report the crystal structure of M2(22-46) WT in complex with enantiomerically pure (*R*)- and (*S*)-rimantadine to explore whether the chirality of drugs has an effect on drug binding and inhibition, as might be expected for enantiospecific binding. Though the crystals of each rimantadine enantiomer complex had different space groups and unit cell dimensions, we observed that the electron density corresponding to bound drug is similar for the two enantiomers. The density indicates a mechanism of binding in which the rimantadine ethylamine can rotate to four positions to form hydrogen bonds with ordered waters in the M2 pore. We observed slight differences between the hydration of the two enantiomers within the pore.

Finally, we employed grand canonical ensemble molecular dynamics simulations (GCMC/MD) to provide further insight into the water network present in the rimantadine binding site. GCMC [345-347] can be used in combination with MD simulations in order to bypass the kinetic barriers associated with the binding and unbinding of occluded water sites. This is done by simulating the system at a constant chemical potential, whilst inserting and deleting waters from a region of interest (defined as the rimantadine binding site, in this case). Additionally, carrying out these simulations at a range of chemical potential values – referred to as GCMC titration – allows the binding free energy of the water network to be rigorously calculated. It is of interest that the titration analysis indicates that a

chiral difference is apparent when the upper water layer of the binding site is displaced compared to the two layers which are sufficiently flexible to eliminate a chiral preference. To validate our GCMC/MD simulations we first calculated the relative binding free energy of the (*R*)- and (*S*) enantiomers to the M2 pore.

8.2 Results and discussion

8.2.1 X-ray crystal structures

We have solved two X-ray crystal structures of (*R*)-rimantadine and (*S*)-rimantadine bound to M2(22-46) WT through co-crystallization experiments (see Table 8.3). Crystals of (*R*)-rimantadine bound to M2(22-46) (PDB ID 6US9) formed at pH 8.5 in the P 2_1 space group with unit cell dimensions a, b, c (Å) = 48.18, 48.70, 71.67 and α, β, γ (˚) = 90, 90, 90, and the diffraction was limited to 2.00 Å. Crystals of (*S*)-rimantadine bound to M2(22-46) (PDB ID 6US8) formed at pH 7.5 in the P 2_1 2_1 2_1 space group with unit cell dimensions a, b, c (Å) = 49.39, 76.09, 98.63 and α, β, γ (˚) = 90, 90, 90. These crystals diffracted to a resolution of 1.70 Å, making this the highest-resolution structure of M2 bound to a drug or inhibitor. [34, 61, 62]

As in previously solved structures of M2 bound to drugs and inhibitors,[61, 62] M2 is in the $Inward_{closed}$ conformation and we observe electron density corresponding to bound drug at the channel's N-terminus near Ser31, with two layers of ordered water molecules between the bound drug and the channel's gating His37 residues (see Figure 8.1a, 8.1b).

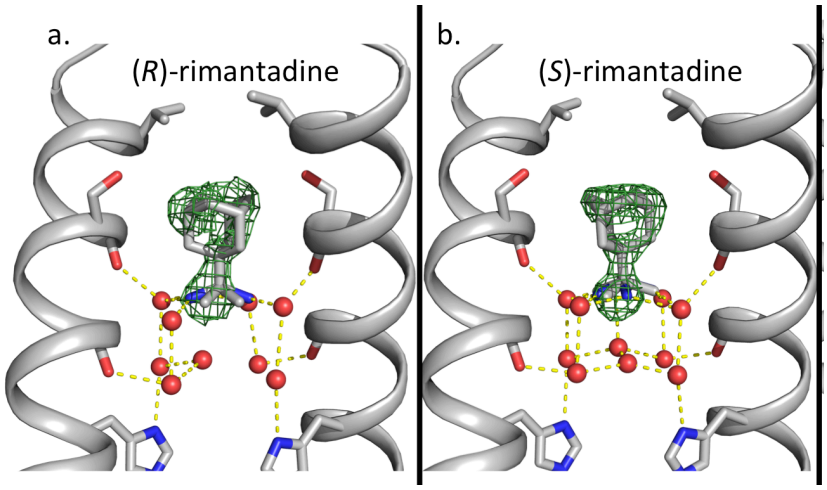

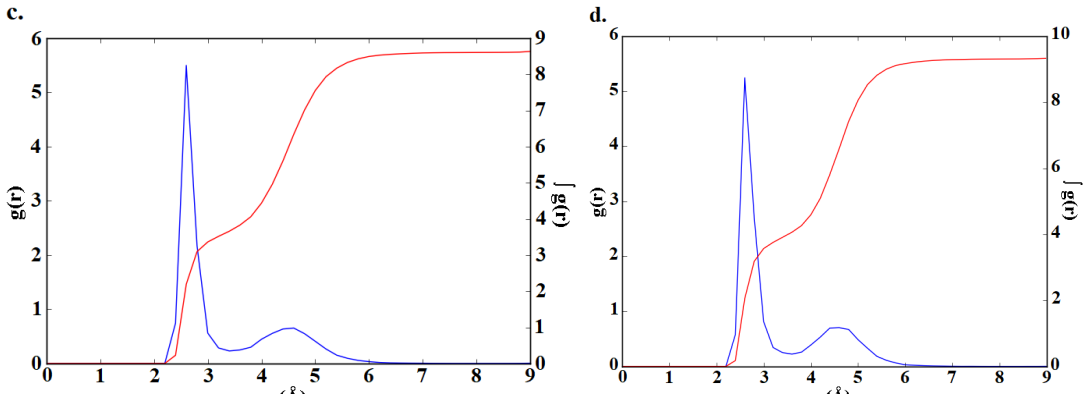

Figure 8.1: (*a*), (*b*) Polder maps calculated in the absence of bound rimantadine are shown here to a contour of 3 σ (dark green mesh) for the X-ray crystal structures of (*R*)-rimantadine (*a*) and (*S*)-rimantadine (*b*) bound to M2(22-46) WT. Front and back monomer helices have been removed to show the contents of the pore. For both structures, the density corresponding to the rimantadine ethylammonium group has been modeled as the average of four rotational conformers. We observed a network of ordered waters between the bound rimantadine and the gating His37 residues; the waters form hydrogen bonds with pore-facing carbonyl groups and also form a vertical H-bond network leading down to the gating His37 residues. (*c*), (*d*), The radial distribution function (RDF) g(r) for (*R*)-rimantadine (*c*) and (*S*)-rimantadine (*d*) between the ammonium group and water oxygen atoms from the 200 ns MD simulation, shows a strong peak at 2.7 Å which corresponds to the upper waters layer, forming hydrogen bonds with the ammonium group of rimantadine and the carbonyl groups of Ala30. The cumulative integrated intensity ∫g(r), shown in the right axis, at 2.7 Å indicates ca. 4 waters. The second broad peak at 4.8 Å corresponds to ca. 5-6 waters of the lower layer, which form hydrogen bonds with the His37 imidazole groups and the carbonyl groups of Gly34.

These waters form hydrogen bonds to pore-facing carbonyl groups from residues Ala30 and Gly34, and also form a vertical hydrogen bonding network leading down to His37. The X-ray crystal structures remained unchanged during 300 ns MD simulations in hydrated POPC bilayers (see Figure 8.2).

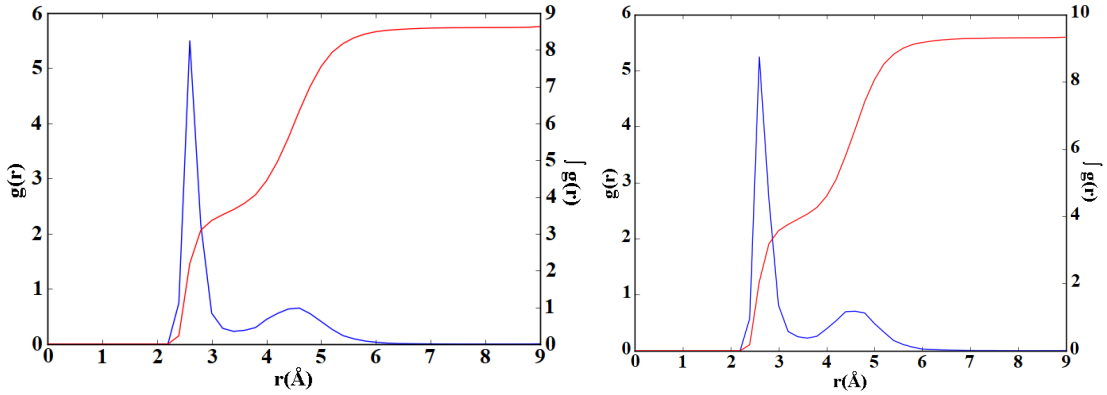

Figure 8.2: (*left*) (*R*)-rimantadine. (*right*) (*S*)-rimantadine. The radial distribution function (RDF) g(r), shown in left axis, between the rimantadine ammonium group and water oxygen atoms from the 200ns MD simulation, shows a strong peak at 2.7 Å corresponds to upper layer waters forming hydrogen bonds with the ammonium group of rimantadine and with the carbonyl groups of Ala30. The cumulative integrated intensity ∫g(r), shown in the right axis, at 2.7 Å indicates c.a. 4 waters. The second broad peak at 4.8 Å corresponds to the c.a. 5-6 waters of the lower layer, which form hydrogen bonds to the His37 imidazole groups and the carbonyl groups of Gly34. These findings are in good agreement with the X-ray crystal structures.

Though enantiomerically pure (*R*)- or (*S*)-rimantadine was used in these crystallization trials, the chirality of the drug is not obvious from the electron density in either structure. This is presumably a result of averaging more than one binding position within the crystal lattice. Thus, we have modeled the bound drug for each of the structures as a superposition of four rotational – by rotation of $C1_{Ad}$-C_{Ethyl} bond - conformers, with the drug ammonium group forming hydrogen bonds to two of the four top layer waters in each position. In our previous crystal structure of racemic rimantadine bound to M2(22-46) WT (PDB ID 6BKL), [61] we observed this same ambiguity regarding the position of the rimantadine ethylammonium group, which we interpreted as an effect of co-crystallizing using racemic rimantadine.

The occupancies of the four rotational conformers of (*R*)- or (*S*)-rimantadine were allowed to float during refinement; alternate conformers were removed from the model if their occupancy was refined to zero. Each structure contains four tetramers per asymmetric unit; the refined occupancies for the four rimantadine rotational conformers for each tetramer are shown in Table 8.4 To summarize, for the structure of (*R*)-rimantadine bound to M2(22-46), three conformers were

observed per tetramer with some variations in the occupancy of each (*R*)-rimantadine conformer depending on the tetramer. In the structure of (*S*)-rimantadine bound to M2(22-46), three of the tetramers have relatively high (> 0.30) occupancy for two of the (*S*)-rimantadine conformers, with the other two conformers having either zero or < 0.05 occupancy. The fourth tetramer has low occupancy (0.01 and 0.11) for two of the conformers and relatively high occupancy (>0.40) for the other two. These data suggest that the binding mechanism remains the same for both enantiomers with the observed slight differences likely due to the hydration of each enantiomer as shown in Figure 8.1. We subsequently explored the hydration of each enantiomer inside the M2 pore using GCMC/MD simulations.

In addition to the density associated with (*S*)-rimantadine in the pore, we unexpectedly observe electron density that we provisionally assign to rimantadine in the structure of the complex at 1.7 Å. The additional (*S*)-rimantadine lies at locations that stabilize the packing of individual tetramers in the crystal lattice (see Figures 8.10 and 8.11). The two tetramers have an antiparallel orientation, and the rimantadine makes contacts to residues near the N-terminus of one tetramer and residues near the C-terminus of the other tetramer. The location of the ethylamonnium group is not clear from the electron density, so we have only modeled the adamantyl group. The C-terminal contacts are similar to those proposed for a weak, exterior site observed in solution and ssNMR studies that indicate binding of the adamantanes to the exterior of the channel's C-terminus at high concentrations of drug (including Leu 40, Ile42, Asp44, Arg45, and Leu46). [50, 58] However, these previous spectroscopic studies did not identify contacts near the N-terminus (Leu26, Val28, Ala29, Ile32). Thus, it is likely that the exterior site see here is a crystallographic artifact.

8.2.2 Electrophysiology and antiviral plaque assays

To study whether chirality has an effect on the functional activity against the M2 WT channel, we determined the association constant (k_{on}), the dissociation constant (k_{off}), and the binding affinity (K_d) for (*R*)- and (*S*)-rimantadine in a two-electrode voltage clamp electrophysiological (TEVC) assay using kinetic studies.

[348-350] Full length M2 WT from the amantadine-sensitive Udorn strain was expressed in oocytes, and a low pH 5.5 solution was applied to activate the M2 channel. Next, a pH 5.5 solution containing testing compound was applied to inhibit the M2 channel. Once the current reached the steady state (highest conductance), compound dissociation was initiated by changing the oocyte bathing solution to pH 5.5 without drug. During the washout, a few pH 8.5 pulses were applied to make sure the current went to baseline to ensure the oocyte quality. The recording traces are shown in Figure 8.3.

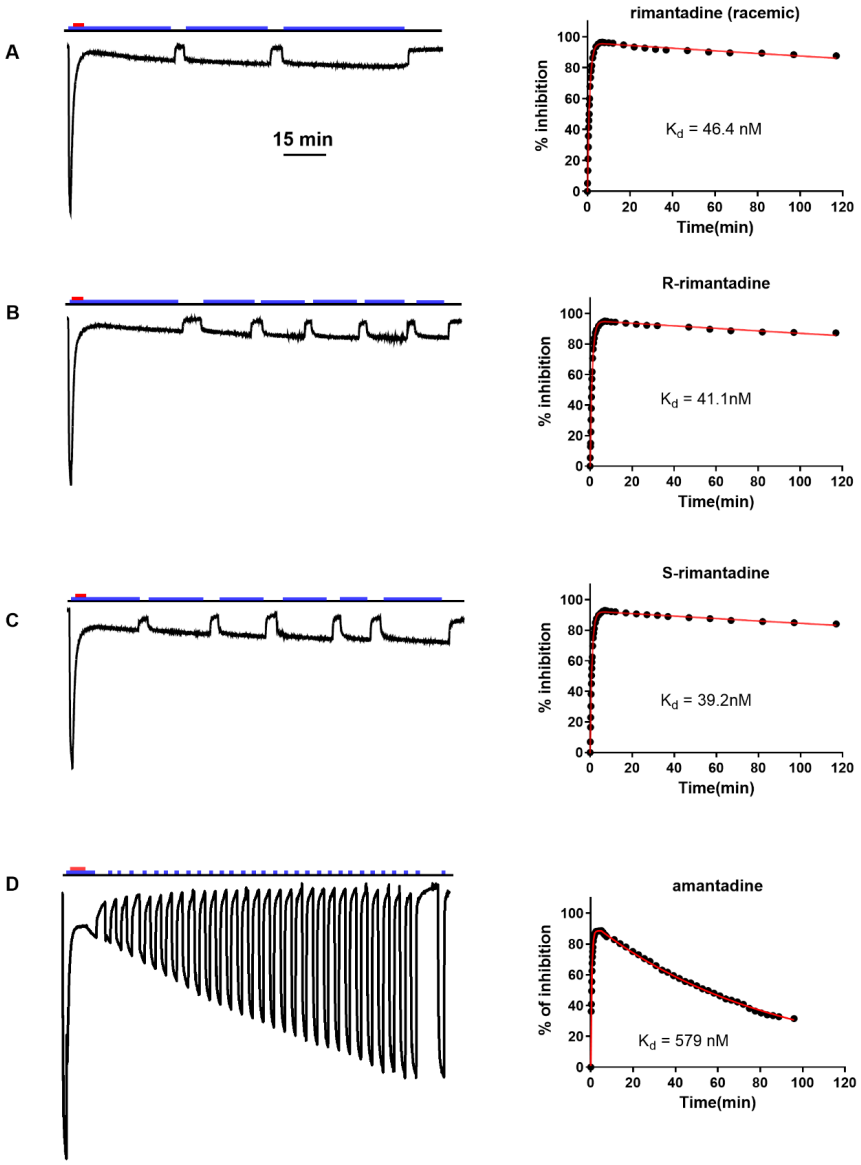

Figure 8.3: Rimantadine enantiomers and amantadine binding kinetics against Udorn M2 WT were determined using a combined application and washout procedure TEVC assay. (*a*)

Racemic rimantadine (*b*) (*R*)-rimantadine, (*c*) (*S*)-rimantadine, or (*d*) amantadine was applied to oocytes for 5 to 7 min after the inward current reached its maximum, then a washout protocol was applied to the oocytes. During the washout, pH 8.5 pulses were applied to make sure the current went to baseline to ensure the oocyte quality. The blue bar above the recording trace indicates the period in which the pH 5.5 Barth solution was applied; the red bar indicates the period in which compounds in pH 5.5 Barth solution were applied. Representative recording traces are shown on the left side of each figure. Data extracted from the recording traces were plotted with an association then dissociation equation in GraphPad Prism 5 as shown in the right side of each figure. The best-fit values are shown in the Table 8.1.

Table 8.1: Summary of the binding affinity of amantadine and rimantadine enantiomers against Udorn M2 WT

	Rimantadine (racemic)	(*R*)-rimantadine	(*S*)-rimantadine	Amantadine
Concentration tested	50 μM	50 μM	50 μM	100 μM
k_{on} ($min^{-1}M^{-1}$)	19600 ± 300	20800 ± 700	22500 ± 300	20500 ± 300
k_{off} (min^{-1})	$(9.1 \pm 0.8)*10^{-4}$	$(9 \pm 2)*10^{-4}$	$(8.8 \pm 0.8)*10^{-4}$	$(119 \pm 2)* 10^{-4}$
$K_d = k_{off}/k_{on}$ (nM)	46 ± 4	41 ± 9	39± 4	580 ± 20

Fitting the binding and washing curves with association and dissociation equations yielded the k_{on}, k_{off}, and K_d values for (*R*)-, (*S*)-, and racemic rimantadine. [350] As shown in Table 8.1, the binding kinetics parameter (k_{on}, k_{off} and K_d) values for (*R*)-, (*S*)- and racemic rimantadine are not significantly different, which suggests that both the (*R*)- and (*S*)-enantiomers of rimantadine bind to the M2 channel with equal potency. We also included amantadine as a control: the k_{on} of amantadine is comparable with that of rimantadine, however the calculated k_{off} of amantadine is more than 10-fold faster than that of (*R*)- and (*S*)-enantiomers of rimantadine, therefore the binding affinity of amantadine to Udorn M2 is about 10-fold weaker than rimantadine to M2. Overall, there is no significant difference among the K_d values for (*R*)- and (*S*)-enantiomers as well as the racemic mixture of rimantadine. We note that a previous study [336] reported 100-fold higher k_{off} values, resulting in significantly higher K_d values for (*R*)- and (*S*)-enantiomers and the racemic mixture of rimantadine with 3.2, 3.9 and 7 μM, respectively, as opposed to the values of 41, 39, and 46 nM,

respectively, reported here. In the previous study, [336] only the binding curve was recorded and used for data fitting to derive both k_{on} and k_{off}, which might result in significant variations of k_{off} values (personal communication with Dr. David Busath, the lead author who performed the electrophysiological assay in the previous study); the time traces were not recorded for sufficient time to allow accurate measurement of k_{off} and thus, the previous values are an upper limit of the true K_d value. In contrast, we performed more stringent kinetic studies by recording both the binding and washing curves in the current study. As such, the k_{off} values were accurately quantified from the washing curve, which was then used to fit the binding curve to determine k_{on}. The validity of this methodology in determining the K_d values of M2-S31N and M2-V27A inhibitors has been demonstrated in several studies, which showed a positive correlation between the K_d values and the cellular antiviral activity. [348-350]

To further confirm that the (*R*)- and (*S*)-enantiomers of rimantadine have indistinguishable potency in blocking the M2 channel, we tested these compounds against the amantadine-sensitive A/Soloman Island/3/2006 (H1N1) strain (see Figure 8.4). As expected, [285] both (*R*)- and (*S*)-rimantadine inhibit viral replication with EC_{50} values of 19.62 and 24.44 nM, respectively. Taken together, results from both the electrophysiological assay and the antiviral plaque assay showed that both (*R*)- and (*S*)-rimantadine have equal potency in blocking the M2 WT channel.

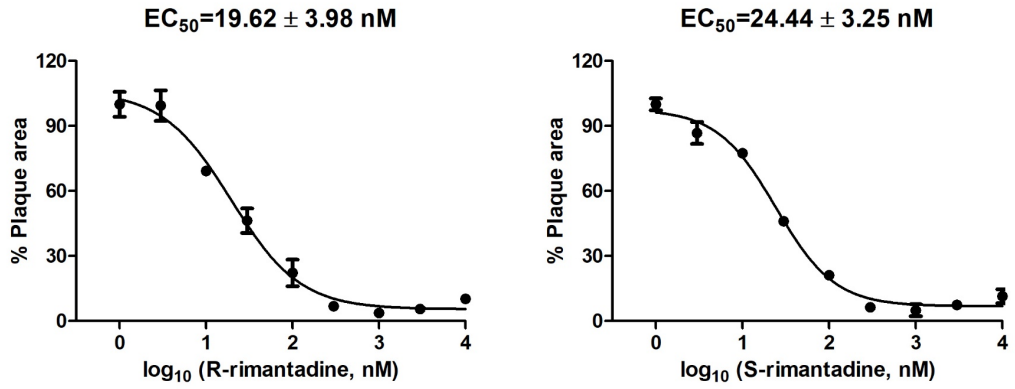

***Figure 8.4*:** Cellular antiviral assay results of (*R*)- and (*S*)-rimantadine against the amantadine-sensitive A/Soloman Island/3/2006 (H1N1) strain. The antiviral potency was determined in a plaque assay. The EC_{50} values are the mean ± standard deviation of two independent repeats.

8.2.3 Binding free energy calculations

To validate our experimental results, the relative binding free energies of binding and hydration for the (*R*)- and (*S*)- enantiomers were calculated using the free energy perturbation method [351, 352] (see Figure 8.5) coupled with MD simulations (FEP/MD) and the multistate Bennett acceptance ratio (MBAR) method for processing the free energy data. [353, 354] The free energy perturbations carried out show that the hydration free energy difference between the two enantiomers (where a positive value would indicate that the (*R*)-enantiomer is favored, and vice versa) is -0.06 ± 0.03 kcal mol^{-1} when starting the calculation from the (*R*)-enantiomer, and 0.000 ± 0.005 kcal mol^{-1} when starting from the (*S*)-enantiomer (the uncertainties given represent the standard errors over the three runs). Given that bulk water is an achiral environment, the true value of this hydration free energy difference is zero, and these values therefore appear correct. This result therefore supports the view that the free energy protocol used is suitable for this perturbation.

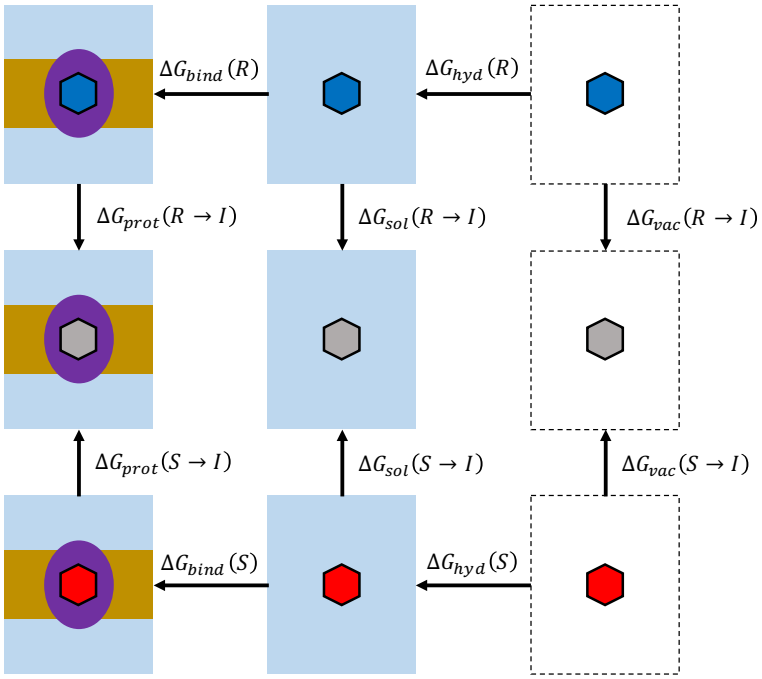

Figure 8.5: Free Energy Perturbation via Intermediate Structure. Thermodynamic cycle depicting the free energy calculations performed, with perturbations between the (*R*)- and (*S*)-

enantiomers (blue and red, respectively), where the calculation is performed via the achiral intermediate 1-Ad-CH_2-NH_3^+ (I, shown in grey).

The relative binding free energy difference between the two enantiomers was calculated as +0.29 ± 0.04 kcal mol^{-1}, and +0.33 ± 0.06 kcal mol^{-1}, when starting the calculations from the (*R*)- or (*S*)-enantiomer, respectively. This indicates a very slight preference for the (*R*)-enantiomer, but it should be noted that the sensitivity of free energy calculations from molecular simulations is typically considered to be around 1 kcal mol^{-1}, [355] in which case these values are not sufficiently different from zero to indicate a clear chiral preference. However, these results favoring a higher affinity of (*R*)-rimantadine are in agreement with our ITC measurements and previous calculations using the BAR method and FEP/MD simulations using different intermediates. [336, 356] The comparison of these results with chemical shift differences observed in ssNMR experiments [341] is not straightforward mainly due to the differences in experimental conditions.

8.2.4 GCMC titration

The titration plots obtained for both (*R*)- and (*S*)-rimantadine are shown in Figure 8.12 where a curve has been fitted to the data, using a set of four sigmoid functions (four was qualitatively chosen to be most appropriate), with 1000 bootstraps – the raw values are given in Table 8.2. These plots are superimposed in Figure 8.6, and the dependence of the water binding free energy on the number of waters, i.e. solvation level (calculated using the equation for $\beta\Delta G^{o}_{bind}(N_i \rightarrow N_f)$, with $N_i = 0$ and a range of N_f values) is shown in Figure 8.8.

In the experimental structure, the number of waters in the upper layer (i.e. close to Ala30) is 4 and in the lower layer (i.e. close to Gly34) is 5. [61] The GCMC titration calculations involve progressively reducing the chemical potential applied to the water molecules in the ligand binding site. As the chemical potential is reduced, the more weakly-bound water molecules are removed from the binding site, until eventually an entirely dry site results (see Figures. 8.6, 8.7, 8.12). In addition, the binding free energy of the water network may be calculated from the

water occupancy as a function of chemical potential data. The resulting free energy data as a function of water occupancy may be used to determine the equilibrium hydration level, which corresponds to the minimum on the curve of the free energy profile (see Figure 8.8).

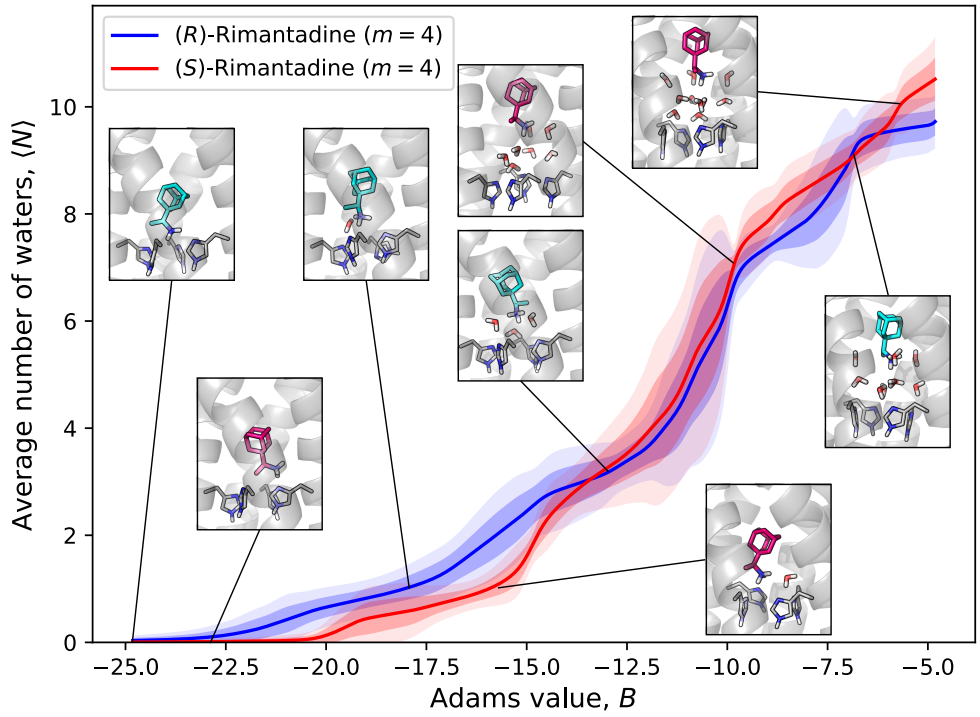

Figure 8.6: Direct comparison (overlay) of the titration plots for the two rimantadine enantiomers, as shown separately in Figures 8.12a and 8.12b, with inset images added to show representative structures from different points on the curve. The (*R*)-enantiomer is shown in cyan and the (*S*)-enantiomer is shown in pink. The *m=4* in the legend refers to the fact that a sum of four sigmoid functions were fitted to the data.

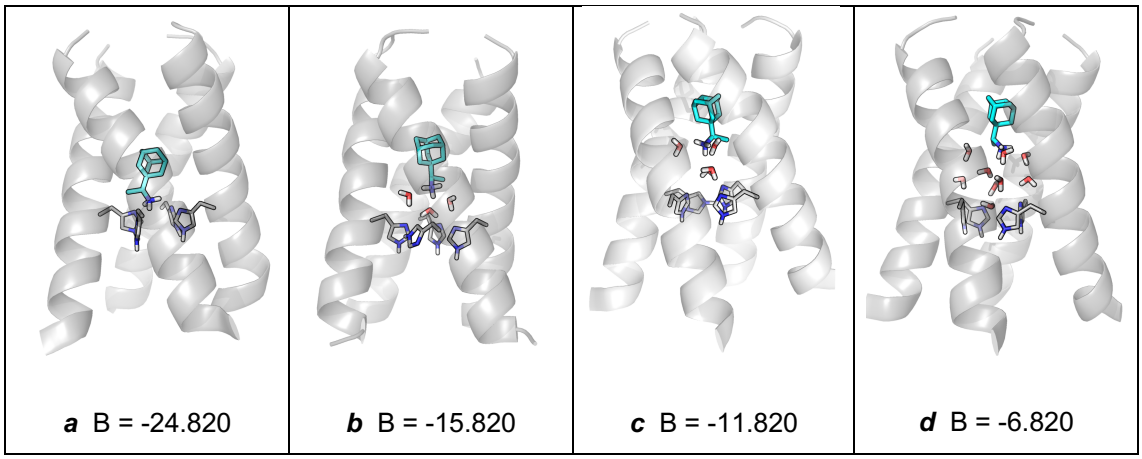

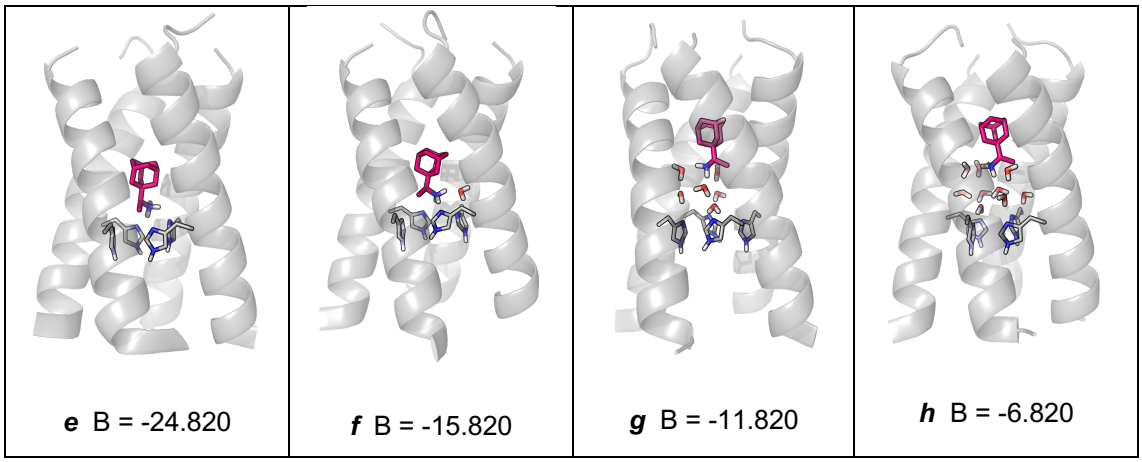

***Figure 8.7*:** A selection of representative frames from the simulations performed, showing the structural trends as the waters are removed from the GCMC region. The (*R*)-enantiomer is shown in cyan, and the (*S*)-enantiomer is shown in pink.

For both of the enantiomers, the free energy profile (see Figure 8.8) shows a minimum for $N = 9$, indicating that this is the most favourable number of water molecules in the binding site, in agreement with our crystal structures. However, there is a very slight disagreement between the values of the water network binding free energy values at equilibrium, with that for the (*R*)-enantiomer calculated as -30 ± 1 kcal mol^{-1}, and that for the (*S*)-enantiomer calculated as -29 ± 1 kcal mol^{-1}. On this scale, this difference of 1 kcal mol^{-1} is unlikely to be significant, though the observation that the water network is marginally more stable for the (*R*)-enantiomer is consistent with the relative ligand binding free energies reported above. Interestingly, the free energy change associated with adding a tenth water to the binding site for the (*R*)- and (*S*)-enantiomers are +0.1 ± 0.1 and +0.3 ± 0.2 kcal mol^{-1}, respectively, indicating that the $N = 10$ state is only slightly less stable at equilibrium.

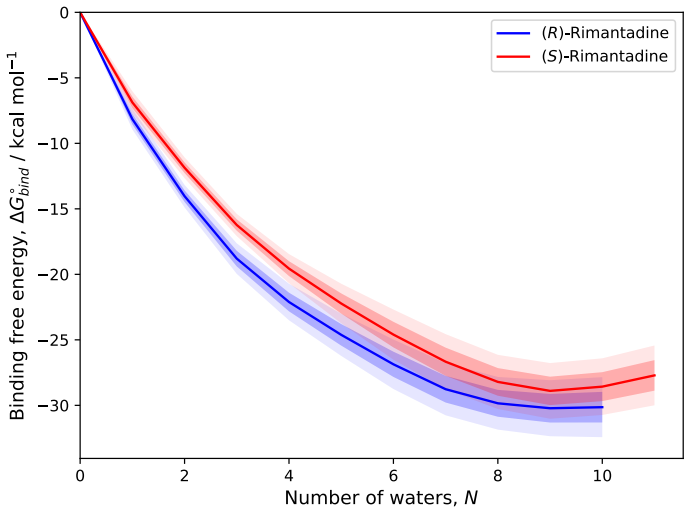

***Figure 8.8*:** Water binding free energy plots for both enantiomers.

However, it is of interest that the free energy profiles show distinct differences, particularly at low values of the chemical potential where the distributions of the water and ligand positions for the (*R*)- and (*S*)-enantiomers are not as consistent as at equilibrium (see Figures 8.6, 8.8 and 8.12). At low values of the chemical potential, when less water is in the binding site, the difference in the water network binding free energies between the two enantiomers becomes more significant. For example, a network of 4 water molecules which form the lower water layer appear to be 2.6 ± 0.6 kcal mol^{-1} more stable in the presence of the (*R*)-enantiomer (*N* = 4 in Table 8.2). This implies that a stereochemical difference may become apparent when the upper water layer is removed from the binding site.

***Table 8.2*:** Calculated water binding free energies $\beta\Delta G^{o}_{bind}$ $(N_i \rightarrow N_f)$, using the equation and the determined titration data. For each enantiomer, the free energy of binding N waters is given (note that these can be at any N positions), along with the difference made by adding the Nth water, for both enantiomers. The uncertainties given are standard deviations from 1000 bootstraps, where each bootstrap involves randomly selecting one value of N for each value of water.

	Binding free energy (kcal mol^{-1})	
	***(R)*-enantiomer**	***(S)*-enantiomer**

Number of waters, N	Water network	N^{th} water	Water network	N^{th} water
1	-8.2 ± 0.4	-8.2 ± 0.4	-6.9 ± 0.4	-6.9 ± 0.4
2	-14.0 ± 0.4	-5.9 ± 0.4	-11.9 ± 0.4	-5.0 ± 0.1
3	-18.8 ± 0.6	-4.8 ± 0.4	-16.2 ± 0.4	-4.4 ± 0.2
4	-22.1 ± 0.7	-3.3 ± 0.4	-19.6 ± 0.6	-3.3 ± 0.4
5	-24.6 ± 0.8	-2.5 ± 0.4	-22.2 ± 0.8	-2.7 ± 0.4
6	-27 ± 1	-2.3 ± 0.3	-25 ± 1	-2.4 ± 0.4
7	-29 ± 1	-1.9 ± 0.2	-27 ± 1	-2.1 ± 0.2
8	-30 ± 1	-1.1 ± 0.2	-28 ± 1	-1.5 ± 0.2
9	-30 ± 1	-0.4 ± 0.3	-29 ± 1	-0.7 ± 0.3
10	-30 ± 1	+0.1 ± 0.1	-29 ± 1	+0.3 ± 0.2
11	N/A	N/A	-28 ± 1	+0.9 ± 0.2

When carrying out titration calculations using GCMC/MD, there is a concern that at B values far from B_{equil}, as waters are added or removed from the system, they may be constantly replenished by diffusion of waters into the GCMC region from bulk water. However, this effect appears to be minimal for these simulations (see Figure 8.14), likely due to the relatively occluded location of the GCMC region. Furthermore, we observed that the effect was significantly less for the (*S*)-enantiomer than the (*R*)-enantiomer.

The general trend observed was that, as the chemical potential value decreases and waters are removed from the GCMC region, waters from the upper layer, i.e. close to Ala30, are removed first, and the ligand gradually descends further into the protein to interact directly with the lower layer, i.e. close to Gly34 (see Figures 8.4b,f), and then the His37 residues (see Figures 8.4a,e). This is shown by a selection of simulation snapshots in Figures 8.4 (see also Figure 8.9). It becomes clear that the (*R*)-enantiomer is more resistant to dehydration (see Figures 8.4b,f and Figures 8.3, 8.12a) and descends further into the channel than the (*S*)-enantiomer (see Figures 8.4a,e and Figure 8.12b) and the data shown in Figure 8.13 shows that the (*R*)-enantiomer appears to show a greater propensity for hydrogen-bonding with the His37 residues.

As discussed in the main text, as the B value decreases and waters are removed, the ligand descends further into the channel. These effects can be summarized graphically using the violin plots shown in Figure 8.9, which show the distribution of the number of waters observed (via their *z*-coordinate, given that this is the normal to the membrane), as well as that of the ligand position within the channel. Figure 8.9a shows that, as stated, that waters are preferentially removed from the upper layer, as the B decreases. At $B_{equil} = -6.820$ (see Figures 8.4d,h), the agreement between the two water distributions is excellent, but at lower B values, differences become apparent between the enantiomers. These differences are more pronounced in Figure 8.7, where the distributions of the ligand position do not agree quite as well as at equilibrium. However, at low B values, it becomes clear that the (*R*)-enantiomer is able to descend further into the channel than the (*S*)-enantiomer (see Figure 8.4a,e) and the data shown in Figure 8.9b shows that the (*R*)-enantiomer appears to show a greater propensity for hydrogen-bonding with the His37 residues. These observations indicate a potential difference in binding further down the channel from chiral molecules that might displace the upper layer of waters.

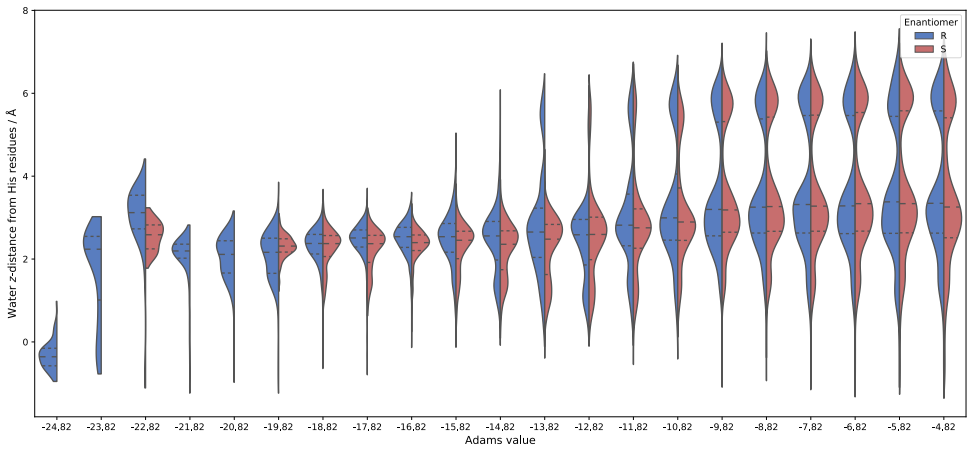

a.

b.

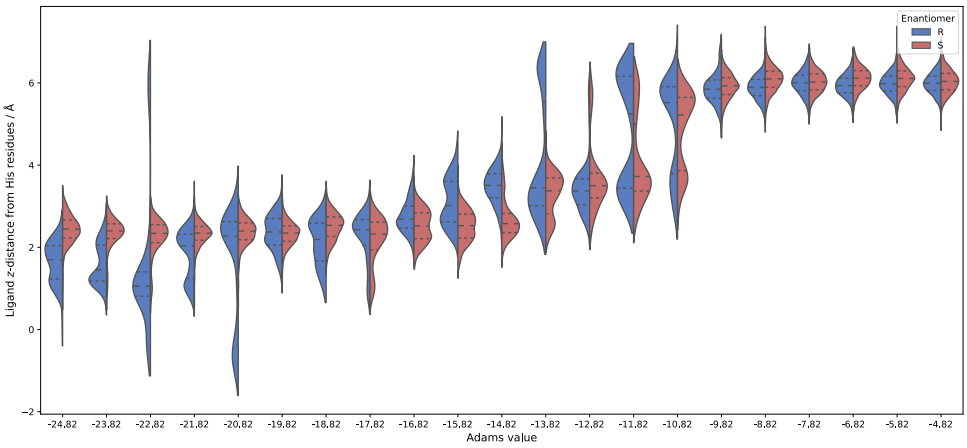

***Figure 8.9*:** Violin plots depicting (*a*) the water distributions observed at each Adams value during the titration calculations; each water point is considered as its z-coordinate (the z-axis is perpendicular to the membrane), relative to the mean z-coordinate of the C_α atoms of the four His37 residues. (*b*) the ligand positions observed at each Adams value during the titration calculations; each point is considered as the z-coordinate (the z-axis is perpendicular to the membrane) of the nitrogen atom of the ligand, relative to the mean z-coordinate of the C_α atoms of the four His37 residues. The data for the (*R*)- and (*S*)-enantiomer are shown in blue and red, respectively. The plots are normalized such that all violins have the same width.

The free energy results obtained also imply that it would be very difficult for a ligand to gain a significant affinity increase by displacing the lower water layer. Given that in the presence of either enantiomer, the binding free energy of the network of 9-10 waters is in the vicinity of c.a. 30 kcal mol^{-1}, displacement of the upper layer would result in a network of 4 waters, with a binding free energy in the vicinity of 20 kcal mol^{-1} (see Table 8.4). This would imply a significant thermodynamic cost associated with the displacement of the lower water layer, in addition to the cost of displacing the upper layer.

However, at lower levels of hydration, due to chirality of the protein, there is a difference in terms of the stability of the water network which can differentiate the binding of a chiral ligand. This is of special interest when considering chiral compounds that can displace the upper water layer, but for an achiral molecule such as spiro-adamantyl amine that displaces the upper water layer this is not important. [61, 94] These observations indicate a potential difference in binding free energy from chiral molecules that might displace the upper layer of waters.

Thus, if chiral compounds were to be developed, it could be that one enantiomer binds more strongly than the other due to better stabilization of the water network.

8.3 Conclusions

The environment within the M2 pore is chiral: L-amino acids form right-handed α-helical monomers which come together to form a left-handed tetrameric helical bundle. Since this chiral environment has the potential to create enantiospecific binding, it was important to investigate whether the chirality of drugs had an effect on drug binding and inhibition. Though the chirality of the M2 protein creates the possibility of preferential binding of rimantadine enantiomers, we do not observe this in X-ray crystal structures of M2(22-46) WT bound to (*R*)- and (*S*)-rimantadine, in EP kinetics assays using the full-length channel, or in antiviral plaque assays. Instead, the crystal structures show that both rimantadine enantiomers bind to the M2 pore, and that the ethylammonium headgroup of both rimantadine enantiomers averages over four orientations. We observe slight differences in the hydration of each rimantadine enantiomer in the crystal structures. However, these slight differences in hydration do not have an effect on drug binding or channel inhibition. We hypothesize that the two layer water network, the upper layer adjacent to Ala30 and the lower layer to Gly34, is sufficiently flexible to mask the chirality of the binding site. The GCMC/MD simulation analysis indicates that, as the upper layer of waters is removed, a more substantial chiral difference is observed in the stability of the water networks, i.e., two layers of water are needed to lose this chiral templating effect. This potential enantiomeric selectivity may be of interest for compounds that are able to displace the upper water layer.

8.4 Materials and methods

8.4.1 Sample preparation and crystallization

The M2TM construct used in this study is as follows:

Ac-SSDPLVVAASIIGILHLILWILDRL-$NH3^{+}$

The peptide was synthesized using previously described methods [40, 266] and purified using HPLC. The peptide was reconstituted into the lipid cubic phase (LCP) using previously described methods [61]: 3 stock solutions of peptide and drug were added to monoolein, the sample was lyophilized, then the dried sample was used to form the cubic phase by adding 20 µL of aqueous solution per 30 mg dried monoolein sample and mixing using a syringe coupler. A detergent additive, MNG-3-C8 ($C_{43}H_{80}O_{22}$, MW = 949.08),4,5 was present in the aqueous phase. Crystallization conditions were screened in plastic LCP plates (Laminex) using a LCP Mosquito robot (TTP Labtech); drops were set up with 100 nL LCP plus 1000 nL precipitant solution. Crystallization trials were carried out at 20˚C. The composition of the LCP and crystallization conditions that yielded the structures described in this paper are as follows:

PDB ID 6US9 ((R)-rimantadine)

LCP: 60 mg monoolein, 1.6 x 10-6 moles M2TM monomer, 1.6 x 10-6 moles (R) rimantadine (4:1 ratio of drug:tetramer); 40 µL of 50 mM MNG-3-C8 in H_2O.

Precipitant solution: 0.015 M Tricine pH 8.5, 24% w/v PEG 4000.

PDB ID 6US8 ((S)-rimantadine)

LCP: 60 mg monoolein, 1.6 x 10-6 moles M2TM monomer, 1.6 x 10-6 moles (S) rimantadine (4:1 ratio of drug:tetramer); 40 µL of 50 mM MNG-3-C8 in H_2O.

Precipitant solution: 0.05 M HEPES pH 7.5, 22% w/v PEG 4000.

8.4.2 Diffraction and refinement

Single crystals were harvested using MiTeGen litholoops and frozen in liquid nitrogen. Data collection was carried out at the Advanced Light Source (ALS) beam 8.3.1 using a Dectris Pilatus3 S 6M detector. Both samples were diffracted under cryogenic temperature (100 K) using a wavelength of 1.1159 Å. Data collection parameters are as follows:

PDB ID 6US9 ((R)-rimantadine): d = 250 mm, t = 0.5 s, oscillation = 1˚, 360 frames.

PDB ID 6US8 ((S)-rimantadine): d = 225 mm, t = 1.0 s, oscillation = 1˚, 360 frames.

Data collection was carried out at 100 K at the Advanced Light Source (ALS) beam 8.3.1. Data processing was carried out in Mosflm [274] and data were scaled in the CCP4 suite. [277] The structure was solved using molecular replacement in Phaser-MR [278] with structure PDB ID 6BKL [61] as a search model in Phaser-MR.8 Refinement was carried out in Phenix9 with model-building in Coot10 and PyMOL.11

Use of the LCP crystallization robot was made possible by National Center for Research Resources Grant 1S10RR027234-01. The authors thank Pil Seok Chae (Hanyang University, Seoul, South Korea) for providing MNG detergent for crystallization trials. Data collection was carried out at ALS 8.3.1. Beamline 8.3.1 at the Advanced Light Source is operated by the University of California Office of the President, Multicampus Research Programs and Initiatives grant MR-15-328599 and NIGMS grants P30 GM124169 and R01 GM124149.

8.4.3 TEVC assay

mRNA synthesis, oocyte culture, microinjection of oocytes, and electrophysiological TEVC recordings were carried out as previously described. [287, 348] The K_d measurement and curve fitting were carried out as previously described. [349, 350] Briefly, the percentage of current during the application of rimantadine enantiomers and washout protocol was plotted with an association then dissociation equation in GraphPad Prism 5.

8.4.4 Plaque reduction assay

Plaque reduction assays were performed in MDCK cells with A/Soloman Island/3/2006 (H1N1) virus as previously described. [287, 349, 357, 358] A/Soloman Island/3/2006 (H1N1) M2 contains the same sequence as A/Udorn/72. Briefly, confluent cells were washed with PBS and infected with virus diluted in DMEM medium supplemented with 0.5% BSA for a final concentration of approximately 100 PFU per well. Viral infection was synchronized for 30 min

at 4 °C, then incubated for 1 h at 37 °C in a 5% CO_2 atmosphere. The inoculum was aspirated, cells were washed and incubated in a DMEM overlay media containing different concentrations of compound, 2 µg/ml N-acetyl trypsin and 1.2% avicel microcrystalline cellulose (FMC BioPolymer, Philadelphia, PA) at 37 °C in a 5% CO_2 atmosphere. Cells were stained 2 days post infection with 0.2% crystal violet dye. EC_{50} values were calculated by plotting the plaque area per well against the rimantadine concentration applied with a dose response function in Prism 5.

8.4.5 Molecular dynamics simulations

Conventional MD simulations

We performed 300 ns MD simulations using an amber99sb force field for the two enantiomers in complex with the X-ray crystal structures embedded in a hydrated lipid bilayer to test the stability of the experimental structures.

The complex of M2TM WT with (*S*)-rimantadine (PDB ID 6US8) or (*R*)-rimantadine (PDB ID 6US9) was embedded in a POPC lipid bilayer extending 30 Å beyond the solutes and the system was placed in an orthorhombic box (90×90×105 $Å^3$). The number of lipids added were ca 200. The bilayer was then solvated by a 30 Å-thick layer of waters. Na^+ and Cl^- ions were placed in the water phase to neutralize the systems and to reach the experimental salt concentration of 0.150 M NaCl. The total number of atoms was ca 80,000. Membrane generation and system solvation was carried out using the “System Builder” utility of Maestro-Desmond 2020 [242, 243] and periodic boundary conditions were applied. The amber99sb force field [359] was used to model all protein and ligand interactions, and the TIP3P [199] model was used for water. Maestro-Desmond (Maestro-Desmond Interoperability Tools, Schrödinger, New York, 2020) was used to assign amber99sb force field parameters to protein, CHARMM36 force field to lipids, while the Generalized Amber Force Field (GAFF) [360] was used for the ligand parameterization with the antechamber module [361] of AMBER18 software; intermolecular interactions were calculated with amber99sb force field. [362]

The particle mesh Ewald method [205, 206] was employed to calculate long-range electrostatic interactions with a grid spacing of 0.8 Å. Van der Waals and short range electrostatic interactions were smoothly truncated at 9.0 Å. The Nosé-Hoover thermostat [248] was utilized to maintain a constant temperature in all simulations, and the Martyna-Tobias-Klein method [248] was used to control the pressure. Periodic boundary conditions were applied. The equations of motion were integrated using the multistep RESPA integrator with an inner time step of 2 fs for bonded interactions and non-bonded interactions within a cutoff of 9 Å. An outer time step of 6.0 fs was used for non-bonded interactions beyond the cut-off. Each system was equilibrated in MD simulations with a modification of the default protocol provided in Desmond, which consists of a series of restrained minimizations and MD simulations designed to relax the system, while not deviating substantially from the initial coordinates. First, two rounds of steepest descent minimization were performed with a maximum of 2000 steps with harmonic restraints of 50 kcal mol^{-1} $Å^{-2}$ applied on all solute atoms, followed by 10000 steps of minimization without restraints. The first simulation was run for 200 ps at a temperature of 10 K in the NVT ensemble with solute heavy atoms restrained with a force constant of 50 kcal mol^{-1} $Å^{-2}$. The temperature was then raised during a 200 ps MD simulation to 310 K in the NVT ensemble with the force constant retained. The heating was followed by equilibration runs. First, two stages of NPT equilibration were performed, one with the heavy atoms of the system restrained for 1 ns and one for solvent and lipids for 10 ns, with a force constant of 10 kcal/mol/$Å^2$ for the harmonic constraints, respectively. Then, a NPT simulation followed with the C_α atoms restrained for 1ns with a force constant of 2 kcal/mol/$Å^2$. The above-mentioned equilibration was followed by a 300 ns NPT simulation using Desmond 2020 [242, 243] without restraints. Within this time, the total energy and the RMSD reached a plateau, and the systems were considered equilibrated. Examination of the probability density function for the amine-water interaction showed that, on average four waters are in hydrogen-bonded distance with the amine, and five are in the lower Gly34 layer ie the simulation results are in agreement with the crystallographic structure. For structural analyses, snapshots of the different systems were created with VMD [217] or Maestro [250] or Chimera [283]. Trajectories were analysed with Maestro, Gromacs [196, 251], and VMD.

8.4.6 GCMC titration calculations

GCMC theory

The sampling of occluded water sites using conventional molecular dynamics (MD) can be very slow, given the long timescales which can be required for water to exchange between buried sites and bulk. [363] Grand canonical Monte Carlo (GCMC) can be used to allow the number of particles within a simulation to vary according to the chemical potential, in order to simulate the grand canonical (μVT) ensemble. [345-347, 364-369] This allows the waters within a region of interest to exchange with bulk water much more rapidly, bypassing the kinetic barriers which can limit water sampling in conventional MD simulations. This is done by proposing MC moves which attempt to insert or delete water molecules from a region of interest, where the probabilities of these moves are given by

$$P_{insert} = \min\left[1, \frac{1}{N+1} e^{B} e^{-\beta \Delta U}\right]$$

$$P_{delete} = \min\left[1, N e^{-B} e^{-\beta \Delta U}\right]$$

where N is the number of water molecules present in the initial state, $\beta = (k_B T)^{-1}$ is the thermodynamic beta, ΔU is the potential energy change associated with the proposed move, and B is the Adams parameter, [367, 369] defined as

$$B = \beta\mu + \ln\left(\frac{V_{GCMC}}{\Lambda^3}\right)$$

where μ is the chemical potential, V_{GCMC} is the volume of the GCMC region, and Λ is the thermodynamic wavelength of water. When the chemical potential of the system is at equilibrium with bulk water, the Adams value is given by [347]

$$B_{equil} = \beta\mu'_{sol} + \ln\left(\frac{V_{GCMC}}{V^{\circ}}\right)$$

where μ'_{sol} is the excess chemical potential of water and V° is the standard state volume of water. In this work, these parameters are taken as -6.09 kcal mol^{-1} and 30.345 Å^3, respectively.

GCMC can be used to simulate the hydration expected for a system at equilibrium, using the B_{equil} value. However, by simulating the system at a range of B values, the difference in water binding free energy between two states

containing different numbers of waters can be determined, via the following equation, [346, 347]

$$\beta\Delta G^{\circ}_{bind}(N_i \rightarrow N_f) = N_f B_f - N_i B_i - (N_f - N_i)\left[\beta\mu'_{sol} + \ln\left(\frac{V_{GCMC}}{V^{\circ}}\right)\right] - \int_{B_i}^{B_f} N(B)dB$$

where B_k is the Adams value at which N_k waters are observed on average. The integral is typically calculated numerically, as the area under a plot of N against B. These are referred to as titration calculations. It should be noted that the free energy difference is not assigned to specific water sites, but rather indicates the free energy difference between states containing different numbers of waters in the GCMC region, with cooperative water-water effects accounted for.

GCMC/MD simulations details

The GCMC simulations were carried out using version 7.3.1 of OpenMM. [370] Version 1.0.0 of the *grand* Python module [371] was used with OpenMM to carry out the GCMC sampling, with the MD sampling carried out using the native OpenMM functionality.

The region in which GCMC moves were carried out was defined as a sphere with radius 6.0 Å (for which $B_{equil} = -6.820$), centred on the average coordinate of the C_α atoms of the Gly34 residues. This was chosen to ensure that the two water layers of interest are covered by the GCMC sampling. Version 1.0.0 of the *grand* Python module [371] was used alongside OpenMM to carry out the GCMC sampling, with the MD sampling carried out using the native OpenMM functionality.

For each enantiomer, an initial equilibration procedure was applied, beginning with a very short minimization, following which the waters present in the GCMC region were deleted. This was followed by GCMC/MD equilibration at B_{equil}, to allow the waters in the GCMC region to be repopulated without bias, and then constant pressure equilibration to allow the volume of the system to equilibrate. The GCMC/MD stage was carried out in three phases to ensure rigorous equilibration of the waters before significant movement of the protein complex: first 1 ps of MD, with 5k moves attempted every 100 fs; then 10 ps of MD, with 100 moves every 200 fs; and finally, 50 ps of MD, with 500 moves every 250 fs.

The constant pressure equilibration was carried out for 500 ps. The resulting equilibrated structure for each enantiomer was used as a starting point for each set of independent repeats, in order to ensure that they all had the same system volume, and therefore sampled the same ensemble.

For each independent set of repeats, for each enantiomer, a further GCMC/MD equilibration was carried out at B_{equil} for 500 ps, with 50 GCMC moves executed every 250 fs. From this, multiple simulations were run at 21 equally-spaced B values, from -24.820 to -4.820. Each of these simulations was equilibrated for 500 ps, with 50 GCMC moves every 250 fs, to allow the number of waters to adjust to the new B value. This was followed by a production run of 2.5 ns, with 20 GCMC moves per 500 fs, with simulation frames written out every 5 ps. The average number of waters observed in the GCMC region, $\langle N \rangle$, was calculated over these production runs. Three sets of these simulations were carried out for each enantiomer, generating three values of $\langle N \rangle$ per B value, per enantiomer (see Table 8.2).

8.4.7 Free energy calculations

Alchemical free energy calculations

In order to determine the relative free energies of both hydration and binding for the two enantiomers, free energy calculations were performed in OpenMM, using version 0.7.1 of the *perses* Python module. [372] This involved perturbing each of the enantiomers into an achiral intermediate compound, in which the methyl group of rimantadine is replaced by a hydrogen atom. Full details of these calculations are provided in the Supporting Information.

For each enantiomer, a structure equilibrated at B_{equil} was taken as the starting structure for the free energy calculations, where both of these starting structures contained 9 water molecules in the GCMC region (note that GCMC sampling was not used). The free energy calculations were performed by alchemically perturbing each enantiomer into an achiral intermediate, in which the methyl group is replaced by a hydrogen atom. This calculation was carried out in vacuum, bulk solvent and the protein binding site, as shown in the thermodynamic

cycle in Figure 8.5. From this, the relative difference in binding free energy and hydration free energy between the two enantiomers were calculated as follows,

$$\Delta\Delta G_{hyd}(R \to S) = \Delta G_{hyd}(S) - \Delta G_{hyd}(R)$$
$$= \Delta G_{sol}(R \to I) - \Delta G_{sol}(S \to I) - \Delta G_{vac}(R \to I) + \Delta G_{vac}(S \to I)$$

$$\Delta\Delta G_{bind}(R \to S) = \Delta G_{bind}(S) - \Delta G_{bind}(R)$$
$$= \Delta G_{prot}(R \to I) - \Delta G_{prot}(S \to I) - \Delta G_{sol}(R \to I) + \Delta G_{sol}(S \to I)$$

Simulations details

Each perturbation was executed using a single topology transformation over 11 λ-windows, with 10 ns MD simulation sampling per window (with a timestep of 4 fs, using hydrogen mass repartitioning), and exchanges between λ-replicas attempted every 1 ps, using version 0.7.1 of the perses Python module[372, 373] for free energy calculations in OpenMM. [370] The free energy data were processed using the multistate Bennett acceptance ratio (MBAR) method[353, 354] as implemented in the pymbar module [374] of OpenMM. Each calculation was run independently three times for each starting structure (in order to investigate the influence of the starting structure on the result). All simulations were performed at a constant pressure of 1 atm (with volume changes attempted every 25 timesteps, and an isotropic barostat used for the solution simulations), while PME was not used during the vacuum simulations. Unless stated otherwise, all simulation conditions were the same as those used for the GCMC/MD titrations mentioned previously.

For the free energy calculations reported here, the AMBER ff14sb force field was used to describe the protein, [211] the lipid17 force field for the membrane,[375] TIP3P for the water [376] and the Joung-Cheatham parameters were used for the ions. [377, 378] The ligands were described using the general AMBER force field (GAFF) [360] with AM1-BCC charges, [379] generated using antechamber. [361] All non-bonded interactions within 12 Å were calculated directly, Lennard-Jones interactions were switched to zero from 10-12 Å, and long-range electrostatic interactions were calculated using the Particle Mesh Ewald method. [380] The simulations were carried out at 300 K, using the BAOAB Langevin integrator [381, 382] (with a friction coefficient of 1 ps^{-1} and a timestep of 2 fs) to integrate the

dynamics and regulate the temperature. All bonds involving hydrogen atoms were constrained, using the SETTLE algorithm for water, [383] and the SHAKE algorithm for the rest of the system. [216, 384] Where constant pressure simulations were carried out, the pressure was maintained at 1 bar with zero surface tension, using a semi-isotropic Monte Carlo barostat, with volume changes attempted every timestep (in order to facilitate rapid equilibration).

8.5 Supporting Information

***Table 8.3*:** Data processing and refinement statistics for X-ray crystal structures of M2(22-46) WT co-crystallized with (*R*)-rimantadine (PDB ID 6US9) and (*S*)-rimantadine (PDB ID 6US8).

Structure	**6US9 ((*R*)-rimantadine)**	**6US8 ((*S*)-rimantadine)**
Space group	P 2_1	P 2_1 2_1 2_1
Cell dimensions		
a, b, c (Å)	48.18, 48.70, 71.67	49.39, 76.09, 98.63
α, β, γ (˚)	90, 90, 90	90, 90, 90
Wavelength (Å)	1.1159	1.1159
Resolution (Å)	48.70 - 2.00 (2.05 - 2.00)	60.25 - 1.70 (1.73 -1.70)
Total reflections	117349 (8139)	256684 (13726)
Unique reflections	21661 (1558)	37869 (1950)
Completeness (%)	96.0 (94.7)	91.5 (91.4)
Multiplicity	5.4	6.8
R_{merge}	0.122 (0.494)	0.089 (0.882)
I/σI	6.8 (2.6)	11.3 (2.1)
Wilson B-factor	15.80	17.41
CC(1/2)	0.997 (0.950)	0.999 (0.872)
Refinement		
Resolution (Å)	48.18 - 2.0 (2.072 - 2.0)	60.25 - 1.70 (1.76 - 1.70)
R_{work}	0.2321 (0.2651)	0.1889 (0.2278)
R_{free}	0.2754 (0.3887)	0.2142 (0.2585)
Number of non-hydrogen atoms	3154	3316
Protein	2928	2958
Ligands	176	269
Water	50	89
RMSD Bond Lengths (Å)	0.007	0.006

RMSD Bond Angles (°)	0.89	0.76
Ramachandran favored (%)	100.00	100.00
Average B factor	20.92	19.34
Protein	20.84	18.06
Ligands	21.81	30.06
Solvent	22.50	29.46

Table 8.4: Refined occupancies for rimantadine rotational alternate conformers.

(*R*)-Rimantadine (PDB ID 6US9)

Alternate conformer	Tetramer 1	Tetramer 2	Tetramer 3	Tetramer 4
A	0.4	0.42	0.59	0.3
B	0.37	0.19	0.14	0.32
C	0.23	0	0.27	0.38
D	0	0.39	0	0

(*S*)-Rimantadine (PDB ID 6US8)

Alternate conformer	Tetramer 1	Tetramer 2	Tetramer 3	Tetramer 4
A	0.11	0.65	0.36	0.58
B	0.42	0.01	0.01	0.38
C	0.46	0.34	0.63	0.04
D	0.01	0	0	0

Table 8.5: Average number of waters observed for each repeat at each Adams value, for both enantiomers.

	Average number of waters, $\langle N \rangle$					
	***(R)*-enantiomer**			***(S)*-enantiomer**		
Adams value, B	**Run 1**	**Run 2**	**Run 3**	**Run 1**	**Run 2**	**Run 3**
-4.820	9.949	9.956	9.323	10.033	10.496	11.047
-5.820	9.028	9.389	10.066	9.753	9.627	10.236
-6.820	9.650	8.925	9.208	8.866	8.851	9.413
-7.820	8.813	7.619	7.512	8.088	9.188	8.778
-8.820	7.528	7.359	7.645	8.047	8.337	7.678
-9.820	6.490	7.101	6.378	7.265	6.901	6.981
-10.820	5.910	5.425	3.713	6.375	3.758	5.611
-11.820	4.172	4.209	3.184	5.501	3.438	3.457
-12.820	3.329	3.044	2.970	4.213	2.975	2.954
-13.820	2.187	3.887	3.000	2.743	2.571	3.219

-14.820	2.620	3.000	2.092	2.000	1.660	2.157
-15.820	2.412	2.281	1.306	0.916	0.576	1.000
-16.820	1.154	1.881	1.282	1.000	1.000	1.000
-17.820	0.434	1.001	1.591	0.199	0.911	0.001
-18.820	0.568	0.412	1.033	1.094	1.000	0.168
-19.820	0.948	0.960	0.760	0.506	0.000	0.000
-20.820	0.159	0.248	0.957	0.000	0.000	0.000
-21.820	0.620	0.053	0.005	0.000	0.000	0.000
-22.820	0.032	0.000	0.360	0.039	0.000	0.074
-23.820	0.004	0.006	0.207	0.000	0.000	0.000
-24.820	0.124	0.031	0.001	0.000	0.000	0.000

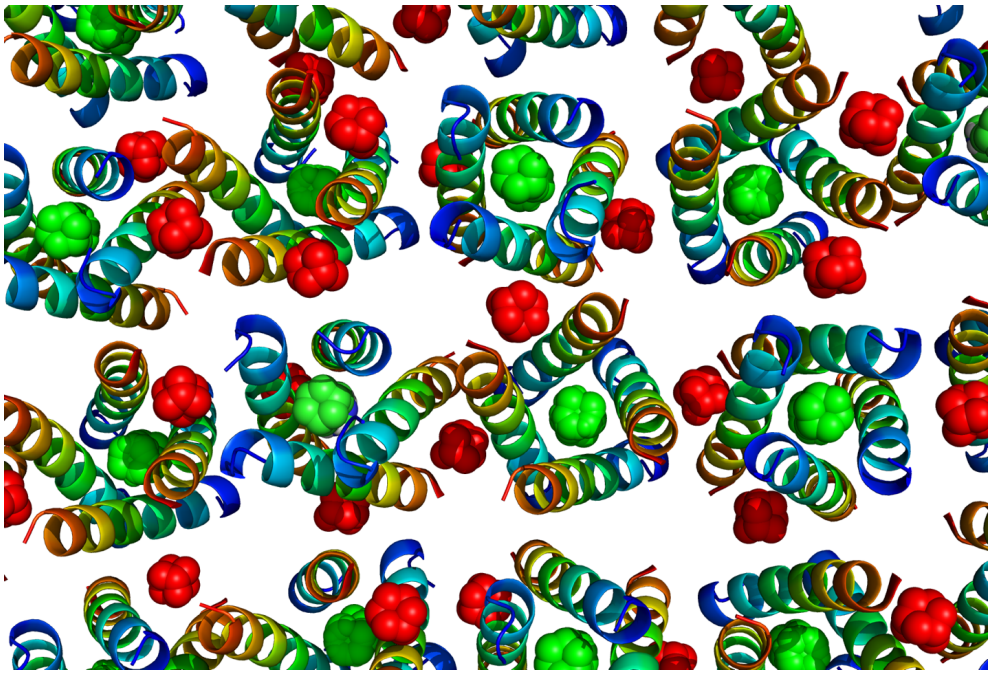

Figure 8.10: Extended unit cell of the 1.70 Å structure of (*S*)-rimantadine bound to M2(22-46) (PDB ID 6US8). Rimantadines in the pore of the channel are shown in green spheres, and rimantadines localized at lattice sites between tetramers are in red. The helices are colored as a rainbow, with blue as the N-terminus to red at the C-terminus.

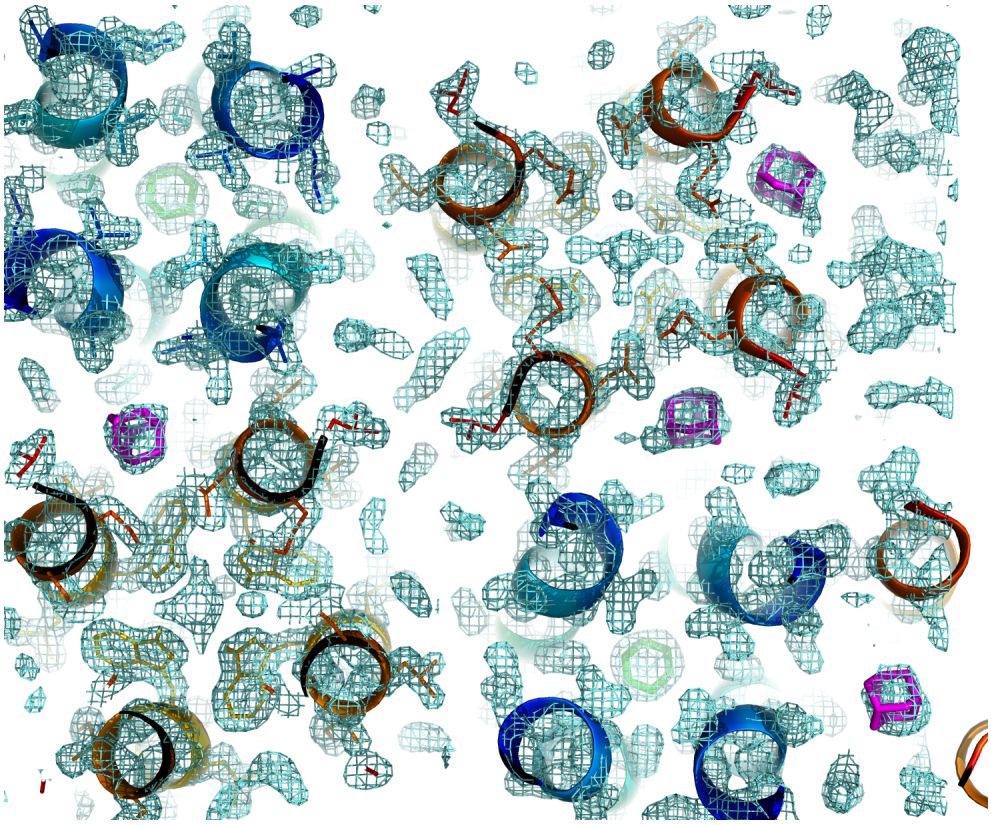

Figure 8.11: 2F0-Fc density contoured at 1s. The view as in Figure 8.10, but with the lattices (*S*)-rimantadine molecules shown in purple, and pore-located rimantadines in light green.

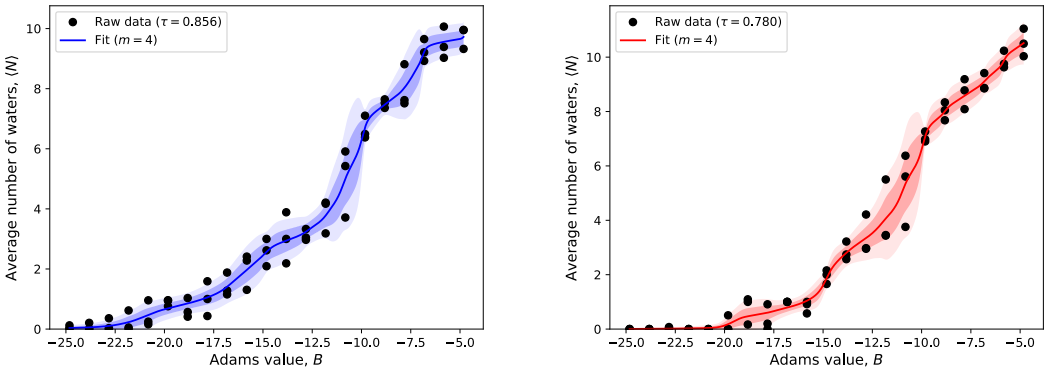

a (*R*)-Rimantadine ***b*** (*S*)-Rimantadine

Figure 8.12: Titration plots for both rimantadine enantiomers, with the average number of waters observed plotted against the B value. The curve was fitted as the mean from 1000 bootstraps of a sum of four sigmoid curves. The inner and outer shaded regions represent 1.0 and 1.96 standard deviations from the mean fit, respectively. The value of the Kendall tau parameter for the raw data is indicated in the legend.

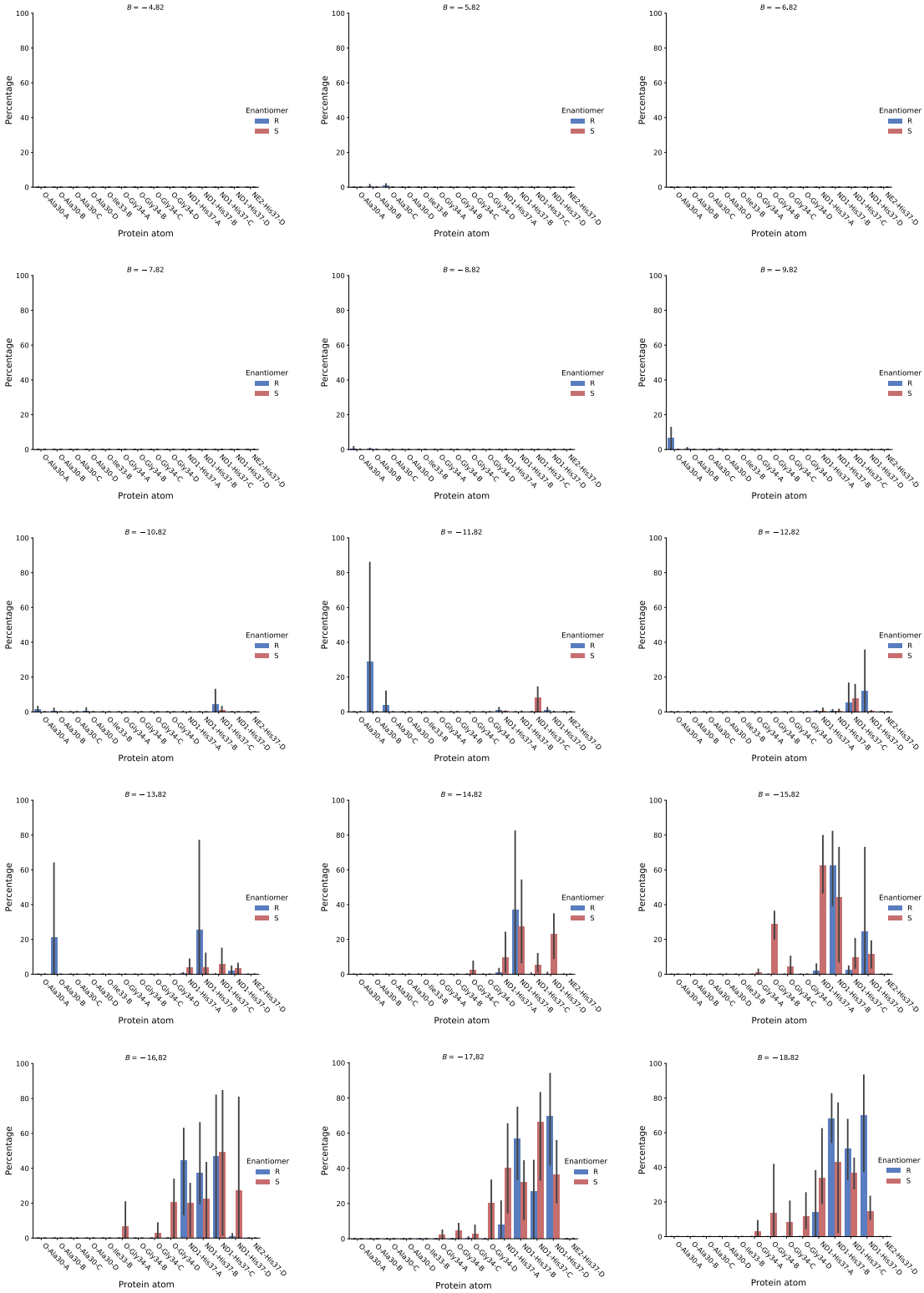
B = −4.82
B = −5.82
B = −6.82
B = −7.82
B = −8.82
B = −9.82
B = −10.82
B = −11.82
B = −12.82
B = −13.82
B = −14.82
B = −15.82
B = −16.82
B = −17.82
B = −18.82
Percentage
Protein atom
Enantiomer
R
S
O-Ala30-A
O-Ala30-B
O-Ala30-C
O-Ala30-D
O-Ile33-B
O-Gly34-A
O-Gly34-B
O-Gly34-C
O-Gly34-D
ND1-His37-A
ND1-His37-B
ND1-His37-C
ND1-His37-D
NE2-His37-D

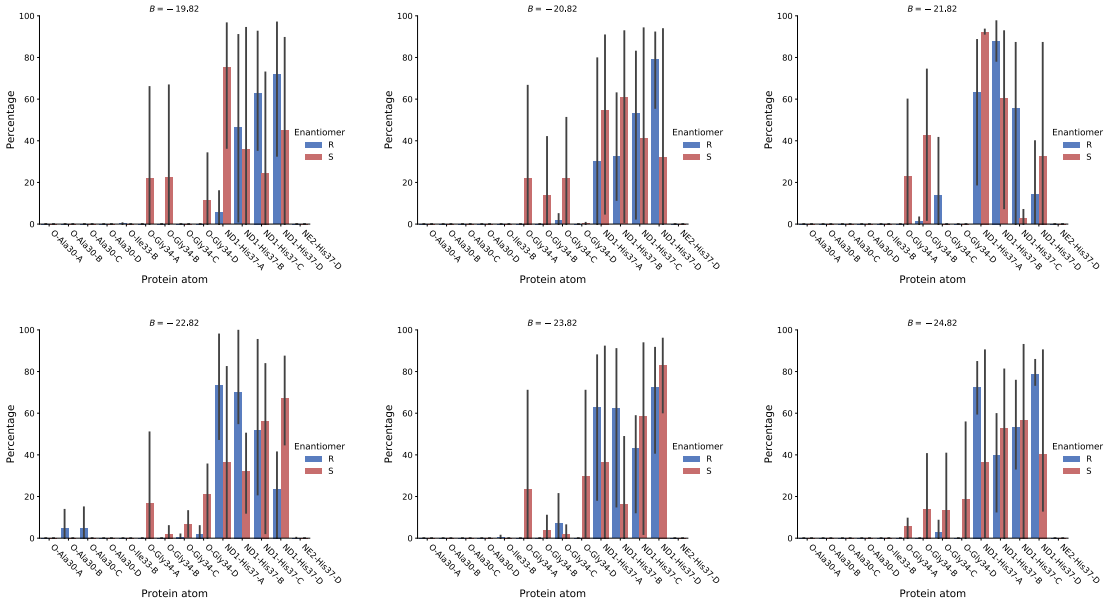

Figure 8.13: Bar charts showing the hydrogen bonding observed between the ligand and the protein at different Adams values. Each bar represents the percentage of the GCMC simulation for which an interaction is seen (within 3.2 Å) with a particular protein atom – bars are not shown for protein atoms which never interact with the ligand. The error bars represent standard deviations over the three repeats.

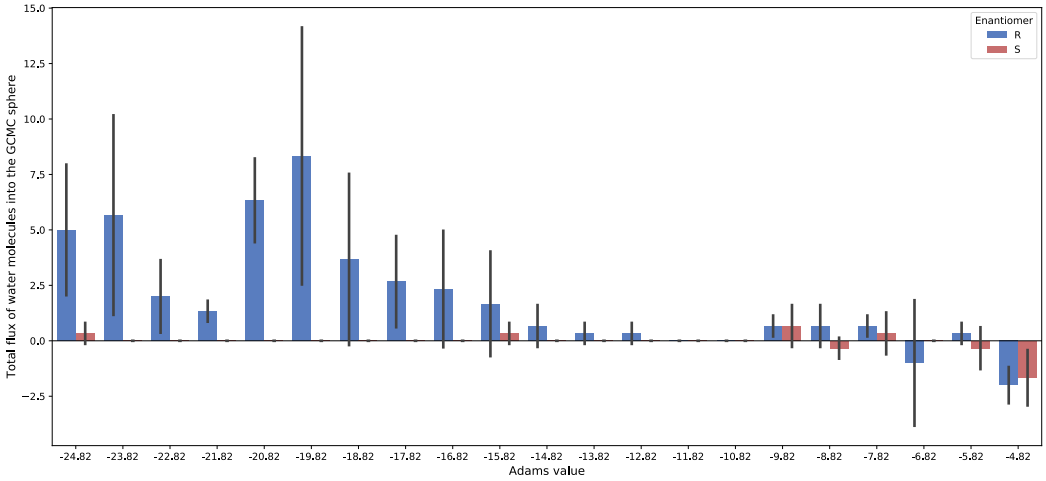

Figure 8.14: Water Diffusion into the GCMC Region. Graph showing the total flux of waters in or out of the GCMC region via MD diffusion, at each Adams value, for both enantiomers. The error bars given represent the standard deviations over the three repeats.

PUBLICATIONS FROM PHD

ACS Medicinal Chemistry Letters
Letter
Cite This: ACS Med. Chem. Lett. 2018, 9, 198−203

Unraveling the Binding, Proton Blockage, and Inhibition of Influenza M2 WT and S31N by Rimantadine Variants

Antonios Drakopoulos,[†] Christina Tzitzoglaki,[†] Kelly McGuire,[‡] Anja Hoffmann,[§] Athina Konstantinidi,[†] Dimitrios Kolokouris,[†] Chunlong Ma,[∥] Kathrin Freudenberger,[⊥] Johanna Hutterer,[⊥] Günter Gauglitz,[⊥] Jun Wang,[∥] Michaela Schmidtke,[§] David D. Busath,[‡] and Antonios Kolocouris*[,†]

THE JOURNAL OF PHYSICAL CHEMISTRY B
Article
Cite This: J. Phys. Chem. B 2018, 122, 9877−9895
pubs.acs.org/JPCB

Comparative Perturbation Effects Exerted by the Influenza A M2 WT Protein Inhibitors Amantadine and the Spiro[pyrrolidine-2,2′-adamantane] Variant AK13 to Membrane Bilayers Studied Using Biophysical Experiments and Molecular Dynamics Simulations

Athina Konstantinidi,[†] Nikolaos Naziris,[‡] Maria Chountoulesi,[‡] Sophia Kiriakidi,[§] Barbara Sartori,[∥] Dimitris Kolokouris,[†] Heinz Amentisch,[∥] Gregor Mali,[⊥] Dimitrios Ntountaniotis,[§] Costas Demetzos,[‡] Thomas Mavromoustakos,[§] and Antonios Kolocouris*[,†]

J|A|C|S
JOURNAL OF THE AMERICAN CHEMICAL SOCIETY
Article
Cite This: J. Am. Chem. Soc. 2018, 140, 15219−15226
pubs.acs.org/JACS

Inhibitors of the M2 Proton Channel Engage and Disrupt Transmembrane Networks of Hydrogen-Bonded Waters

Jessica L. Thomaston,[†] Nicholas F. Polizzi,[†,∥] Athina Konstantinidi,[‡,∥] Jun Wang,[§] Antonios Kolocouris,*[,‡] and William F. DeGrado*[,†]

Contents lists available at ScienceDirect
BBA - Biomembranes
journal homepage: www.elsevier.com/locate/bbamem

The boundary lipid around DMPC-spanning influenza A M2 transmembrane domain channels: Its structure and potential for drug accommodation

Athina Konstantinidi[a], Maria Chountoulesi[b], Nikolaos Naziris[b], Barbara Sartori[c], Heinz Amenitsch[c], Gregor Mali[d], Tomaž Čendak[d], Maria Plakantonaki[e], Iro Triantafyllakou[e], Theodore Tselios[e], Costas Demetzos[b], David D. Busath[f], Thomas Mavromoustakos[g,*], Antonios Kolocouris[b,*]

Biochemistry
pubs.acs.org/biochemistry
Article

X-ray Crystal Structures of the Influenza M2 Proton Channel Drug-Resistant V27A Mutant Bound to a Spiro-Adamantyl Amine Inhibitor Reveal the Mechanism of Adamantane Resistance

Jessica L. Thomaston,* Athina Konstantinidi, Lijun Liu, George Lambrinidis, Jingquan Tan, Martin Caffrey, Jun Wang, William F. Degrado,* and Antonios Kolocouris*

Biochemistry
pubs.acs.org/biochemistry
Article

Rimantadine Binds to and Inhibits the Influenza A M2 Proton Channel without Enantiomeric Specificity

Jessica L. Thomaston, Marley L. Samways, Athina Konstantinidi, Chunlong Ma, Yanmei Hu, Hannah E. Bruce Macdonald, Jun Wang, Jonathan W. Essex, William F. DeGrado,* and Antonios Kolocouris*

REFERENCES

1. Zebedee, S.L. and R.A. Lamb, *Influenza A virus M2 protein: monoclonal antibody restriction of virus growth and detection of M2 in virions.* J Virol, 1988. **62**(8): p. 2762-72.

2. Bouvier, N.M. and P. Palese, *The biology of influenza viruses.* Vaccine, 2008. **26 Suppl 4**: p. D49-53.

3. Lamb, R.A., *Genes and Proteins of the Influenza Viruses*, in *The Influenza Viruses*. 1989, Springer US: Boston, MA. p. 1–87.

4. Villalon-Letelier, F., A.G. Brooks, P.M. Saunders, S.L. Londrigan, and P.C. Reading, *Host Cell Restriction Factors that Limit Influenza A Infection.* Viruses, 2017. **9**(12).

5. Lamb, R.A. and P.W. Choppin, *The gene structure and replication of influenza virus.* Annu Rev Biochem, 1983. **52**: p. 467-506.

6. Clancy, S., *Genetics of the Influenza Virus.* Nature Education, 2008. **1**(1): p. 83.

7. Nayak, D.P., R.A. Balogun, H. Yamada, Z.H. Zhou, and S. Barman, *Influenza virus morphogenesis and budding.* Virus Res, 2009. **143**(2): p. 147-61.

8. Sakaguchi, T., Q. Tu, L.H. Pinto, and R.A. Lamb, *The active oligomeric state of the minimalistic influenza virus M2 ion channel is a tetramer.* Proc Natl Acad Sci U S A, 1997. **94**(10): p. 5000-5.

9. Schroeder, C., H. Heider, E. Moncke-Buchner, and T.I. Lin, *The influenza virus ion channel and maturation cofactor M2 is a cholesterol-binding protein.* Eur Biophys J, 2005. **34**(1): p. 52-66.

10. Palese, P., *The genes of influenza virus.* Cell, 1977. **10**(1): p. 1-10.

11. von Itzstein, M., *The war against influenza: discovery and development of sialidase inhibitors.* Nat. Rev. Drug. Discov., 2007. **6**(12): p. 967-74.

12. Hay, A.J., A.J. Wolstenholme, J.J. Skehel, and M.H. Smith, *The molecular basis of the specific anti-influenza action of amantadine.* EMBO J., 1985. **4**(11): p. 3021-3024.

13. Lakadamyali, M., M.J. Rust, H.P. Babcock, and X. Zhuang, *Visualizing infection of individual influenza viruses.* Proc .Natl. Acad. Sci. U. S. A., 2003. **100**(16): p. 9280-9285.

14. Boulo, S., H. Akarsu, R.W. Ruigrok, and F. Baudin, *Nuclear traffic of influenza virus proteins and ribonucleoprotein complexes.* Virus Res, 2007. **124**(1-2): p. 12-21.

15. Eisfeld, A.J., G. Neumann, and Y. Kawaoka, *At the centre: influenza A virus ribonucleoproteins.* Nat. Rev. Microbiol., 2015. **13**(1): p. 28-41.

16. Cady, S.D., W. Luo, F. Hu, and M. Hong, *Structure and function of the influenza A M2 proton channel.* Biochemistry, 2009. **48**(31): p. 7356-7364.

17. Chizhmakov, I.V., F.M. Geraghty, D.C. Ogden, A. Hayhurst, M. Antoniou, and A.J. Hay, *Selective proton permeability and pH regulation of the influenza virus M2 channel expressed in mouse erythroleukaemia cells.* J. Physiol., 1996. **494 (Pt 2)**(Pt 2): p. 329-336.

18. Lin, T.I. and C. Schroeder, *Definitive assignment of proton selectivity and attoampere unitary current to the M2 ion channel protein of influenza A virus.* J. Virol., 2001. **75**(8): p. 3647-3656.

19. Mould, J.A., J.E. Drury, S.M. Frings, U.B. Kaupp, A. Pekosz, R.A. Lamb, and L.H. Pinto, *Permeation and activation of the M2 ion channel of influenza A virus.* J. Biol. Chem., 2000. **275**(40): p. 31038-31050.

20. Pinto, L.H., L.J. Holsinger, and R.A. Lamb, *Influenza virus M2 protein has ion channel activity.* Cell, 1992. **69**(3): p. 517-528.

21. Shimbo, K., D.L. Brassard, R.A. Lamb, and L.H. Pinto, *Ion selectivity and activation of the M2 ion channel of influenza virus.* Biophys. J., 1996. **70**(3): p. 1335-1346.

22. Lamb, R.A., K.J. Holsinger, and L.H. Pinto, *The influenza A virus M2 ion channel protein and its role in the influenza virus life cycle*, in *Cellular Receptors for Animal Viruses*, E. Wimmer, Editor. 1994, Cold Spring Harbor Press: Cold Spring Harbor Laboratory Press, Plainview, NY. p. 303-321.

23. Hu, J., R. Fu, K. Nishimura, L. Zhang, H.X. Zhou, D.D. Busath, V. Vijayvergiya, and T.A. Cross, *Histidines, heart of the hydrogen ion channel*

from influenza A virus: toward an understanding of conductance and proton selectivity. Proc. Natl. Acad. Sci. U. S. A., 2006. **103**(18): p. 6865-6870.

24. Sugrue, R.J., G. Bahadur, M.C. Zambon, M. Hall-Smith, A.R. Douglas, and A.J. Hay, *Specific structural alteration of the influenza haemagglutinin by amantadine.* EMBO J., 1990. **9**(11): p. 3469-3476.

25. Park, E.K., M.R. Castrucci, A. Portner, and Y. Kawaoka, *The M2 ectodomain is important for its incorporation into influenza A virions.* J. Virol., 1998. **72**(3): p. 2449–2455.

26. Lamb, R.A., S.L. Zebedee, and C.D. Richardson, *Influenza virus M2 protein is an integral membrane protein expressed on the infected-cell surface.* Cell, 1985. **40**(3): p. 627-633.

27. McCown, M.F. and A. Pekosz, *Distinct domains of the influenza a virus M2 protein cytoplasmic tail mediate binding to the M1 protein and facilitate infectious virus production.* J. Virol., 2006. **80**(16): p. 8178-8189.

28. Pinto, L.H. and R.A. Lamb, *The M2 proton channels of influenza A and B viruses.* J. Biol. Chem., 2006. **281**(14): p. 8997-9000.

29. Ma, C.L., A.L. Polishchuk, Y. Ohigashi, A.L. Stouffer, A. Schon, E. Magavern, X.H. Jing, J.D. Lear, E. Freire, R.A. Lamb, W.F. DeGrado, and L.H. Pinto, *Identification of the functional core of the influenza A virus A/M2 proton-selective ion channel.* Proc. Natl. Acad. Sci. U. S. A., 2009. **106**(30): p. 12283-12288.

30. Sharma, M., M. Yi, H. Dong, H. Qin, E. Peterson, D.D. Busath, H.X. Zhou, and T.A. Cross, *Insight into the mechanism of the influenza A proton channel from a structure in a lipid bilayer.* Science, 2010. **330**(6003): p. 509-512.

31. Jin, H., G.P. Leser, J. Zhang, and R.A. Lamb, *Influenza virus hemagglutinin and neuraminidase cytoplasmic tails control particle shape.* EMBO J., 1997. **16**(6): p. 1236-1247.

32. Duff, K.C. and R.H. Ashley, *The transmembrane domain of influenza A M2 protein forms amantadine-sensitive proton channels in planar lipid bilayers.* Virol., 1992. **190**(1): p. 485-489.

33. Salom, D., B.R. Hill, J.D. Lear, and W.F. DeGrado, *pH-dependent tetramerization and amantadine binding of the transmembrane helix of M2 from the influenza A virus.* Biochemistry, 2000. **39**(46): p. 14160-14170.

34. Stouffer, A.L., R. Acharya, D. Salom, A.S. Levine, L. Di Costanzo, C.S. Soto, V. Tereshko, V. Nanda, S. Stayrook, and W.F. DeGrado, *Structural basis for the function and inhibition of an influenza virus proton channel.* Nature, 2008. **451**(7178): p. 596-599.

35. Liang, R., J.M.J. Swanson, J.J. Madsen, M. Hong, W.F. DeGrado, and G.A. Voth, *Acid activation mechanism of the influenza A M2 proton channel.* Proc. Natl. Acad. Sci. U. S. A., 2016. **113**(45): p. E6955-E6964.

36. Pinto, L.H. and R.A. Lamb, *Controlling influenza virus replication by inhibiting its proton channel.* Mol. Biosyst., 2007. **3**(1): p. 18-23.

37. Wang, C., R.A. Lamb, and L.H. Pinto, *Activation of the M2 ion channel of influenza virus: a role for the transmembrane domain histidine residue.* Biophys. J., 1995. **69**(4): p. 1363-1371.

38. Tang, Y., F. Zaitseva, R.A. Lamb, and L.H. Pinto, *The gate of the influenza virus M2 proton channel is formed by a single tryptophan residue.* J. Biol. Chem., 2002. **277**(42): p. 39880-39886.

39. Helenius, A., *Unpacking the incoming influenza virus.* Cell, 1992. **69**(4): p. 577-8.

40. Thomaston, J.L., M. Alfonso-Prieto, R.A. Woldeyes, J.S. Fraser, M.L. Klein, G. Fiorin, and W.F. DeGrado, *High-resolution structures of the M2 channel from influenza A virus reveal dynamic pathways for proton stabilization and transduction.* Proc. Natl. Acad. Sci. U. S. A., 2015. **112**(46): p. 14260-14265.

41. Thomaston, J.L., R.A. Woldeyes, T. Nakane, A. Yamashita, T. Tanaka, K. Koiwai, A.S. Brewster, B.A. Barad, Y. Chen, T. Lemmin, M. Uervirojnangkoorn, T. Arima, J. Kobayashi, T. Masuda, M. Suzuki, M. Sugahara, N.K. Sauter, R. Tanaka, O. Nureki, K. Tono, Y. Joti, E. Nango, S. Iwata, F. Yumoto, J.S. Fraser, and W.F. DeGrado, *XFEL structures of the influenza M2 proton channel: room temperature water networks and*

insights into proton conduction. Proc. Natl. Acad. Sci. U. S. A., 2017. **114**(51): p. 13357-13362.

42. Hu, F., W. Luo, and M. Hong, *Mechanisms of proton conduction and gating in influenza M2 proton channels from solid-state NMR.* Science, 2010. **330**(6003): p. 505-508.

43. Acharya, R., V. Carnevale, G. Fiorin, B.G. Levine, A.L. Polishchuk, V. Balannik, I. Samish, R.A. Lamb, L.H. Pinto, W.F. DeGrado, and M.L. Klein, *Structure and mechanism of proton transport through the transmembrane tetrameric M2 protein bundle of the influenza A virus.* Proc. Natl. Acad. Sci. U. S. A., 2010. **107**(34): p. 15075-15080.

44. Williams, J.K., Y. Zhang, K. Schmidt-Rohr, and M. Hong, *pH-dependent conformation, dynamics, and aromatic interaction of the gating tryptophan residue of the influenza M2 proton channel from solid-state NMR.* Biophys J, 2013. **104**(8): p. 1698-708.

45. Wang, J., R.M. Pielak, M.A. McClintock, and J.J. Chou, *Solution structure and functional analysis of the influenza B proton channel.* Nat Struct Mol Biol, 2009. **16**(12): p. 1267-71.

46. Rossman, J.S. and R.A. Lamb, *Influenza virus assembly and budding.* Virol., 2011. **411**(2): p. 229-236.

47. Rossman, J.S., X. Jing, G.P. Leser, and R.A. Lamb, *Influenza virus M2 protein mediates ESCRT-independent membrane scission.* Cell, 2010. **142**(6): p. 902-913.

48. Li, H. and V. Papadopoulos, *Peripheral-type benzodiazepine receptor function in cholesterol transport. Identification of a putative cholesterol recognition/interaction amino acid sequence and consensus pattern.* Endocrinology, 1998. **139**(12): p. 4991-4997.

49. Cherezov, V., D.M. Rosenbaum, M.A. Hanson, S.G.F. Rasmussen, F.S. Thian, T.S. Kobilka, H.-J. Choi, P. Kuhn, W.I. Weis, B.K. Kobilka, and R.C. Stevens, *High-resolution crystal structure of an engineered human β2-adrenergic G protein–coupled receptor.* Science, 2007. **318**(5854): p. 1258-1265.

50. Schnell, J.R. and J.J. Chou, *Structure and mechanism of the M2 proton channel of influenza A virus.* Nature, 2008. **451**(7178): p. 591-595.

51. Tobler, K., M.L. Kelly, L.H. Pinto, and R.A. Lamb, *Effect of cytoplasmic tail truncations on the activity of the M2 ion channel of influenza A virus.* J. Virol., 1999. **73**(12): p. 9695-9701.

52. Pielak, R.M., J.R. Schnell, and J.J. Chou, *Mechanism of drug inhibition and drug resistance of influenza A M2 channel.* Proc. Natl. Acad. Sci. U. S. A., 2009. **106**(18): p. 7379-7384.

53. Cross, T.A., H. Dong, M. Sharma, D.D. Busath, and H.X. Zhou, *M2 protein from influenza A: from multiple structures to biophysical and functional insights.* Curr. Opin. Virol., 2012. **2**(2): p. 128-33.

54. Cross, T.A., M. Sharma, M. Yi, and H.X. Zhou, *Influence of solubilizing environments on membrane protein structures.* Trends Biochem. Sci., 2011. **36**(2): p. 117-125.

55. Wang, J., S. Kim, F. Kovacs, and T.A. Cross, *Structure of the transmembrane region of the M2 protein H+ channel.* Protein Sci., 2008. **10**(11): p. 2241-2250.

56. Nishimura, K., S. Kim, L. Zhang, and T.A. Cross, *The closed state of a H+ channel helical bundle combining precise orientational and distance restraints from solid state NMR.* Biochemistry, 2002. **41**(44): p. 13170-13177.

57. Hu, J., T. Asbury, S. Achuthan, C.G. Li, R. Bertram, J.R. Quine, R.Q. Fu, and T.A. Cross, *Backbone structure of the amantadine-blocked trans-membrane domain M2 proton channel from Influenza A virus.* Biophys. J., 2007. **92**(12): p. 4335-4343.

58. Cady, S.D., K. Schmidt-Rohr, J. Wang, C.S. Soto, W.F. Degrado, and M. Hong, *Structure of the amantadine binding site of influenza M2 proton channels in lipid bilayers.* Nature 2010. **463**(7281): p. 689-692.

59. Pielak, R.M. and J.J. Chou, *Solution NMR structure of the V27A drug resistant mutant of influenza A M2 channel.* Biochem. Biophys. Res. Commun., 2010. **401**(1): p. 58-63.

60. Pielak, R.M., K. Oxenoid, and J.J. Chou, *Structural investigation of rimantadine inhibition of the AM2-BM2 chimera channel of influenza viruses.* Structure, 2011. **19**(11): p. 1655-1663.

61. Thomaston, J.L., N.F. Polizzi, A. Konstantinidi, J. Wang, A. Kolocouris, and W.F. DeGrado, *Inhibitors of the M2 proton channel engage and disrupt transmembrane networks of hydrogen-bonded waters.* J. Am. Chem. Soc., 2018. **140**(45): p. 15219-15226.

62. Thomaston, J.L., A. Konstantinidi, L. Liu, G. Lambrinidis, J. Tan, M. Caffrey, J. Wang, W.F. Degrado, and A. Kolocouris, *X-ray crystal structures of the influenza M2 proton channel drug-resistant V27A mutant bound to a spiro-adamantyl amine inhibitor reveal the mechanism of adamantane resistance.* Biochemistry, 2020. **59**(4): p. 627-634.

63. Sansom, M.S.P. and I.D. Kerr, *Influenza virus M2 protein: a molecular modelling study of the ion channel.* Protein Eng. Des. Sel., 1993. **6**(1): p. 65-74.

64. Bauer, C.M., L.H. Pinto, T.A. Cross, and R.A. Lamb, *The influenza virus M2 ion channel protein: probing the structure of the transmembrane domain in intact cells by using engineered disulfide cross-linking.* Virol., 1999. **254**(1): p. 196-209.

65. Kukol, A., P.D. Adams, L.M. Rice, A.T. Brunger, and T.I. Arkin, *Experimentally based orientational refinement of membrane protein models: A structure for the Influenza A M2 H+ channel.* J. Mol. Biol., 1999. **286**(3): p. 951-962.

66. Pinto, L.H., G.R. Dieckmann, C.S. Gandhi, C.G. Papworth, J. Braman, M.A. Shaughnessy, J.D. Lear, R.A. Lamb, and W.F. DeGrado, *A functionally defined model for the M2 proton channel of influenza A virus suggests a mechanism for its ion selectivity.* Proc. Natl. Acad. Sci. U. S. A., 1997. **94**(21): p. 11301-11306.

67. Tian, C., K. Tobler, R.A. Lamb, L.H. Pinto, and T.A. Cross, *Expression and initial structural insights from solid-state NMR of the M2 proton channel from influenza A virus.* Biochemistry, 2002. **41**(37): p. 11294-11300.

68. Tian, C., P.F. Gao, L.H. Pinto, R.A. Lamb, and T.A. Cross, *Initial structural and dynamic characterization of the M2 protein transmembrane and amphipathic helices in lipid bilayers.* Protein. Sci., 2003. **12**(11): p. 2597-2605.

69. Kovacs, F.A. and T.A. Cross, *Transmembrane four-helix bundle of influenza A M2 protein channel: structural implications from helix tilt and orientation.* Biophys. J., 1997. **73**(5): p. 2511-2517.

70. Kovacs, F.A., J.K. Denny, Z. Song, J.R. Quine, and T.A. Cross, *Helix tilt of the M2 transmembrane peptide from influenza A virus: an intrinsic property.* J. Mol. Biol., 2000. **295**(1): p. 117-125.

71. Song, Z., F.A. Kovacs, J. Wang, J.K. Denny, S.C. Shekar, J.R. Quine, and T.A. Cross, *Transmembrane domain of M2 protein from influenza A virus studied by solid-state (15)N polarization inversion spin exchange at magic angle NMR.* Biophys. J., 2000. **79**(2): p. 767-775.

72. Sansom, M.S., I.D. Kerr, G.R. Smith, and H.S. Son, *The influenza A virus M2 channel: a molecular modeling and simulation study.* Virology, 1997. **233**(1): p. 163-173.

73. Wang, C., K. Takeuchi, L.H. Pinto, and R.A. Lamb, *Ion channel activity of influenza A virus M2 protein: characterization of the amantadine block.* J. Virol., 1993. **67**(9): p. 5585-5594.

74. Oxenoid, K. and J.J. Chou, *The structure of phospholamban pentamer reveals a channel-like architecture in membranes.* Proc. Natl. Acad. Sci. U. S. A., 2005. **102**(31): p. 10870-10875.

75. Wollheim, F.A., *Approaches to rheumatoid arthritis in 2000.* Curr Opin Rheumatol, 2001. **13**(3): p. 193-201.

76. Cady, S.D., T.V. Mishanina, and M. Hong, *Structure of amantadine-bound M2 transmembrane peptide of influenza A in lipid bilayers from magic-angle-spinning solid-state NMR: the role of Ser31 in amantadine binding.* J. Mol. Biol., 2009. **385**(4): p. 1127-1141.

77. Cady, S.D. and M. Hong, *Amantadine-induced conformational and dynamical changes of the influenza M2 transmembrane proton channel.*

Proceedings of the National Academy of Sciences, 2008. **105**(5): p. 1483-1488.

78. Wu, C.H., A. Ramamoorthy, and S.J. Opella, *High-resolution heteronuclear dipolar solid-state NMR spectroscopy.* J. Magn. Reson. A, 1994. **109**(2): p. 270-272.

79. Yi, M., T.A. Cross, and H.-X. Zhou, *A secondary gate as a mechanism for inhibition of the M2 proton channel by amantadine.* J. Phys. Chem. B, 2008. **112**(27): p. 7977-7979.

80. Hu, J., R.Q. Fu, and T.A. Cross, *The chemical and dynamical influence of the anti-viral drug amantadine on the M2 proton channel transmembrane domain.* Biophys J., 2007. **93**(1): p. 276-283.

81. Betakova, T., F. Ciampor, and A.J. Hay, *Influence of residue 44 on the activity of the M2 proton channel of influenza A virus.* J .Gen. Virol., 2005. **86**(Pt 1): p. 181-184.

82. Pielak, R.M. and J.J. Chou, *Flu channel drug resistance: a tale of two sites.* Protein Cell, 2010. **1**(3): p. 246-258.

83. Gullingsrud, J. and K. Schulten, *Lipid bilayer pressure profiles and mechanosensitive channel gating.* Biophys. J., 2004. **86**(6): p. 3496-3509.

84. Sharma, M., C. Li, D.D. Busath, H.-X. Zhou, and T.A. Cross, *Drug sensitivity, drug-resistant mutations, and structures of three conductance domains of viral porins.* Biochim. Biophys. Acta - Biomembr.

, 2011. **1808**(2): p. 538-546.

85. Cady, S., T. Wang, and M. Hong, *Membrane-dependent effects of a cytoplasmic helix on the structure and drug binding of the influenza virus M2 protein.* J. Am. Chem. Soc., 2011. **133**(30): p. 11572-11579.

86. Jing, X., C. Ma, Y. Ohigashi, F.A. Oliveira, T.S. Jardetzky, L.H. Pinto, and R.A. Lamb, *Functional studies indicate amantadine binds to the pore of the influenza A virus M2 proton-selective ion channel.* Proc. Natl. Acad. Sci. U. S. A., 2008. **105**(31): p. 10967-10972.

87. Cady, S.D., J. Wang, Y. Wu, W.F. DeGrado, and M. Hong, *Specific binding of adamantane drugs and direction of their polar amines in the pore of the influenza M2 transmembrane domain in lipid bilayers and dodecylphosphocholine micelles determined by NMR spectroscopy.* J. Am. Chem. Soc., 2011. **133**(12): p. 4274-4284.

88. Balannik, V., J. Wang, Y. Ohigashi, X. Jing, E. Magavern, R.A. Lamb, W.F. Degrado, and L.H. Pinto, *Design and pharmacological characterization of inhibitors of amantadine-resistant mutants of the M2 ion channel of influenza A virus.* Biochemistry, 2009. **48**(50): p. 11872-11882.

89. Wang, J., Y. Wu, C. Ma, G. Fiorin, L.H. Pinto, R.A. Lamb, M.L. Klein, and W.F. Degrado, *Structure and inhibition of the drug-resistant S31N mutant of the M2 ion channel of influenza A virus.* Proc. Natl. Acad. Sci. U. S. A., 2013. **110**(4): p. 1315-1320.

90. Hu, F.H., K. Schmidt-Rohr, and M. Hong, *NMR detection of pH-dependent histidine-water proton exchange reveals the conduction mechanism of a transmembrane proton channel.* J. Am. Chem. Soc., 2012. **134**(8): p. 3703-3713.

91. Li, C., H. Qin, F.P. Gao, and T.A. Cross, *Solid-state NMR characterization of conformational plasticity within the transmembrane domain of the influenza A M2 proton channel.* Biochim. Biophys. Acta - Biomembr., 2007. **1768**(12): p. 3162-3170.

92. Mandala, V.S., M.D. Gelenter, and M. Hong, *Transport-relevant protein conformational dynamics and water dynamics on multiple time scales in an archetypal proton channel: insights from solid-state NMR.* J. Am. Chem. Soc., 2018. **140**(4): p. 1514-1524.

93. Hu, F., W. Luo, S.D. Cady, and M. Hong, *Conformational plasticity of the influenza A M2 transmembrane helix in lipid bilayers under varying pH, drug binding, and membrane thickness.* Biochim. Biophys. Acta, 2011. **1808**(1): p. 415-23.

94. Wang, J., C.L. Ma, G. Fiorin, V. Carnevale, T. Wang, F.H. Hu, R.A. Lamb, L.H. Pinto, M. Hong, M.L. Klein, and W.F. DeGrado, *Molecular dynamics*

simulation directed rational design of inhibitors targeting drug-resistant mutants of influenza A virus M2. J. Am. Chem. Soc., 2011. **133**(32): p. 12834-12841.

95. Sugrue, R.J. and A.J. Hay, *Structural characteristics of the M2 protein of influenza a viruses: evidence that it forms a tetrameric channel.* Virol., 1991. **180**(2): p. 617-624.

96. Luo, W., S.D. Cady, and M. Hong, *Immobilization of the influenza A M2 transmembrane peptide in virus envelope-mimetic lipid membranes: a solid-state NMR investigation.* Biochemistry, 2009. **48**(27): p. 6361-6368.

97. Ohigashi, Y., C. Ma, X. Jing, V. Balannick, L.H. Pinto, and R.A. Lamb, *An amantadine-sensitive chimeric BM2 ion channel of influenza B virus has implications for the mechanism of drug inhibition.* Proc. Natl. Acad. Sci. U. S. A., 2009. **106**(44): p. 18775-18779.

98. Can, T.V., M. Sharma, I. Hung, P.L. Gor'kov, W.W. Brey, and T.A. Cross, *Magic angle spinning and oriented sample solid-state NMR structural restraints combine for influenza A M2 protein functional insights.* J. Am. Chem. Soc., 2012. **134**(22): p. 9022-9025.

99. Miao, Y., H. Qin, R. Fu, M. Sharma, T.V. Can, I. Hung, S. Luca, P.L. Gor'kov, W.W. Brey, and T.A. Cross, *M2 proton channel structural validation from full-length protein samples in synthetic bilayers and E. coli membranes.* Angew. Chem. Int. Ed. Engl., 2012. **51**(33): p. 8383-8386.

100. Hong, M., K.J. Fritzsching, and J.K. Williams, *Hydrogen-bonding partner of the proton-conducting histidine in the influenza M2 proton channel revealed from 1H chemical shifts.* J. Am. Chem. Soc., 2012. **134**(36): p. 14753-14755.

101. Miao, Y., R. Fu, H.X. Zhou, and T.A. Cross, *Dynamic short hydrogen bonds in histidine tetrad of full-length M2 proton channel reveal tetrameric structural heterogeneity and functional mechanism.* Structure, 2015. **23**(12): p. 2300-2308.

102. Caffrey, M. and V. Cherezov, *Crystallizing membrane proteins using lipidic mesophases.* Nat. Protoc., 2009. **4**(5): p. 706-731.

103. Liang, R., H. Li, J.M. Swanson, and G.A. Voth, *Multiscale simulation reveals a multifaceted mechanism of proton permeation through the influenza A M2 proton channel.* Proc. Natl. Acad. Sci. U. S. A., 2014. **111**(26): p. 9396-9401.

104. Wright, A.K., P. Batsomboon, J. Dai, I. Hung, H.X. Zhou, G.B. Dudley, and T.A. Cross, *Differential binding of rimantadine enantiomers to influenza A M2 proton channel.* J. Am. Chem. Soc., 2016. **138**(5): p. 1506-1509.

105. Leidner, F., N. Kurt Yilmaz, J. Paulsen, Y.A. Muller, and C.A. Schiffer, *Hydration structure and dynamics of inhibitor-bound HIV-1 protease.* J. Chem. Theory Comput., 2018. **14**(5): p. 2784-2796.

106. Spyrakis, F., M.H. Ahmed, A.S. Bayden, P. Cozzini, A. Mozzarelli, and G.E. Kellogg, *The roles of water in the protein matrix: a largely untapped resource for drug discovery.* J. Med. Chem., 2017. **60**(16): p. 6781-6827.

107. DiFrancesco, M.L., U.P. Hansen, G. Thiel, A. Moroni, and I. Schroeder, *Effect of cytosolic pH on inward currents reveals structural characteristics of the proton transport cycle in the influenza A protein M2 in cell-free membrane patches of xenopus oocytes.* PLoS One, 2014. **9**(9): p. e107406.

108. Fu, R., Y. Miao, H. Qin, and T.A. Cross, *Observation of the imidazole-imidazolium hydrogen bonds responsible for selective proton conductance in the influenza A M2 channel.* J. Am. Chem. Soc., 2020. **142**(5): p. 2115-2119.

109. Chen, H., Y. Wu, and G.A. Voth, *Proton transport behavior through the influenza A M2 channel: insights from molecular simulation.* Biophys J., 2007. **93**(10): p. 3470-3479.

110. Kass, I. and I.T. Arkin, *How pH opens a H+ channel: the gating mechanism of influenza A M2.* Structure, 2005. **13**(12): p. 1789-1798.

111. Wu, Y. and G.A. Voth, *A computational study of the closed and open states of the influenza a M2 proton channel.* Biophys. J., 2005. **89**(4): p. 2402-2411.

112. Mould, J.A., H.-C. Li, C.S. Dudlak, J.D. Lear, A. Pekosz, R.A. Lamb, and L.H. Pinto, *Mechanism for proton conduction of the M2 ion channel of influenza A virus.* J. Biol. Chem., 2000. **275**(12): p. 8592-8599.

113. Pielak, R.M. and J.J. Chou, *Kinetic analysis of the M2 proton conduction of the influenza virus.* J. Am. Chem. Soc., 2010. **132**(50): p. 17695-17697.

114. Peterson, E., T. Ryser, S. Funk, D. Inouye, M. Sharma, H. Qin, T.A. Cross, and D.D. Busath, *Functional reconstitution of influenza A M2(22-62).* Biochim. Biophys. Acta, 2011. **1808**(2): p. 516-521.

115. Leiding, T., J. Wang, J. Martinsson, W.F. DeGrado, and S.P. Årsköld, *Proton and cation transport activity of the M2 proton channel from influenza A virus.* Proc. Natl. Acad. Sci. U.S.A., 2010. **107**(35): p. 15409-15414.

116. Andreas, L.B., M.T. Eddy, R.M. Pielak, J.J. Chou, and R.G. Griffin, *Magic angle spinning NMR investigation of influenza A M2(18-60): support for an allosteric mechanism of inhibition.* J. Am. Chem. Soc., 2010. **132**(32): p. 10958-10960.

117. Andreas, L.B., M.T. Eddy, J.J. Chou, and R.G. Griffin, *Magic-angle-spinning NMR of the drug resistant S31N M2 proton transporter from influenza A.* J. Am. Chem. Soc., 2012. **134**(17): p. 7215-7218.

118. Colvin, M.T., L.B. Andreas, J.J. Chou, and R.G. Griffin, *Proton association constants of His 37 in the influenza-A M218-60 dimer-of-dimers.* Biochemistry, 2014. **53**(38): p. 5987-5994.

119. Andreas, L.B., M. Reese, M.T. Eddy, V. Gelev, Q.Z. Ni, E.A. Miller, L. Emsley, G. Pintacuda, J.J. Chou, and R.G. Griffin, *Structure and mechanism of the influenza A M218–60 dimer of dimers.* J. Am. Chem. Soc., 2015. **137**(47): p. 14877-14886.

120. Sakaguchi, T., Q.A. TU, L.H. Pinto, and R.A. Lamb, *The active oligomeric state of the minimalistic influenza virus M2 ion channel is a tetramer.* Proc. Natl. Acad. Sci. USA, 1997. **94**: p. 5000-5005.

121. Movellan, K.T., M. Wegstroth, K. Overkamp, A. Leonov, S. Becker, and L.B. Andreas, *Imidazole-Imidazole Hydrogen Bonding in the pH-Sensing*

Histidine Side Chains of Influenza A M2. J Am Chem Soc, 2020. **142**(6): p. 2704-2708.

122. Reif, B., S.E. Ashbrook, L. Emsley, and M. Hong, *Solid-state NMR spectroscopy.* Nature Reviews Methods Primers, 2021. **1**(1).

123. Raja, P.M.V. and A.R. Barron, *Physical Methods in Chemistry and Nano Science*. OpenStax CNX. 2019, http://cnx.org/contents/ba27839d-5042-4a40-afcf-c0e6e39fb454@25.2.

124. Schmidt-Rohr, K. and H.W. Spiess, *Multidimensional solid-state NMR and Polymers*. Magnetic Resonance in Chemistry, ed. W.S. Veeman. Vol. 478. 1994, New York: Academic Press. 759-759.

125. Facelli, J.C., *Chemical shift tensors: theory and application to molecular structural problems.* Prog. Nucl. Magn. Reson. Spectrosc., 2011. **58**(3-4): p. 176-201.

126. Andrew, E.R., A. Bradbury, and R.G. Eades, *Nuclear magnetic resonance spectra from a crystal rotated at high speed.* Nature, 1958. **182**(4650): p. 1659-1659.

127. Schaefer, J. and E.O. Stejskal, *Carbon-13 nuclear magnetic resonance of polymers spinning at the magic angle.* J. Am. Chem. Soc., 1976. **98**(4): p. 1031-1032.

128. . Introduction to solid- state NMR spectroscopy, ed. M.J. Duer. 2004: Blackwell Science.

129. Pines, A., M.G. Gibby, and J.S. Waugh, *Proton-enhanced NMR of dilute spins in solids.* J. Chem. Phys., 1973. **59**(2): p. 569-590.

130. Mabrey, S. and J.M. Sturtevant, *Investigation of phase transitions of lipids and lipid mixtures by sensitivity differential scanning calorimetry.* Proc. Natl. Acad. Sci. U. S. A., 1976. **73**(11): p. 3862-3866.

131. McElhaney, R.N., *The use of differential scanning calorimetry and differential thermal analysis in studies of model and biological membranes.* Chem. Phys. Lipids, 1982. **30**(2-3): p. 229-259.

132. Chiu, M.H. and E.J. Prenner, *Differential scanning calorimetry: An invaluable tool for a detailed thermodynamic characterization of macromolecules and their interactions.* J. Pharm. Bioallied Sci., 2011. **3**(1): p. 39-59.

133. Demetzos, C., *Differential Scanning Calorimetry (DSC): a tool to study the thermal behavior of lipid bilayers and liposomal stability.* J. Liposome. Res., 2008. **18**(3): p. 159-173.

134. Chountoulesi, M., N. Naziris, T. Mavromoustakos, and C. Demetzos, *A differential scanning calorimetry (DSC) experimental protocol for evaluating the modified thermotropic behavior of liposomes with incorporated guest molecules*. Supramolecules in Drug Discovery and Drug Delivery. Methods in Molecular Biology, ed. T. Mavromoustakos, A.G. Tzakos, and S. Durdagi. Vol. 2207. 2021, New York, NY: Humana. 299-312.

135. Fotakis, C., D. Christodouleas, P. Zoumpoulakis, E. Kritsi, N.P. Benetis, T. Mavromoustakos, H. Reis, A. Gili, M.G. Papadopoulos, and M. Zervou, *Comparative biophysical studies of sartan class drug molecules losartan and candesartan (CV-11974) with membrane bilayers.* J. Phys. Chem. B., 2011. **115**(19): p. 6180-6192.

136. Sadeghpour, A., M. Rappolt, D. Ntountaniotis, P. Chatzigeorgiou, K. Viras, G. Megariotis, M.G. Papadopoulos, E. Siapi, G. Mali, and T. Mavromoustakos, *Comparative study of interactions of aliskiren and AT1 receptor antagonists with lipid bilayers.* Biochim. Biophys. Acta, Biomembr., 2015. **1848**(4): p. 984-994.

137. Leonis, G., E.C. Semidalas, P. Chatzigeorgiou, E. Pollatos, C.E. Semidalas, M. Rappolt, K. Viras, and T. Mavromoustakos, *Chapter five - Vinblastine: cholesterol interactions in lipid bilayers.* Advances in Biomembranes and Lipid Self-Assembly, 2019. **29**: p. 127-157.

138. Matsingou, C. and C. Demetzos, *Calorimetric study on the induction of interdigitated phase in hydrated DPPC bilayers by bioactive labdanes and correlation to their liposome stability: The role of chemical structure.* Chem. Phys. Lipids, 2007. **145**(1): p. 45-62.

139. Matsingou, C. and C. Demetzos, *The perturbing effect of cholesterol on the interaction between labdanes and DPPC bilayers.* Thermochimica Acta, 2007. **452**(2): p. 116-123.

140. Koukoulitsa, C., I. Kyrikou, C. Demetzos, and T. Mavromoustakos, *The role of the anticancer drug vinorelbine in lipid bilayers using differential scanning calorimetry and molecular modeling.* Chem. Phys. Lipids, 2006. **144**(1): p. 85-95.

141. Kyrikou, I., A. Georgopoulos, S. Hatziantoniou, T. Mavromoustakos, and C. Demetzos, *A comparative study of the effects of cholesterol and sclareol, a bioactive labdane type diterpene, on phospholipid bilayers.* Chem. Phys. Lipids, 2005. **133**(2): p. 125-134.

142. Haines, P.J., *Thermal methods of analysis: principles, applications and problems*. 1995, Oxford: Blackie Academic & Professional.

143. Gugliuzza, A., *Differential scanning calorimetry in membrane characterization*. Encyclopedia of Membranes, ed. E. Drioli and L. Giorno. 2015: Springer, Berlin, Heidelberg. 1-3.

144. Hatziantonioy, S. and C. Demetzos, *Lipids of membranes: chemistry, biological role and applications as drug carriers.* Stud. Nat. Prod. Chem., 2008. **34**: p. 173-202.

145. Ford, J. and P. Timmins, *Pharmaceutical thermal analysis, techniques and applications*. Ellis Horwood: Chichester. 1989.

146. Gardikis, K., S. Hatziantoniou, K. Viras, M. Wagner, and C. Demetzos, *Interaction of dendrimers*

with model lipid membranes assessed by DSC and RAMAN spectroscopy. Nano-encapsulation Technologies: Frontiers of Nanotherapy, ed. M. Reza. 2006, The Netherlands: Springer.

147. Konstantinidi, A., N. Naziris, M. Chountoulesi, S. Kiriakidi, B. Sartori, D. Kolokouris, H. Amenitsch, G. Mali, D. Ntountaniotis, C. Demetzos, T. Mavromoustakos, and A. Kolocouris, *Comparative perturbation effects exerted by the influenza A M2 WT protein inhibitors amantadine and the spiro[pyrrolidine-2,2'-adamantane] variant AK13 to membrane bilayers*

studied using biophysical experiments and molecular dynamics simulations. J. Phys. Chem. B, 2018. **122**(43): p. 9877-9895.

148. Konstantinidi, A., M. Chountoulesi, N. Naziris, B. Sartori, H. Amenitsch, G. Mali, T. Cendak, M. Plakantonaki, I. Triantafyllakou, T. Tselios, C. Demetzos, D.D. Busath, T. Mavromoustakos, and A. Kolocouris, *The boundary lipid around DMPC-spanning influenza A M2 transmembrane domain channels: Its structure and potential for drug accommodation.* Biochim. Biophys. Acta - Biomembr., 2020. **1862**(3): p. 183156.

149. Li, T., A.J. Senesi, and B. Lee, *Small angle X-ray scattering for nanoparticle research.* Chem. Rev., 2016. **116**(18): p. 11128-11180.

150. Bolze, J., V. Kogan, D. Beckers, and M. Fransen, *High-performance small- and wide-angle X-ray scattering (SAXS/WAXS) experiments on a multi-functional laboratory goniometer platform with easily exchangeable X-ray modules.* Rev. Sci. Instrum., 2018. **89**(8): p. 085115.

151. *Modern aspects of small-angle scattering*, H. Brumberger, Editor. 1995, Springer, Netherlands. p. XV, 463.

152. Thiele, E., *Equation of state for hard spheres.* J. Chem. Phys., 1963. **39**(2): p. 474-479.

153. Pedersen, J.S., *Analysis of small-angle scattering data from colloids and polymer solutions: modeling and least-squares fitting.* Adv. Colloid Interface Sci., 1997. **70**: p. 171-210.

154. Ren, Y., Z. Ma, and P.G. Bruce, *Ordered mesoporous metal oxides: synthesis and applications.* Chem. Soc. Rev., 2012. **41**(14): p. 4909-4927.

155. Blanton, T.N., C.L. Barnes, and M. Lelental, *Preparation of silver behenate coatings to provide low- to mid-angle diffraction calibration.* J. Appl. Crystallogr., 2000. **33**(1): p. 172-173.

156. Zhang, F., J. Ilavsky, G.G. Long, J.P.G. Quintana, A.J. Allen, and P.R. Jemian, *Glassy carbon as an absolute intensity calibration standard for small-angle scattering.* Metall. Mater. Trans. A, 2010. **41**(5): p. 1151-1158.

157. Orthaber, D., A. Bergmann, and O. Glatter, *SAXS experiments on absolute scale with Kratky systems using water as a secondary standard.* J. Appl. Crystallogr., 2000. **33**(2): p. 218-225.

158. Renaud, G., R. Lazzari, and F. Leroy, *Probing surface and interface morphology with grazing incidence small angle X-ray scattering.* Surf. Sci. Rep., 2009. **64**(8): p. 255-380.

159. Wang, W., N.S. Murthy, and D.T. Grubb, *'Butterfly' small-angle X-ray scattering patterns in semicrystalline polymers are double-elliptical.* Polymer, 2007. **48**(12): p. 3393-3399.

160. Allen, M.P., *Introduction to molecular dynamics simulation*, in *Computational soft matter: from synthetic polymers to proteins*, K.B. Norbert Attig, Helmut Grubmuller, Kurt Kremer, Editor. 2004, John von Neumann Institute for Computing: Julich. p. 1-28.

161. Kollman, P., *Free energy calculations: applications to chemical and biochemical phenomena.* Chem. Rev., 2002. **93**(7): p. 2395-2417.

162. Pohorille, A., C. Jarzynski, and C. Chipot, *Good practices in free-energy calculations.* J Phys Chem B, 2010. **114**(32): p. 10235-53.

163. Cournia, Z., B. Allen, and W. Sherman, *Relative binding free energy calculations in drug discovery: recent advances and practical considerations.* J. Chem. Inf. Model., 2017. **57**(12): p. 2911-2937.

164. Landau, L.D., *Statistical Physics*. 1938, Oxford: The Clarendon Press: Oxford: The Clarendon Press.

165. Zwanzig, R.W., *High-temperature equation of state by a perturbation method. i. nonpolar gases.* J. Chem. Phys., 1954. **22**(8): p. 1420-1426.

166. Steinbrecher, T., I. Joung, and D.A. Case, *Soft-core potentials in thermodynamic integration: comparing one- and two-step transformations.* J. Comput. Chem., 2011. **32**(15): p. 3253-3263.

167. Shirts, M.R. and V.S. Pande, *Comparison of efficiency and bias of free energies computed by exponential averaging, the Bennett acceptance ratio, and thermodynamic integration.* J. Chem. Phys., 2005. **122**(14): p. 144107.

168. Paliwal, H. and M.R. Shirts, *A benchmark test set for alchemical free energy transformations and its use to quantify error in common free energy methods.* J .Chem. Theory Comput., 2011. **7**(12): p. 4115-34.

169. Kolocouris, N., G.B. Foscolos, A. Kolocouris, P. Marakos, N. Pouli, G. Fytas, S. Ikeda, and E. De Clercq, *Synthesis and antiviral activity evaluation of some aminoadamantane derivatives.* J. Med. Chem., 1994. **37**: p. 2896-2902.

170. Kolocouris, A., C. Tzitzoglaki, F.B. Johnson, R. Zell, A.K. Wright, T.A. Cross, I. Tietjen, D. Fedida, and D.D. Busath, *Aminoadamantanes with persistent in vitro efficacy against H1N1 (2009) influenza A.* J. Med. Chem., 2014. **57**(11): p. 4629-39.

171. Wang, J., J.X. Qiu, C. Soto, and W.F. DeGrado, *Structural and dynamic mechanisms for the function and inhibition of the M2 proton channel from influenza A virus.* Curr. Opin. Struct. Biol., 2011. **21**(1): p. 68-80.

172. Gkeka, P., S. Eleftheratos, A. Kolocouris, and Z. Cournia, *Free Energy Calculations Reveal the Origin of Binding Preference for Aminoadamantane Blockers of Influenza A/M2TM Pore.* J Chem Theory Comput, 2013. **9**(2): p. 1272-81.

173. Homeyer, N., H. Ioannidis, F. Kolarov, G. Gauglitz, C. Zikos, A. Kolocouris, and H. Gohlke, *Interpreting Thermodynamic Profiles of Aminoadamantane Compounds Inhibiting the M2 Proton Channel of Influenza A by Free Energy Calculations.* J Chem Inf Model, 2016. **56**(1): p. 110-126.

174. Ioannidis, H., A. Drakopoulos, C. Tzitzoglaki, N. Homeyer, F. Kolarov, P. Gkeka, K. Freudenberger, C. Liolios, G. Gauglitz, Z. Cournia, H. Gohlke, and A. Kolocouris, *Alchemical free energy calculations and isothermal titration calorimetry measurements of aminoadamantanes bound to the closed state of influenza A/M2TM.* J. Chem. Inf. Model., 2016. **56**(5): p. 862-76.

175. Gleed, M.L., H. Ioannidis, A. Kolocouris, and D.D. Busath, *Resistance-Mutation (N31) Effects on Drug Orientation and Channel Hydration in*

Amantadine-Bound Influenza A M2. J Phys Chem B, 2015. **119**(35): p. 11548-59.

176. Tzitzoglaki, C., A. Wright, K. Freudenberger, A. Hoffmann, I. Tietjen, I. Stylianakis, F. Kolarov, D. Fedida, M. Schmidtke, G. Gauglitz, T.A. Cross, and A. Kolocouris, *Binding and proton blockage by amantadine variants of the influenza M2WT and M2S31N explained.* J. Med. Chem., 2017. **60**(5): p. 1716-1733.

177. Tzitzoglaki, C., A. Wright, I. Tejen, F. Kolarov, K. Freudenberger, D. Fedida, G. Gauglitz, T. Cross, and K. A, *Aminoadamantanes bound to influenza WT and S31N M2TM - Evidence for a weak binding - no blocking inhibition of proton conductance of S31N M2 protein.* Accepted.

178. Williams, J.K., D. Tietze, J. Wang, Y. Wu, W.F. DeGrado, and M. Hong, *Drug-induced conformational and dynamical changes of the S31N mutant of the influenza M2 proton channel investigated by solid-state NMR.* J. Am. Chem. Soc., 2013. **135**(26): p. 9885-97.

179. Kolocouris, A., C. Zikos, and R.W. Broadhurst, *19F NMR detection of the complex between amantadine and the receptor portion of the influenza A M2 ion channel in DPC micelles.* Bioorganic Med. Chem. Lett., 2007. **17**(14): p. 3947-52.

180. Chipot, C., F. Dehez, J.R. Schnell, N. Zitzmann, E. Pebay-Peyroula, L.J. Catoire, B. Miroux, E.R.S. Kunji, G. Veglia, T.A. Cross, and P. Schanda, *Perturbations of Native Membrane Protein Structure in Alkyl Phosphocholine Detergents: A Critical Assessment of NMR and Biophysical Studies.* Chem Rev, 2018. **118**(7): p. 3559-3607.

181. Cristian, L., J.D. Lear, and W.F. DeGrado, *Use of thiol-disulfide equilibria to measure the energetics of assembly of transmembrane helices in phospholipid bilayers.* Proc Natl Acad Sci U S A, 2003. **100**(25): p. 14772-7.

182. Li, C., M. Yi, J. Hu, H.X. Zhou, and T.A. Cross, *Solid-state NMR and MD simulations of the antiviral drug amantadine solubilized in DMPC bilayers.* Biophys J, 2008. **94**(4): p. 1295-302.

183. Duff, K.C., A.J. Cudmore, and J.P. Bradshaw, *The location of amantadine hydrochloride and free base within phospholipid multilayers: a neutron and X-ray diffraction study.* Biochimica et Biophysica Acta (BBA) - Biomembranes, 1993. **1145**(1): p. 149-156.

184. Subczynski, W.K., J. Wojas, V. Pezeshk, and A. Pezeshk, *Partitioning and localization of spin-labeled amantadine in lipid bilayers: An EPR study.* J. Pharm. Sci., 1998. **87**(10): p. 1249-54.

185. Chew, C.F., A. Guy, and P.C. Biggin, *Distribution and dynamics of adamantanes in a lipid bilayer.* Biophys J, 2008. **95**(12): p. 5627-36.

186. Amenitsch, H., M. Rappolt, M. Kriechbaum, H. Mio, P. Laggner, and S. Bernstorff, *First performance assessment of the small-angle X-ray scattering beamline at ELETTRA.* J. Synchrotron Radiat., 1998. **5**(Pt 3): p. 506-8.

187. Suwalsky, M., M. Jemiola-Rzeminska, M. Altamirano, F. Villena, N. Dukes, and K. Strzalka, *Interactions of the antiviral and antiparkinson agent amantadine with lipid membranes and human erythrocytes.* Biophys Chem, 2015. **202**: p. 13-20.

188. Khondker, A., A.K. Dhaliwal, R.J. Alsop, J. Tang, M. Backholm, A.-C. Shi, and M.C. Rheinstädter, *Caffeine in drug cocktails: The formation of "water pockets" in membranes.* Physics in Canada, 2017. **74**(4): p. 174-175.

189. Khondker, A., A. Dhaliwal, R.J. Alsop, J. Tang, M. Backholm, A.C. Shi, and M.C. Rheinstadter, *Partitioning of caffeine in lipid bilayers reduces membrane fluidity and increases membrane thickness.* Phys Chem Chem Phys, 2017. **19**(10): p. 7101-7111.

190. Mavromoustakos, T., E. Theodoropoulou, D. Papahatjis, T. Kourouli, v.-P. Yang, M. Trumbore, and A. Makriyannis, *Studies on the thermotropic effects of cannabinoids on phosphatidylcholine bilayers using differential scanning calorimetry and small angle X-ray diffraction.* Biochimica et Biophysica Acta (BBA) - Biomembranes, 1996. **1281**(2): p. 235-244.

191. Boggara, M.B., M. Mihailescu, and R. Krishnamoorti, *Structural association of nonsteroidal anti-inflammatory drugs with lipid membranes.* J Am Chem Soc, 2012. **134**(48): p. 19669-76.

192. Gu, R.X., L.A. Liu, D.Q. Wei, J.G. Du, L. Liu, and H. Liu, *Free energy calculations on the two drug binding sites in the M2 proton channel.* J Am Chem Soc, 2011. **133**(28): p. 10817-25.

193. Hammersley, A.P., *ESRF97HA02T, ``FIT2D: An introduction and overview''*, in *ESRF Internal Report*. 1997.

194. Zhang, R., S. Tristram-Nagle, W. Sun, R.L. Headrick, T.C. Irving, R.M. Suter, and J.F. Nagle, *Small-angle X-ray scattering from lipid bilayers is well described by modified Caillé theory but not by paracrystalline theory.* Biophys. J., 1996. **70**(1): p. 349-357.

195. Rappolt, M., *Bilayer thickness estimations with “poor” diffraction data.* J. Appl. Phys., 2010. **107**(8): p. 084701.

196. Hess, B., C. Kutzner, D. van der Spoel, and E. Lindahl, *GROMACS 4: algorithms for highly efficient, load-balanced, and scalable molecular simulation.* J. Chem. Theory. Comput., 2008. **4**(3): p. 435-47.

197. Klauda, J.B., R.M. Venable, J.A. Freites, J.W. O'Connor, D.J. Tobias, C. Mondragon-Ramirez, I. Vorobyov, A.D. MacKerell, Jr., and R.W. Pastor, *Update of the CHARMM all-atom additive force field for lipids: validation on six lipid types.* J Phys Chem B, 2010. **114**(23): p. 7830-43.

198. Vanommeslaeghe, K., E. Hatcher, C. Acharya, S. Kundu, S. Zhong, J. Shim, E. Darian, O. Guvench, P. Lopes, I. Vorobyov, and A.D. Mackerell, Jr., *CHARMM general force field: A force field for drug-like molecules compatible with the CHARMM all-atom additive biological force fields.* J Comput Chem, 2010. **31**(4): p. 671-90.

199. Jorgensen, W.L., J. Chandrasekhar, J.D. Madura, R.W. Impey, and M.L. Klein, *Comparison of simple potential functions for simulating liquid water.* J. Chem. Phys., 1983. **79**(2): p. 926-935.

200. Jo, S., T. Kim, V.G. Iyer, and W. Im, *CHARMM-GUI: a web-based graphical user interface for CHARMM.* J Comput Chem, 2008. **29**(11): p. 1859-65.

201. Zoete, V., M.A. Cuendet, A. Grosdidier, and O. Michielin, *SwissParam: a fast force field generation tool for small organic molecules.* J Comput Chem, 2011. **32**(11): p. 2359-68.

202. Halgren, T.A., *Merck molecular force field. I. Basis, form, scope, parameterization, and performance of MMFF94.* J. Comp. Chem, 1996. **17**: p. 490-519.

203. Berendsen, H.J.C., J.P.M. Postma, W.F. van Gunsteren, A. DiNola, and J.R. Haak, *Molecular dynamics with coupling to an external bath.* The Journal of Chemical Physics, 1984. **81**(8): p. 3684-3690.

204. Koynova, R. and M. Caffrey, *Phases and phase transitions of the phosphatidylcholines.* Biochim. Biophys. Acta, Rev. Biomembr., 1998. **1376**(1): p. 91-145.

205. Darden, T., D. York, and L. Pedersen, *Particle mesh Ewald: An N·log(N) method for Ewald sums in large systems.* J. Chem. Phys., 1993. **98**(12): p. 10089-10092.

206. Essmann, U., L. Perera, M.L. Berkowitz, T. Darden, H. Lee, and L.G. Pedersen, *A smooth particle mesh Ewald method.* J. Chem. Phys., 1995. **103**(19): p. 8577-8593.

207. Case, D.A., T.E. Cheatham, 3rd, T. Darden, H. Gohlke, R. Luo, K.M. Merz, Jr., A. Onufriev, C. Simmerling, B. Wang, and R.J. Woods, *The Amber biomolecular simulation programs.* J. Comput. Chem., 2005. **26**(16): p. 1668-88.

208. Salomon-Ferrer, R., D.A. Case, and R.C. Walker, *An overview of the Amber biomolecular simulation package.* Wiley Interdisciplinary Reviews: Computational Molecular Science, 2013. **3**(2): p. 198-210.

209. *Schrödinger, Desmond 3.1, user manual*. 2012, New York, NY: Schrödinger Press, LLC.

210. Case D.A., Berryman J.T., R.M. Betz, Cai Q., Cerutti D.S., I. T.E. Cheatham, Darden T.A., Duke R.E., Gohlke H., Goetz A.W., Gusarov S., Homeyer N., Janowski P., Kaus J., Kolossváry I., Kovalenko A., Lee T.S.,

LeGrand S., Luchko T., Luo R., Madej B., K.M, and V. B., *The Amber molecular dynamics package. AMBER, 2014, 14*. 2014.

211. Maier, J.A., C. Martinez, K. Kasavajhala, L. Wickstrom, K.E. Hauser, and C. Simmerling, *ff14SB: Improving the Accuracy of Protein Side Chain and Backbone Parameters from ff99SB.* J Chem Theory Comput, 2015. **11**(8): p. 3696-713.

212. Dickson, C.J., B.D. Madej, A.A. Skjevik, R.M. Betz, K. Teigen, I.R. Gould, and R.C. Walker, *Lipid14: The Amber Lipid Force Field.* J Chem Theory Comput, 2014. **10**(2): p. 865-879.

213. Zgarbova, M., M. Otyepka, J. Sponer, A. Mladek, P. Banas, T.E. Cheatham, 3rd, and P. Jurecka, *Refinement of the Cornell et al. Nucleic Acids Force Field Based on Reference Quantum Chemical Calculations of Glycosidic Torsion Profiles.* J Chem Theory Comput, 2011. **7**(9): p. 2886-2902.

214. Press, W.H., S.A. Teukolsky, W.T. Vetterling, and B.P. Flannery, *Numerical recipes: The art of scientific computing*. 3rd ed. 2007, New York: Cambridge University Press.

215. Pastor, R.W., B.R. Brooks, and A. Szabo, *An analysis of the accuracy of Langevin and molecular dynamics algorithms.* Molecular Physics, 2006. **65**(6): p. 1409-1419.

216. Ryckaert, J.-P., G. Ciccotti, and H.J.C. Berendsen, *Numerical integration of the cartesian equations of motion of a system with constraints: molecular dynamics of n-alkanes.* Journal of Computational Physics, 1977. **23**(3): p. 327-341.

217. Humphrey, W., A. Dalke, and K. Schulten, *VMD: visual molecular dynamics.* J. Mol. Graph., 1996. **14**(1): p. 33-38.

218. Roe, D.R. and T.E. Cheatham, 3rd, *PTRAJ and CPPTRAJ: Software for Processing and Analysis of Molecular Dynamics Trajectory Data.* J Chem Theory Comput, 2013. **9**(7): p. 3084-95.

219. Matsingou, C., S. Hatziantoniou, A. Georgopoulos, K. Dimas, A. Terzis, and C. Demetzos, *Labdane-type diterpenes: thermal effects on phospholipid*

bilayers, incorporation into liposomes and biological activity. Chem Phys Lipids, 2005. **138**(1-2): p. 1-11.

220. Matsingou, C. and C. Demetzos, *Effect of the nature of the 3beta-substitution in manoyl oxides on the thermotropic behavior of DPPC lipid bilayer and on DPPC liposomes.* J. Liposome Res., 2007. **17**(2): p. 89-105.

221. Nomura, K., M. Lintuluoto, and K. Morigaki, *Hydration and temperature dependence of 13C and 1H NMR spectra of the DMPC phospholipid membrane and complete resonance assignment of its crystalline state.* J. Phys. Chem. B, 2011. **115**(50): p. 14991-5001.

222. Janiak, M.J., D.M. Small, and G.G. Shipley, *Nature of the thermal pretransition of synthetic phospholipids: dimyristoyl- and dipalmitoyllecithin.* Biochemistry, 2002. **15**(21): p. 4575-4580.

223. Mavromoustakos, T., D. Papahatjis, and P. Laggner, *Differential membrane fluidization by active and inactive cannabinoid analogues.* Biochim Biophys Acta, 2001. **1512**(2): p. 183-90.

224. Liossi Adamantia, S., D. Ntountaniotis, T.F. Kellici, M.V. Chatziathanasiadou, G. Megariotis, M. Mania, J. Becker-Baldus, M. Kriechbaum, A. Krajnc, E. Christodoulou, C. Glaubitz, M. Rappolt, H. Amenitsch, G. Mali, D.N. Theodorou, G. Valsami, M. Pitsikalis, H. Iatrou, A.G. Tzakos, and T. Mavromoustakos, *Exploring the interactions of irbesartan and irbesartan-2-hydroxypropyl-beta-cyclodextrin complex with model membranes.* Biochim. Biophys. Acta, Biomembr., 2017. **1859**(6): p. 1089-1098.

225. Dannenberg, J.J., *An Introduction to Hydrogen Bonding By George A. Jeffrey (University of Pittsburgh). Oxford University Press: New York and Oxford. 1997. ix + 303 pp. $60.00. ISBN 0-19-509549-9.* Journal of the American Chemical Society, 1998. **120**(22): p. 5604-5604.

226. Saotome, K., K.C. Duong-Ly, and K.P. Howard, *Influenza A M2 protein conformation depends on choice of model membrane.* Biopolymers, 2015. **104**(4): p. 405-11.

227. Schmidt, N.W., A. Mishra, J. Wang, W.F. DeGrado, and G.C. Wong, *Influenza virus A M2 protein generates negative gaussian membrane curvature necessary for budding and scission.* J. Am. Chem. Soc., 2013. **135**(37): p. 13710-13719.

228. Qin, H., Y. Miao, T.A. Cross, and R. Fu, *Beyond structural biology to functional biology: Solid-state NMR experiments and strategies for understanding the M2 proton channel conductance.* J. Phys. Chem. B, 2017. **121**(18): p. 4799-4809.

229. Markiewicz, B.N., T. Lemmin, W. Zhang, I.A. Ahmed, H. Jo, G. Fiorin, T. Troxler, W.F. DeGrado, and F. Gai, *Infrared and fluorescence assessment of the hydration status of the tryptophan gate in the influenza A M2 proton channel.* Phys. Chem. Chem. Phys., 2016. **18**(41): p. 28939-28950.

230. Cady, S.D. and M. Hong, *Effects of amantadine on the dynamics of membrane-bound influenza A M2 transmembrane peptide studied by NMR relaxation.* J. Biomol. NMR, 2009. **45**(1-2): p. 185-96.

231. Cristian, L., J.D. Lear, and W.F. DeGrado, *Use of thiol-disulfide equilibria to measure the energetics of assembly of transmembrane helices in phospholipid bilayers.* Proc. Natl. Acad. Sci. U. S. A., 2003. **100**(25): p. 14772-7.

232. Wang, T. and M. Hong, *Investigation of the curvature induction and membrane localization of the influenza virus M2 protein using static and off-magic-angle spinning solid-state nuclear magnetic resonance of oriented bicelles.* Biochemistry, 2015. **54**(13): p. 2214-26.

233. Pan, J., A. Dalzini, and L. Song, *Cholesterol and phosphatidylethanolamine lipids exert opposite effects on membrane modulations caused by the M2 amphipathic helix.* Biochim. Biophys. Acta, Biomembr., 2019. **1861**(1): p. 201-209.

234. Cross, T.A., D.T. Murray, and A. Watts, *Helical membrane protein conformations and their environment.* Eur. Biophys. J., 2013. **42**(10): p. 731-55.

235. Paulino, J., X. Pang, I. Hung, H.X. Zhou, and T.A. Cross, *Influenza A M2 Channel Clustering at High Protein/Lipid Ratios: Viral Budding Implications.* Biophys. J., 2019. **116**(6): p. 1075-1084.

236. Szlenk, C.T., J.B. Gc, and S. Natesan, *Does the lipid bilayer orchestrate access and binding of ligands to transmembrane orthosteric/allosteric sites of G protein-coupled receptors?* Mol. Pharmacol., 2019. **96**(5): p. 527-541.

237. Tselios, T., L. Probert, I. Daliani, E. Matsoukas, A. Troganis, I.P. Gerothanassis, T. Mavromoustakos, G.J. Moore, and J.M. Matsoukas, *Design and synthesis of a potent cyclic analogue of the myelin basic protein epitope MBP72-85: importance of the Ala81 carboxyl group and of a cyclic conformation for induction of experimental allergic encephalomyelitis.* J. Med. Chem., 1999. **42**(7): p. 1170-7.

238. Ieronymaki, M., M.E. Androutsou, A. Pantelia, I. Friligou, M. Crisp, K. High, K. Penkman, D. Gatos, and T. Tselios, *Use of the 2-chlorotrityl chloride resin for microwave-assisted solid phase peptide synthesis.* Biopolymers, 2015. **104**(5): p. 506-14.

239. Tapeinou, A., M.T. Matsoukas, C. Simal, and T. Tselios, *Review cyclic peptides on a merry-go-round; towards drug design.* Biopolymers, 2015. **104**(5): p. 453-61.

240. Emmanouil, M., V. Tseveleki, I. Triantafyllakou, A. Nteli, T. Tselios, and L. Probert, *A cyclic altered peptide analogue based on myelin basic protein 87-99 provides lasting prophylactic and therapeutic protection against acute experimental autoimmune encephalomyelitis.* Molecules, 2018. **23**(2): p. 304.

241. Friligou, I., E. Papadimitriou, D. Gatos, J. Matsoukas, and T. Tselios, *Microwave-assisted solid-phase peptide synthesis of the 60-110 domain of human pleiotrophin on 2-chlorotrityl resin.* J. Amino Acids, 2011. **40**(5): p. 1431-40.

242. Bowers, K.J., E. Chow, H. Xu, R.O. Dror, M.P. Eastwood, B.A. Gregersen, J.L. Klepeis, I. Kolossvary, M.A. Moraes, F.D. Sacerdoti, J.K. Salmon, Y. Shan, and D.E. Shaw, *Scalable algorithms for molecular dynamics*

simulations on commodity clusters, in *Proceedings of the 2006 ACM/IEEE conference on Supercomputing*. 2006, ACM: Tampa, Florida. p. 84.

243. Schrodinger, L., *Maestro-Desmond Interoperability Tools, version 3.1.* 2012.

244. Jorgensen, W.L., D.S. Maxwell, and J. Tirado-Rives, *Development and testing of the OPLS all-atom force field on conformational energetics and properties of organic liquids.* J. Am. Chem. Soc., 1996. **118**(45): p. 11225-11236.

245. Kaminski, G.A., R.A. Friesner, J. Tirado-Rives, and W.L. Jorgensen, *Evaluation and reparametrization of the OPLS-AA force field for proteins via comparison with accurate quantum chemical calculations on peptides.* J. Phys. Chem. B, 2001. **105**(28): p. 6474-6487.

246. Rizzo, R.C. and W.L. Jorgensen, *OPLS all-atom model for amines: resolution of the amine hydration problem.* J. Am. Chem. Soc., 1999. **121**(20): p. 4827-4836.

247. Hornak, V., R. Abel, A. Okur, B. Strockbine, A. Roitberg, and C. Simmerling, *Comparison of multiple Amber force fields and development of improved protein backbone parameters.* Proteins, 2006. **65**(3): p. 712-25.

248. Martyna, G.J., D.J. Tobias, and M.L. Klein, *Constant pressure molecular dynamics algorithms.* J. Chem. Phys., 1994. **101**(5): p. 4177-4189.

249. Humphreys, D.D., R.A. Friesner, and B.J. Berne, *A Multiple-Time-Step Molecular Dynamics Algorithm for Macromolecules.* The Journal of Physical Chemistry, 1994. **98**(27): p. 6885-6892.

250. Schrodinger, L., *Schrödinger, Maestro 8.5, User Manual*. 2008, New York, NY: Schrödinger Press, LLC.

251. Berendsen, H.J.C., D. van der Spoel, and R. van Drunen, *GROMACS: a message-passing parallel molecular dynamics implementation.* Comput. Phys. Commun., 1995. **91**(1): p. 43-56.

252. Mori, T., F. Ogushi, and Y. Sugita, *Analysis of lipid surface area in protein-membrane systems combining Voronoi tessellation and Monte Carlo integration methods.* J. Comput. Chem., 2012. **33**(3): p. 286-93.

253. Heimburg, T., *A model for the lipid pretransition: coupling of ripple formation with the chain-melting transition.* Biophys. J., 2000. **78**(3): p. 1154-65.

254. Posch, M., U. Rakusch, C. Mollay, and P. Laggner, *Cooperative effects in the interaction between melittin and phosphatidylcholine model membranes. Studies by temperature scanning densitometry.* J. Biol. Chem., 1983. **258**(3): p. 1761-1766.

255. Lohner, K., A. Latal, R.I. Lehrer, and T. Ganz, *Differential scanning microcalorimetry indicates that human defensin, HNP-2, interacts specifically with biomembrane mimetic systems.* Biochemistry, 1997. **36**(6): p. 1525-31.

256. Liao, S.Y., M. Lee, and M. Hong, *Interplay between membrane curvature and protein conformational equilibrium investigated by solid-state NMR.* J. Struct. Biol., 2019. **206**(1): p. 20-28.

257. Balgavý, P., M. Dubničková, N. Kučerka, M.A. Kiselev, S.P. Yaradaikin, and D. Uhríková, *Bilayer thickness and lipid interface area in unilamellar extruded 1,2-diacylphosphatidylcholine liposomes: a small-angle neutron scattering study.* Biochim. Biophys. Acta, Biomembr., 2001. **1512**(1): p. 40-52.

258. Olsen, R.W., *Picrotoxin-like channel blockers of GABAA receptors.* Proc .Natl. Acad. Sci. U. S. A., 2006. **103**(16): p. 6081.

259. Wanka, L., K. Iqbal, and P.R. Schreiner, *The lipophilic bullet hits the targets: medicinal chemistry of adamantane derivatives.* Chem. Rev., 2013. **113**(5): p. 3516-3604.

260. CDC, *Situation Update: Summary of Weekly FluView Report.* 2018.

261. Taubenberger, J.K. and D.M. Morens, *1918 influenza: the mother of all pandemics.* Emerg. Infect. Dis., 2006. **12**(1): p. 15-22.

262. Shaw, M.L., *The next wave of influenza drugs.* ACS Infect. Dis., 2017. **3**(10): p. 691-694.

263. Martin, K. and A. Helenius, *Nuclear transport of influenza virus ribonucleoproteins: The viral matrix protein (M1) promotes export and inhibits import.* Cell, 1991. **67**(1): p. 117-130.

264. Balannik, V., V. Carnevale, G. Fiorin, B.G. Levine, R.A. Lamb, M.L. Klein, W.F. Degrado, and L.H. Pinto, *Functional studies and modeling of pore-lining residue mutants of the influenza a virus M2 ion channel.* Biochemistry, 2010. **49**(4): p. 696-708.

265. Venkataraman, P., R.A. Lamb, and L.H. Pinto, *Chemical rescue of histidine selectivity filter mutants of the M2 ion channel of influenza A virus.* J. Biol. Chem., 2005. **280**(22): p. 21463-21472.

266. Thomaston, J.L. and W.F. DeGrado, *Crystal structure of the drug-resistant S31N influenza M2 proton channel.* Protein. Sci., 2016. **25**(8): p. 1551-1554.

267. Alhadeff, R., D. Assa, P. Astrahan, M. Krugliak, and I.T. Arkin, *Computational and experimental analysis of drug binding to the Influenza M2 channel.* Biochim. Biophys. Acta, 2014. **1838**(4): p. 1068-1073.

268. Leonov, H., P. Astrahan, M. Krugliak, and I.T. Arkin, *How do aminoadamantanes block the influenza M2 channel, and how does resistance develop?* J. Am. Chem. Soc., 2011. **133**(25): p. 9903-9911.

269. Wang, J., F. Li, and C. Ma, *Recent progress in designing inhibitors that target the drug-resistant M2 proton channels from the influenza A viruses.* Peptide Science, 2015. **104**(4): p. 291-309.

270. Swanson, J.M.J., C.M. Maupin, H. Chen, M.K. Petersen, J. Xu, Y. Wu, and G.A. Voth, *Proton solvation and transport in aqueous and biomolecular systems: insights from computer simulations.* J. Phys. Chem. B, 2007. **111**(17): p. 4300-4314.

271. Liebschner, D., P.V. Afonine, N.W. Moriarty, B.K. Poon, O.V. Sobolev, T.C. Terwilliger, and P.D. Adams, *Polder maps: improving OMIT maps by excluding bulk solvent.* Acta Crystallogr. D ACTA CRYSTALLOGR D, 2017. **73**(Pt 2): p. 148-157.

272. Chae, P.S., S.G.F. Rasmussen, R. Rana, K. Gotfryd, R. Chandra, M.A. Goren, A.C. Kruse, S. Nurva, C.J. Loland, Y. Pierre, D. Drew, J.-L. Popot, D. Picot, B.G. Fox, L. Guan, U. Gether, B. Byrne, B. Kobilka, and S.H. Gellman, *Maltose-neopentyl glycol (MNG) amphiphiles for solubilization,*

stabilization and crystallization of membrane proteins. Nat. Methods, 2010. **7**(12): p. 1003-1008.

273. Cho, K.H., M. Husri, A. Amin, K. Gotfryd, H.J. Lee, J. Go, J.W. Kim, C.J. Loland, L. Guan, B. Byrne, and P.S. Chae, *Maltose neopentyl glycol-3 (MNG-3) analogues for membrane protein study.* Analyst., 2015. **140**(9): p. 3157-3163.

274. Battye, T.G.G., L. Kontogiannis, O. Johnson, H.R. Powell, and A.G.W. Leslie, *iMOSFLM: a new graphical interface for diffraction-image processing with MOSFLM.* Acta Crystallogr. D ACTA CRYSTALLOGR D, 2011. **67**: p. 271-281.

275. Evans, P., *Scaling and assessment of data quality.* Acta Crystallogr. D ACTA CRYSTALLOGR D, 2006. **62**(1): p. 72-82.

276. Cowtan, K., P. Emsley, and K.S. Wilson, *From crystal to structure with CCP4.* Acta Crystallogr. D ACTA CRYSTALLOGR D, 2011. **67**(4): p. 233-234.

277. Winn, M.D., C.C. Ballard, K.D. Cowtan, E.J. Dodson, P. Emsley, P.R. Evans, R.M. Keegan, E.B. Krissinel, A.G.W. Leslie, A. McCoy, S.J. McNicholas, G.N. Murshudov, N.S. Pannu, E.A. Potterton, H.R. Powell, R.J. Read, A. Vagin, and K.S. Wilson, *Overview of the CCP4 suite and current developments.* Acta Crystallogr. D ACTA CRYSTALLOGR D, 2011. **67**(Pt 4): p. 235-242.

278. McCoy, A.J., R.W. Grosse-Kunstleve, P.D. Adams, M.D. Winn, L.C. Storoni, and R.J. Read, *Phaser crystallographic software.* J. Appl. Crystallogr., 2007. **40**: p. 658-674.

279. Lebedev, A.A. and M.N. Isupov, *Space-group and origin ambiguity in macromolecular structures with pseudo-symmetry and its treatment with the program Zanuda.* Acta Crystallogr. D ACTA CRYSTALLOGR D, 2014. **70**(9): p. 2430-2443.

280. Adams, P.D., P.V. Afonine, G. Bunkoczi, V.B. Chen, I.W. Davis, N. Echols, J.J. Headd, L.W. Hung, G.J. Kapral, R.W. Grosse-Kunstleve, A.J. McCoy, N.W. Moriarty, R. Oeffner, R.J. Read, D.C. Richardson, J.S. Richardson,

T.C. Terwilliger, and P.H. Zwart, *PHENIX: a comprehensive Python-based system for macromolecular structure solution.* Acta Crystallogr. D ACTA CRYSTALLOGR D, 2010. **66**: p. 213-221.

281. Emsley, P., B. Lohkamp, W.G. Scott, and K. Cowtan, *Features and development of Coot.* Acta Crystallogr. D ACTA CRYSTALLOGR D, 2010. **66**: p. 486-501.

282. Schrodinger, L., *The PyMOL molecular graphics system, version 1.3r1*. 2010.

283. Pettersen, E.F., T.D. Goddard, C.C. Huang, G.S. Couch, D.M. Greenblatt, E.C. Meng, and T.E. Ferrin, *UCSF Chimera—a visualization system for exploratory research and analysis.* J. Comput. Chem., 2004. **25**(13): p. 1605-1612.

284. Xavier, D., G. Karl, J. Bernhard, S. Dieter, v.G.W. F., and M.A. E., *Peptide folding: when simulation meets experiment.* Angew Chem Int Ed Engl, 1999. **38**(1-2): p. 236-240.

285. Drakopoulos, A., C. Tzitzoglaki, C. Ma, K. Freudenberger, A. Hoffmann, Y. Hu, G. Gauglitz, M. Schmidtke, J. Wang, and A. Kolocouris, *Affinity of rimantadine enantiomers against influenza A/M2 protein revisited.* ACS Med. Chem. Lett., 2017. **8**(2): p. 145-150.

286. Balgi, A.D., J. Wang, D.Y.H. Cheng, C. Ma, T.A. Pfeifer, Y. Shimizu, H.J. Anderson, L.H. Pinto, R.A. Lamb, W.F. DeGrado, and M. Roberge, *Inhibitors of the influenza A virus M2 proton channel discovered using a high-throughput yeast growth restoration assay.* PLoS One, 2013. **8**(2): p. e55271.

287. Hu, Y., R. Musharrafieh, C. Ma, J. Zhang, D.F. Smee, W.F. DeGrado, and J. Wang, *An M2-V27A channel blocker demonstrates potent in vitro and in vivo antiviral activities against amantadine-sensitive and -resistant influenza A viruses.* Antiviral Res., 2017. **140**: p. 45-54.

288. Kolocouris, A., P. Spearpoint, S.R. Martin, A.J. Hay, M. Lopez-Querol, F.X. Sureda, E. Padalko, J. Neyts, and E. De Clercq, *Comparisons of the influenza virus A M2 channel binding affinities, anti-influenza virus*

potencies and NMDA antagonistic activities of 2-alkyl-2-aminoadamantanes and analogues. Bioorg. Med. Chem. Lett., 2008. **18**(23): p. 6156-6160.

289. Walsh, S.T.R., R.P. Cheng, W.W. Wright, D.O.V. Alonso, V. Daggett, J.M. Vanderkooi, and W.F. DeGrado, *The hydration of amides in helices; a comprehensive picture from molecular dynamics, IR, and NMR.* Protein Sci., 2003. **12**(3): p. 520-531.

290. Kim, W., W. Zhu, G.L. Hendricks, D. Van Tyne, A.D. Steele, C.E. Keohane, N. Fricke, A.L. Conery, S. Shen, W. Pan, K. Lee, R. Rajamuthiah, B.B. Fuchs, P.M. Vlahovska, W.M. Wuest, M.S. Gilmore, H. Gao, F.M. Ausubel, and E. Mylonakis, *A new class of synthetic retinoid antibiotics effective against bacterial persisters.* Nature, 2018. **556**: p. 103.

291. Raska, I. and A. Toropov, *Comparison of QSPR models of octanol/water partition coefficient for vitamins and non vitamins.* Eur. J. Med. Chem., 2006. **41**(11): p. 1271-1278.

292. Vijayakumar, V., B.G. Alka, B.K. Godwal, and S.K. Sikka, *Pressure induced phase transitions and equation of state of adamantane.* J. Phys. Condens. Matter, 2001. **13**(9): p. 1961.

293. Durrant, M.G., D.L. Eggett, and D.D. Busath, *Investigation of a recent rise of dual amantadine-resistance mutations in the influenza A M2 sequence.* BMC Genet., 2015. **16**(2): p. S3.

294. Mould, J.A., J.E. Drury, S.M. Frings, U.B. Kaupp, A. Pekosz, R.A. Lamb, and L.H. Pinto, *Permeation and activation of the M-2 ion channel of influenza A virus.* Journal of Biological Chemistry, 2000. **275**(40): p. 31038-31050.

295. Sakaguchi T, L.G., Lamb RA, *The ion channel activity of the influenza virus M2 protein affects transport through the Golgi apparatus.* The Journal of Cell Biology, 1996. **133**(4): p. 733-747.

296. Sheu, T.G., A.M. Fry, R.J. Garten, V.M. Deyde, T. Shwe, L. Bullion, P.J. Peebles, Y. Li, A.I. Klimov, and L.V. Gubareva, *Dual Resistance to Adamantanes and Oseltamivir Among Seasonal Influenza A(H1N1)*

Viruses: 2008–2010. The Journal of Infectious Diseases, 2011. **203**(1): p. 13-17.

297. Zhou, J., L. Zou, X. Zhang, J. Liao, H. Ni, N. Hou, Y. Wang, H. Li, J. Wu, M. Jonges, A. Meijer, M. Koopmans, and C. Ke, *Adamantane- and oseltamivir-resistant seasonal A (H1N1) and pandemic A (H1N1) 2009 influenza viruses in Guangdong, China, during 2008 and 2009.* Journal of clinical microbiology, 2011. **49**(7): p. 2651-2655.

298. Garcia, V. and S. Aris-Brosou, *Comparative dynamics and distribution of influenza drug resistance acquisition to protein m2 and neuraminidase inhibitors.* Molecular biology and evolution, 2014. **31**(2): p. 355-363.

299. Dong, G., C. Peng, J. Luo, C. Wang, L. Han, B. Wu, G. Ji, and H. He, *Adamantane-resistant influenza A viruses in the world (1902-2013): frequency and distribution of M2 gene mutations.* PLoS One, 2015. **10**(3): p. e0119115.

300. Furuse, Y., A. Suzuki, and H. Oshitani, *Large-Scale Sequence Analysis of M Gene of Influenza A Viruses from Different Species: Mechanisms for Emergence and Spread of Amantadine Resistance.* Antimicrobial Agents and Chemotherapy, 2009. **53**(10): p. 4457-4463.

301. Baranovich, T., J. Bahl, B.M. Marathe, M. Culhane, E. Stigger-Rosser, D. Darnell, B.S. Kaplan, J.F. Lowe, R.J. Webby, and E.A. Govorkova, *Influenza A viruses of swine circulating in the United States during 2009-2014 are susceptible to neuraminidase inhibitors but show lineage-dependent resistance to adamantanes.* Antiviral Research, 2015. **117**: p. 10-19.

302. Moasser, E., A. Moasser, and H. Zaraket, *Incidence of antiviral drug resistance markers among human influenza A viruses in the Eastern Mediterranean Region, 2005–2016.* Infection, Genetics and Evolution, 2019. **67**: p. 60-66.

303. Suzuki, H., R. Saito, H. Masuda, H. Oshitani, M. Sato, and I. Sato, *Emergence of amantadine-resistant influenza A viruses: epidemiological study.* Journal of Infection and Chemotherapy, 2003. **9**(3): p. 195-200.

304. Rey-Carrizo, M., M. Barniol-Xicota, C. Ma, M. Frigolé-Vivas, E. Torres, L. Naesens, S. Llabrés, J. Juárez-Jiménez, F.J. Luque, W.F. DeGrado, R.A. Lamb, L.H. Pinto, and S. Vázquez, *Easily accessible polycyclic amines that inhibit the wild-type and amantadine-resistant mutants of the M2 channel of influenza A virus.* Journal of Medicinal Chemistry, 2014. **57**(13): p. 5738-5747.

305. Rey-Carrizo, M., S. Gazzarrini, S. Llabrés, M. Frigolé-Vivas, J. Juárez-Jiménez, M. Font-Bardia, L. Naesens, A. Moroni, F.J. Luque, and S. Vázquez, *New polycyclic dual inhibitors of the wild type and the V27A mutant M2 channel of the influenza A virus with unexpected binding mode.* European Journal of Medicinal Chemistry, 2015. **96**: p. 318-329.

306. Rey-Carrizo, M., E. Torres, C. Ma, M. Barniol-Xicota, J. Wang, Y. Wu, L. Naesens, W.F. DeGrado, R.A. Lamb, L.H. Pinto, and S. Vázquez, *3-Azatetracyclo[5.2.1.1(5,8).0(1,5)]undecane derivatives: from wild-type inhibitors of the M2 ion channel of influenza A virus to derivatives with potent activity against the V27A mutant.* Journal of Medicinal Chemistry, 2013. **56**(22): p. 9265-9274.

307. Höfer, N., D. Aragão, and M. Caffrey, *Crystallizing transmembrane peptides in lipidic mesophases.* Biophysical Journal, 2010. **99**(3): p. L23-L25.

308. Liu, W. and M. Caffrey, *Gramicidin structure and disposition in highly curved membranes.* Journal of Structural Biology, 2005. **150**(1): p. 23-40.

309. Thomaston, J.L.W., Y.; Polizzi, N.; Liu, L.; Wang, J.; DeGrado, W. F., *X-ray crystal structure of the influenza A M2 proton channel S31N mutant in two conformational states: an open and shut case.* J. Am. Chem. Soc., 2019. **141**(29): p. 11481-11488.

310. Kabsch, W., *XDS.* Acta Crystallographica Section D, 2010. **66**(2): p. 125-132.

311. Strong, M., M.R. Sawaya, S. Wang, M. Phillips, D. Cascio, and D. Eisenberg, *Toward the structural genomics of complexes: Crystal structure of a PE/PPE protein complex from Mycobacterium tuberculosis.* Proceedings of the National Academy of Sciences, 2006. **103**(21): p. 8060.

312. Coleman, R.G. and K.A. Sharp, *Finding and characterizing tunnels in macromolecules with application to ion channels and pores.* Biophys. J., 2009. **96**(2): p. 632-645.

313. Humphreys, D.D., R.A. Friesner, and B.J. Berne, *A multiple-time-step molecular dynamics algorithm for macromolecules.* J. Phys. Chem., 1994. **98**(27): p. 6885-6892.

314. Khurana, E., M. Dal Peraro, R. DeVane, S. Vemparala, W.F. DeGrado, and M.L. Klein, *Molecular dynamics calculations suggest a conduction mechanism for the M2 proton channel from influenza A virus.* Proc Natl Acad Sci U S A, 2009. **106**(4): p. 1069-74.

315. Yi, M., T.A. Cross, and H.X. Zhou, *A secondary gate as a mechanism for inhibition of the M2 proton channel by amantadine.* J Phys Chem B, 2008. **112**(27): p. 7977-9.

316. Pielak, R.M. and J.J. Chou, *Solution NMR structure of the V27A drug resistant mutant of influenza A M2 channel.* Biochemical and Biophysical Research Communications, 2010. **401**(1): p. 58-63.

317. Duff, K.C. and R.H. Ashley, *The transmembrane domain of influenza A M2 protein forms amantadine-sensitive proton channels in planar lipid bilayers.* Virology, 1992. **190**(1): p. 485-489.

318. Ma, C.L., A.L. Polishchuk, Y. Ohigashi, A.L. Stouffer, A. Schon, E. Magavern, X.H. Jing, J.D. Lear, E. Freire, R.A. Lamb, W.F. DeGrado, and L.H. Pinto, *Identification of the functional core of the influenza A virus A/M2 proton-selective ion channel.* Proceedings of the National Academy of Sciences, 2009. **106**(30): p. 12283-12288.

319. Roberts, K.L., G.P. Leser, C. Ma, and R.A. Lamb, *The amphipathic helix of influenza A virus M2 protein is required for filamentous bud formation and scission of filamentous and spherical particles.* Journal of Virology, 2013. **87**(18): p. 9973-9982.

320. Sugrue, R.J., R.B. Belshe, and A.J. Hay, *Palmitoylation of the influenza a virus M2 protein.* Virology, 1990. **179**(1): p. 51-56.

321. Pielak, R.M., J.R. Schnell, and J.J. Chou, *Mechanism of drug inhibition and drug resistance of influenza A M2 channel.* Proceedings of the National Academy of Sciences of the United States of America, 2009. **106**(18): p. 7379-7384.

322. Claridge, J.K., J. Aittoniemi, D.M. Cooper, and J.R. Schnell, *Isotropic Bicelles Stabilize the Juxtamembrane Region of the Influenza M2 Protein for Solution NMR Studies.* Biochemistry, 2013. **52**(47): p. 8420-8429.

323. Llabres, S., J. Juarez-Jimenez, M. Masetti, R. Leiva, S. Vazquez, S. Gazzarrini, A. Moroni, A. Cavalli, and F.J. Luque, *Mechanism of the pseudoirreversible binding of amantadine to the M2 proton channel.* J. Am. Chem. Soc., 2016. **138**(47): p. 15345-15358.

324. Mustafa, M., D.J. Henderson, and D.D. Busath, *Free-energy profiles for ions in the influenza M2-TMD channel.* Proteins, 2009. **76**(4): p. 794-807.

325. Wei, C. and A. Pohorille, *Activation and proton transport mechanism in influenza A M2 channel.* Biophys. J., 2013. **105**(9): p. 2036-2045.

326. To, J., W. Surya, and J. Torres, *Targeting the Channel Activity of Viroporins.* Adv Protein Chem Struct Biol, 2016. **104**: p. 307-355.

327. Bright, R.A., M.J. Medina, X.Y. Xu, G. Perez-Oronoz, T.R. Wallis, X.H.M. Davis, L. Povinelli, N.J. Cox, and A.I. Klimov, *Incidence of adamantane resistance among influenza A (H3N2) viruses isolated worldwide from 1994 to 2005: a cause for concern.* Lancet, 2005. **366**(9492): p. 1175-1181.

328. Lampejo, T., *Influenza and antiviral resistance: an overview.* European journal of clinical microbiology & infectious diseases : official publication of the European Society of Clinical Microbiology, 2020. **39**(7): p. 1201-1208.

329. Chizhmakov, I.V., F.M. Geraghty, D.C. Ogden, A. Hayhurst, M. Antoniou, and A.J. Hay, *Selective proton permeability and pH regulation of the influenza virus M2 channel expressed in mouse erythroleukaemia cells.* Journal of Physiology-London, 1996. **494**(2): p. 329-336.

330. Lin, T.I. and C. Schroeder, *Definitive assignment of proton selectivity and attoampere unitary current to the M2 ion channel protein of influenza A virus.* Journal of Virology, 2001. **75**(8): p. 3647-3656.

331. Shimbo, K., D.L. Brassard, R.A. Lamb, and L.H. Pinto, *Ion selectivity and activation of the M2 ion channel of influenza virus.* Biophysical Journal, 1996. **70**(3): p. 1335-1346.

332. Tang, Y.J., F. Zaitseva, R.A. Lamb, and L.H. Pinto, *The gate of the influenza virus M-2 proton channel is formed by a single tryptophan residue.* Journal of Biological Chemistry, 2002. **277**(42): p. 39880-39886.

333. Wang, C., R.A. Lamb, and L.H. Pinto, *Activation of the M2 ion channel of influenza virus: a role for the transmembrane domain histidine residue.* Biophysical Journal, 1995. **69**(4): p. 1363-71.

334. Hay, A.J., A.J. Wolstenholme, J.J. Skehel, and M.H. Smith, *The molecular basis of the specific anti-influenza action of amantadine.* The EMBO Journal, 1985. **4**(11): p. 3021-3024.

335. Wang, C., K. Takeuchi, L.H. Pinto, and R.A. Lamb, *Ion-channel activity of influenza-A virus M(2) protein - characterization of the amantadine block.* J. Virol., 1993. **67**(9): p. 5585-5594.

336. Drakopoulos, A., C. Tzitzoglaki, K. McGuire, A. Hoffmann, A. Konstantinidi, D. Kolokouris, C. Ma, K. Freudenberger, J. Hutterer, G. Gauglitz, J. Wang, M. Schmidtke, D.D. Busath, and A. Kolocouris, *Unraveling the Binding, Proton Blockage, and Inhibition of Influenza M2 WT and S31N by Rimantadine Variants.* ACS Medicinal Chemistry Letters, 2018. **9**(3): p. 198-203.

337. Duque, M.D., C. Ma, E. Torres, J. Wang, L. Naesens, J. Juárez-Jiménez, P. Camps, F.J. Luque, W.F. DeGrado, R.A. Lamb, L.H. Pinto, and S. Vázquez, *Exploring the Size Limit of Templates for Inhibitors of the M2 Ion Channel of Influenza A Virus.* Journal of Medicinal Chemistry, 2011. **54**(8): p. 2646-2657.

338. Skehel, J.J., A.J. Hay, and J.A. Armstrong, *On the mechanism of inhibition of influenza virus replication by amantadine hydrochloride.* J Gen Virol, 1978. **38**(1): p. 97-110.

339. Ciampor, F., P.M. Bayley, M.V. Nermut, E.M.A. Hirst, R.J. Sugrue, and A.J. Hay, *Evidence that the amantadine-induced, M2-mediated conversion of*

influenza-A virus hemagglutinin to the low pH conformation occurs in an acidic transgolgi compartment. Virology, 1992. **188**(1): p. 14-24.

340. Sugrue, R.J., G. Bahadur, M.C. Zambon, M. Hall-Smith, A.R. Douglas, and A.J. Hay, *Specific structural alteration of the influenza haemagglutinin by amantadine.* The EMBO Journal, 1990. **9**(11): p. 3469-3476.

341. Wright, A.K., P. Batsomboon, J. Dai, I. Hung, H.-X. Zhou, G.B. Dudley, and T.A. Cross, *Differential Binding of Rimantadine Enantiomers to Influenza A M2 Proton Channel.* Journal of the American Chemical Society, 2016. **138**(5): p. 1506-1509.

342. Drakopoulos, A., C. Tzitzoglaki, C. Ma, K. Freudenberger, A. Hoffmann, Y. Hu, G. Gauglitz, M. Schmidtke, J. Wang, and A. Kolocouris, *Affinity of rimantadine enantiomers against influenza A/M2 protein revisited.* ACS Medicinal Chemistry Letters, 2017. **8**(2): p. 145-150.

343. Aldrich, P.E., E.C. Hermann, W.E. Meier, M. Paulshock, W.W. Prichard, J.A. Synder, and J.C. Watts, *Antiviral agents. 2. Structure-activity relations of compounds related to 1-adamantanamine.* Journal of Medicinal Chemistry, 1971. **14**(6): p. 535-543.

344. Skehel, J.J., A.J. Hay, and J.A. Armstrong, *On the mechanism of inhibition of influenza virus replication by amantadine hydrochloride.* J. Gen. Virol., 1978. **38**(1): p. 97-110.

345. Bruce Macdonald, H.E., C. Cave-Ayland, G.A. Ross, and J.W. Essex, *Ligand Binding Free Energies with Adaptive Water Networks: Two-Dimensional Grand Canonical Alchemical Perturbations.* Journal of Chemical Theory and Computation, 2018. **14**(12): p. 6586-6597.

346. Ross, G.A., M.S. Bodnarchuk, and J.W. Essex, *Water Sites, Networks, And Free Energies with Grand Canonical Monte Carlo.* Journal of the American Chemical Society, 2015. **137**(47): p. 14930-14943.

347. Ross, G.A., H.E. Bruce Macdonald, C. Cave-Ayland, A.I. Cabedo Martinez, and J.W. Essex, *Replica-Exchange and Standard State Binding Free Energies with Grand Canonical Monte Carlo.* Journal of Chemical Theory and Computation, 2017. **13**(12): p. 6373-6381.

348. Musharrafieh, R., P. Lagarias, C. Ma, R. Hau, A. Romano, G. Lambrinidis, A. Kolocouris, and J. Wang, *Investigation of the Drug Resistance Mechanism of M2-S31N Channel Blockers through Biomolecular Simulations and Viral Passage Experiments.* ACS Pharmacology & Translational Science, 2020. **3**(4): p. 666-675.

349. Musharrafieh, R., C. Ma, and J. Wang, *Profiling the in vitro drug-resistance mechanism of influenza A viruses towards the AM2-S31N proton channel blockers.* Antiviral Res., 2018. **153**: p. 10-22.

350. Wang, Y., Y. Hu, S. Xu, Y. Zhang, R. Musharrafieh, R.K. Hau, C. Ma, and J. Wang, *In Vitro Pharmacokinetic Optimizations of AM2-S31N Channel Blockers Led to the Discovery of Slow-Binding Inhibitors with Potent Antiviral Activity against Drug-Resistant Influenza A Viruses.* Journal of Medicinal Chemistry, 2018. **61**(3): p. 1074-1085.

351. Tembre, B.L. and J.A. Mc Cammon, *Ligand-receptor interactions.* Computers & Chemistry, 1984. **8**(4): p. 281-283.

352. Zwanzig, R.W., *High-Temperature Equation of State by a Perturbation Method. I. Nonpolar Gases.* The Journal of Chemical Physics, 1954. **22**(8): p. 1420-1426.

353. Bennett, C.H., *Efficient estimation of free energy differences from Monte Carlo data.* J. Comput. Phys., 1976. **22**(2): p. 245-268.

354. Shirts, M.R. and J.D. Chodera, *Statistically optimal analysis of samples from multiple equilibrium states.* The Journal of Chemical Physics, 2008. **129**(12): p. 124105-124105.

355. Cournia, Z., B. Allen, and W. Sherman, *Relative Binding Free Energy Calculations in Drug Discovery: Recent Advances and Practical Considerations.* Journal of Chemical Information and Modeling, 2017. **57**(12): p. 2911-2937.

356. Ioannidis, H., A. Drakopoulos, C. Tzitzoglaki, N. Homeyer, F. Kolarov, P. Gkeka, K. Freudenberger, C. Liolios, G. Gauglitz, Z. Cournia, H. Gohlke, and A. Kolocouris, *Alchemical Free Energy Calculations and Isothermal Titration Calorimetry Measurements of Aminoadamantanes Bound to the*

Closed State of Influenza A/M2TM. Journal of Chemical Information and Modeling, 2016. **56**(5): p. 862-876.

357. Ma, C., F. Li, R.G. Musharrafieh, and J. Wang, *Discovery of cyclosporine A and its analogs as broad-spectrum anti-influenza drugs with a high in vitro genetic barrier of drug resistance.* Antiviral Research, 2016. **133**: p. 62-72.

358. Ma, C., J. Zhang, and J. Wang, *Pharmacological Characterization of the Spectrum of Antiviral Activity and Genetic Barrier to Drug Resistance of M2-S31N Channel Blockers.* Molecular pharmacology, 2016. **90**(3): p. 188-198.

359. Lindorff-Larsen, K., S. Piana, K. Palmo, P. Maragakis, J.L. Klepeis, R.O. Dror, and D.E. Shaw, *Improved side-chain torsion potentials for the Amber ff99SB protein force field.* Proteins: Structure, Function, and Bioinformatics, 2010. **78**(8): p. 1950-1958.

360. Wang, J., R.M. Wolf, J.W. Caldwell, P.A. Kollman, and D.A. Case, *Development and testing of a general amber force field.* J Comput Chem, 2004. **25**(9): p. 1157-74.

361. Wang, J., W. Wang, P.A. Kollman, and D.A. Case, *Automatic atom type and bond type perception in molecular mechanical calculations.* J Mol Graph Model, 2006. **25**(2): p. 247-60.

362. Case, D.A., I.Y. Ben-Shalom, S.R. Brozell, D.S. Cerutti, T.E. Cheatham III, V.W.D. Cruzeiro, T.A. Darden, R.E. Duke, D. Ghoreishi, M.K. Gilson, H. Gohlke, A.W. Goetz, D. Greene, R. Harris, N. Homeyer, S. Izadi, A. Kovalenko, T. Kurtzman, T.S. Lee, S. LeGrand, P. Li, C. Lin, J. Liu, T. Luchko, R. Luo, D.J. Mermelstein, K.M. Merz, Y. Miao, G. Monard, C. Nguyen, H. Nguyen, I. Omelyan, A. Onufriev, F. Pan, R. Qi, D.R. Roe, A. Roitberg, C. Sagui, S. Schott-Verdugo, J. Shen, C.L. Simmerling, J. Smith, R. SalomonFerrer, J. Swails, R.C. Walker, J. Wang, H. Wei, R.M. Wolf, X. Wu, L. Xiao, D.M. York, and P.A. Kollman, *AMBER18.* 2018.

363. Laage, D., T. Elsaesser, and J.T. Hynes, *Water Dynamics in the Hydration Shells of Biomolecules.* Chemical Reviews, 2017. **117**(16): p. 10694-10725.

364. Deng, Y. and B. Roux, *Computation of binding free energy with molecular dynamics and grand canonical Monte Carlo simulations.* J Chem Phys, 2008. **128**(11): p. 115103.

365. Woo, H.-J., A.R. Dinner, and B. Roux, *Grand canonical Monte Carlo simulations of water in protein environments.* Journal of Chemical Physics, 2004. **121**: p. 6392-6400.

366. Mezei, M., *Grand-canonical ensemble Monte Carlo study of dense liquid.* Molecular Physics, 1987. **61**(3): p. 565-582.

367. Adams, D.J., *Grand canonical ensemble Monte Carlo for a Lennard-Jones fluid.* Molecular Physics, 1975. **29**(1): p. 307-311.

368. Mezei, M., *A cavity-biased (T, V, μ) Monte Carlo method for the computer simulation of fluids.* Molecular Physics, 1980. **40**(4): p. 901-906.

369. Adams, D.J., *Chemical potential of hard-sphere fluids by Monte Carlo methods.* Molecular Physics, 1974. **28**(5): p. 1241-1252.

370. Eastman, P., J. Swails, J.D. Chodera, R.T. McGibbon, Y. Zhao, K.A. Beauchamp, L.P. Wang, A.C. Simmonett, M.P. Harrigan, C.D. Stern, R.P. Wiewiora, B.R. Brooks, and V.S. Pande, *OpenMM 7: Rapid development of high performance algorithms for molecular dynamics.* PLoS Comput Biol, 2017. **13**(7): p. e1005659.

371. Samways, M.L., H.E. Bruce Macdonald, and J.W. Essex, *grand: A Python Module for Grand Canonical Water Sampling in OpenMM.* Journal of Chemical Information and Modeling, 2020. **60**(10): p. 4436-4441.

372. Rufa, D.A., H.E. Bruce Macdonald, J. Fass, M. Wieder, P.B. Grinaway, A.E. Roitberg, O. Isayev, and J.D. Chodera, *Towards chemical accuracy for alchemical free energy calculations with hybrid physics-based machine learning / molecular mechanics potentials.* bioRxiv, 2020: p. 2020.07.29.227959.

373. Grinaway, P.B.B., J. M.; Bruce Macdonald, H. E.; Rufa, D. A.; Chodera, J. D. , *Perses.* 2020.

374. Beauchamp, K.A.C., J. D.; Naden, L.; Shirts, M. R.; Martiniani, S.; Stern, C. D.; McGibbon, R. T.; Gowers, R.; Dotson, D., *Pymbar.* 2019.

375. Dickson, C.J., B.D. Madej, A.A. Skjevik, R.M. Betz, K. Teigen, I.R. Gould, and R.C. Walker, *Lipid14: The Amber Lipid Force Field.* Journal of Chemical Theory and Computation, 2014. **10**(2): p. 865-879.

376. Jorgensen, W.L., J. Chandrasekhar, J.D. Madura, R.W. Impey, and M.L. Klein, *Comparison of simple potential functions for simulating liquid water.* The Journal of Chemical Physics, 1983. **79**(2): p. 926-935.

377. Joung, I.S. and T.E. Cheatham, *Molecular Dynamics Simulations of the Dynamic and Energetic Properties of Alkali and Halide Ions Using Water-Model-Specific Ion Parameters.* The Journal of Physical Chemistry B, 2009. **113**(40): p. 13279-13290.

378. Joung, I.S. and T.E. Cheatham, *Determination of Alkali and Halide Monovalent Ion Parameters for Use in Explicitly Solvated Biomolecular Simulations.* The Journal of Physical Chemistry B, 2008. **112**(30): p. 9020-9041.

379. Jakalian, A., D.B. Jack, and C.I. Bayly, *Fast, efficient generation of high-quality atomic charges. AM1-BCC model: II. Parameterization and validation.* Journal of Computational Chemistry, 2002. **23**(16): p. 1623-1641.

380. Darden, T., D. York, and L. Pedersen, *Particle mesh Ewald: An N·log(N) method for Ewald sums in large systems.* The Journal of Chemical Physics, 1993. **98**(12): p. 10089-10092.

381. Leimkuhler, B. and C. Matthews, *Rational Construction of Stochastic Numerical Methods for Molecular Sampling.* Applied Mathematics Research eXpress, 2013. **2013**(1): p. 34-56.

382. Fass, J., D.A. Sivak, G.E. Crooks, K.A. Beauchamp, B. Leimkuhler, and J.D. Chodera, *Quantifying Configuration-Sampling Error in Langevin Simulations of Complex Molecular Systems.* Entropy (Basel, Switzerland), 2018. **20**(5).

383. Miyamoto, S. and P.A. Kollman, *Settle: An analytical version of the SHAKE and RATTLE algorithm for rigid water models.* Journal of Computational Chemistry, 1992. **13**(8): p. 952-962.

384. Yoneya, M., H.J.C. Berendsen, and K. Hirasawa, *A Non-Iterative Matrix Method for Constraint Molecular Dynamics Simulations.* Molecular Simulation, 1994. **13**(6): p. 395-405.